2018-01-23

Fe-Catalyzed Ca-H Oxidation of Tertiary Amines: Synthetic and Mechanistic Studies

Christopher J. Legacy
Worcester Polytechnic Institute

Worcester Polytechnic Institute
Department of Chemistry and Biochemistry

Fe-Catalyzed C_α-H Oxidation of Tertiary Amines: Synthetic and Mechanistic Studies

A Dissertation Submitted in Partial Fulfillment of the Requirements for the Degree of Doctor of Philosophy in Chemistry

Presented by
Christopher J. Legacy

Advisor: Marion H. Emmert

-**Dec 2017**-

Acknowledgements

It is my pleasure to thank the many people who made this dissertation possible with their never-ending support and encouragement. Foremost, I would like to express my sincerest gratitude to my advisor Dr. Marion H. Emmert for the continuous support and encouragement, and the opportunity to carry out meaningful research in a field I am passionate about. Her motivation, advice, patience, and unsurpassed knowledge have been invaluable. Her counsel has not only helped me with my research and thesis, but also in becoming a better scientist and professional, for which I am forever grateful.

I would like to thank the other members of my committee. The guidance and feedback provided by Dr. John C. MacDonald, Dr. Shawn C. Burdette, and Dr. Amy. M. Peterson has been a valuable source of information and support.

I would also like to thank my undergraduate advisor, Dr. Sergio Granados-Focil for providing me with a strong foundation in chemistry through many patient conversations.

I would like to thank all the group members of the Emmert Research Group for providing a stimulating, cooperative and productive research environment. I am especially grateful to Anqi Wang for his assistance, positive attitude and friendship, and to Dhammika Bandara for helping me gain a solid footing in the Emmert lab upon my arrival.

I would also like to thank Andy Butler and Daryl Johnson for their continuous support. Their dedication to instrument maintenance and research support is a shining example of unwavering professionalism.

I am indebted to everyone in the Chemistry and Biochemistry department at Worcester Polytechnic Institute for providing me with a research environment in which I was able to advance my understanding of chemistry.

To Anne-Marie: I cannot imagine having succeeded without your loving support and scientific input. This is for us.

My heartfelt thanks goes to my sister Katie for her grounded perspective and to my brothers Byron and Matt, without whom my sanity would remain elusive.

Lastly, and most importantly, I wish to thank my father, for a lifetime of support and wisdom, and for showing me the value of dedicated, persistent work.

To you all I dedicate this dissertation.

Abstract

Presented herein is the development, optimization and mechanistic investigation of an Fe catalyzed reaction for the C_α-H oxidation of tertiary aliphatic amines to form amides, and related synthetic reactions. Traditional amide synthesis typically involves nucleophilic substitution, and thus produces stoichiometric waste. The need to develop safer, more efficient methodologies for amide synthesis is well documented. The field of transition metal catalysis has made progress toward meeting this synthetic need by developing a variety of transition metal-catalyzed reactions for the oxidation of primary, secondary and benzylic amines. However, tertiary aliphatic C_α-H amine oxidation had not been developed. Guided by literature precedent, and inspired by cytochrome P450, initial investigations involved the evaluation of Fe-based transition metal catalysts with a variety of mono- and bidentate ligands, oxidants and solvents. Ultimately, the ligands picolinic acid and pyridine, the oxidant *tert*-butyl peroxybenzoate, and water as additive were identified as key players in this catalytic reaction. Through the systematic evaluation of reaction conditions, the C_α-H oxidation of tripropylamine to form *N*,*N*-dipropylpropanamide was optimized to afford 63% yield. The C_α-H oxidation of a variety of other amine substrates, including the complex pharmaceutical amines Lidocaine and Donepezil, were optimized to afford amide product in synthetically useful yields. Preliminary mechanistic investigations revealed water to be the source of the O atom in amide formation. Furthermore, these studies suggested that the amine substrate forms an iminium ion after C-H activation, which then undergoes nucleophilic attack by water to form a hemiaminal intermediate. These results allowed us to hypothesize that other nucleophiles, such as CN^-, may be used to attack the iminium ion intermediate and thus afford other products. Using slightly modified reaction conditions, this catalytic system was optimized to perform C_α -H cyanation of dimethylaniline. This finding expanded the utility of the reaction as well as supported the mechanistic hypothesis of the presence of an iminium intermediate.

Once the Fe/picolinic acid-catalyzed reaction for the C_α-H oxidation of tertiary aliphatic amines was firmly established, detailed mechanistic investigations were conducted using tripropylamine as substrate. Using *in-situ* IR spectroscopy, the structure of the resting state of the catalyst was probed. These studies revealed that picolinic acid binds to the Fe center in a 1:1 ratio to produce the catalytically active species. Amine substrate as well as water and pyridine were also found to be

coordinated to the Fe center. Furthermore, initial rate kinetics were used to establish the dependence of the reaction rate on the concentration of each reaction component. Through these investigations, the kinetic order in each reagent was established and a rate law determined. Additionally, a primary kinetic isotope effect was observed using deuterated substrate, which implicated C-H bond cleavage as the turnover-limiting step in the catalytic cycle. Finally, Eyring studies and oxidant radical probe reactions were conducted, and implicated a concerted $2e^-$ turnover-limiting step. This finding is in contrast to many mechanisms of Fe-catalyzed oxidation reactions found in the literature and allowed us to propose the unprecedented, detailed mechanistic hypothesis described herein.

The research presented here establishes an unprecedented amide synthesis methodology through the use of both simple and complex amines. Because this catalytic reaction selectively oxidizes the C_α-H bonds of amines, a high percentage of atoms in the starting material are incorporated into the amide product, and it thus affords a significant increase in atom economy. The mechanistic work offers unique insight into $2e^-$ Fe-oxidation catalysis, and may serve as a foundation for additional optimization, including industrial scale-up.

Table of Contents

1 Introduction

1.1 Importance of Amide Synthesis

Amides are pervasive chemical substructures that can be found in a wide variety of chemical classes, such as pharmaceuticals and natural products, and in many high tensile strength materials such as nylon and Kevlar, and heat- and flame-resistant materials like Nomex that are critical to our society [1]. Furthermore, the active pharmaceutical ingredients (APIs) of the drugs Abilify™ and Zetia™, as well as many others, contain one or more amide functional groups (Figure 1).

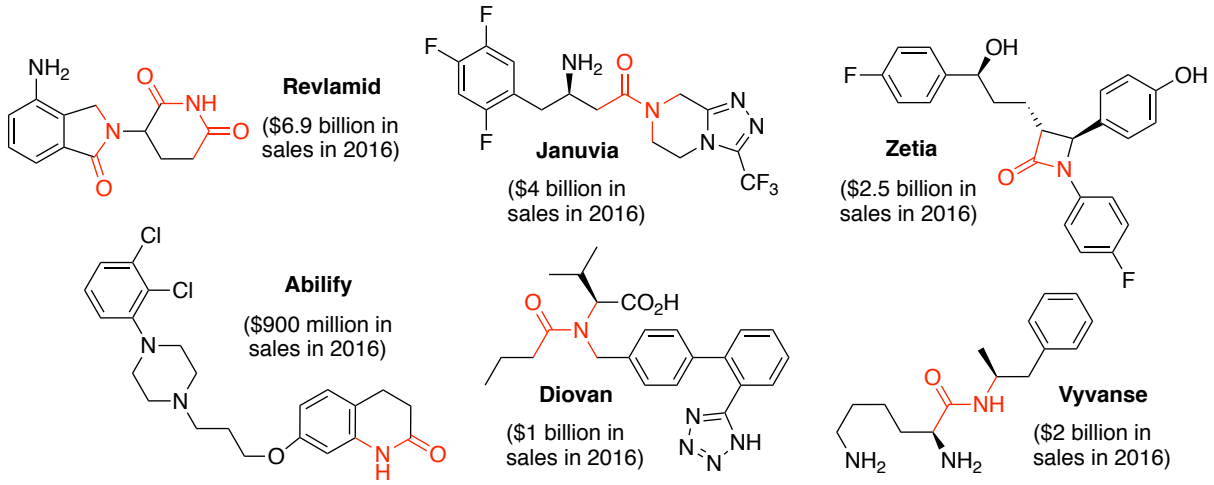

Figure 1: Mass-Produced Pharmaceuticals Containing Amide Functional Groups.

Amides are also defining substructures in proteins and are thus crucial to their study [2]. Although there are many well-established traditional synthetic methodologies that afford amides, they suffer from deficiencies such as low atom economies and harsh conditions [3]. Most rely on nucleophilic substitution reactions using toxic reagents such as acid chlorides and nitriles in the presence of base, and thus generate stoichiometric amounts of chemical waste (Scheme 1). Because of the high demand for amide-containing compounds as well as the unsustainable nature of traditional amide syntheses, research that explores milder and more economic methodologies is highly attractive [4].

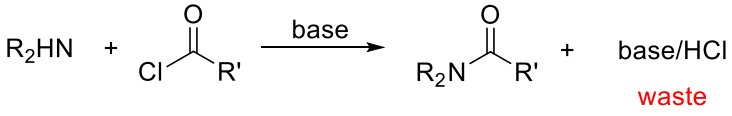

Scheme 1: Conventional Synthesis of Amides.

The described challenges have not gone unnoticed in the pharmaceutical industry, where amide synthesis is heavily utilized. According to the ACS Green Chemistry Institute, a general consensus among many of the world's major pharmaceutical companies, including AstraZeneca, Johnson & Johnson, Merck and Pfizer, is that discovering efficient — preferably catalytic — methodologies for amide formation is one of the most important and challenging problems currently faced by the pharmaceutical industry [3].

1.2 Transition Metal Catalysis for Sustainability

Transition metals have long been known to possess catalytic properties, and many have been incorporated into important chemical processes [5-8]. Transition metal catalysts are of great interest to synthetic chemists due to their ability to lower the activation energy of chemical transformations, thus enabling new reactions and/or allowing reactions to proceed under milder conditions. Catalysis also promotes more environmentally-friendly—and thus human-friendly—synthetic practices by allowing chemical reactions to proceed with relatively benign reagents. This "green" approach promotes the advancement of synthetic chemistry while using less energy and improving sustainability [9].

Many traditional protocols in synthetic chemistry rely on stoichiometric amounts of toxic reagents, with the vast majority having been developed solely with the target molecule in mind, with little attention given to cost, efficiency or safety. Of the many reaction classes with the potential for improvement with transition metal catalysis, oxidation reactions stand out for their use of particularly harsh reagents. Oxidants such as *meta*-chloroperoxybenzoic acid and pyridinium chlorochromate are commonly used in these reactions [10, 11]. Since benign stoichiometric oxidation reagents are not widely available to synthetic chemists, milder oxidation methodologies are strong candidates for current research in the catalysis field [12]. Transition metal catalysts can facilitate oxidation with the use of relatively mild oxidants such as hydrogen peroxide and air [13, 14]. In addition to being less toxic, these oxidants promote environmentally-friendly chemistry by forming only water as the side product [15]. Thus, transition metal-catalyzed oxidation reactions offer alternatives to traditional, unsustainable chemical practices.

1.3 Transition Metal-Catalyzed C-H Activation

One application of transition metal catalysts, the activation of otherwise inert carbon-hydrogen (C-H) bonds, has garnered a significant amount of attention from the scientific community [16]. To cleave and functionalize highly stable C-H bonds in an efficient, selective, and functional-group tolerant manner has been a long-standing challenge for synthetic chemists due to their high bond dissociation energies (Scheme 2) [17].

Bond	ΔH° kJ/mol
CH_3-H	435
CH_3-Cl	351
CH_3-Br	293
CH_3-I	234

Scheme 2: Bond Dissociation Energies of Selected C-H Bonds.

It is well documented that transition metals with vacant coordination sites, along with compatible ligands have the ability bring specific, otherwise unreactive C-H bonds of substrates into close proximity to the metal center and facilitate the stepwise chemical reactions necessary to overcome the large bond dissociation energies of C-H bonds. For decades, the field of transition metal catalysis has been making strides toward fully exploiting transition metals to solve important synthetic problems. One of the key aspects of environmentally-conscious synthetic chemistry (herein referred to as Green Chemistry) is the improvement of reaction atom economy [18]. That is, synthetic reactions must be optimized to include as much starting material mass in the final product, with little going to waste, or else be replaced with new, greener methodologies. Transition metal-catalyzed-reactions are in alignment with this goal, as direct C-H bond functionalization typically circumvents the need for wasteful protecting groups or stoichiometric leaving groups [19].

1.3.1 General Mechanisms of C-H Activation

Transition metal catalysts have allowed chemists to design unprecedented synthetic reactions by enabling C-H bond cleavage and subsequent functionalization, many times in one pot/step [20]. Although a multitude of specific mechanistic

hypotheses have been proposed over the decades, the mechanisms C-H activation fall into one of the following general categories (Scheme 3).

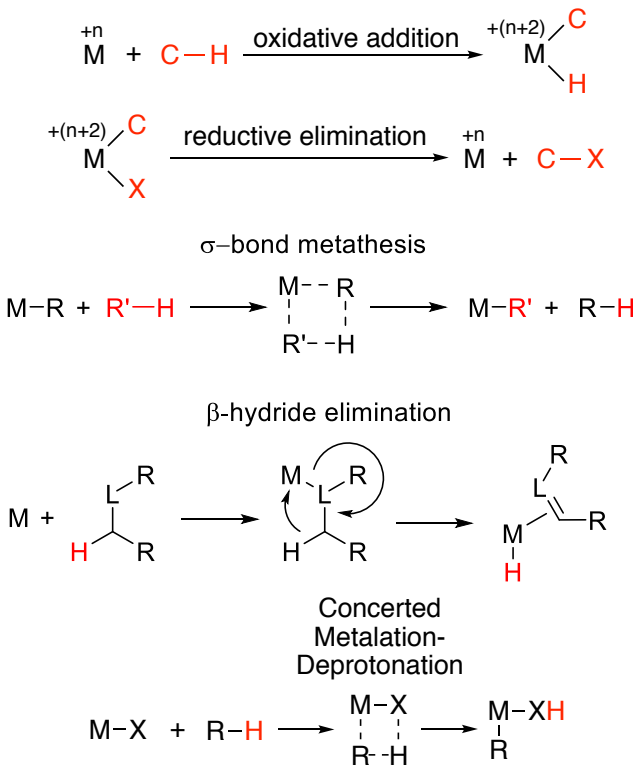

Scheme 3: Mechanisms of C-H Activation.

In oxidative addition, the substrate containing the C-H bond is brought into the coordination sphere of the transition metal catalyst due to a vacant $2e^-$ coordination site on the metal. It is here that the C-H bond is cleaved and new [M]-C and [M]-H bonds are formed. It directly follows that the oxidation state of the metal center and is increased by two during this process. Reductive elimination, the reverse of oxidative addition, usually involves the release of a product molecule, and is characterized by a reduction in oxidation state. In σ-bond metathesis, essentially the same net reactivity occurs, but this time through a concerted process. The mechanism of σ-bond metathesis tends to occur with d^0 transition metal complexes where oxidative addition pathways cannot be accessed because of restrictions regarding the accessible oxidation states of the metal. A third general class of C-H activation mechanisms is β-hydride elimination. This mechanism is common when the coordinated substrate has a H atom in the β-position and the metal has an empty $2e^-$ coordination site. Notably, the C-H bond typically has to be in a syn coplanar configuration with the [M]-L bond (M-L-C-H bond as shown in (Scheme 3) in order for elimination to occur.

Finally, C-H activation is known to proceed through the concerted metalation-deprotonation mechanism. This reaction pathway occurs in the presence of a metal-bound, nucleophilic X-type ligand such as acetate. In this reaction, the organic substrate is deprotonated by the X-type ligand and coordinates to the metal center in one concerted step [20].

1.3.2 Palladium as a Transition Metal Catalyst for C_α-H Amine Oxidation

The efficacy of Pd for Cα-H amine oxidation has been previously demonstrated [21]. The catalytic system shown in Scheme 4 uses a $PdCl_2$ catalyst with PPh_3 ligand in the presence of molecular oxygen to achieve the one-step aerobic oxidation of benzylic amines.

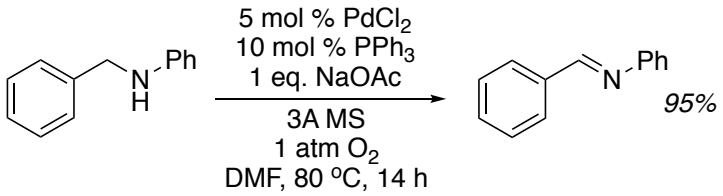

Scheme 4: Pd-Catalyzed C_α-H Oxidation of Benzylic Amines.

This system is particularly efficient due to high reaction yields, relatively low reaction temperatures and the use of O_2 as the sole oxidant, circumventing the need for the harsh oxidants that are often required in oxidation reactions. Notably, this system is active only with amine substrates containing benzylic C_α-H bonds and is not compatible with aliphatic amines.

1.3.3 Copper as a Transition Metal Catalyst for C_α-H Amine Oxidation

Many late transition metals such as platinum, palladium, iridium, rhodium, and ruthenium have demonstrated potent catalytic properties for C-H activation [22-26]. However, due to their relatively high costs and toxicities, more effort has been focused on exploring the catalytic properties and applications of the cheaper, less toxic, and more abundant first-row transition metals. Furthermore, the ability of Cu catalysts to perform C_α-H amine oxidation transformations is documented [27]. For example, CuCl has been used to achieve the C_α-H oxidation of benzylamine substrates bearing a variety of substituents (Scheme 5).

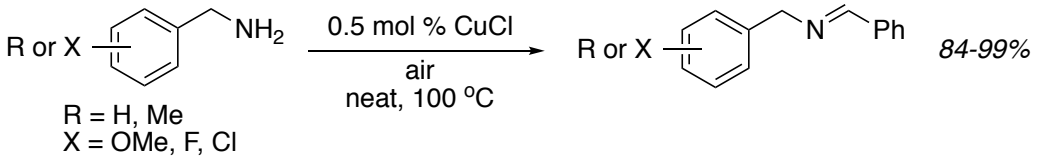

Scheme 5: Cu-Catalyzed C_α-H Oxidation of Benzylic Amines.

The efficiency of this synthetic reaction is exemplified by its use of air as the sole oxidant, as well as very low catalyst loadings and high reaction yields. Moreover, the reaction is neat and does not rely on additional solvent. However, this methodology is limited by relatively high reaction temperatures as well as a limited substrate scope.

Another example of C_α-H amine oxidation using a Cu catalyst can be seen in Scheme 6. This oxidative Mannich-type reaction utilizes a variety of Cu^I and Cu^{II} salts with *tert*-butyl hydroperoxide or molecular oxygen as oxidant to achieve oxidation at the C_α-H position on the amine substrates [28].

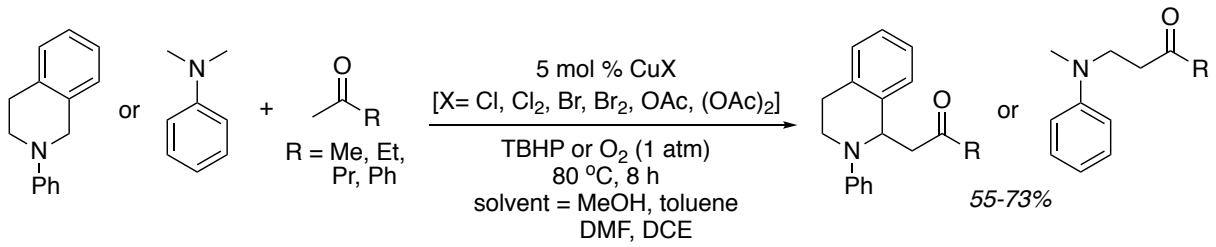

Scheme 6: Cu-Cataylzed C_α-H Oxidation of Tertiary Amines.

Although this reaction is limited by a narrow substrate scope, its short reaction time and low temperature, as well as the use of O_2 or relatively benign TBHP as oxidant make it a relatively efficient protocol for C_α-H amine functionalization. Notable, this methodology affords activation at the aliphatic C_α-H bond of dimethylaniline.

1.3.4 Iron as a Transition Metal Catalyst for C_α-H Amine Oxidation

Although Cu has shown great potential as a synthetic catalyst, it is not the only first-row transition metal to demonstrate its potential for α-amine oxidation. Fe, in particular, has exhibited great potential regarding C_α-H activation of a variety of amine substrates [29].

A methodology for direct Cα-H oxidation of amines was first reported by Murahashi and coworkers [30]. These systems utilize a Ru catalyst to achieve methyl

C_α-H oxidation of aniline derivatives, and thus form new C-O bonds with ^{t}BuOOH. (Scheme 7).

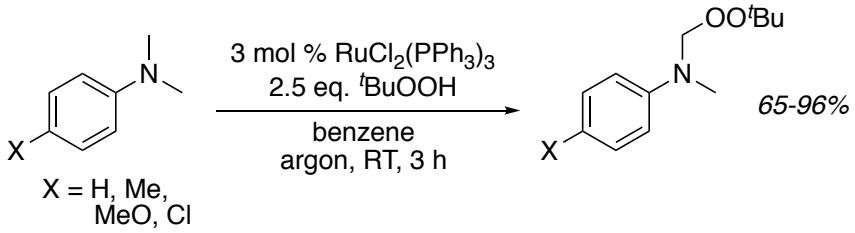

Scheme 7: Ru-Catalyzed C_α-H Oxidation of Dimethylaniline Using ^{t}BuOOH.

This efficient catalytic system proceeds at room temperature for 3 h. Additionally, the toxic oxidation reagents required for classical oxidative synthesis are not necessary for oxidation. This work afforded an unprecedented protocol for amine C_α-H functionalization, and established the utility of transition metals for forming new C_α-O bonds on amine substrates.

Since Murahashi's work, many Fe-catalyzed amine C_α-H amine oxidations have been established. For example, Scheme 8 shows the Fe-catalyzed Cα-H oxidation of primary benzylamine derivatives to form imines [31].

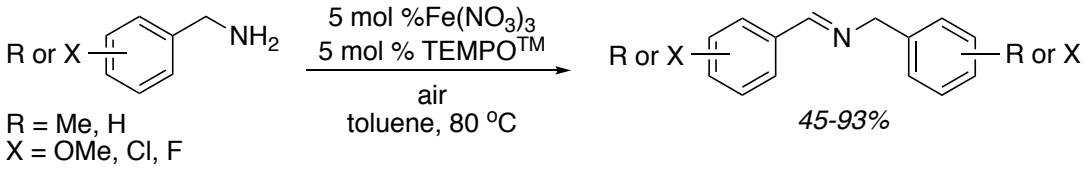

Scheme 8: Fe-Cataylzed C_α-H Oxidation of Benzylamines.

This methodology uses relatively cheap and abundant $Fe(NO_3)_3$ as catalyst with air as oxidant. Additionally, the use of the stable radical TEMPO^{TM} in Fe-catalyzed reactions is not uncommon, as the majority of these processes proceed through $1e^-$ pathways. Notably, this system lacks versatility, as it is only compatible with primary amines with benzylic C_α-H bonds—a common deficiency in transition metal-catalyzed amine oxidation literature.

The system shown in Scheme 9 uses an $FeCl_3{\cdot}6H_2O$ catalyst with *tert*-butyl hydroperoxide as oxidant to achieve C_α-H functionalization adjacent to a heteroatom [32].

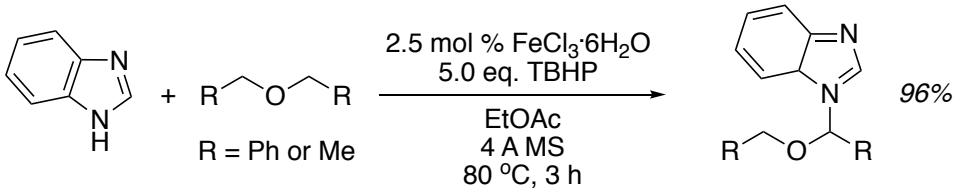

Scheme 9: Fe-Cataylzed C_α-H Functionalization.

As is typical with transition metal catalysis, this reaction uses low catalyst loading, relatively low temperatures and a short reaction time to achieve N-alkylation of azoles via C_α-H bond oxidation. Notably, when the radical scavenger TEMPO™ was added to the reaction in a 1:1 ratio with TBHP, no trace of the product was observed. This result implicates a $1e^-$ reaction pathway, as is common with Fe/peroxide catalyzed methodologies.

1.3.5 Transition Metal-Catalyzed C_α-H Amine Functionalization

Several transition metal-catalyzed synthetic methodologies for the C_α-H functionalization of cyclic and aromatic amines have been developed [33, 34]. For example, $CuCl_2$ has been employed as a catalyst for the C_α-H cyanation of N-phenyltetrahydroisoquinoline (Scheme 10). This system utilizes O_2 as oxidant at room temperature to achieve synthetically useful yields of the α-aminonitrile product.

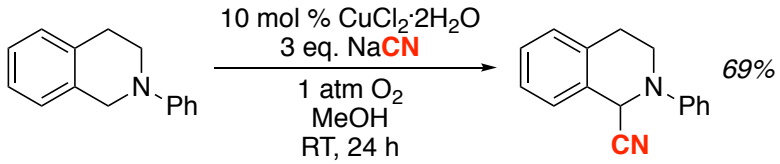

Scheme 10: $CuCl_2$-Catalyzed Cα-H Cyanation of *N*-Phenyltetrahydroisoquinoline.

Fe has also been utilized as an active catalyst for the Cα-H cyanation of dimethylaniline derivatives (Scheme 11). $FeCl_2$ has been used with *tert*-butyl hydroperoxide as oxidant with trimethylsilyl cyanide (TMSCN) as the source of CN. This protocol affords high yields of the α-aminonitrile product at room temperature with short reaction times.

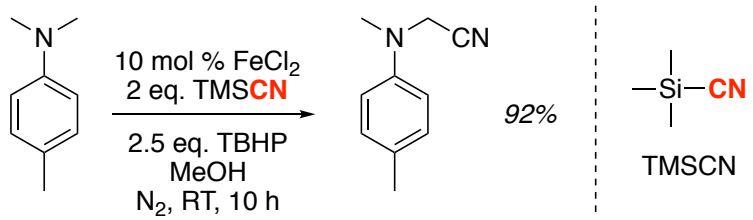

Scheme 11: $FeCl_2$-Catalyzed Cα-H Cyanation of *N,N*-Dimethyl-*p*-toluidine.

Mechanistic studies of transition metal-catalyzed Cα-H amine oxidation reactions have been conducted [35]. Cα-H amine functionalization reactions, such as those shown in Schemes 10 and 11 above, as well as Murahashi's system shown in Scheme 7 above, are believed to proceed through a series of $1e^-$ single electron transfer (SET)/hydrogen atom transfer (HAT) steps to form an *in-situ* iminium ion intermediate, which is in equilibrium with a hemiaminal species formed by nucleophilic attack of either the TBHP oxidant or MeOH solvent (Scheme 12). Once the iminium ion is formed, it then undergoes nucleophilic attack to form the C_α-H functionalized amine.

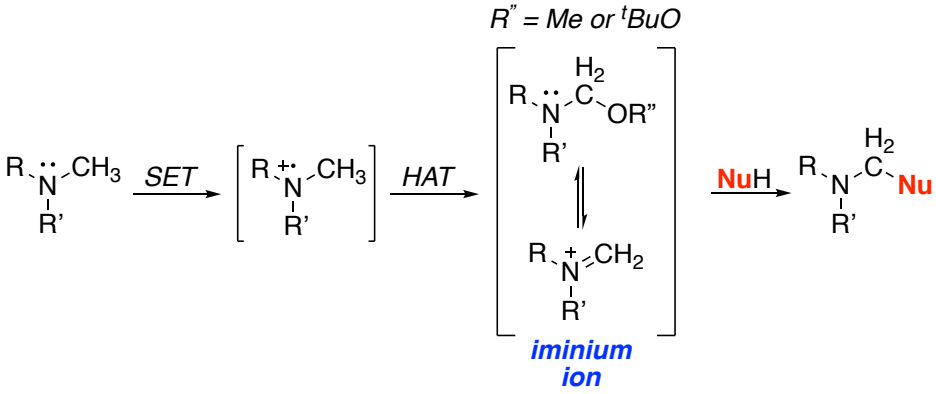

Scheme 12: Mechanism of Cα-H Amine Functionalization.

1.4 Gif Chemistry

One of the earliest examples of the selective oxidation of aliphatic hydrocarbons in referred to as Gif Chemistry [36]. Initially, this system utilized Fe^{II} as catalyst and air as oxidant to achieve the oxidation of adamantane (Scheme 13). The system also relied on pyridine as solvent and AcOH to dissolve the Zn^0—an electron source in the reaction.

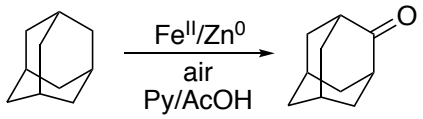

Scheme 13: The Fe-Catalyzed Oxidation of Adamantane with Gif Chemistry.

Over the years since its discovery, Fe/pyridine-based Gif chemistry continued to evolve to include the use of H_2O_2 as oxidant. Additionally, the eventual use of picolinic acid (**1**) as ligand drastically reduced reaction times, in some cases from several hours to merely a few minutes [37, 38]. This particular iteration of the Gif system is referred to as $GoAgg^{III}$ (Scheme 14).

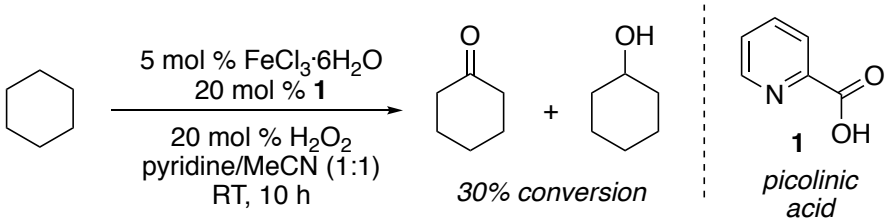

Scheme 14: Oxidation of Cyclohexane with $GoAgg^{III}$ System.

This system is highly active, as evidenced by its ability to cleave highly stable, unactivated sp^3 C-H bonds. However, synthetic applications are limited due to poor reaction yields and low product selectivity.

1.5 Biomimetic Fe Catalysts for C-H Oxidation

Aliphatic C-H bonds are among the most stable—and thus least reactive—chemical bonds in synthetic chemistry. In spite of the relatively high activation barrier of aliphatic C-H bond cleavage, enzymes in nature have evolved to perform this chemistry efficiently. Additionally, these enzymes have the ability to selectively oxidize specific sites on substrates that contain many C-H bonds that possess only minor differences in reactivity [39]. The efficiency of these enzymes has not gone

unnoticed by the field of transition metal catalysis, and a substantial effort has been made in recent years to mimic their chemistry using small-molecule catalysts. One example of the effort made to produce biomimetic synthetic catalysts for oxidation synthesis is a class of non-heme Fe catalysts referred to as (N4)Fe^{II} catalysts [40]. These catalysts mimic the active site in the ubiquitous enzyme Cytochrome P450 (CYP450); examples of these catalysts include BPMEN and BPMCN ligands, as shown in Scheme 15.

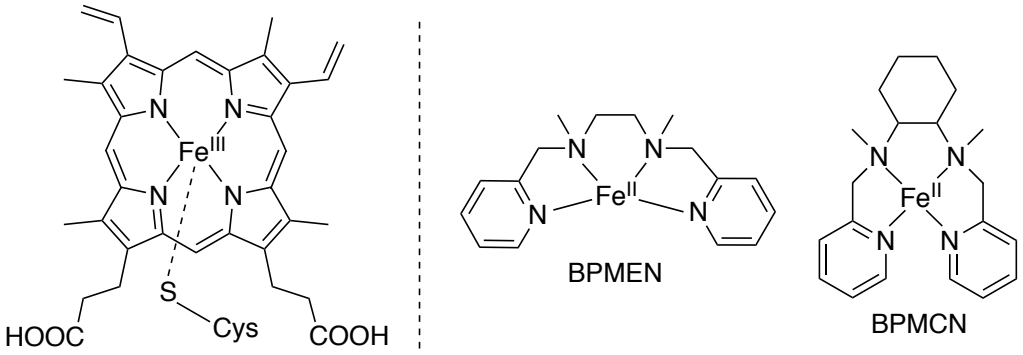

Scheme 15: The Active Site of CYP450 (left). Biomimetic (N4)Fe^{II} Oxidation Catalysts (right).

Among its many functions in the human body, CYP450 is responsible for the metabolism of 70-80% of all drugs used for clinical use [41]. A critical reaction pathway of CYP450 drug metabolism is the radical rebound mechanism (Scheme 16, top). Although CYP450 is able to activate O_2 for substrate oxidation, biomimetic Fe catalyst systems utilize peroxides such as H_2O_2. Peroxide oxidants allow the system to bypass the thermodynamically uphill process of O_2 activation by forming the reactive peroxo species directly (Scheme 16, bottom).

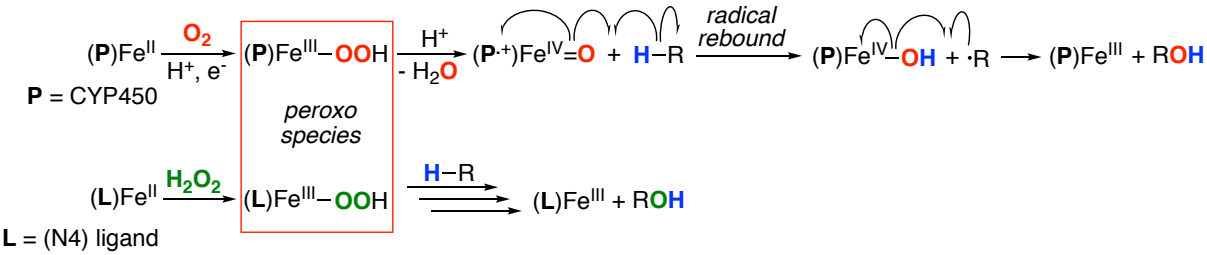

Scheme 16: Dioxygen Activation by CYP450 (top). Direct Formation of Fe^{III} Peroxo Species with (N4)Fe^{II}/H_2O_2 (bottom).

Synthetic CYP450 biomimetic (N4)Fe^{II} catalyst systems have been established, and have been utilized for a variety of oxidative synthesis reactions [42]. For example, the epoxidation of *n*-alkenes has been developed using an Fe^{II}/BPMEN system with H_2O_2 as oxidant (Scheme 17).

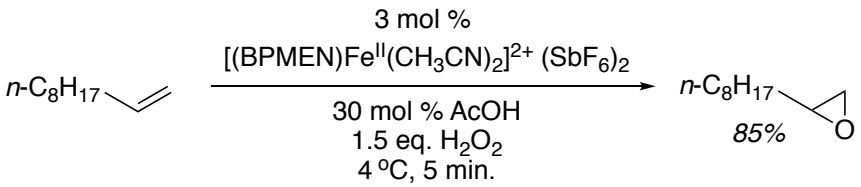

Scheme 17: Epoxidation of Alkenes Using CYP450 Biomimetic Catalysis.

These Fe/peroxide catalytic systems tend to be highly reactive, as is evidenced by the high oxidation product yield achieved with merely 5 min. reaction time at near-freezing temperatures [43].

1.6 Transition Metal-Catalyzed Amide Formation

1.6.1 Background

Traditional organic chemistry has afforded a broad library of methodologies for the synthesis of amides, but the vast majority have been developed solely with the target molecule in mind, with little attention given to cost, efficiency or safety. Many current synthetic strategies for these important functional groups use toxic reagents and produce the relatively large volume of waste associated with stoichiometric substitution reactions. In more recent years, significant progress has been made in the effort to establish efficient oxidative transition metal-catalyzed amide syntheses [44-49]. One can envision this approach to be particular attractive due to the possible high atom economy afforded by direct C_α-H oxidation of amines when reagents such as O_2 or air are used as oxidant (Scheme 18),

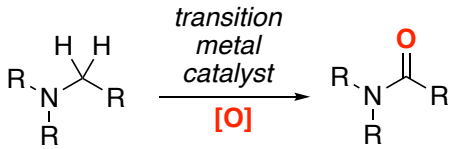

Scheme 18: Transition Metal-Catalyzed Amide Synthesis.

1.6.2 Primary amine oxidation

Significant progress has been made toward the sustainable synthesis of amides from amines. For example, in 2008, Mizuno and coworkers reported the Ru catalyzed oxidation of primary amines to yield primary amides using air as an oxidant and water as solvent (Scheme 19). Both of these characteristics serve to enhance

the efficiency of this reaction and are in alignment with Green Chemistry principles. [50, 51].

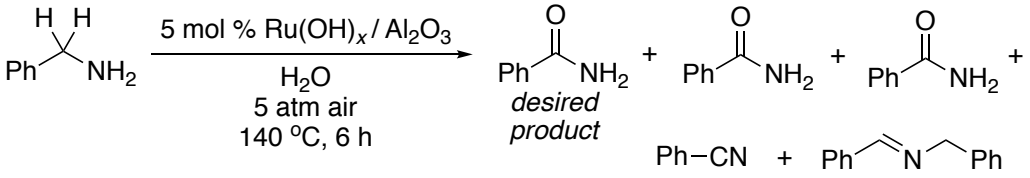

Scheme 19: Ru-Catalyzed Cα-H Oxidation of Primary Amines.

However, this system suffers several drawbacks. When developing a synthetic methodology, achieving high yield of the target product while minimizing unwanted side-products is essential to the efficacy of the reaction. In Mizuno's system (Scheme 19), a variety of oxidation products are formed. This characteristic is potentially problematic from an industrial perspective since separation of the desired product may be troublesome. Additionally, although the system uses air as oxidant, the necessity of high reaction temperatures renders this catalytic system relatively inefficient.

As shown in Scheme 20, Manganese Oxide Octahedral Molecular Sieves (OMS-2) have been reported to successfully oxidize C_α-H bonds on primary benzylic amines aerobically and with short a reaction time.

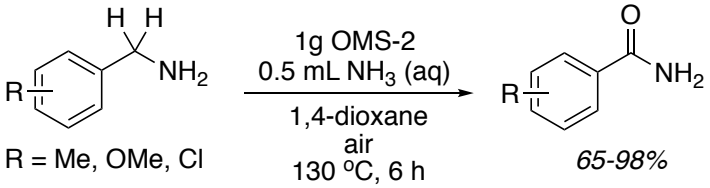

Scheme 20: Mn-Catalyzed Cα-H Oxidation of Benzylamine Derivatives.

Additionally, the use of cheap and abundant Mn greatly increases the efficiency of this reaction. However, like many other examples of amide formation via transition metal-catalyzed amine C_α-H oxidation, this protocol requires high temperatures and lacks substrate versatility; substrates must contain activated C_α-H bonds for oxidation to occur. Moreover, this methodology employs a heterogeneous catalyst which makes the reaction mechanism difficult to examine and is therefore difficult to optimize rationally.

A few methodologies utilize Cu catalysts to achieve amide formation via C_α-H oxidation of amines [52]. The methodology in Scheme 21 employs CuBr as catalyst with K_2CO_3 as base in DMSO. Much like the catalytic systems shown in Scheme 19 and Scheme 20, this Cu-mediated oxidation requires the use of benzylic substrates which contain activated, benzylic C-H bonds. In spite of the lowered activation energy of these bonds (BDE = 90 kcal/mol vs. 105 kcal/mol for aliphatic C-H bonds), the reaction requires high reaction temperatures of approx. 150 °C .

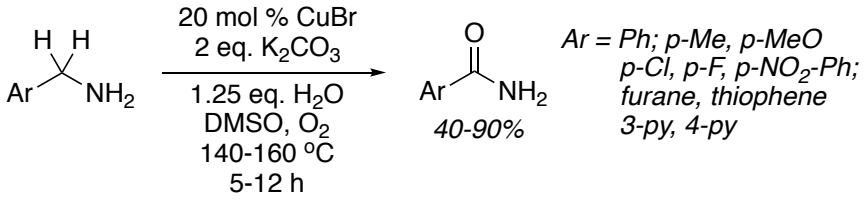

Scheme 21: Cu-Catalyzed Cα-H Oxidation of Benzylamine Derivatives.

1.6.3 Secondary amine oxidation

As seen in section 1.6.2, there are several documented examples of primary amine C_α-H oxidation to form amides. However, these systems are not capable of oxidizing secondary or tertiary amine substrates. In contrast to primary amine oxidation there are significantly fewer examples of secondary amine oxidation in the literature. For example, supported Au catalysts have been discovered to selectively oxidize secondary cyclic amines to form the corresponding amides [53, 54]. As seen in Scheme 22, both heterogeneous Au catalysts and polyvinylpyrrolidone (PVP)-mounted Au nanoparticles are capable of forming lactams from the corresponding cyclic secondary amines.

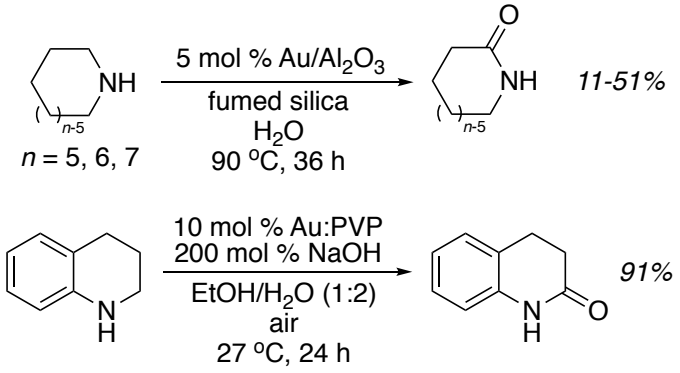

Scheme 22: Au-Catalyzed Oxidation of Cyclic Secondary Amines.

Although these reactions afford the amide product in synthetically useful yields with relatively mild reaction temperatures, analogous to previous examples, versatility is limited by narrow substrate scopes. Furthermore, both systems in Scheme 22 rely on heterogeneous catalysts, which complicates mechanistic exploration and thus rational understanding of the reaction mechanism. Moreover, the relatively high cost of Au nanoparticles (compared to Fe or Cu) make this reaction less suitable for large-scale industrial processes.

The transition metal Ru has been utilized in the C_α-H oxidation of secondary amines to form amides [55, 56]. For example, $RuCl_3$ has been shown to be an affective catalyst for the selective C_α-H oxidation of glycine residues for peptide backbone modification (Scheme 23). This methodology affords high amide yields, but the reaction is limited exclusively to the peptide substrate, which greatly limits its synthetic utility.

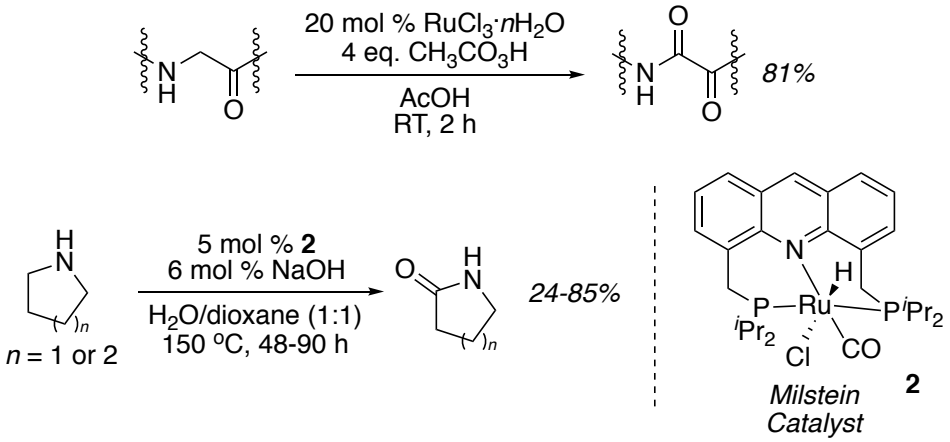

Scheme 23: Ru-Catalyzed C_α-H Oxidation of Secondary Amines.

Additionally, the Ru-based Milstein Catalyst has been employed for the selective C_α-H oxidation of secondary cyclic amines (Scheme 23). Although more synthetically feasible than the glycine oxidation reaction, it suffers from mixed yields and harsh reaction conditions. This system is also limited to cyclic amine substrates, and does afford access to non-cyclic amides.

1.6.4 Tertiary amine oxidation

Literature examples of C_α-H oxidation of tertiary amines are rare. Although there are several reports in the literature that demonstrate functionalization at the α-position of tertiary amines (e.g. C-C bond formation) [57], limited progress has been made regarding the C-O bond formation in this position that is necessary for amide synthesis. Prior to the work presented herein, to the best of our knowledge, only two examples of direct C-H oxidation to form tertiary amides existed in the literature [58, 59]. These systems employ CuI as catalyst in combination with molecular oxygen or air as oxidant to achieve C_α-H tertiary amine oxidation of complex pharmaceutical molecules (Scheme 24). Analogous to the systems described in section 1.3.5, these reactions are proposed to proceed through an iminium ion intermediate.

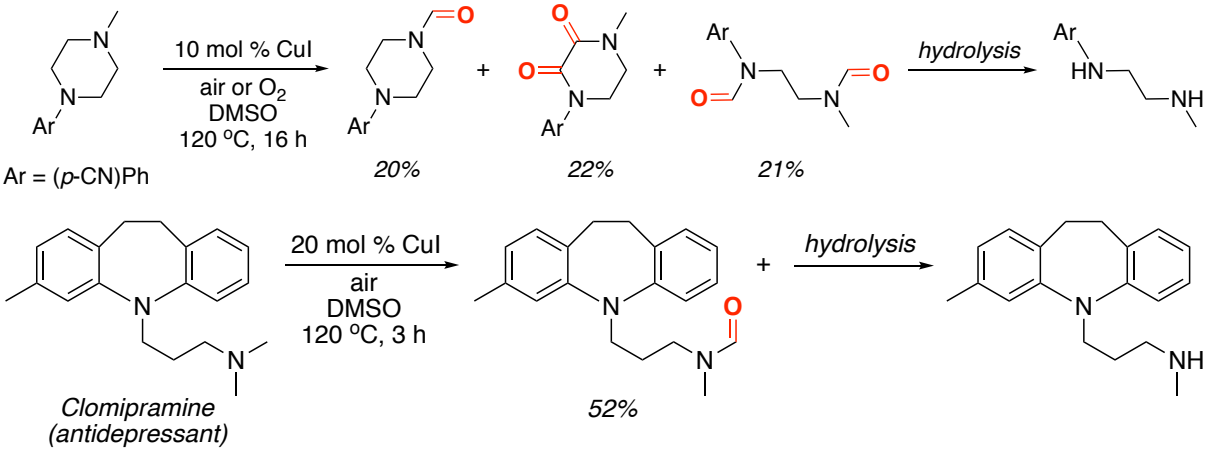

Scheme 24: CuI-Catalyzed Cα-H Oxidation of Tertiary Amine Complex Pharmaceutical Drugs.

These studies are particularly interesting from the standpoint of drug metabolism. Both systems seen in Scheme 24 afford amide and dealkylation reaction products that are known *in-vivo* metabolites of CYP450 [60, 61]. Consequently, this research is advantageous to the rapid identification of drug metabolites and thus the drug discovery cycle. However, from a synthetic perspective, this system is characterized by major deficiencies. Although this methodology utilizes Cu (a cheaper alternative to Ru or Au) and benign molecular oxygen as oxidant, it suffers from an extremely narrow substrate scope, as it is limited to the complex molecule substrates seen in Scheme 24. Furthermore, high reaction temperatures, non-synthetically useful yields and a lack of product selectivity render this protocol highly inefficient.

2 Project Objectives

As discussed in detail in the introduction to this thesis, known catalysts that promote the transition metal-catalyzed, oxidative formation of amides showed clear limitations with respect to the employable substrates. We reasoned that this is due to the fact that aliphatic, acyclic tertiary amines pose unique challenges regarding C_α-H oxidation. First, acyclic tertiary amines are more sterically hindered than their primary or secondary counterparts due to free σ-bond rotation around the nitrogen atom. Second, many reports of amine oxidation via C-H activation involve the functionalization of relatively weak allylic or benzylic C-H bonds. Because aliphatic tertiary amines often lack such activated C_α-H bonds, transformations of these substrates could be expected to be challenging. One purpose of this research project was to overcome these challenges by exploring the potential of homogeneous Fe catalyst/peroxide systems for the C_α-H oxidation of aliphatic, tertiary amines, with a specific focus on oxidations that yield amide products, an unknown reaction at this projects start (Scheme 25).

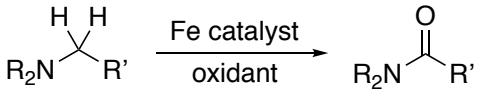

Scheme 25: Fe-Catalyzed C_α-H Oxidation of Tertiary Amines.

Through extensive evaluation of catalyst, ligand, oxidant and solvent, as well as systematic reaction optimization, a homogeneous Fe-Catalyzed methodology for the selective C_α-H oxidation of small and complex, aliphatic, tertiary amines was established. This system relies on $FeCl_3$/picolinic acid (**1**) as catalyst in conjuction with the oxidant $PhCO_3{}^tBu$, in pyridine solvent (Scheme 26). In addition to amide formation, our system produced dealkylated secondary amine products. These dealkylation products are believed to occur due to hydrolysis. Additionally, they are analogous to the dealkylated products formed during CYP450 drug metabolism (1.6.4).

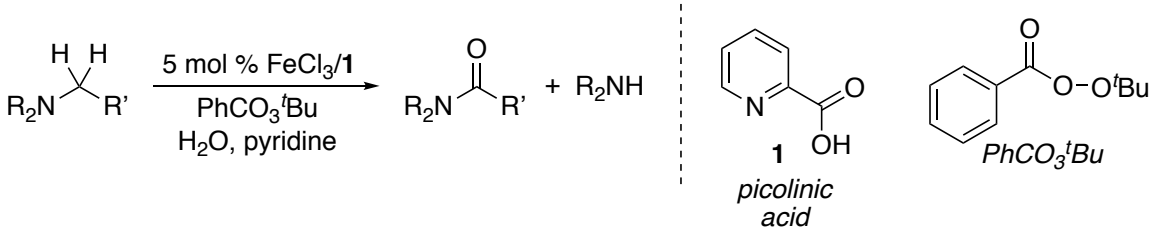

Scheme 26: Fe-Picolinic Acid-Catalyzed C_α-H Oxidation of Tertiary Amines.

Another purpose of this research was to gain detailed mechanistic understanding of this system. Although the Fe**/1-**catalyzed system has been extensively studied (Section 1.4 above), its use with the oxidant $PhCO_3{}^tBu$ is unprecedented and therefore the mechanism of our system is unknown. Because pyridine is thought to act as an Fe-bound ligand in these systems [63], we sought to gain structural knowledge of the catalyst. This information may allow us to substitute the use of pyridine with other more benign solvents/ligands. Additionally, our system demonstrates particularly high selectivity for C-H bonds when complex molecules are used as substrate. The source of this selectivity is unknown and could potentially be elucidated by mechanistic studies.

3 Results and Discussion

3.1 Optimization of Tripropylamine Oxidation

3.1.1 Initial Evaluation of Catalyst Systems

The transition metals Pd, Ru, Cu and Fe have all demonstrated their potential for the further development of amine oxidation reactions (Section 1.3 above). Consequently, initial investigations of transition metal-catalyzed tertiary C_α–H amine oxidation involved the systematic evaluation these catalysts, coupled with various mono- and bidentate N- and P-coordinated L-type ligands (Schemes 27 through 30 below) for the C_α–H oxidation of NPr_3. Notably, two C_α–H bonds would be cleaved in this transformation. Thus, we hypothesized that a theoretical minimum of 2 eq. oxidant would be needed and was used in our initial optimization conditions. Additionally, analogous to many other C_α–H amine oxidation reactions in the literature (Section 1.3.5), we hypothesized that our desired transformation would proceed through an iminium intermediate (Scheme 12), and undergo nucleophilic attack by H_2O to form the new C_α–O bond. Consequently, 1 eq. H_2O was added to these reactions. Reaction yields were determined by calibrated GC analysis.

Concurrently, Pd and Ru were evaluated as catalysts for NPr_3 oxidation. We hypothesized that they may be active for the C_α–H oxidation of NPr_3 due to their ability to mediate C-H oxidation with other amine substrates (Section 1.6.3 above). The catalyst $RuCl_3$ was initially evaluated due to literature precedent that showed efficient C_α–H oxidation of secondary [64] and aromatic tertiary amines [65]. However, these systems provided no trace of amide formation from our target substrate NPr_3 in these initial studies (Scheme 27).

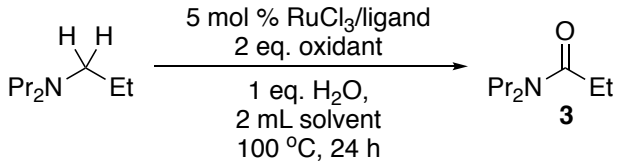

Ligand	Oxidant	Solvent	% Amide
3-NO_2-pyridine	air	toluene	0%
P(Ph-OMe)$_3$	air	toluene	0%
8-OH-quinoline	air	toluene	0%
8-NH_2-quinoline	$PhCO_3{}^tBu$	pyridine	0%

Scheme 27: Evaluation of Ru-Catalyzed Cα–H Oxidation of NPr_3.

Pd has also been established to facilitate a variety of C-H activation reactions [66]. The catalysts $Pd(OAc)_2$ and $PdCl_2$, in particular, have been active in these systems [67, 68] Although the Pd catalyst systems presented in Scheme 28 produced a maximum of 3% amide product, they served as an early proof-of-concept for our reaction by demonstrating that C_α–H oxidation of aliphatic tertiary amines was feasible under catalytic conditions.

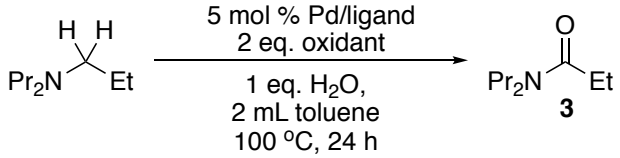

Catalyst	Ligand	Oxidant	% Amide
$Pd(OAc)_2$	py	air	trace
$Pd(OAc)_2$	3-NO_2-pyridine	air	1 ± 1%
$Pd(OAc)_2$	3-NO_2-pyridine	mCPBA	1 ± 1%
$Pd(OAc)_2$	3-NO_2-pyridine	benzoquinone	0%
$Pd(OAc)_2$	3-NO_2-pyridine	O_2	0%
$Pd(OAc)_2$	3-NO_2-pyridine	H_2O_2	2 ± 1%
$Pd(OPiv)_2$	$P(Ph)_3$	air	3 ± 1%

Scheme 28: Evaluation of Pd-Catalyzed Cα–H Oxidation of NPr_3.

Due to the documented efficacy of CuBr catalyst, combined with ^tBuOOH oxidant [69, 70] in amine C_α–H functionalization reactions, we hypothesized that this catalyst system may mediate C_α–H cleavage of NPr_3. These investigations proved more fruitful than those of Pd, and provided us with reaction yields up to 17% using the ligand 8-hydroxyquinoline in pyridine at 100 °C (Scheme 29). Although these results were encouraging, optimization additional optimization did not afford higher amide yields.

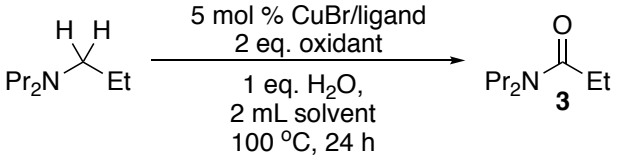

Ligand	Oxidant	Solvent	% Amide
3-NO_2-pyridine	air	toluene	0%
8-NH_2-quinoline	$PhCO_3{}^tBu$	toluene	6 ± 1%
none	^{t}BuOOH	pyridine	7 ± 1%
none	^{t}BuOOH	toluene	11 ± 1%
8-NH_2-quinoline	^{t}BuOOH	pyridine	12 ± 1%
8-OH-quinoline	^{t}BuOOH	pyridine	17 ± 1%

Scheme 29: Evaluation of Cu-Catalyzed Cα–H Oxidation of NPr_3.

Concurrent with the Cu studies, we investigated Fe catalyst systems with a variety of peroxide oxidants. The Gif systems described in Section 1.4 above, in particular the highly active $FeCl_3$-catalyzed $GoAgg^{III}$ system, were of particular interest due to their ability to selectively oxidize unactivated, aliphatic C-H bonds. We hypothesized that $FeCl_3$ catalysts coupled with peroxide oxidant may provide the desired reactivity to achieve C_α–H activation of NPr_3. Additionally, the $GoAgg^{III}$ Gif system relies upon picolinic acid as ligand. We hypothesized that this ligand, or other mono- or bidentate pyridine-type ligands may increase catalytic activity (Scheme 30).

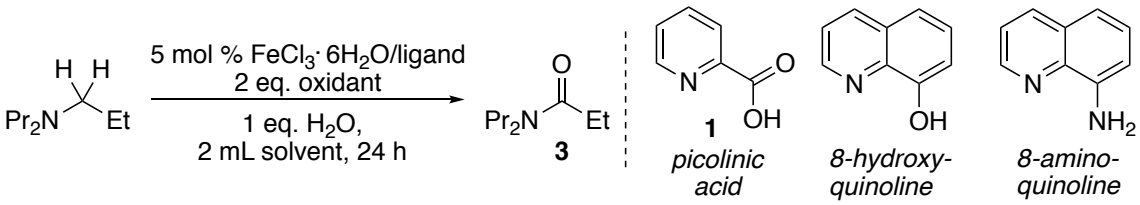

Ligand	Oxidant	Solvent	Temp.	% Amide
8-NH_2-quinoline	DDQ	pyridine	100 °C	1 ± 1%
8-NH_2-quinoline	H_2O_2	pyridine	100 °C	2 ± 1%
8-NH_2-quinoline	$PhCO_3{}^tBu$	DMF	100 °C	2 ± 1%
8-NH_2-quinoline	$PhCO_3{}^tBu$	AcOH	100 °C	3 ± 1%
2-CH_3-pyridine	$PhCO_3{}^tBu$	pyridine	100 °C	9 ± 1%
8-NH_2-quinoline	^{t}BuOOH	pyridine	100 °C	11 ± 1%
3-NO_2-pyridine	$PhCO_3{}^tBu$	pyridine	100 °C	18 ± 1%
picolinic acid	$PhCO_3{}^tBu$	pyridine	100 °C	19 ± 1%
picolinic acid	$PhCO_3{}^tBu$	pyridine	80 °C	**22** ± 1%

Scheme 30: Evaluation of Fe-Catalyzed Cα–H Oxidation of NPr_3.

Ultimately, these investigations revealed the efficacy of (1) $FeCl_3$ precatalyst coupled with the ligand picolinic acid (**1**); (2) the peroxyester $PhCO_3{}^tBu$ oxidant; and (3) pyridine solvent for C_α–H oxidation of NPr_3 to form the corresponding amide **3**.

Early optimization studies of this system afforded high yield of amide **3** (22%) with the mildest conditions and was thus identified as a strong candidate for further optimization.

3.1.2 Evaluation of Oxidants in Fe-Picolinic Acid System

As seen in Scheme 30, 5 mol % $FeCl_3$/**1** with 2 eq. $PhCO_3{}^tBu$ in pyridine afforded 22% of amide **3**. These conditions are closely related to the $GoAgg^{III}$ Gif system (Section 1.4 above), with the exception of $PhCO_3{}^tBu$ as oxidant. Unlike the Gif system, H_2O_2 provided merely 2% reaction yield. This observation allowed us to postulate that the choice of oxidant in this catalytic system may have a dramatic effect on reaction yield. To this end, several peroxide-based oxidants were evaluated for the C_α–H oxidation of NPr_3. These results are summarized in Scheme 31.

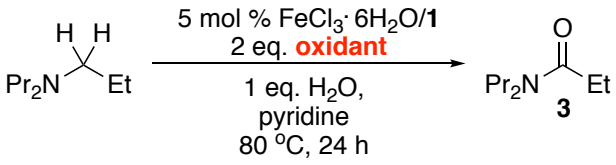

Oxidant	% Amide
H_2O_2	1± 1%
$^tBuO\text{-}O^tBu$	3 ± 1%
^tBuOOH	12 ± 1%
$PhCO_3{}^tBu$	**19** ± 1%

Scheme 31: Evaluation of Oxidants for Fe-Picolinic Acid-Catalyzed Oxidation of NPr_3.

The peroxyester $PhCO_3{}^tBu$ unambiguously provided the highest reaction yield and was thus used in further optimization studies. Notably, the asymmetric peroxides provided relatively high yields while the symmetric H_2O_2 and $^tBuO\text{-}O^tBu$ peroxides provided very low amide yields. These findings suggested that homolytic cleavage of oxidant may be disadvantageous to this system.

3.1.3 Evaluation of Ligands

As seen in Section 1.4, the introduction of the ligand picolinic acid into Gif oxidation systems increased catalytic turnover and reaction yield up to 50 times over original AcOH-based Gif systems [71]. Consequently, we expected changes in the

ligand framework of the catalyst to significantly affect reaction yields. To this end, a variety of mono- and bidentate N-coordinated ligands were evaluated. As shown in Scheme 32, the ligand picolinic acid provided the highest reaction yield of **3** (48%) and was used in further studies.

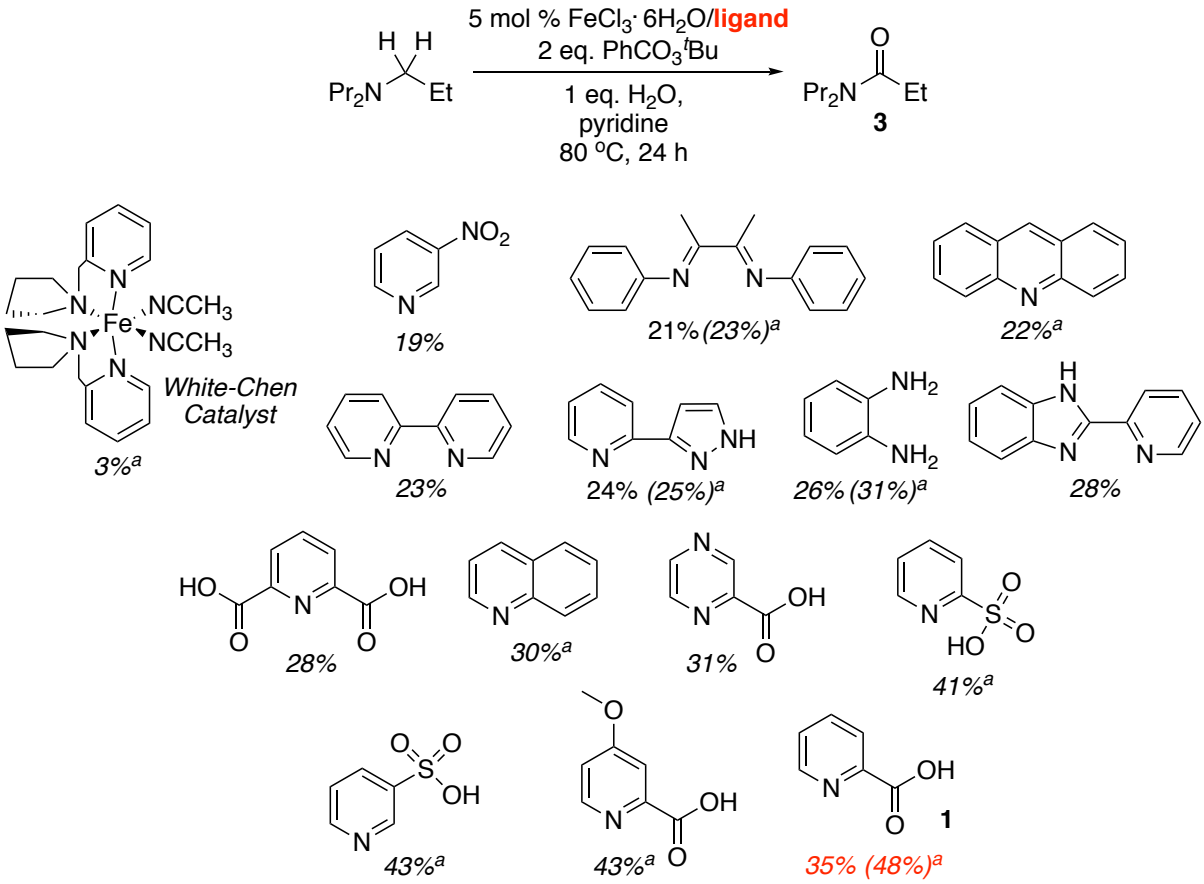

Scheme 32: Evaluation Ligands for Fe-Catalyzed Oxidation of NPr_3. [a] 3 eq. $PhCO_3{}^tBu$, 50 °C.

3.1.4 Optimization of Reaction Temperature

Previous optimization studies provided a maximum of 48% amide yield. Due to relatively high bond dissociation energy (BDE = 105 kcal/mol) of aliphatic C-H bonds, we hypothesized that higher reaction temperatures may increase reaction yields. Therefore, temperature optimization studies were conducted using the conditions shown in Scheme 33.

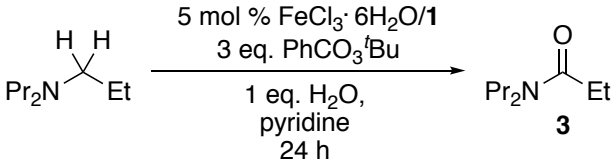

Temp (°C)	% Amide
25	0%
40	23 ± 1%
50	**47 ± 2%**
60	48 ± 2%
70	47 ± 1%
80	48 ± 2%
90	48 ± 3%
100	43 ± 1%
120	35 ± 3%

Scheme 33: Evaluation Reaction Temperatures for Fe-Catalyzed Oxidation of NPr_3.

Contrary to our hypothesis, these studies revealed that our initial optimization temperature of 100 °C could be *lowered* to 50 °C to afford maximum amide yields under these conditions. Additionally, the lower temperature increased the energy efficiency and safety of the reaction and is in alignment with the our goal of promoting sustainable chemistry.

3.1.5 Optimization of Reaction Time

As part of our effort to optimize the Fe-catalyzed C_α–H oxidation of NPr_3, a systematic study of reaction time was conducted (Scheme 34).

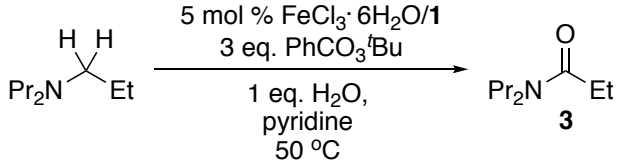

Time	% Amide
5 mins.	4 ± 1%
2 h	35 ± 1%
4 h	34 ± 1%
8 h	**42 ± 1%**
24 h	40 ± 2%
48 h	41 ± 1%
72 h	42 ± 2%

Scheme 34: Evaluation of Reaction Time for Fe-Catalyzed Oxidation of NPr_3.

A minimum reaction time of 8 h was determined to provide maximum amide yield under these conditions.

3.1.6 Optimization of Water Loading

At the onset of our investigations, 1 eq. H_2O was used for the C_α–H oxidation of NPr_3 (Schemes 30 through 34 above). Under these conditions, a synthetically useful yield of 47% amide product was achieved at 50 °C. Analogous to the amine oxidation systems described in Section 1.3.5, we hypothesized that our reaction may proceed through the iminium ion intermediate **4**, which then undergoes nucleophilic attack by H_2O to form the hemiminal **5** (Scheme 35).

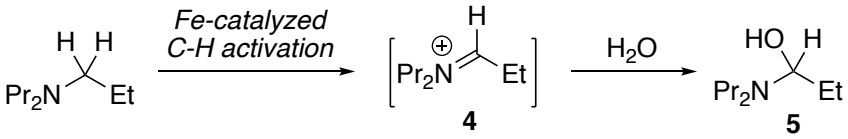

Scheme 35: Nucleophilic Attack by H_2O to Form C_α–O Bond.

Consequently, we postulated that the concentration of H_2O may play a crucial role in this reaction. To investigate this possibility, H_2O optimization studies were conducted (Scheme 36).

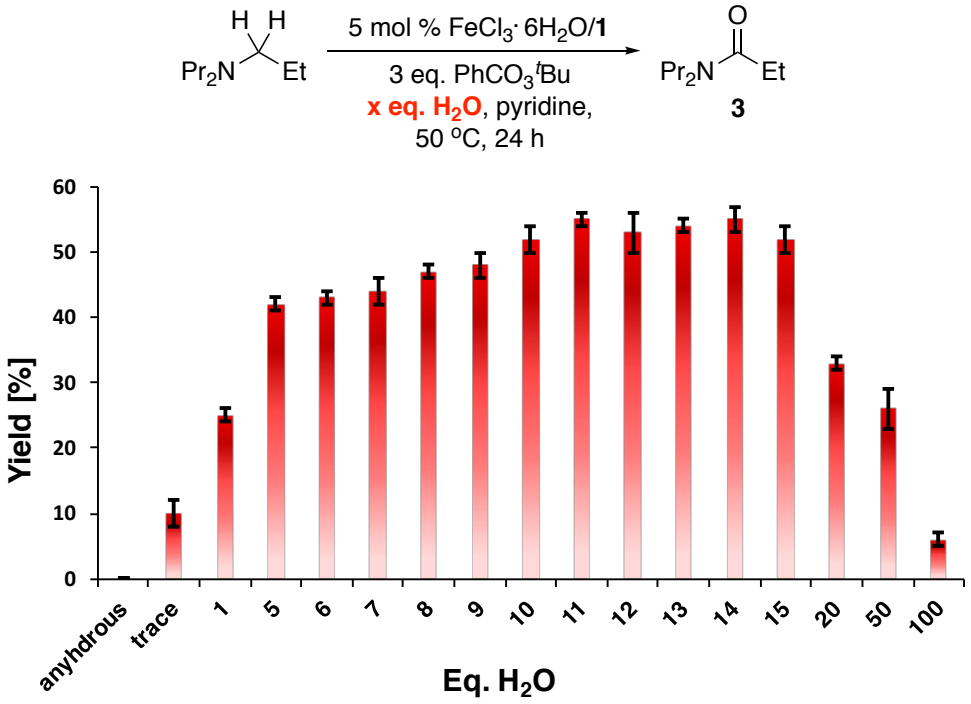

Scheme 36: Optimization of H_2O Loading for Fe-Catalyzed Oxidation of NPr_3.

Ultimately, it was revealed that the reaction produced 55% amide yield when an H_2O loading of 11 eq. was used. Additionally, the observation of a strong dependence of product formation on the water content suggests that H_2O is inherently involved in the mechanism of the reaction.

3.1.7 Optimization of TBPB Loading

Due to the crucial role of H_2O_2 as oxidant in the similar Fe-picolinic acid-catalyzed $GoAgg^{III}$ Gif system (Section 1.4 above), we expected $PhCO_3{}^tBu$ concentration to have a significant effect on amide yields. Therefore, studies were conducted to optimize the loading of $PhCO_3{}^tBu$ for the C_α–H oxidation of NPr_3 (Scheme 37).

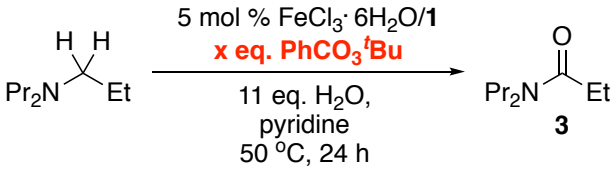

Eq. $PhCO_3{}^tBu$	% Amide
1.5	16 ± 3%
2.5	54 ± 2%
3.0	**63 ± 3%**
4.5	45 ± 2%
6.0	39 ± 2%

Scheme 37: Optimization of $PhCO_3{}^tBu$ Loading for Fe-Catalyzed Oxidation of NPr_3.

These findings show 3 eq. $PhCO_3{}^tBu$ loading to provide the highest reaction yields, and provided 63% amide formation. The product **3** shows that two C_α–H on NPr_3 substrate are cleaved in this reaction, and thus only 2 eq. oxidant would be theoretically required. The necessity of 3 eq. $PhCO_3{}^tBu$ to achieve maximum yield of **3** suggests the presence of side-reactions.

The highlighted conditions seen in Scheme 37 represent the fully optimized conditions for NPr_3 oxidation, and were used as a starting point for further investigations.

3.2 Preliminary Mechanistic Hypothesis

The Fe-picolinic acid-catalyzed C_α–H amine oxidation reaction presented herein is similar to the $GoAgg^{III}$ Gif oxidation reaction and other CYP450 biomimetic catalyst systems (Sections 1.4 and 1.5 above), both in catalyst and reaction products. Based on this literature, as well as that presented in Section 1.3.5, we proposed the general reaction mechanism shown in Scheme 38. We hypothesized three possible Fe-catalyzed pathways that could lead to the formation of the iminium intermediate **4**: (1) a radical rebound mechanism (Scheme 16), which would involve the direct hydroxylation of the amine substrate by an Fe-oxo species (2) a single electron oxidation followed by proton transfer, or (3) a concerted proton coupled electron transfer (PCET) reaction. Once the iminium ion **4** is formed *in situ*, it subsequently undergoes nucleophilic attack by H_2O to form the hemiaminal intermediate **5**. A second C-H activation step could occur to form the desired amide product **3**.

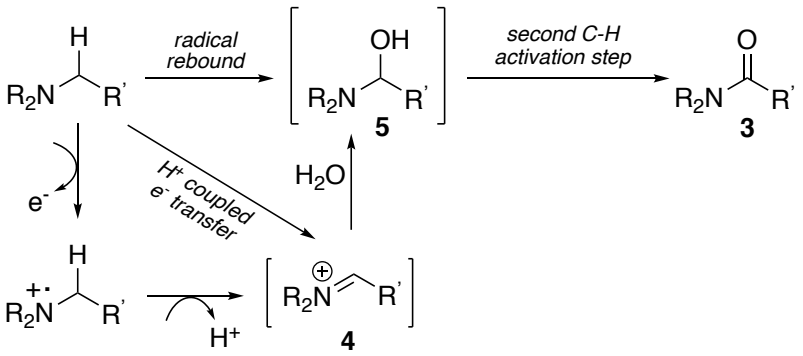

Scheme 38: Preliminary Mechanistic Hypothesis for Fe-Catalyzed Oxidation of Tertiary Amines.

3.2.1 Dealkylation Studies

The $PhCO_3{}^tBu$ loading studies shown in Section 3.1.7 revealed that oxidant loadings higher than the theoretical 2 equivalents needed for complete conversion were needed to achieve maximum amide yield. This result suggests that the reaction proceeds through undesirable side-reactions. Consequently, we analyzed the crude reaction mixture by GCMS to gain a better understanding of potential side-products (Scheme 39).

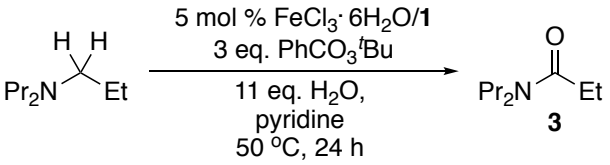

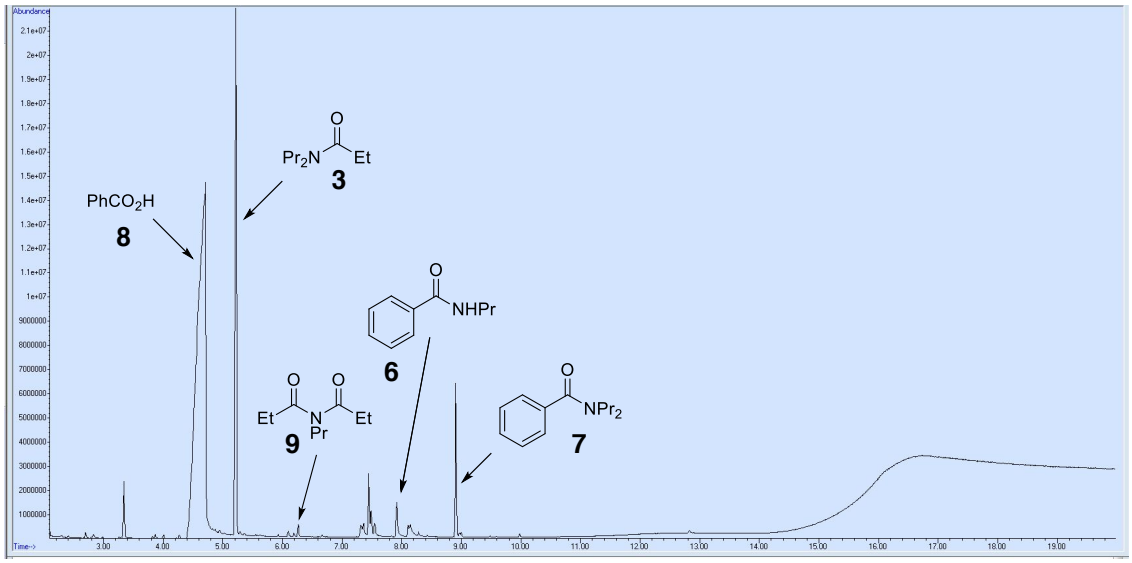

Scheme 39: GCMS Analysis of Fe-Catalyzed Oxidation of NPr_3.

GCMS analysis of the NPr_3 oxidation reaction mixture revealed the presence of several side-products in addition to the desired amide product **3**. As shown in Scheme 35, we hypothesized that Fe-catalyzed C_α–H oxidation of NPr_3 proceeds through the hemiaminal intermediate **5.** We further hypothesized that side-products **6** and **7** shown in Scheme 39 were the result of hydrolysis of hemiaminal **5** (in the presence of pyridine) followed by nucleophilic attack of $PhCO_3{}^tBu$ (Scheme 40). These findings revealed the presence of a competing, undesirable side-reaction and thus afforded insight into the necessity of superstoichiometric equivalents $PhCO_3{}^tBu$ in this system.

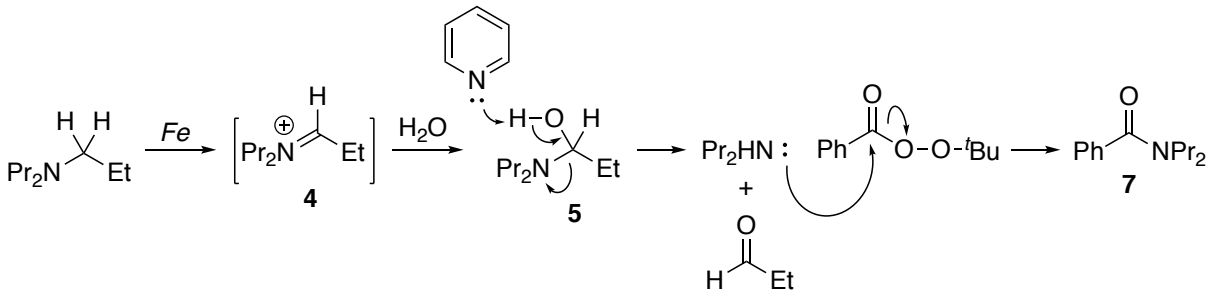

Scheme 40: Hydrolysis of Hemiaminal Followed by Nucleophilic Attack of $PhCO_3tBu$.

Based on the proposed general reaction pathway shown in Scheme 40, we hypothesized that increased H_2O loading would accelerate hydrolysis of hemiaminal **5** and thus outcompete amide formation. To that end, Fe-catalyzed oxidation of NBu_3 was conducted under optimized reaction conditions with varying ratios of H_2O:pyridine (Scheme 41). This substrate was chosen due to its lower volatility compared to NPr_3, and therefore to aid in the detection of hydrolysis products. In order to directly detect $HNBu_2$ in the reaction, a NaOH workup was used to liberate the amine from side-product **7**. Yields were determined by quantitative ^1H NMR analysis.

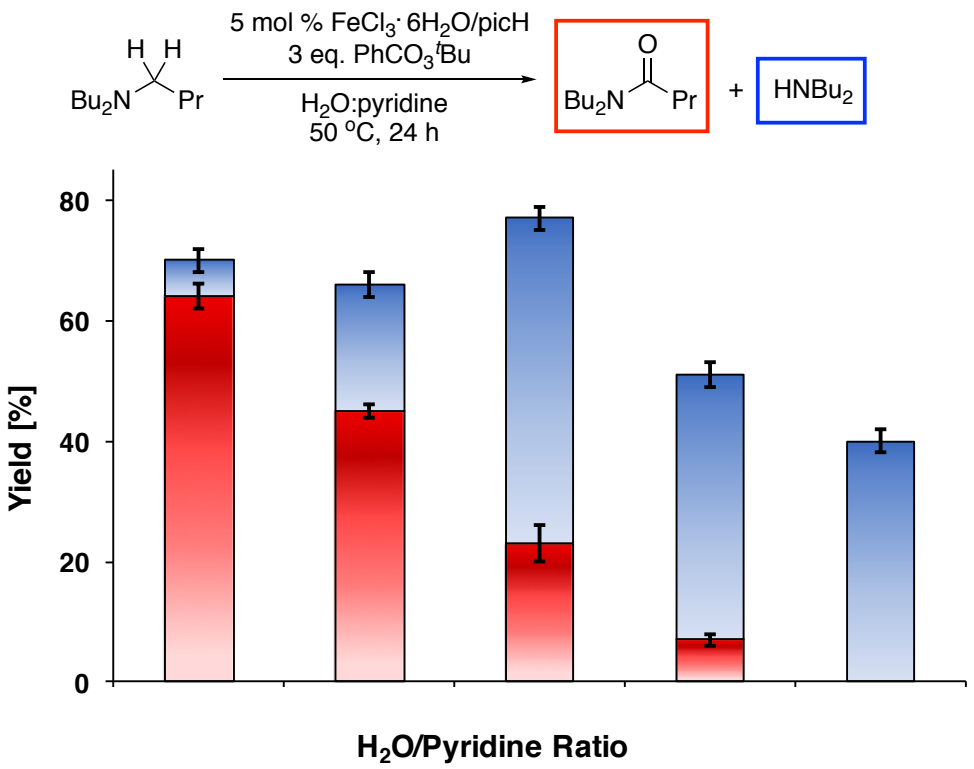

Scheme 41: Ratios of Amide to Hydrolysis Side-Products as a Function of H_2O Concentration.

When optimized H_2O loadings are used in the system (approx. 10 eq.), high yields of the desired amide product were observed with only small amounts of hydrolysis side-products detected. However, the yields of secondary amine side-product increased with increased H_2O:pyridine ratio. Based on this observation, we concluded that the selectivity for amide formation versus dealkylation should be determined by the relative rates of dealkylation versus oxidation of a common hemiaminal intermediate **5** (Scheme 42).

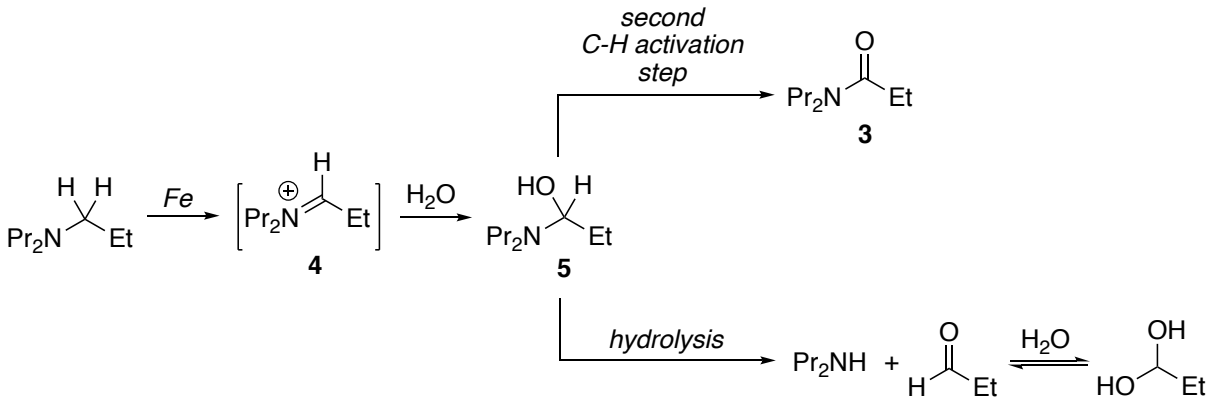

Scheme 42: Proposed Reaction Pathways From Common Hemiaminal Intermediate

Additionally, we propose that the aldehyde side-product would be in equilibrium with H_2O to form a gem diol, which would account for the driving force of hydrolysis at higher H_2O loadings [72].

3.3 Substrate Scope

3.3.1 Oxidation of Simple Amines

Once the optimized reaction conditions for the oxidation of NPr_3 were established, other simple amine substrates were optimized using the Design of Experiments (DOE) approach [73]. At this stage of the research, the key factors that had been identified as affecting amide yield were (1) temperature; (2) reaction duration; (3) $PhCO_3{}^tBu$ loading and (4) H_2O loading. Our purpose of using the DOE approach was to minimize the number of redundant experiments, as well as the overall number of experiments needed for optimization by systematically and concurrently conducting experiments that narrowed—and eventually optimized—the ranges of the parameters mentioned above.

In analogy to the optimization studies conducted for the $FeCl_3$/**1**-catalyzed C_α–H oxidation of NPr_3, amide yields were optimized for the small molecule amine substrates shown in (Scheme 43). These studies established the versatility of the catalytic system by providing synthetically useful amide yields with a variety of symmetric tertiary amines (Scheme 43, top row). Additionally, various asymmetric amines were optimized, thus expanding the synthetic relevance of this reaction (Scheme 43, bottom row). Finally, the substrate dibenzylamine was oxidized with this system to afford 59% amide yield, which suggested that this system may be viable for the oxidation of secondary amines as well.

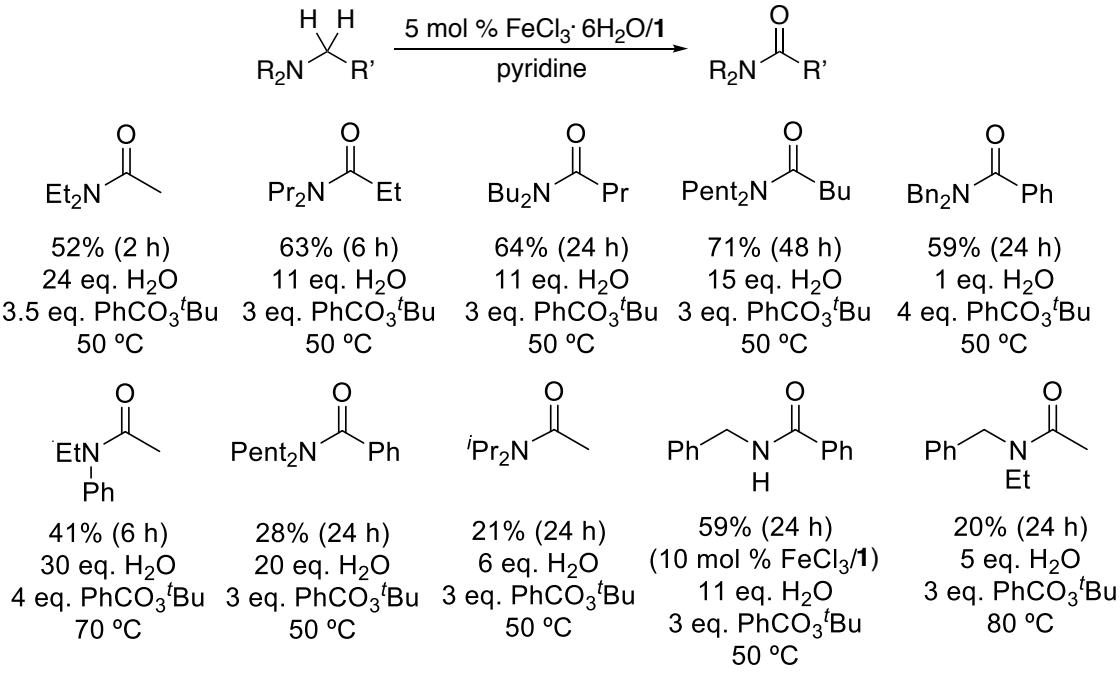

Scheme 43: Substrate Scope of Fe-Catalyzed Oxidation of Amines to Form Amides.

To further establish the versatility of this C_α–H amine reaction, the Fe-catalyzed system was optimized for compatibility with the complex pharmaceutical drugs Lidocaine and Donepezil (Scheme 44). LCMS analysis of the reaction mixtures showed the amides **10** and **11** to be the major reaction products. Additionally, and in analogy to the side-products discovered in the Fe-catalyzed C_α–H oxidation of NPr_3 (Scheme 39), oxidative dealkylation products **10A** and **11A** were present in low abundance.

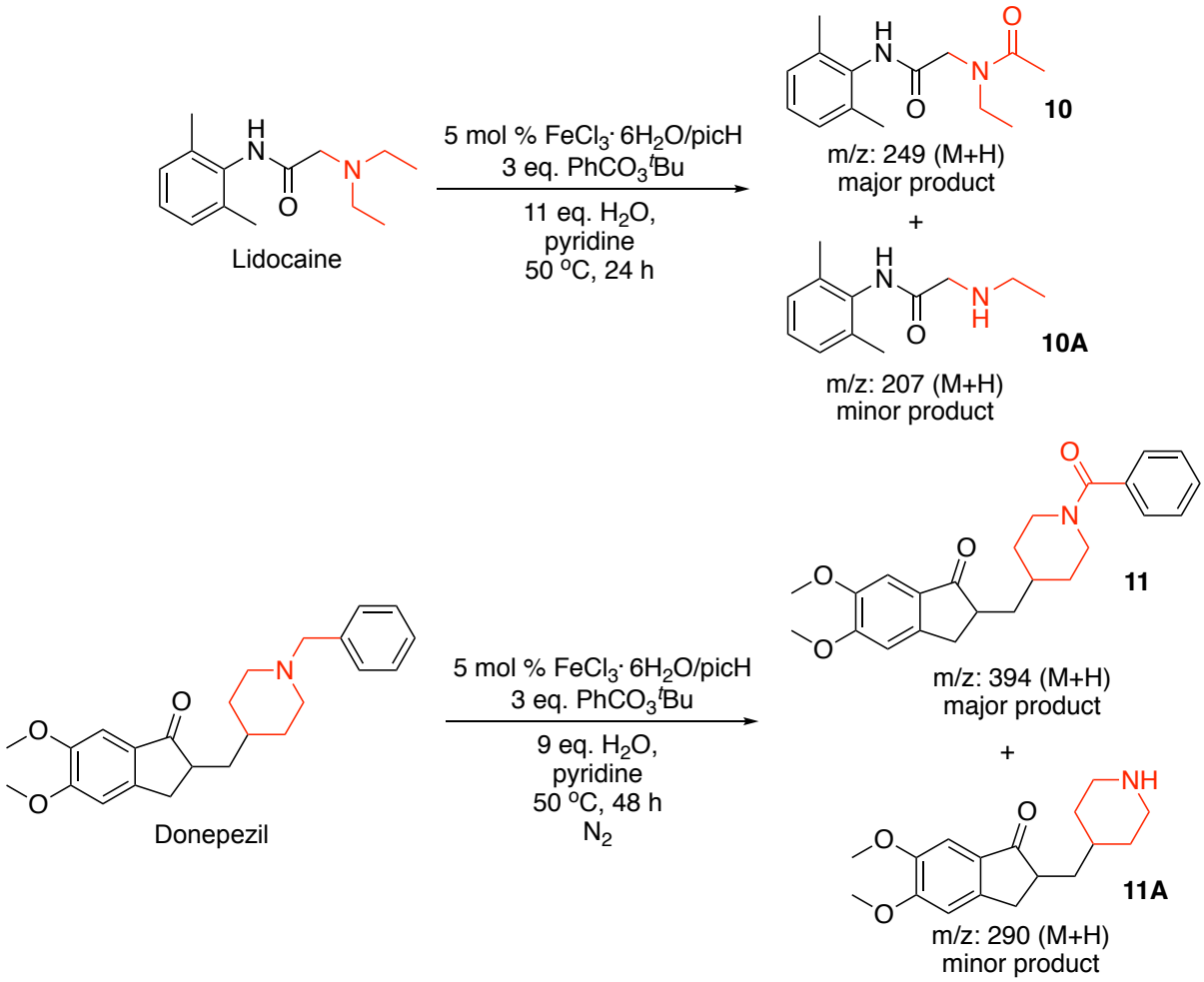

Scheme 44: Fe-Catalyzed Oxidation of Complex Pharmaceuticals.

At this stage of our research, it was clear that our efforts extended beyond chemical synthesis. In addition to amide formation, our Fe-catalyzed system was also producing known metabolites (**10**, **10A**, **11**, and **11A**) of the CYP450 drug metabolism of Lidocaine and Donepezil (Scheme 44) as well as established products of Gif oxidation of amines [74]. However, both the process of CYP450 drug metabolism and Gif amine oxidation systems appeared to be significantly less selective than our established Fe-catalyzed system, as these reactions also afford O-demethylation, N-oxidation, and aromatic hydroxylation products [75, 76]. We speculated that, while affording similar reactivity to CYP450 and Gif systems, our Fe-picolinic acid-catalyzed tertiary amine C_{α}–H oxidation reaction may provide *complimentary* reactivity to these long-established chemical reactions.

3.4 Preliminary Mechanistic Investigations

3.4.1 Background Studies

To gain insight into the role of oxidant and catalyst, as well as the effects of air under our optimized reaction conditions, a comprehensive background study was conducted. The system was examined using various combinations of $FeCl_3$ precatalyst, picolinic acid, $PhCO_3{}^tBu$ and air/N_2 atmosphere (Scheme 45). The reaction's dependence on NPr_3, H_2O and pyridine solvent had already been established (Scheme 30 and Scheme 36, respectively), and their molar amounts were kept constant. The data in Scheme 45 allowed the following conclusions: First, an O_2-mediated background reaction was present in this system, and afforded 12% amide yield in the *absence* of Fe-picolinic acid catalyst. This reaction did not proceed under N_2 atmosphere (Scheme 45, Entries 2 and 5). Furthermore, Entries 1 and 6 in Scheme 45 show that picolinic acid *alone* does not affect reactivity of the system in the absence of $FeCl_3$. This result highlights the role of Fe as a transition metal catalyst in this reaction. Next, we observed no reactivity in the absence of $PhCO_3{}^tBu$, regardless of the presence of Fe-picolinic acid or O_2 (Scheme 45, Entries 3 and 4). This finding is consistent with our hypothesis that the peroxyester is acting as an oxidant in analogy to the role of peroxides in Gif GoAgg^{III} systems [77]. Finally, when the optimized reaction conditions are used under N_2, analogous amide yields are achieved (Scheme 45, Entry 7). This result suggests that O_2 does not play a role in *catalyzed* amide formation, although it seems to mediate amide formation through an alternative, non-catalyzed pathway.

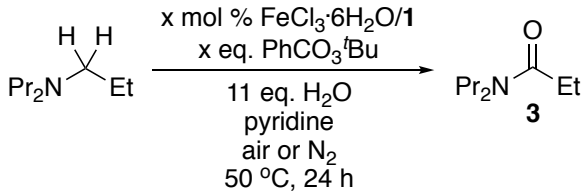

Entry	Mol % $FeCl_3$	Mol % 1	Atm.	Eq. $PhCO_3{}^tBu$	% Amide
1	0	5	N_2	3	0%
2	0	0	N_2	3	0%
3	5	5	Air	0	0%
4	5	5	N_2	0	0%
5	0	0	air	3	12 ± 1%
6	0	5	air	3	15 ± 1%
7	5	5	N_2	3	58 ± 2%

Scheme 45: Background Studies for Fe-Catalyzed Oxidation of NPr_3.

3.4.2 Radical Scavenger Studies

One mechanistic possibility for the background reaction observed in Scheme 45 (Entries 2 and 5) involves the formation of radical intermediates. Molecular oxygen is known to participate in CYP450 mediated, $1e^-$ oxidation pathways (Scheme 16). Additionally, our Fe-catalyzed system closely resembles the Gif $GoAgg^{III}$ system, which is biomimetic of CYP450 catalysis (Section 1.4 above). Consequently, we hypothesized that radical species may be involved in the non-catalyzed background reaction seen in Scheme 45 above. We postulated that ^{t}BuOOH may play a role in this reaction as well, and may be generated *in-situ* by nucleophilic attack on $PhCO_3{}^tBu$ by oxidative dealkylation side-products (Scheme 46, top). The peroxide species ^{t}BuOOH readily forms the stable radical ^{t}BuO· in the presence of pyridine (Scheme 46, bottom). [78, 79].

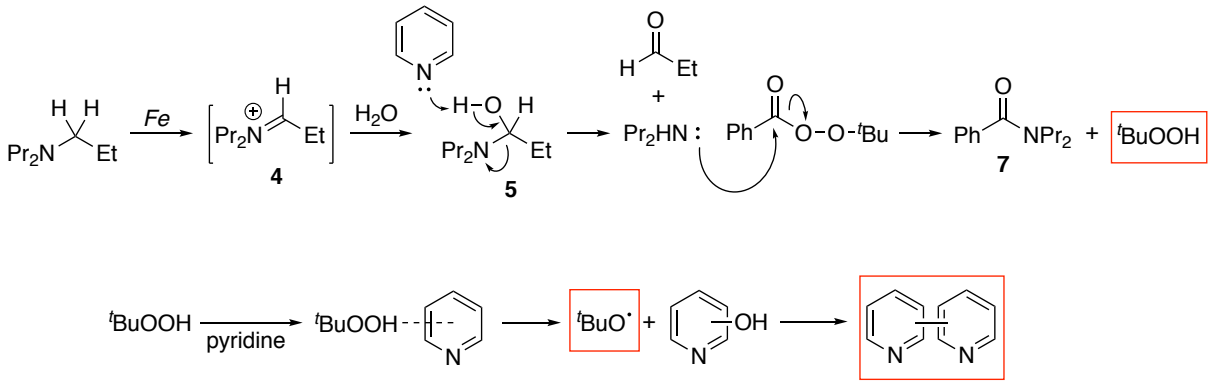

Scheme 46: Proposed Pathway for Formation of ^{t}BuOOH from Fe-Catalyzed Amine Oxidation System (top); Formation of ^{t}BuO• from ^{t}BuOOH in Pyridine (bottom).

Additionally, GCMS analysis of the crude reaction mixture of our catalyst system revealed the formation of multiple isomers of bipyridine, which further supports our hypothesis that the ^{t}BuO• radical may be generated in situ (Scheme 47).

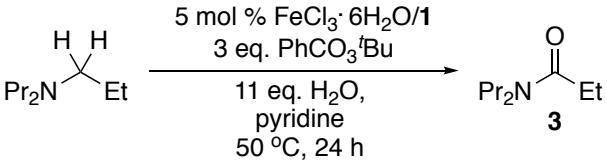

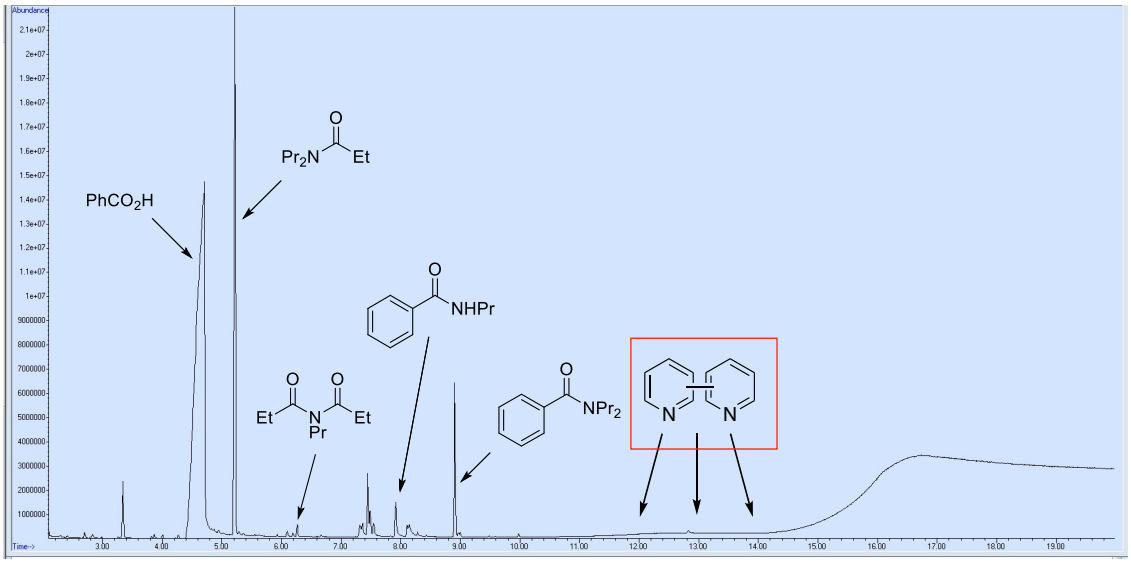

Scheme 47: GCMS Analysis of Fe-Catalyzed Oxidation of NPr_3 Showing Formation of Bipyridines.

In order to investigate the possibility of radical mediated $1e^-$ reaction pathways, radical trap studies were performed using TEMPO, a well-studied and widely used radical inhibitor [80]. These studies were conducted both in the presence and absence of $FeCl_3$ (Scheme 48).

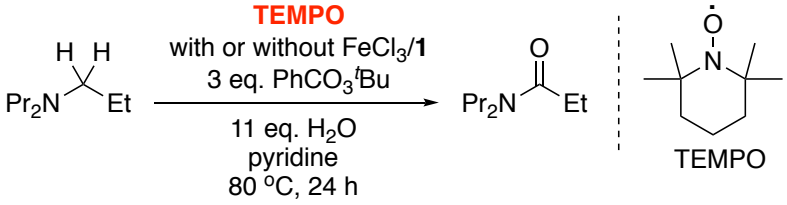

TEMPO mol %	% Amide (5 mol % $FeCl_3$/1)	% Amide (no catalyst)
0	48 ± 2%	18 ± 3%
5	42 ± 2%	13 ± 1%
20	29 ± 1%	5 ± 3%
50	14 ± 3%	0%
100	4 ± 2%	0%

Scheme 48: Radical Inhibition in Fe-Catalyzed Oxidation of NPr_3.

Overall, the presence of TEMPO in our system resulted in lower reaction yields; surprisingly, amide formation was observed at all tested TEMPO loadings up to 100 mol %, which suggested that Fe-catalyzed amide formation may not involve free radical species. However, when 20 mol % TEMPO™ was added in the *absence*

of $FeCl_3$—in analogy to the conditions used to observe the background reaction—the reaction yield was reduced to 5%. Amide formation was completely inhibited at loadings equal or greater than 50 mol %. These findings were consistent with our hypothesis that, while the Fe-catalyzed amide reaction may not proceed through a radical pathway, a radical background reaction may be present.

3.4.3 Iminium Intermediate Studies

Possibly due to the promiscuity of iminium ions, we postulated that additional nucleophiles may be utilized for C_α-H functionalization of amines from the iminium intermediate **4**. This hypothesis is supported by the literature, which includes methodologies for oxidative amine C_α-H functionalization to form new C_α-alkyl [81], -alkenyl [82], -alkynyl [83], -Ar [84], -Ac [85], and –CN [86] bonds. Based on this literature as well as our proposed mechanism (Scheme 38), we hypothesized that the addition of CN- to our system would enable C_α-CN bond formation on the amine substrate thus providing a direct and efficient pathway to α-amino nitriles, a synthetically important class of molecules [87]. To explore this possibility, we subjected dimethylaniline to our optimized conditions for Fe-picolinic acid-catalyzed amide synthesis. Initially, the reaction afforded trace amounts of the cyanated product, but with light optimization, and the addition of 18-crown-6 to increase the solubility of the KCN salt, the reaction was tuned to afford 80% of the α-aminonitrile (Scheme 49, top). This result supported the presence of an *in situ* generated iminium ion. Since our project objective was to oxidize *unactivated* aliphatic C_α-H bonds on tertiary amine substrates, we further tested this hypothesis with tributylamine as substrate (Scheme 49, bottom). To our gratification, 54% of the α-aminonitrile **12** was formed, and strongly supported the hypothesis that our Fe-catalyzed C_α-H oxidation reaction indeed proceeds through an iminium intermediate.

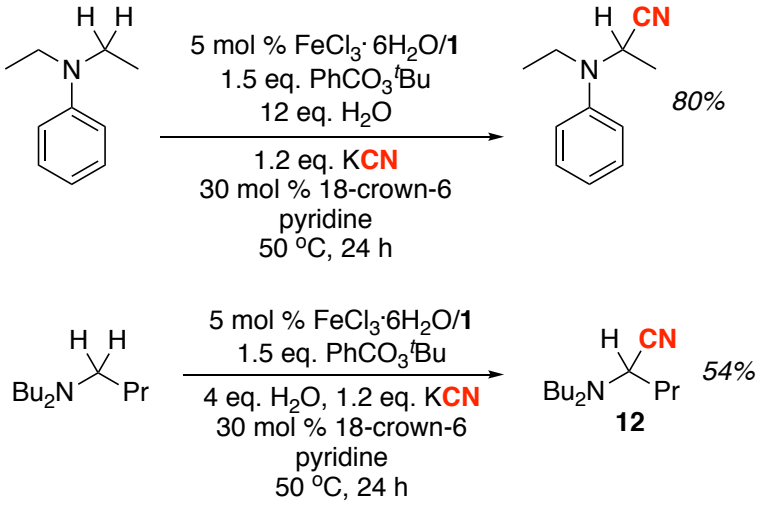

Scheme 49: Fe-Picolinic Acid-Catalyzed C_α–H Cyanation of Dimethylaniline (top); C_α–H Cyanation of Dibutylamine

3.4.4 *In Situ* Synthesis of Hemiaminal Intermediate

We hypothesized that the iminium ion **4**, in the presence of H_2O would undergo nucleophilic attack to form the hemiaminal reaction intermediate **5** (Scheme 38). The presence of oxidative delakylation products in the reaction mixture further supports this hypothesis (Scheme 47). Furthermore, the IR characteristics of similar hemiaminals are known in the literature [88]. In order to potentially observe hemiaminal **5**, or any other reaction intermediates, we employed *in situ* IR (ReactIR 15) to generate the reaction profile shown in Scheme 50. The Mettler Toledo ReactIR 15 instrument is accompanied by ConcIRT software, which was used for the identification of reaction components. The ConcIRT algorithm estimated the number of reaction components in the chemical system, and generated accurate component profiles and calculated pure spectra for each component. Two of the most prominent IR signals in the Fe-catalyzed amine oxidation reaction are the oxidant $PhCO_3{}^tBu$ and the major side-product $PhCO_2H$ (Scheme 50, top). Notably, these IR absorbance signals are inversely proportional, which indicates that $PhCO_3{}^tBu$ is directly converted to $PhCO_2H$ during the reaction. The detected reaction intermediate (Scheme 50, red) shows maximum signal when approximately 50% of the $PhCO_3{}^tBu$ signal has diminished. This suggests that the intermediate is generated as a direct result of oxidant consumption. Once the reaction IR profile was acquired, the ConcIRT software was instructed to generate the pure component spectra shown in Scheme 50 (bottom).

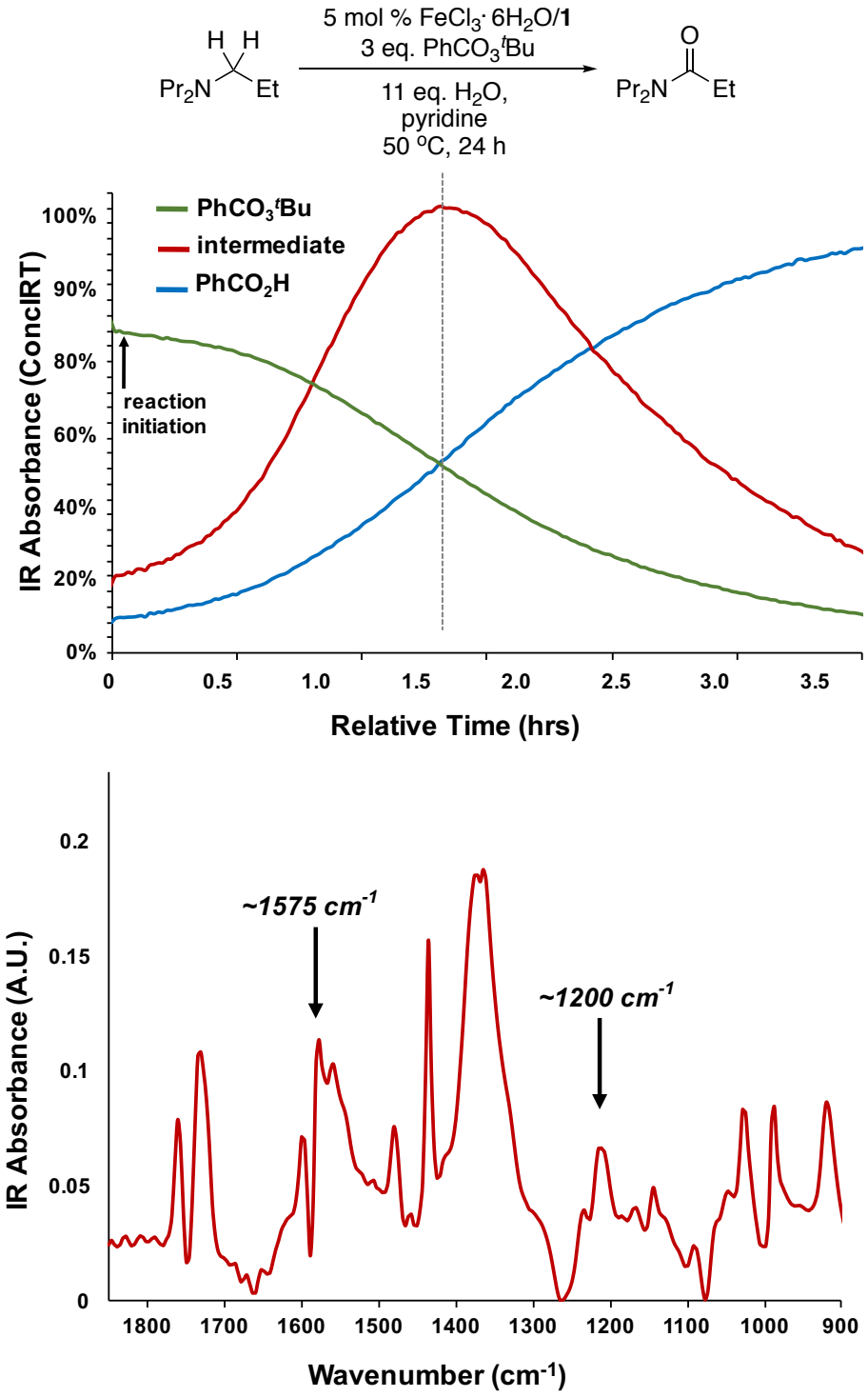

Scheme 50: *In Situ* IR Reaction Profile of Fe-Catalyzed C_α–H Oxidation of NPr_3 (top); Pure Spectrum of Reaction Intermediate (bottom).

Although the generated pure component spectrum shown in Scheme 50 (bottom) cannot be interpreted with 100% certainty, it can be compared to IR spectra of hemiaminals and related compounds found in the literature, and found to possess similar spectral characteristics [88].

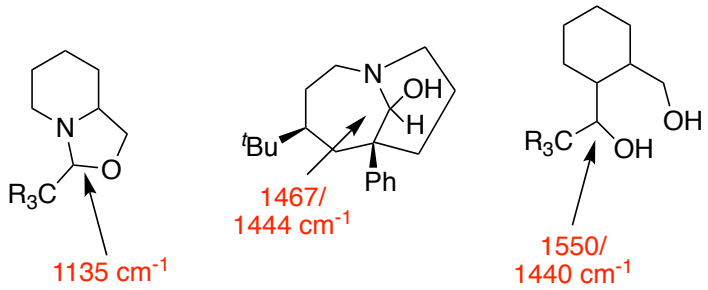

Scheme 51: Literature IR Characteristics of Hemiaminals and Related Compounds.

We reasoned that if our reaction indeed proceeds through a hemiaminal intermediate, then non-catalyzed *in situ* synthesis of hemiaminal **5**, followed by the subsequent addition of the catalytic components would afford amide **3** with comparable yields to the full catalytic system (Scheme 52). The catalytic oxidative dealkylation products dipropylamine and propionaldehyde (shown in Scheme 46, top) were reacted in pyridine to afford independently synthesized intermediate **5.** The reaction mixture was then subjected to our Fe-cataylzed conditions. To our gratification, this system afforded 54% yield of **3**, in analogy to our optimized catalytic system. This result suggested that both amide product **3**, as well as the oxidative dealkylation products observed in the Fe-catalyzed reaction mixture (Scheme 47) are formed through a common hemiaminal intermediate.

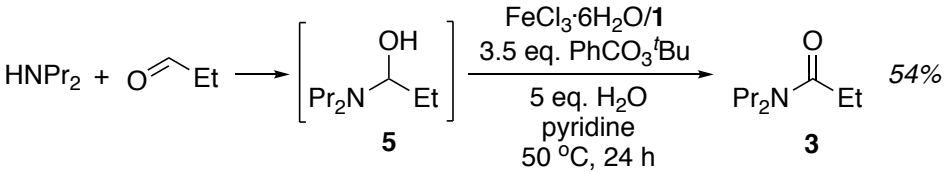

Scheme 52: *In Situ* Synthesis of Hemiaminal Intermediate for Amide Formation.

3.4.5 Incorporation of ^{18}O into Amide Product

The data shown in Sections 3.4.3 and 3.4.4 supports our mechanistic hypothesis (Scheme 38 above) of the formation of an Fe-catalyzed iminium ion followed by subsequent hemiaminal formation. We further hypothesized that the source of oxygen for C_α-O bond formation on the amine substrate was H_2O, which nucleophilically attacks the iminium ion. However, our optimized catalytic conditions were conducted under air in the presence of $PhCO_3{}^tBu$ oxidant, both of which are potential sources of [O]. In order to trace the source of incorporated oxygen in amide formation, we subjected tributylamine to our Fe-catalyzed conditions, under a N_2 atmosphere, using 11 equiv of $H_2{}^{18}O$ (97 % ^{18}O ; Scheme 53, top). Notably, 89 % incorporation of ^{18}O into the amide product was observed and suggested that the source of [O] for amide formation was H_2O. To eliminate the possibility of ^{18}O incorporation into the amide product *after* initial C-O bond formation, independently synthesized *N,N*-dibutylbutanamide was subjected to analagous reaction conditions (Scheme 53, bottom). These conditions did not result in more than 3 % ^{18}O incorporation into the amide, which makes ^{18}O exchange in the product after Fe-catalyzed amide formation unlikely. Overall, these data suggest that ^{18}O is introduced into the product in an intermediate. Potential pathways are nucleophilic attack of $H_2{}^{18}O$ at an iminium intermediate or direct amine hydroxylation by a ^{18}O-labeled Fe–oxo species. Collectively, these results allowed us to rule out the possibility of a CYP450-type O_2 activation mechanism (Scheme 16, top).

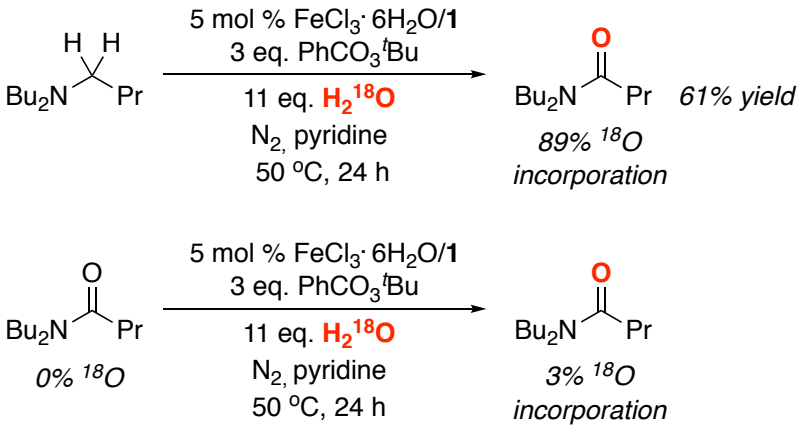

Scheme 53: Fe-Catalyzed Oxidation of NBu_3 with $H_2{}^{18}O$ (top); [O] Exchange Between $H_2{}^{18}O$ and amide product (bottom).

3.5 Revised Mechanistic Hypothesis

The data presented above allowed us to propose the following revised reaction mechanism (Scheme 54).

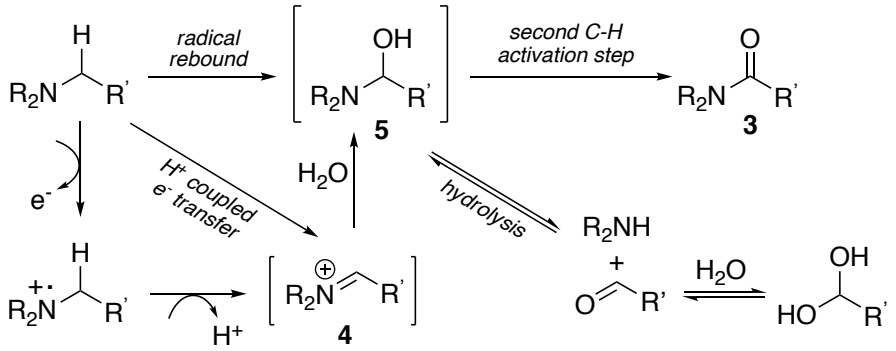

Scheme 54: Revised Mechanism for Fe-Catalyzed Amide Formation.

The background studies shown in Scheme 45 implicate Fe as a catalyst in the reaction. We hypothesized three possible Fe-catalyzed pathways that could lead to the formation of the iminium intermediate **4**: (1) a radical rebound mechanism, which would involve the direct hydroxylation of the amine substrate by an Fe-oxo species (2) a single electron oxidation followed by proton transfer, or (3) a concerted proton coupled electron transfer (PCET) reaction.

Our system's high dependence on water was clear from the onset; H_2O loadings higher than 15 eq. resulted in a steep reduction in amide yield, while total exclusion of water from the reaction afforded no trace of amide products, even under aerobic conditions (Scheme 36). Using ^{18}O labeled water and mass spectrometry, we determined the source of O in the new C_α-O bond on the amine substrate to be H_2O (Scheme 53). Furthermore, in situ formation of the hemiaminal species shown in Scheme 52 led to analogous amide yields in the presence of the standard catalytic reaction conditions. Based on these data as well as literature precedent [89], we hypothesize that our Fe-catalyzed amide synthesis reaction proceeds through an iminium ion **4** which can then be attacked by water to form the hemiaminal intermediate **5**. This hypothesis was further supported by the catalytic synthesis of the α-aminonitrile product (Scheme 55) upon addition of the CN^- nucleophile under conditions that were analogous to those for amide formation. Once hemiaminal formation is achieved, either a second C-H activation step could occur to form the

amide product, or the hemiaminal intermediate could decompose via hydrolysis (Scheme 46) to form the secondary amine and aldehyde oxidative dealkylation products. The relative rates of amide formation to oxidative delakylation are determined by the concentration of H_2O.

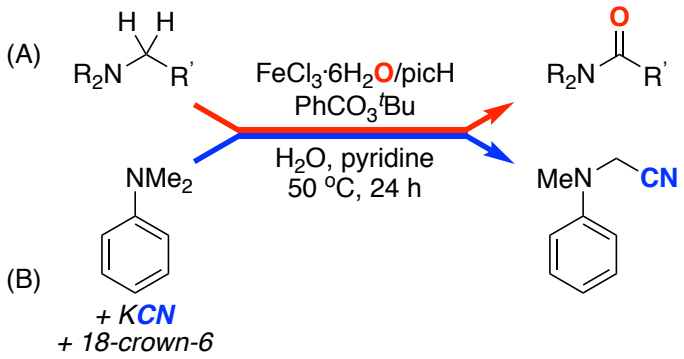

Scheme 55: Fe-Catalyzed Amide Formation (A); Fe-Catalyzed Cyanation (B).

3.6 Detailed Mechanistic Studies

3.6.1 Purpose of Mechanistic Investigation

Although our preliminary mechanistic investigations afforded some insight into the mechanism of this Fe-catalyzed C_α–H amine oxidation reaction, they left many unanswered questions. For example, the specific mechanism of Fe-catalyzed C-H activation in this catalytic system was unknown. Based on our preliminary mechanistic results described above, we were unable to distinguish between the C-H activation pathways shown in Scheme 54; whether the amine substrate was undergoing direct C-H hydroxylation by an Fe=O species (Scheme 16, top) or whether the role of Fe was simply to mediate $1e^-$ oxidation of the substrate was unclear (Scheme 54). Additionally, information regarding the rate-limiting step was not available from our initial investigation. Consequently, further rational reaction optimization was not possible. The structure of the catalyst resting state was also poorly understood. This knowledge may allow us to logically design ligands which would accelerate the reaction rate and possibly increase amide yields. Finally, the system's kinetic dependence on each reagent was not known. Although the Fe-picolonic acid catalyst has been extensively studied in other systems (i.e. the $GoAgg^{III}$ Gif oxidation system) its use with $PhCO_3{}^tBu$ for selective C_α-H amine functionalization is unprecedented. While promoting similar reactivity to the process

of CYP450 drug metabolism, as well as CYP450 biomimetic catalysts (Scheme 15), this catalytic system affords unique selectivity when applied to the oxidation of complex pharmaceutical substrates, as evidenced by a lack of O-demethylation, N-oxidation or aromatic hydroxylation products in these reactions. Additionally, the role of pyridine is not known. In accordance with the Principles of Green Chemistry, we desired to circumvent the need for toxic reagents in this system. However, the system's evident dependence on pyridine, coupled with a lack of mechanistic knowledge regarding its role made this objective difficult. In order to shed light on these areas and gain an enhanced mechanistic understanding of this catalytic system, we have conducted detailed studies to establish (1) the kinetic order in each reaction component (2) the resting state of the catalyst, and (3) the identity and mechanism of the turnover-limiting step in the catalytic cycle. From these results, a reaction rate law was determined and a detailed catalytic cycle was proposed.

3.6.2 Method of Initial Rates

At the onset of our detailed mechanistic investigations, we sought to determine which methods and instruments would aid us in this endeavor. We quickly determined that the well-established method of initial rates would likely play a role in this research [90]. This method is designed to afford reaction rates for kinetic analysis at the onset of a chemical reaction. The power of this method lies in its ability to provide the reaction rate—and thus the change in rate—regarding the change in concentration of *only one* chosen reaction component. This is true because the reaction rate is measured before the reaction has progressed beyond 5% conversion. This detail is crucial, as it allows for the approximation that the concentrations of all other reagents in the system have not significantly changed [91]. Notably, the method of initial rates only affords information for the catalytic cycle between the resting state of the catalyst (the lowest energy form of the catalyst) and the rate limiting step (the reaction step with the highest activation energy). Once the cycle passes the rate-limiting step, all subsequent reaction steps are energetically downhill and thus occur on a time scale too fast to acquire meaningful data.

One possibility for acquiring reaction rates with the initial rates method is with the use of calibrated GC of quantitative NMR. However, these techniques are time consuming, as analysis must be manually conducted throughout the duration of the

reaction. Additionally, the reaction must be disturbed during this process; reaction aliquots must be taken out of the reaction vessel intermittently. Because of these potential issues, we determined that *in-situ* techniques may facilitate our research more efficiently. A literature search revealed that *in-situ* IR techniques have been employed to acquire initial rates data in catalytic systems [92-94]. Consequently, we decided to utilize this technique to investigate the mechanism of our Fe- catalyzed C_α–H amine oxidation system. We ultimately employed a Mettler Toledo ReactIR 15 instrument for *in situ* initial rates measurements in our reactions. The Mettler Toledo ReactIR 15 instrument is accompanied by ConcIRT analytical software, which was used to measure initial rates by observing the consumption of the oxidant $PhCO_3{}^tBu$ over time, in accordance with (Eq. 1) [95].

$$\text{rate} = -\frac{d[R]}{dt} = \frac{d[P]}{dt} \qquad (Eq.1)$$

Equation 1: Relationship of Rate to Concentration of Reactants and Products.

Alternatively, as seen in Eq. 1, reaction rates can be measured by observing the increase of product concentration over time. However, the amide product **3** afforded an IR signal too weak to accurately monitor, in particular during the first period of the reaction. Therefore, the oxidant $PhCO_3{}^tBu$, which possesses a prominent C=O band at 1757 cm^{-1}, was used as a handle in these experiments (Scheme 56).

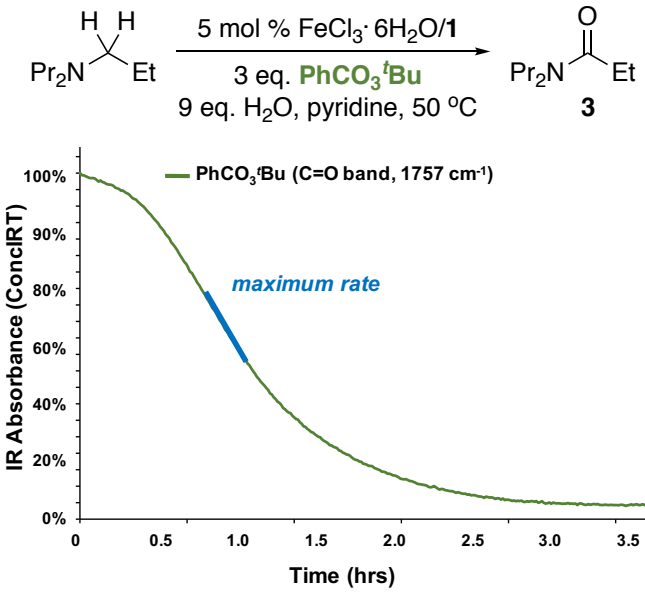

Scheme 56: Typical Kinetic Curve for Fe-Catalyzed Oxidation of NPr_3.

3.7 Kinetic Studies

3.7.1 Relationship Between Reaction Yield and Reaction Rate

The optimized reaction conditions for Fe-picolinic acid catalyzed C_α–H oxidation of NPr_3 are shown in Scheme 57. A maximum yield of amide **3** (63%) was achieved when $FeCl_3 \cdot 6H_2O$ was used with picolinic acid in a 1:1 ratio.

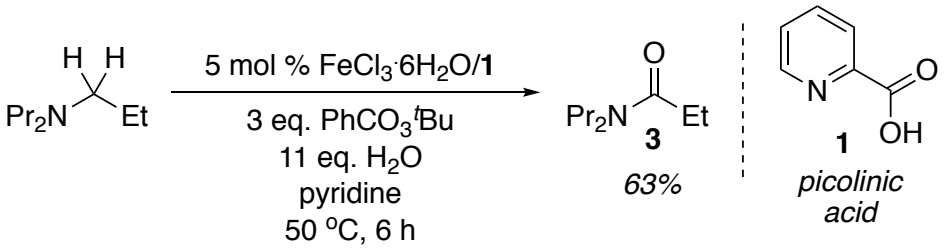

Scheme 57: Optimized Conditions for Fe-Catalyzed Oxidation of NPr_3.

We hypothesized that the reaction conditions that provided maximum product yield would also afford the fastest reaction rate. Therefore, we postulated that using a 1:1 ratio of Fe to **1** would maximally accelerate the catalytic cycle. To test this hypothesis, initial rates were measured for various Fe/picolinic acid (**1**) ratios, using 5 mol % Fe while varying the loading of **1** from 2.5 mol % to 10 mol % (Scheme 58). Indeed, a maximum overall reaction rate was observed using an $FeCl_3 \cdot 6H_2O$/**1** ratio of 1:1. We concluded from these data that the highest initial reaction rates as measure by oxidant consumption can also be expected to result in the highest product yields. As such, oxidant consumption is a valid measurement for reaction progress, and following the disappearance of $PhCO_3{}^tBu$ can be expected to provide detailed insight into the mechanism of forming the amide product.

3.7.2 Catalytic Relevance of X-Type Ligands

As demonstrated previously in Scheme 32 above the chosen ligand drastically affects reaction yield. Consequently, we hypothesized that changing the X-type ligand on the Fe center from Cl to an alternative ligand may also affect reaction rates and yields. To investigate, we substituted $FeCl_3 \cdot 6H_2O$ in our Fe-Catalyzed amine oxidation reaction for a variety of alternative Fe^{III} salts (Scheme 59).

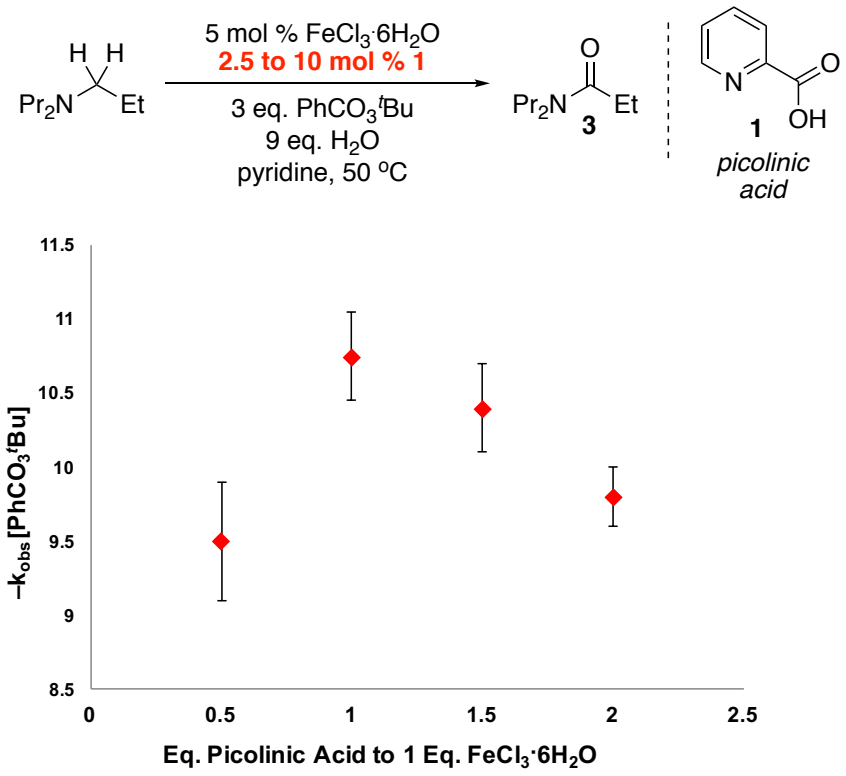

Scheme 58: Initial Reaction Rates of Fe-Catalyzed Oxidation of NPr_3 vs. Fe/**1** Ratio.

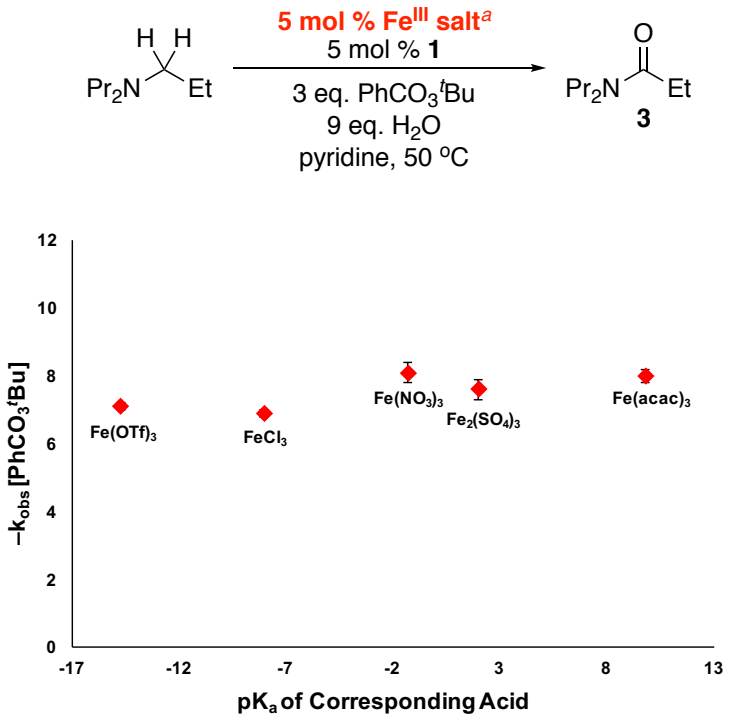

Scheme 59: Reaction Rate of Fe-Catalyzed Oxidation of NPr_3 with Alternative Fe Salts. [a]2.5 mol % $Fe_2(SO_4)_3$ was used.

Contrary to our hypothesis, these studies revealed that X-type ligands on the Fe center had little effect on the initial reaction rate, even across a broad spectrum of pK_a's (-14.7 to 9.8). This result suggested that the Cl-ligands on the $FeCl_3$ catalyst may not play a role in catalysis and can be expected to be absent in the structure of the active Fe catalyst.

3.7.3 Catalytic Relevance of Picolinic Acid

Based on the well-established activity of the Fe-picolinic acid catalyst in $GoAgg^{III}$ Gif oxidation systems (Section 1.4 above) as well as the observed dependence of picolinic acid **1** in our system, we hypothesized that this ligand is catalytically relevant for Fe-catalyzed amine C_α-H oxidation of tertiary amines. To explore the catalytic relevance of **1**, we investigated the catalytic system's activity upon initial exclusion of **1** (Scheme 60).

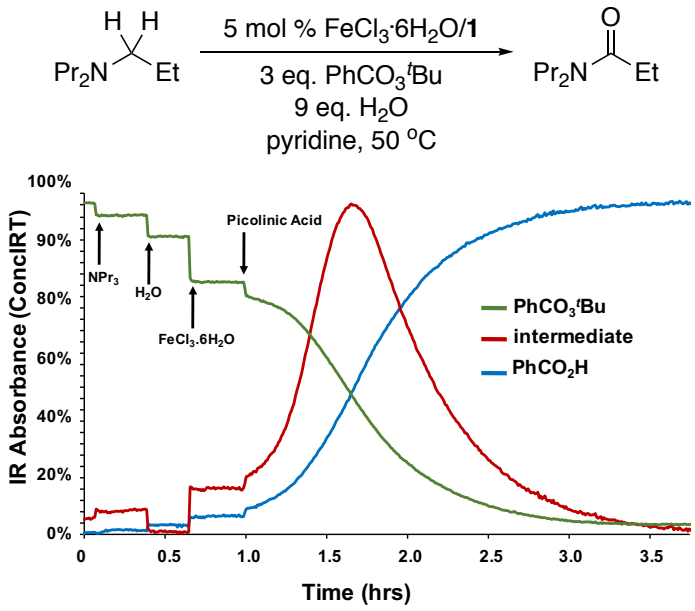

Scheme 60: Kinetic Profile of Fe-Catalyzed Oxidation of NPr_3 Upon Sequential Addition of Reagents.

ReactIR analysis determined that, in the absence of **1**, the catalytic system does not initiate, as demonstrated by the green curves with zero slope in Scheme 60 upon addition of NPr_3, H_2O, or $FeCl_3$, indicating no changes in the concentration of $PhCO_3{}^tBu$ even in the presence of all other reactants. However, upon addition of **1**, the reaction quickly proceeds, as indicated by the consumption of $PhCO_3{}^tBu$ as well

as the formation of $PhCO_2H$ and the observed reaction intermediate (Scheme 60, blue and red curves, respectively). Collectively, these findings implicate picolinic acid **1** as a catalytically active, potentially Fe-bound ligand.

3.7.4 Kinetic Order in Fe Catalyst

In order to investigate the role of each reaction component in the catalytic cycle, as well as ultimately establish the kinetic rate law, we sought to determine the kinetic order in each reagent for the Fe-picolinic acid-catalyzed C_α-H Oxidation of NPr_3. We first sought to examine the order of this reaction in the Fe-picolinic acid catalyst. As an Fe-picolinic acid ratio of 1:1 afforded the maximum reaction rate (see Scheme 58 above), this ratio was used in all subsequently described studies. We examined the order in catalyst by varying loadings of $FeCl_3 \cdot 6H_2O$-picolinic acid (0.5 to 40 mol %) in pyridine (15 mL) at 50 °C. The reactions were monitored by *in-situ* IR and the initial rate was determined for each catalyst concentration. As shown in Scheme 61, a plot of initial reaction rate ($-k_{obs}$ [$PhCO_3{}^tBu$]) vs. mol % $FeCl_3 \cdot 6H_2O$-picolinic acid shows a linear trend at catalyst loadings of 0.5-2.0 mol %, which indicates a first-order dependence in catalyst at these concentrations. As the loadings of catalyst were increased (3.0 to 17 mol %), the system approached saturation kinetics, indicated by approaching a maximum initial reaction rate at 17 mol % catalyst. Beyond a catalyst loading of 17 mol %, a sharp decrease in reaction rate was observed, possibly indicating a change in the prevalent catalyst species and/or the formation of a different catalyst reservoir species. One explanation for this may be the polymerization of the Fe species at higher concentrations, which has similarly been observed for other Fe/**1** systems [96]. Overall, the first order in Fe/**1** at low, catalytically relevant concentrations suggests that the active Fe catalyst is a mononuclear species, which also supports the previously established conclusion that Fe is the active catalyst in the developed amine oxidation system.

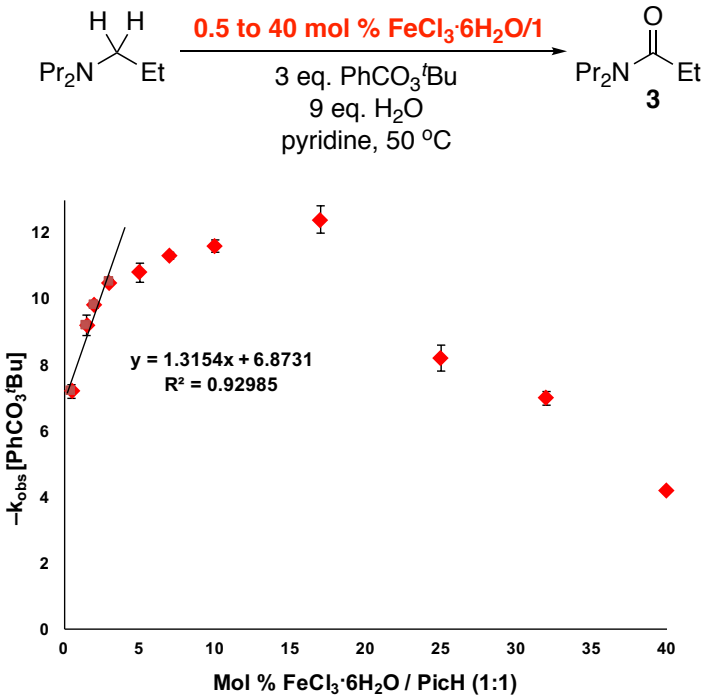

Scheme 61: Plot of Initial Rate -k_{obs}[$PhCO_3{}^tBu$] Versus mol % $FeCl_3$-Picolinic acid (1:1).

3.7.5 Kinetic Order in Oxidant

We next sought to determine the kinetic order in $PhCO_3{}^tBu$ using an analogous procedure, varying the loadings of $PhCO_3{}^tBu$ in the reaction solution (1.0-4.0 eq.; 2.5 to 10 mmol). A plot of initial reaction rate (-k_{obs} [$PhCO_3{}^tBu$]) vs. equivalents of $PhCO_3{}^tBu$ added (Scheme 62) shows a positive linear trend, which indicates a first-order dependence in [$PhCO_3{}^tBu$]. This finding indicates that one equivalent of oxidant enters the catalytic cycle before the rate-limiting step.

3.7.6 Kinetic Order in Amine Substrate

Similarly, the order in amine substrate (NPr_3) was determined, with varying concentrations of NPr_3 (0.25-1.0 eq.; 630 μmol to 2.5 mmol). A plot of initial reaction rate (-k_{obs} [$PhCO_3{}^tBu$]) vs. equivalents NPr_3 (Scheme 63) shows a linear trend, which indicates a first-order dependence in [NPr_3] suggesting that 1 equivalent of NPr_3 substrate enters the catalytic cycle before the rate-limiting step.

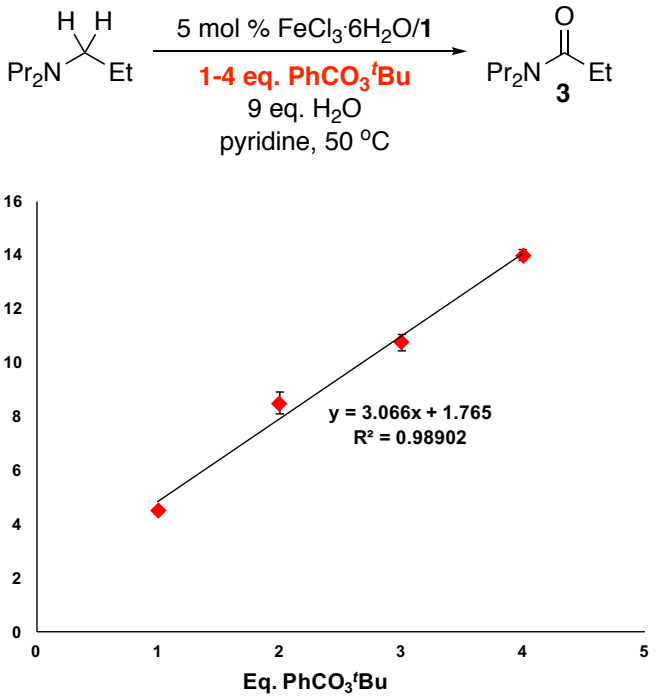

Scheme 62: Plot of Initial Rate -k_{obs}[$PhCO_3{}^tBu$] Versus Eq. $PhCO_3{}^tBu$.

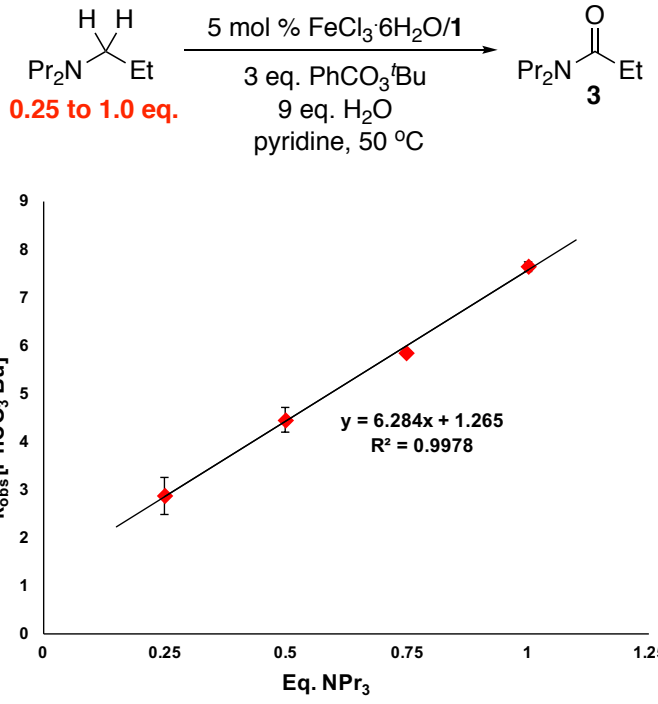

Scheme 63: Plot of Initial Rate -k_{obs}[$PhCO_3{}^tBu$] Versus Eq. NPr_3.

3.7.7 Kinetic Order in Water

Next, the order in H_2O was investigated by varying concentrations of H_2O (0.4 to 20 equiv.) in pyridine (15 mL). A plot of inverse initial reaction rate (1/-k_{obs} [$PhCO_3{}^tBu$]) vs. equiv. H_2O (Scheme 64) shows a linear trend between H_2O loadings of 0.4 to 2.5 equiv., which indicates a negative second-order dependence in H_2O at these concentrations. This suggests that 2 equivalents of H_2O leave the catalytic cycle between the resting state and the rate-limiting step. As the loadings of H_2O were increased (5.0 to 20 eq.), the difference in rate from loading to loading lessened, which is indicative of saturation kinetics. Overall, these data suggest that H_2O, despite being an important reactant in the reaction mixture (see section 3.4.5, ^{18}O studies above), inhibits catalytic turnover.

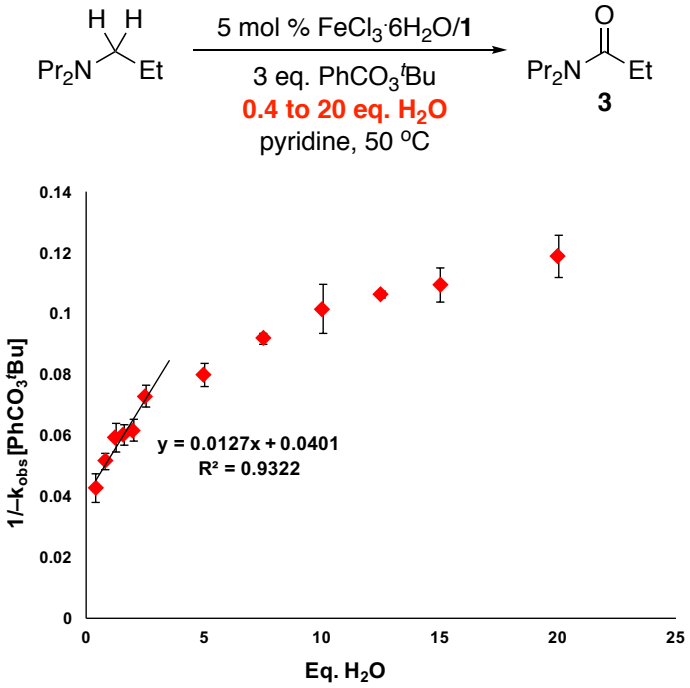

Scheme 64: Plot of Inverse Initial Rate (1/-k_{obs}[$PhCO_3{}^tBu$]) Versus Eq. H_2O.

3.7.8 Kinetic Order in Pyridine

We hypothesized that pyridine may act as ligand in our Fe-catalyzed system. Consequently, the order in pyridine was investigated. However, as pyridine was also solvent in our catalytic system, a co-solvent had to be identified. EtOAc was used as cosolvent to perform these analyses due to its ability to promote reactivity in the system (8%), albeit diminished from the optimized conditions in the presence of

pyridine (68%). Notably, EtOAc was the only solvent other than pyridine to afford amide yield. The experiments were conducted using varying concentrations of pyridine (2.5 to 10 equiv.) in EtOAc (15 mL). A plot of initial reaction rate ($-k_{obs}$ [$PhCO_3{}^tBu$]) vs. equivalents pyridine in solution (Scheme 65) shows a linear trend with no change in slope at pyridine loadings. This indicates a zeroth order dependence on the pyridine concentrations under these conditions. This finding indicates that pyridine neither enters nor leaves the cycle before the rate-limiting step. It should be noted that this result does not suggest pyridine is not *involved* in the cycle (e.g. by coordination to Fe); rather, the data imply that neither coordination to nor dissociation from the Fe center occur before the rate-limiting step.

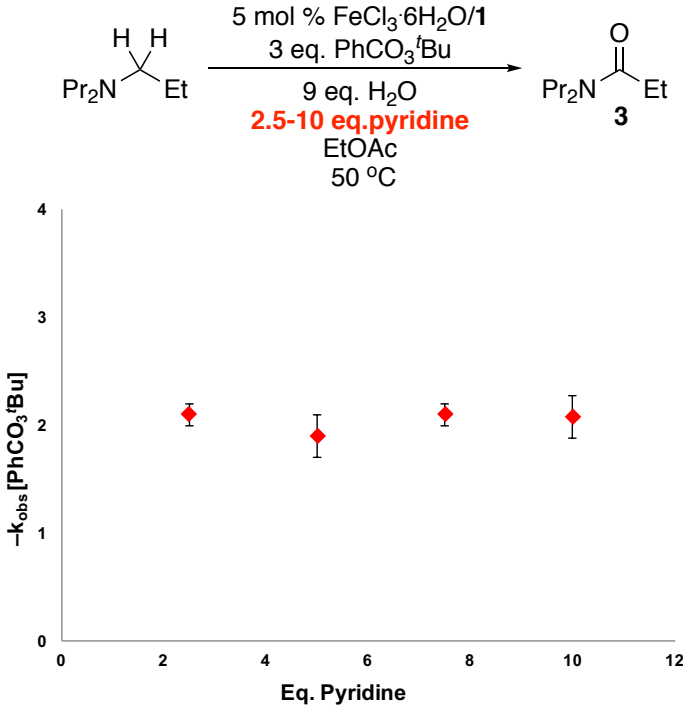

Scheme 65: Plot of Initial Rate $-k_{obs}$[$PhCO_3{}^tBu$] Versus Eq. Pyridine in EtOAc.

3.7.9 Catalytic Relevance of Pyridine

Pyridine has been implicated as an active ligand in Fe-catalyzed oxidation systems, including Gif oxidations [97]. Consequently, we postulated that the overall reaction rate may change as a function of the electron donating/withdrawing effect of pyridine ligand, if pyridine is coordinated to the active catalyst. To test this hypothesis, various substituted pyridines were employed as solvents, and the initial reaction rate in each solvent was measured by *in-situ* IR analysis. A Hammett plot of

the resulting data (Scheme 66) indicated that simple pyridine provided overall the fastest reaction rate, while pyridines with electron-rich substituents (4-Me/MeO) or electron-withdrawing substitutents (4-Cl, 3-F, 4-CF_3) all resulted in lower initial rates. Interestingly, two straight lines can be drawn through the data points obtained, suggesting that a change of rate-determining step occurs when comparing reactions with electronically differentiated substituents. The data for pyridine itself place it in an intermediate region, suggesting that the relevant reaction steps are likely of similar rate with pyridine. This data is consistent with pyridine promoting dissociation and association steps at an Fe center, as both of these steps would result in charge buildup in the rate-limiting step. Fundamentally, though, the presence of Hammett relationships with relatively large slopes indicate that pyridines are not simply acting as solvents, but that they are in close proximity to the reaction site. This suggests that a minimum of one equivalent of pyridine binds to the Fe center during catalysis.

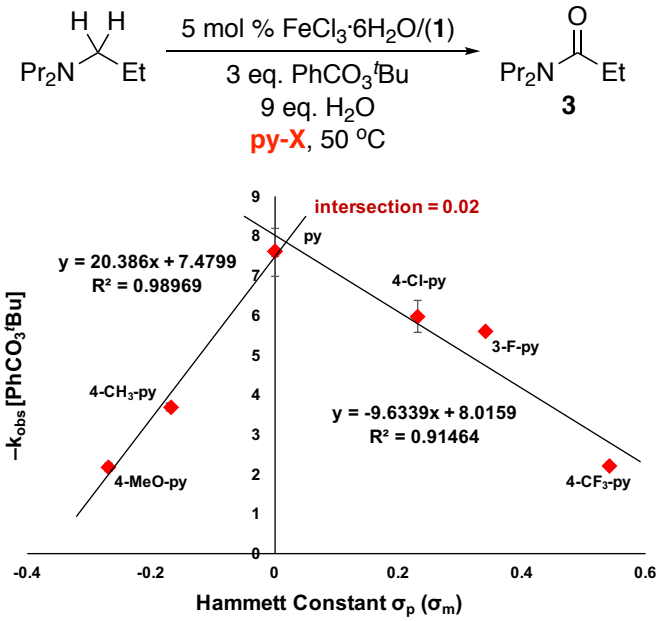

Scheme 66: Hammett Plot for Fe-Catalyzed Oxidation of NPr_3 with Substituted Pyridines.

3.7.10 Kinetic Order in Benzoic Acid

Our initial investigations showed $PhCO_2H$ to be a product of our catalytic system (Scheme 39 above). Additionally, the kinetic profile of the reaction showed that the increase in $PhCO_2H$ during the reaction was directly proportional to the consumption of $PhCO_3{}^tBu$ (Scheme 50 above); thus, $PhCO_2H$ formation is a direct

result of catalytic turnover. To probe the possibility of $PhCO_2H$ influencing catalysis, for example by promoting or inhibiting turnover, its kinetic order was investigated by adding $PhCO_2H$ (2.5 to 10 mmol) to the reaction mixture. A plot of initial reaction rate ($-k_{obs}$ [$PhCO_3{}^tBu$]) vs. equivalents added $PhCO_2H$ (Scheme 67) shows a negative linear trend, which indicates a negative first order dependence on [$PhCO_2H$]. One possibility for the observed kinetics is that $PhCO_2H$ protonates the amine substrate in equilibrium. The substrate would then have to be deprotonated before it can enter the catalytic cycle and may explain the observed inhibition effect of $PhCO_2H$.

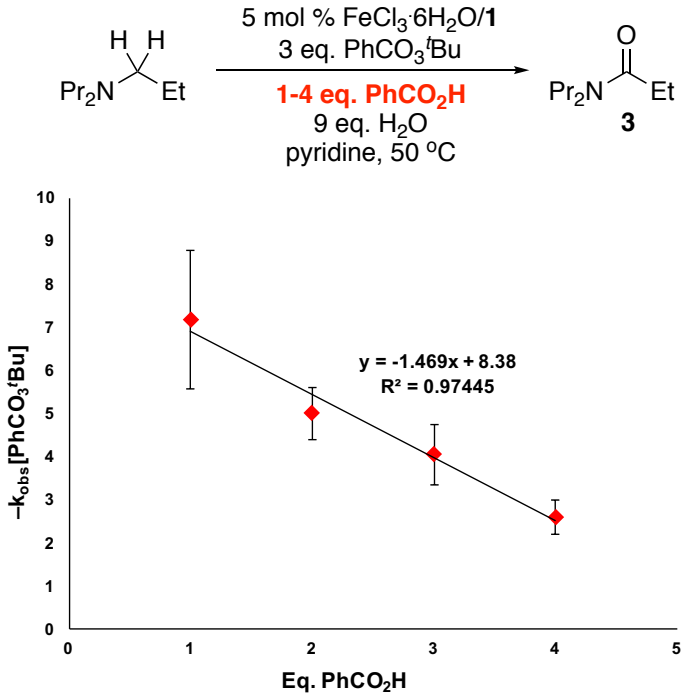

Scheme 67: Plot of initial rate [$-PhCO_3{}^tBu$] versus equiv. $PhCO_2H$.

3.7.11 Kinetic Order in *tert*-Butanol

$PhCO_2H$ was observed to be a product in this reaction, likely as the result of $PhCO_3{}^tBu$ consumption (Scheme 39). We postulated that ^{t}BuOH may also be a side-product of this process (Scheme 68), and therefore studies probing its kinetic order were initiated by adding different amounts of ^{t}BuOH (1.0-4.0 eq.; 2.5 to 10 mmol) to the reaction mixture in pyridine. A plot of initial reaction rate ($-k_{obs}$ [$PhCO_3{}^tBu$]) vs. equivalents added ^{t}BuOH shows a linear trend with no change in slope, which indicates a zero order dependence in [^{t}BuOH]. This indicates either that ^{t}BuOH coordination to Fe does not change or that ^{t}BuOH does not play a role in the catalytic cycle between resting state and rate-limiting step (Scheme 69).

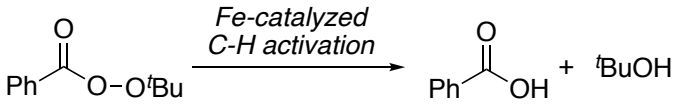

Scheme 68: Consumption of $PhCO_3{}^tBu$ to Generate $PhCO_2H$ and ^{t}BuOH.

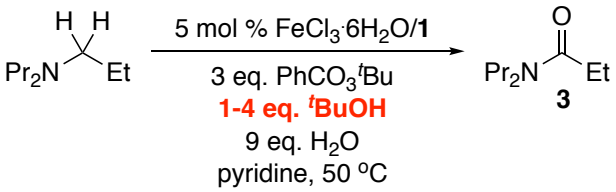

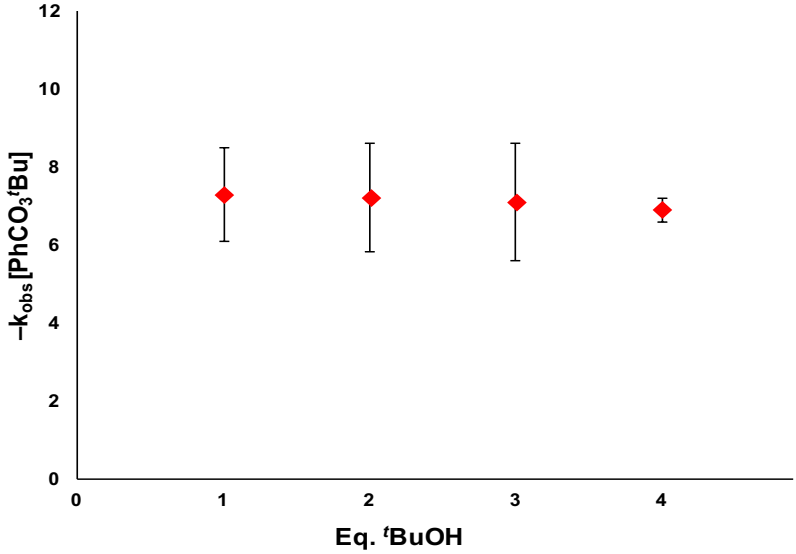

Scheme 69: Plot of Initial Rate [-$PhCO_3{}^tBu$] Versus Eq. ^{t}BuOH.

3.7.12 Intermolecular Kinetic Isotope Effect (KIE)

At the onset of our investigations, the rate-determining step of the reaction was unknown. However, because our system mediates the oxidation of *unactivated amine* C_α-H bonds, we hypothesized that C-H activation may be the rate-limiting step in the catalytic cycle.

Deuterated substrates in C-H activation reactions react with molecules in the system in the same manner, but often exhibit differences in reaction rates due to the mass difference in zero-point energy between the C-H and C-D bonds when in the transition state [98]. The difference in rates of such reactions is defined as the kinetic isotope effect of the reaction. If C-H activation occurs at or before the rate-limiting step, slower reaction rates are typically observed in molecules with C-D bonds when comparing C-H cleavage rates of independent reactions. If C-H activation occurs

after the rate-limiting step, then no KIE would be observed due to the relatively small difference in rate of these fast processes [99].

In these experiments, the intermolecular kinetic isotope effect of the system was determined. Two separate reactions were conducted, one with NEt_3—which contains an α-C–H bond—and one with NEt_3-D_{15}—which contains an analogous α-C–D bond.

The relative ratio of these independently determined reaction rate constants (k_H/k_D) afforded the intermolecular kinetic isotope effect of the reaction. In this amine oxidation system, k_H/k_D was determined to be 1.7 ± 0.1 (Scheme 70). This result is consistent with C-H bond cleavage occurring at or before the rate-determining step of the catalytic cycle [99]

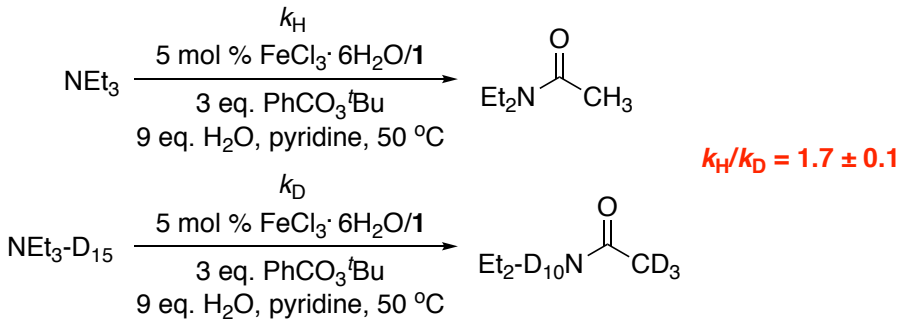

Scheme 70: Kinetic Isotope Effect of Deuterated NEt_3.

3.7.13 Reaction Rate Law

Based on the kinetic data from the initial rates studies (summarized in Table 1), a general catalytic cycle was proposed (Scheme 71) and the overall rate law was formulated.

Entry	Description of Result
1	Reaction is first order in [Fe-picolinic acid (1:1)] (resting state **A**)
2	Reaction is first order in [$PhCO_3{}^tBu$]
3	Reaction is first order in [NPr_3]
4	Reaction is negative second order in [H_2O]
5	Reaction is zeroth order in [pyridine]
6	Reaction is negative first order in [$PhCO_2H$]
7	Reaction is zeroth order in [^tBuOH]
8	Cl ligands expected to absent in structure of active catalyst
9	At least one eq. pyridine is bound to active catalyst

Table 1: Summary of Conclusions from Initial Rates Data.

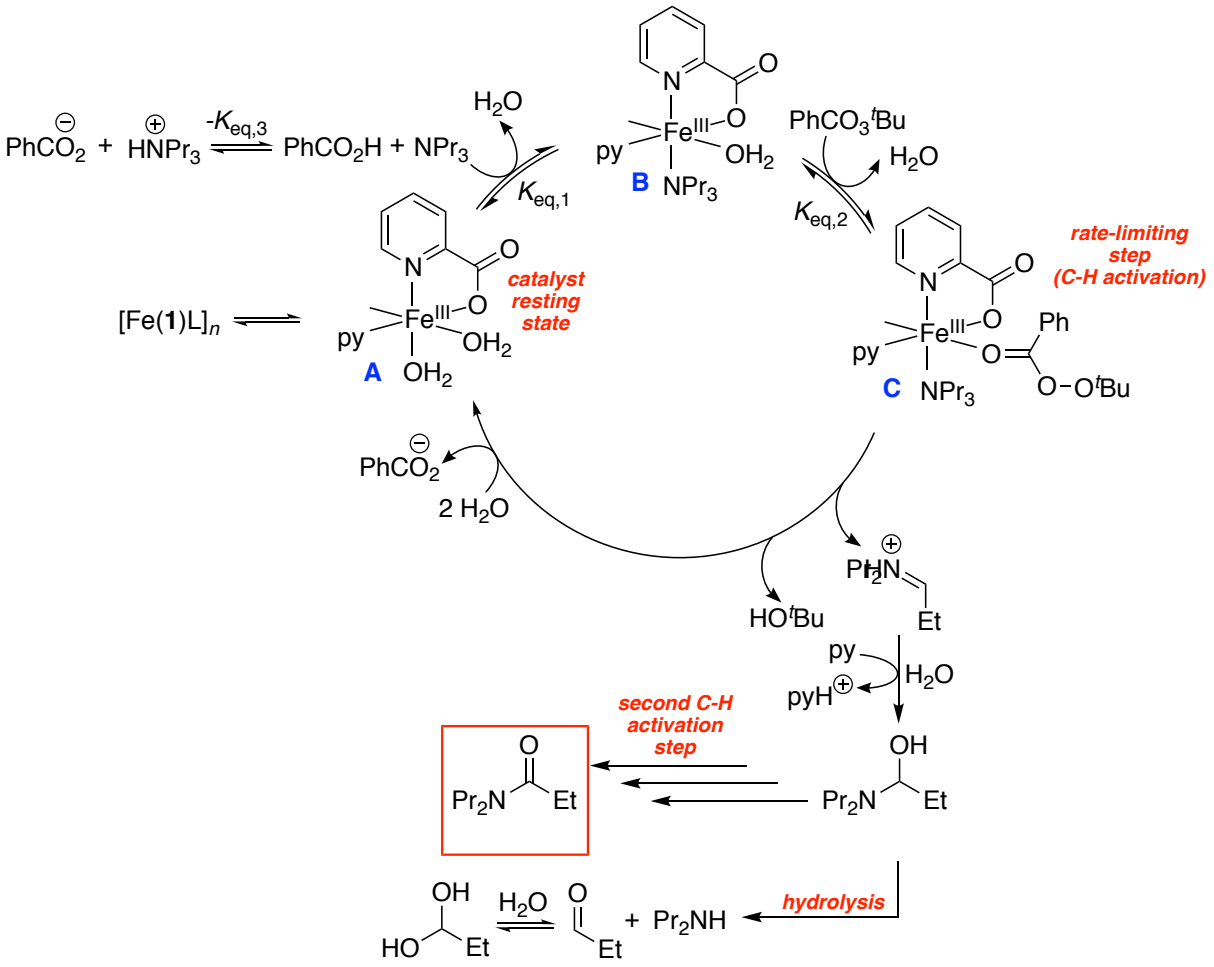

Scheme 71: General Catalytic Cycle Based on Initial Rates Studies.

The overall reaction rate can be expressed in terms of the rate of the rate-limiting step (rls) multiplied by the concentration of the intermediate which undergoes the rls. In our catalytic cycle, we propose that **C** is such an intermediate. Thus, the reaction rate can be formulated as Eq. 2. Intermediate **C** is the catalytic species directly before the rls.

$$\text{rate} = k_{rls}[\mathbf{C}] \qquad (Eq.\ 2)$$

Intermediate **C** is proposed to be in equilibrium with **B** via dissociation of H_2O and coordination of $PhCO_3{}^tBu$. Eq. 3 expresses the pre-equilibrium assumption in a chemical equation, resulting in a mathematical equation (Eq. 4), which relates the relative concentrations of each species and the respective equilibrium constant, $K_{eq,\,2}$.

Solving Eq. 4 for [**C**] and adding the resulting equation into Eq. 2 results in a new rate law (Eq. 5).

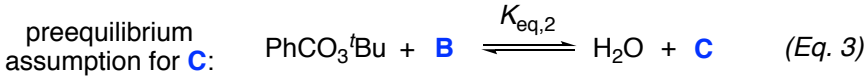

$$K_{eq,2} = \frac{[H_2O]\,[\mathbf{C}]}{[PhCO_3{}^tBu]\,[\mathbf{B}]} \qquad (Eq.\ 4)$$

$$\text{rate} = \frac{k_{rls}\,K_{eq,2}\,[PhCO_3{}^tBu]\,[\mathbf{B}]}{[H_2O]} \qquad (Eq.\ 5)$$

Similarly, [**B**] can be described in a pre-equilibrium assumption, forming **B** from resting state **A** (which accounts for [Fe/picolinic acid]) by coordination of NPr_3 and decoordination of H_2O (Eq. 6/7).

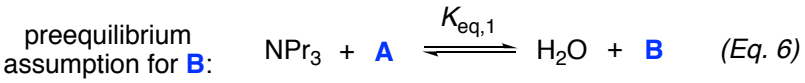

$$K_{eq,1} = \frac{[H_2O]\,[\mathbf{B}]}{[NPr_3]\,[\mathbf{A}]} \qquad (Eq.\ 7)$$

Solving for [**B**] in Eq. 7 and inserting the resulting Eq. 8 into Eq. 5, the reaction rate can be defined as shown in Eq. 10.

$$[\mathbf{B}] = \frac{K_{eq,2}\,[NPr_3]\,[\mathbf{A}]}{[H_2O]} \qquad (Eq.\ 8)$$

$$\text{rate} = \frac{k_{rls}\,K_{eq,1}\,[NPr_3]\,K_{eq,2}\,[\mathbf{A}]\,[PhCO_3{}^tBu]}{[H_2O]^2} \qquad (Eq.\ 9)$$

$$\text{rate} = \frac{k\,[NPr_3]\,[\mathbf{A}]\,[PhCO_3{}^tBu]}{[H_2O]^2} \qquad (Eq.\ 10)$$

Finally, $K_{eq,\,3}$, which accounts for [$PhCO_2H$], can be expressed as Eq. 11 and Eq. 12.

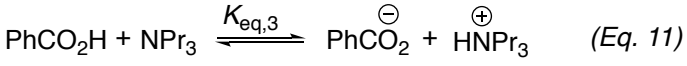

$$K_{eq,3} = \frac{[PhCO_2^{\ominus}]\,[HNPr_3^{\oplus}]}{[PhCO_2H]\,[NPr_3]} \qquad (Eq.\ 12)$$

Solving Eq. 12 for [NPr_3] affords Eq. 13, which can then be inserted into Eq. 10 to give the final rate equation, Eq. 14.

$$[NPr_3] = \frac{[PhCO_2^{\ominus}][HNPr_3^{\oplus}]}{K_{eq,3}\,[PhCO_2H]} \qquad \textit{(Eq. 13)}$$

$$\text{rate} = \frac{k\,[PhCO_2^{\ominus}][HNPr_3^{\oplus}]\,[\mathbf{A}]\,[PhCO_3{}^tBu]}{[PhCO_2H]\,[H_2O]^2} \qquad \textit{(Eq. 14)}$$

The resulting equation accounts for the kinetic orders of all reactants, suggesting that the general mechanism shown in Scheme 71 is consistent with the kinetic data.

3.8 Investigation of Catalyst Resting State via Ligand Coordination Studies

The data acquired from the initial rate studies afforded valuable insights into the catalytic cycle and catalyst structure. However, the complete structure of the catalyst could not be determined with initial rates studies alone; Scheme 71 shows that one coordination site in **A** is still undetermined. Consequently, subsequent studies focused on elucidating the structure of the catalyst resting state via coordination studies. Furthermore, we sought to confirm the coordination of the proposed ligands **1** and pyridine in the structure of **A**.

3.8.1 Pyridine Binding

In-situ analysis was conducted to further examine pyridine binding to $FeCl_3{\cdot}6H_2O$ in H_2O (Scheme 72). When 0.3 equiv. aliquots of $FeCl_3{\cdot}6H_2O$ were added to 3 eq. pyridine in H_2O, free pyridine signal proportionally diminished with the addition of the first two aliquots, and then disappeared with the addition of a third (Scheme 72, top). The *in-situ* IR data result suggests Fe/pyridine binding with a maximum stoichiometry of 3:1.

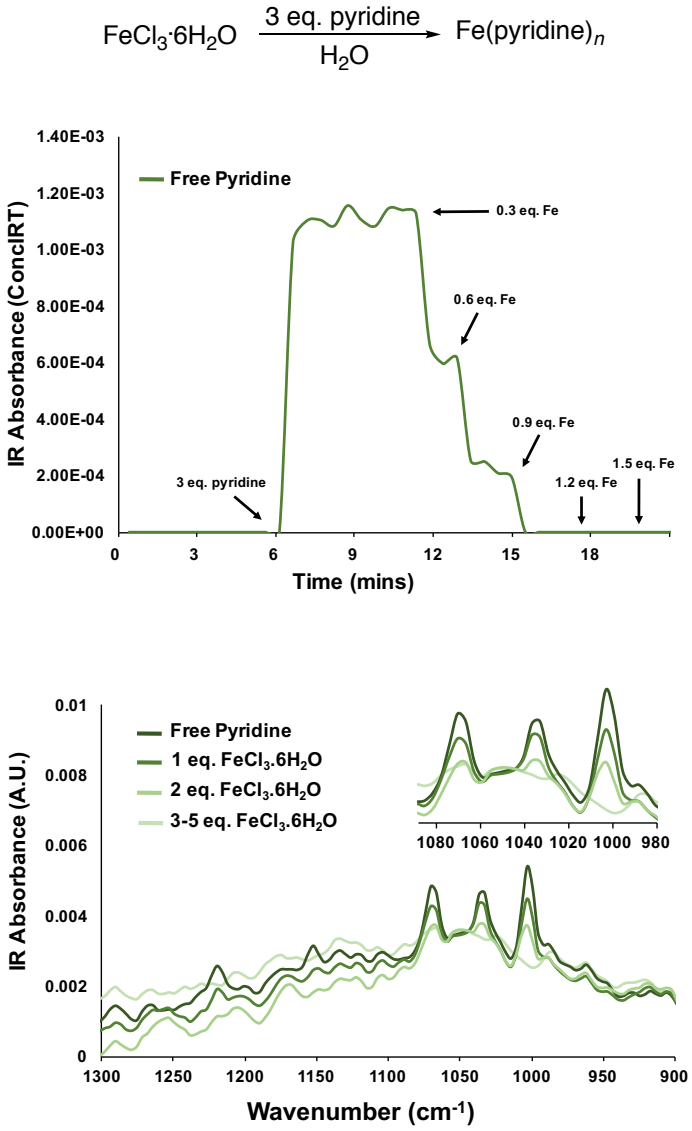

Scheme 72: Titration of $FeCl_3 \cdot 6H_2O$ into pyridine in H_2O (top); IR spectra of $FeCl_3(pyridine)_n$ (bottom).

3.8.2 Picolinic Acid Binding

Our initial investigations have clearly established that the catalytic activity of the system depends on the presence of picolinic acid (**1**), and that a 1:1 ratio of Fe/**1** leads to highest catalytic activity (Scheme 60, pg. 56). Therefore, we hypothesized that **1** is binding to the Fe center in a chelating fashion to promote catalysis. To test our hypothesis, 0.5 eq. aliquots of **1** were sequentially added to a solution of 1.0 eq. $FeCl_3 \cdot 6H_2O$ in pyridine. *In-situ* IR analysis was employed to monitor chemical changes over the course of the reaction (Scheme 73A). Three distinct signals representing different components in the mixture could be clearly distinguished with this analysis: free (non-coordinated) ligand **1**, whose identity was established by

comparison with an external reference spectrum (blue curve in Scheme 73); and two Fe-picolinic acid species (green and red curve). Since the green spectrum appeared as first distinguishable species at an Fe/**1** ratio of 1:0.5, we reasoned that the species was an Fe complex with 1 eq. of **1** bound. In analogy, the red IR curve appeared only after adding more **1** to the solution, suggesting that it represents an Fe species with two molecules of **1** bound. The pure component spectra for each component was calculated using ConcIRT software. The resulting IR spectra are shown in Scheme 73B. Non-coordinated picolinic acid has a characteristic C=O stretch at ~1720 cm^{-1} (blue spectrum) that shifts to ~1670 cm^{-1} upon coordination to Fe (green and red spectra). This observation can be rationalized by the changing electronics of the ligand — and therefore the vibrational mode of the C=O moiety — upon binding to the Fe center. No shift in the C=O shift of picolinic acid was observed beyond a loading of 2 eq. These studies revealed that picolinic acid indeed binds to $FeCl_3$, with a maximum stoichiometry of 2:1.

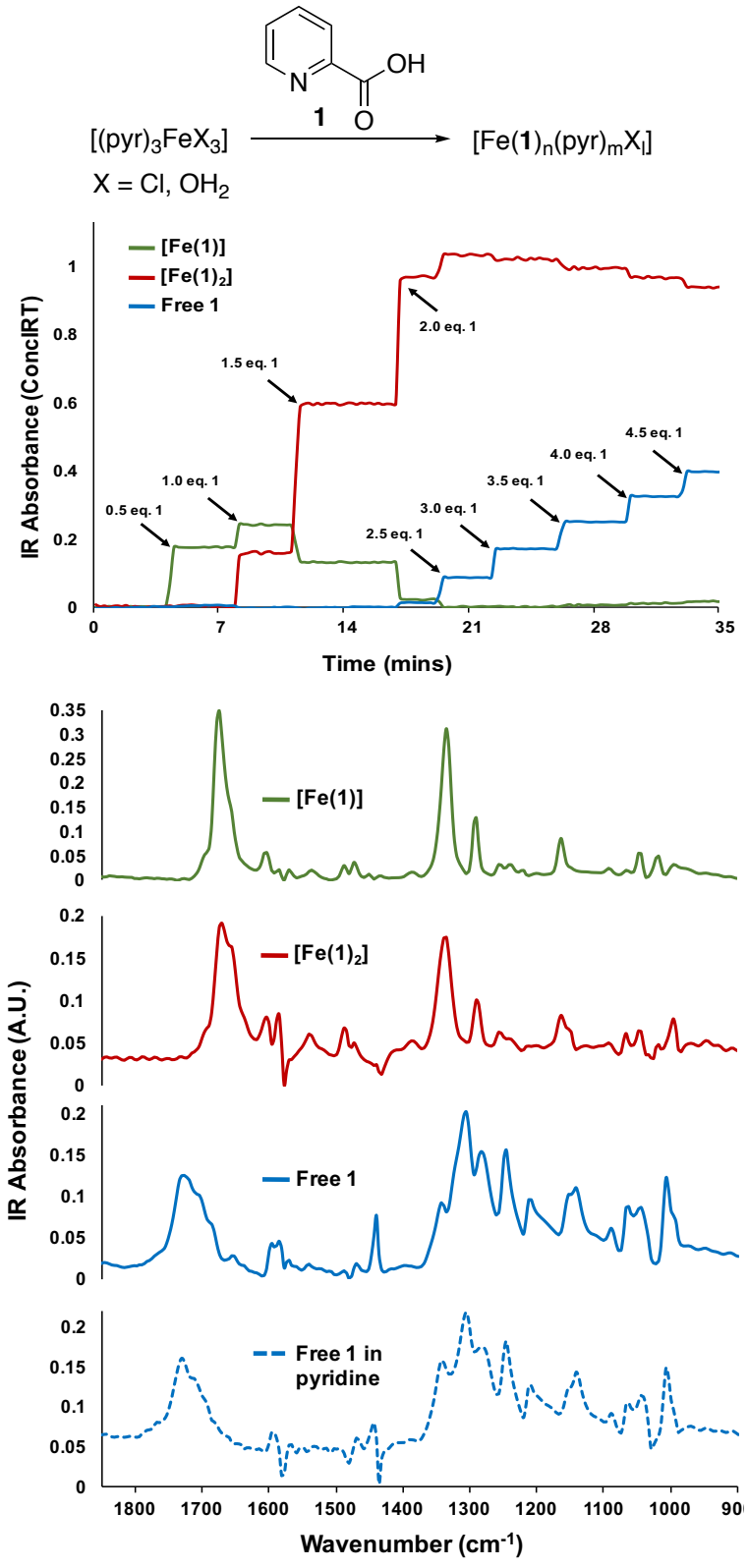

Scheme 73: *in-situ* FTIR spectra (bottom) and Progression of Spectra Appearance for the Titration of Picolinic Acid into $FeCl_3$ in Pyridine.

3.8.3 Amine Binding Studies

Based on the observed first order dependence on [NPr_3], we hypothesized that NPr_3 is binding to the Fe center. To investigate potential amine binding to Fe, 0.5 eq. aliquots of NPr_3 were titrated into a solution of 1.0 eq. Fe/picolinic acid (1:1) and 10 eq. H_2O in pyridine solvent (Scheme 74).

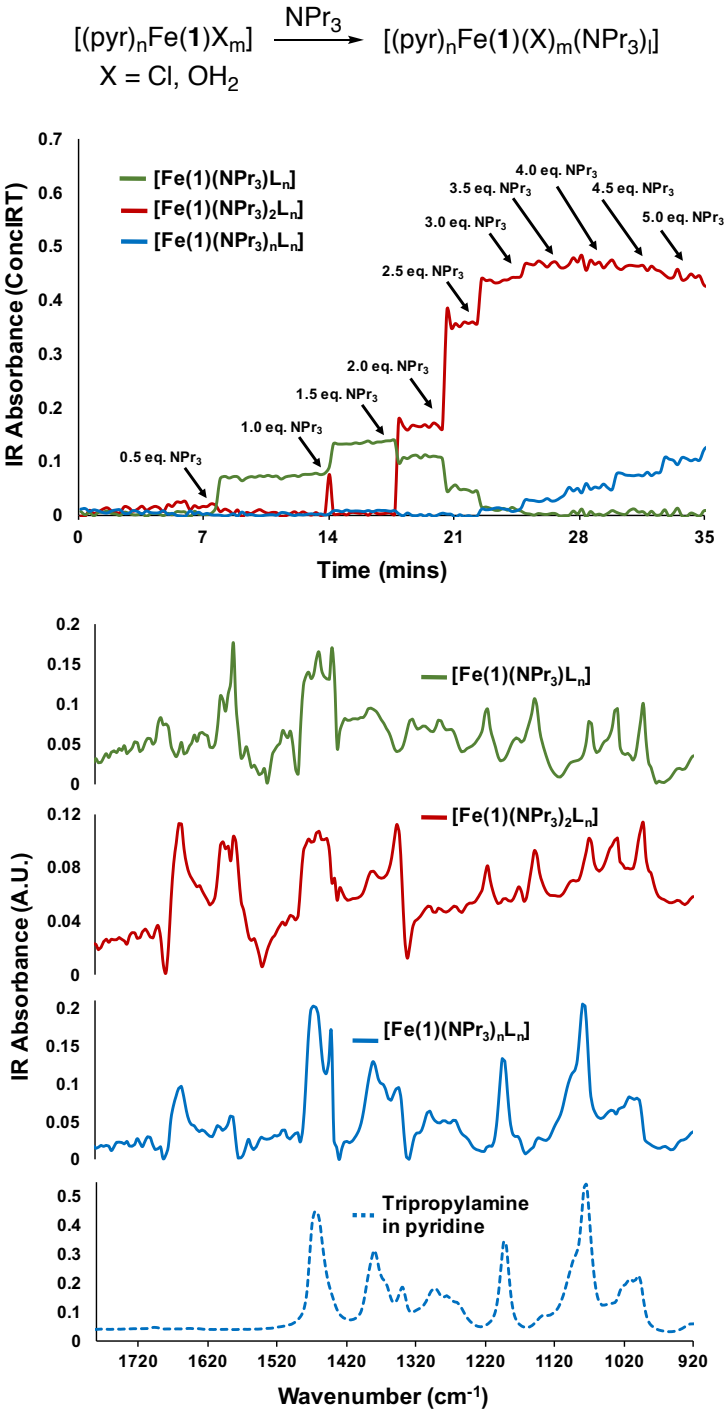

Scheme 74: IR Absorbance for the Titration of NPr_3 into $FeCl_3$/Picolinic Acid (1:1) in Pyridine/H_2O.

Upon addition of the first 0.5 eq. NPr_3, a new IR signal is observed which corresponds to a complex [Fe(**1**)(NPr_3)L_n] (green curve), in which one equivalent of amine is bound to the Fe center. This signal is characterized by the expected band (C=O stretch of picH) at 1686 cm^{-1} (Scheme 74, bottom). The signal continues to in increase up to addition of overall 1.0 eq. NPr_3. Once the NPr_3 loading is further increased (to 1.5 eq.), a second signal (Scheme 74A, red curve) likely corresponding to a complex [Fe(**1**)(NPr_3)$_2L_n$] with two molecules of amines bound; the respective C=O stretch for this new species is shifted to 1656 cm^{-1} (Scheme 74, bottom). This signal continues to grow beyond 1.5 eq. added NPr_3; at the same time, the signal of [Fe(**1**)(NPr_3)L_n] is further reduced. Beyond a loading of 2.5 eq. NPr_3, the signal corresponding to [Fe(**1**)(NPr_3)L_n] disappears, consistent with its proposed structure. Moreover, a new signal (Scheme 74, top, blue) begins to increase, which also belongs to an Fe complex, likely [Fe(**1**)(NPr_3)$_3$L]. The calculated IR spectrum corresponding to the blue curve primarily matches the IR spectrum of free NPr_3, with the exception that is also shows a characteristic C=O stretch at 1656 cm^{-1} (Scheme 74, bottom).

3.9 Investigations of the Turnover-Limiting Step

3.9.1 Eyring Studies

To further investigate the nature of the turnover-limiting step in the catalytic cycle, the initial rate of the reaction was measured as a function of temperature (Scheme 75). Based on these data, a plot of ln(k_{obs}/T) vs. 1/T (K^{-1}) was constructed, which allowed calculations of activation enthalpy and entropy with the help of the Eyring Equation (Eq. 13).

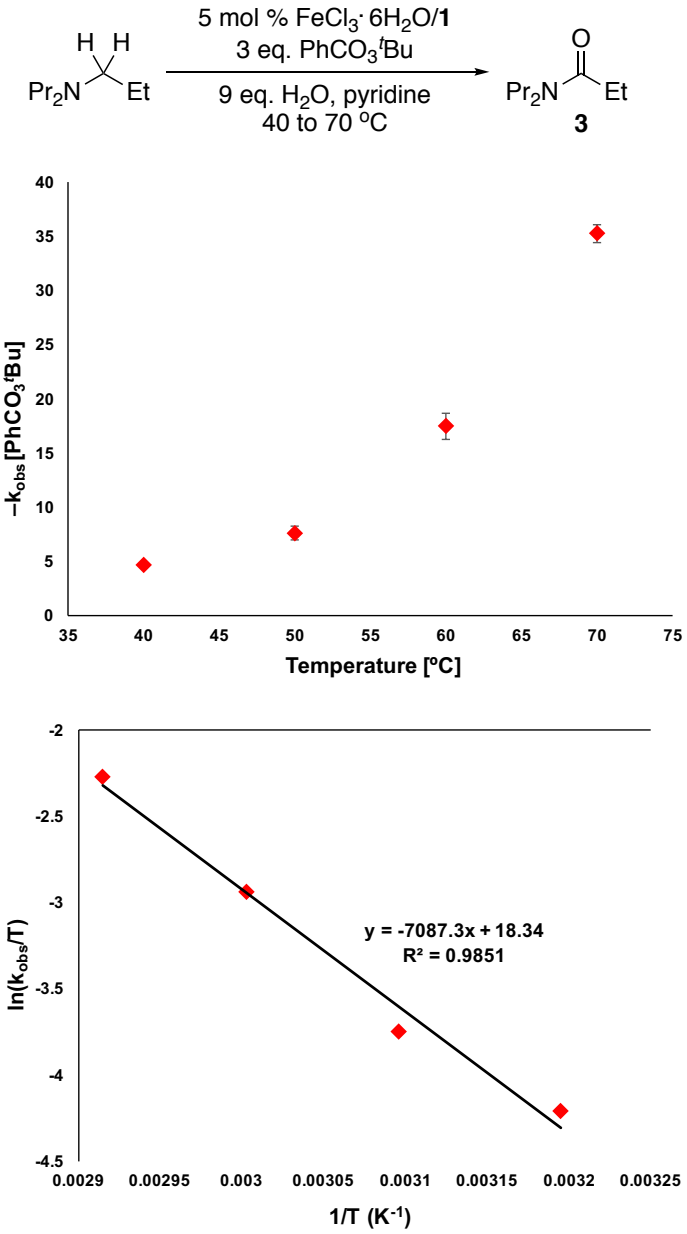

Scheme 75: Plot of Initial Rate [-$PhCO_3{}^tBu$] Versus T (top). Plot of ln(k_{obs}/T) Versus 1/T (bottom).

Based on the resulting slope and intercept of the plot in Scheme 75, $\Delta H^{\ddagger}$ was calculated to be 14.1 kcal/mol and $\Delta S^{\ddagger}$ was determined to be -10.8 cal/(K mol), respectively. Notably, the negative value of suggests a high order in the transition state of the reaction. This is in agreement with a concerted, turnover-limiting, C-H bond breaking step, when considering the value obtained from the kinetic isotope effect studies (k_H/k_D=1.75).

$$\ln\frac{k}{T} = -\frac{\Delta H^{\ddagger}}{R}\cdot\frac{1}{T} + \ln\frac{k_B}{h} + \frac{\Delta S^{\ddagger}}{R} \qquad \textit{(Eq. 13)}$$

3.9.2 Investigation of Homolytic/Heterolytic Oxidant Pathways

With the knowledge of the reaction's first-order dependence on [$PhCO_3{}^tBu$], we hypothesized that the oxidant played a direct role in C-H bond cleavage. To distinguish between one electron (homolytic O-O bond cleavage) and two electron (heterolytic O-O bond cleavage) pathways and to probe the nature of amine C_α-H oxidation with the peroxy ester as oxidant, the $PhCO_3{}^tBu$ analogue **13** was synthesized and employed under our standard NPr_3 oxidation conditions (Scheme 76A). Based on literature precedent, homolytic O-O bond cleavage of the peroxide moiety would lead to the formation of acetone and thus implicate a $1e^-$ C-H oxidation pathway, possibly via radical intermediates (Scheme 76B). In contrast, heterolytic O-O bond cleavage is expected to produce tertiary alcohol product **14**, which would be consistent with concerted C-H cleavage via ß-hydride elimination pathways.

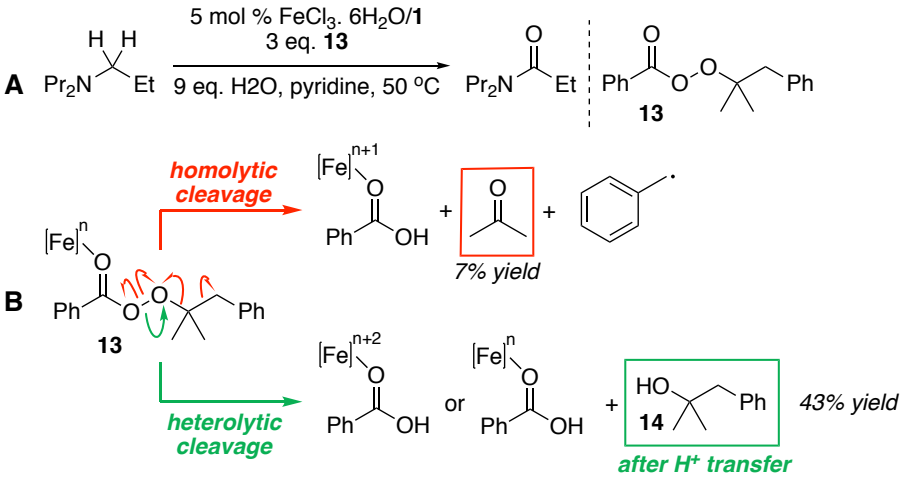

Scheme 76: (A) Standard C_α-H oxidation Reaction with $PhCO_3{}^tBu$ analogue. (B) Potential O-O Bond Cleavage Pathways and Products.

To distinguish between these two potential reaction pathways, oxidant **13** was reacted with NPr_3 under standard conditions until complete disappearance of **13** was observed via *in-situ* IR (Scheme 77). GCMS and quantitative ^1H NMR analysis revealed acetone as a minor product in the reaction (7% yield) while the alcohol product **14** was observed in much higher yield (43%).

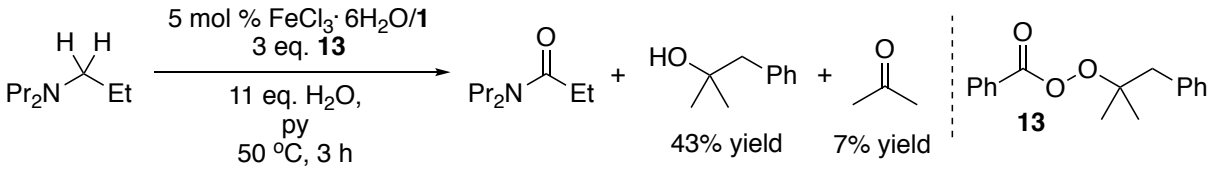

Scheme 77: Reaction with $PhCO_3{}^tBu$ analogue under standard conditions.

These results suggest primarily a two electron pathway for heterolytic O-O bond and C-H bond cleavage; however, some amount of homolytic O-O bond cleavage is also observed. These results are consistent with the radical scavenger studies shown in Section 3.4.2 (Scheme 48), which suggest the presence of both radical and non-radical pathways. Overall, based on recovery of **14** as major product in the study discussed here, we conclude that previously discussed amine C_α-H cleavage via radical rebound or stepwise e^-/H^+ transfer mechanisms are unlikely (Scheme 78), as both of these pathways would include one electron radical pathways.

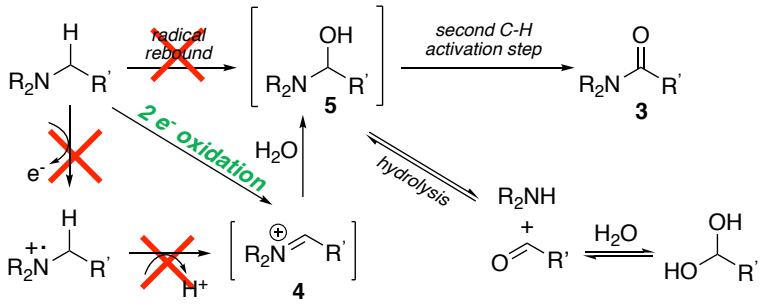

Scheme 78: Proposed General Mechanism Showing $2e^-$ C-H Bond Oxidation.

Therefore, a concerted 2 electron oxidation pathway to access the prior proposed iminium intermediate **4** is most consistent with the obtained data.

3.9.3 Proposed Catalytic Cycle with Rate-Determining Step

The data presented in Sections 3.9.1 and 3.9.2 allowed us to propose the following catalytic cycle, which incorporates a concerted C_α-H Oxidation Mechanism (Scheme 79), which breaks the O-O bond of the oxidant heterolytically and accesses the iminium intermediate after the rate-limiting step.

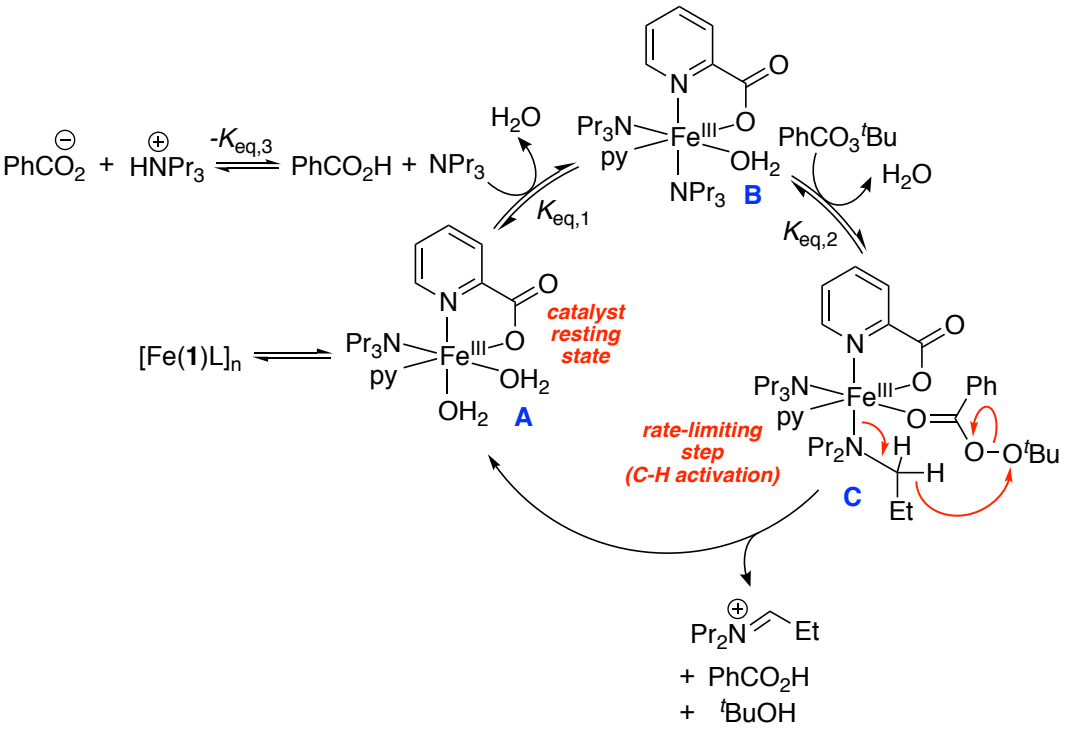

Scheme 79: Proposed Catalytic Cycle Showing a Concerted C_α-H Oxidation Mechanism.

This amended catalytic cycle shows a concerted C_α-H oxidation mechanism at **C**, which is consistent with the Eyring data presented in Section 3.9.1 (in that it accounts for the obtained negative value of $\Delta S^{\ddagger}$) as well as the KIE studies shown in Section 3.7.12 and the oxidant studies in Section 3.9.3.

3.10 Reaction Process Kinetics

3.10.1 Product Promotion (Self-Promoting Reaction) or Catalyst Activation Prior to Catalytic Turnover

As discussed shortly at the beginning of the kinetic studies in Section 3.7 above, an initiation period is a key feature of all kinetic traces obtained in the discussed investigations. To elucidate the mechanistic features that cause this initiation period, several different studies were performed, as described in detail in this and the following sections.

Literature precedent suggested two possible mechanistic causes for an initiation period [100]. One possibility is that the catalytic reaction is self-promoting; this is typically possible for reactions that are accelerated by the reaction product(s). To test if the Fe catalyzed amine oxidation at hand fits into this category of reactions, kinetic traces obtained under standard reaction conditions were compared with kinetic traces obtained upon addition of 5 mol % of different reaction products added at the onset of the reaction (Scheme 80). Interestingly, addition of small amounts of these products had no significant effect on the kinetic traces, both regarding the length of the initiation period or the maximum rate. This suggested that the reaction is not self-promoting.

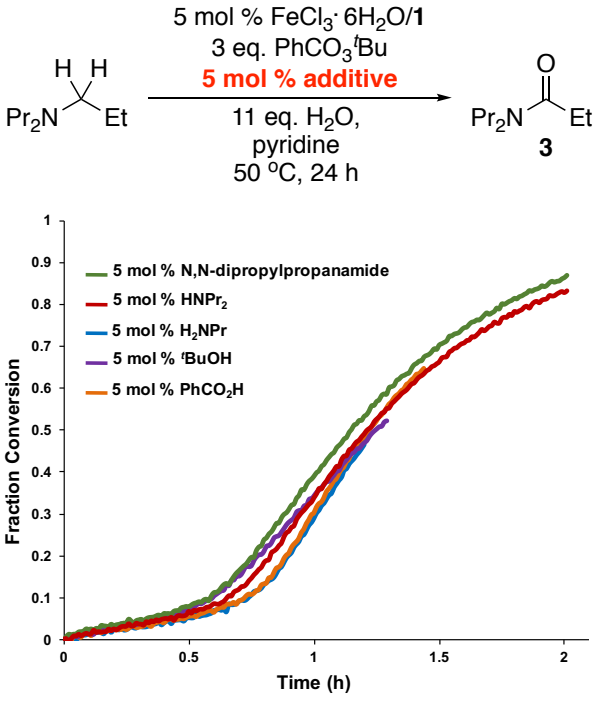

Scheme 80: Effect of Product Addition on Initiation Period Length.

The second general possibility that can account for the presence of an initiation period in reactions is the presence of an initial, non-catalyzed product or catalyst formation reaction, *i.e.* a series of reactions that modify the catalyst in a fashion that activates it [100].

Having ruled out the possibility of reaction self-promotion, we hypothesized that varying the stoichiometric concentrations of starting materials may have an effect on the length of the initiation period and thus allow us to elucidate factors that influence catalytic activation. The results of these studies are discussed in the next sections.

3.10.2 Influence of [$PhCO_3{}^tBu$] on Initiation Period

Scheme 81 (top) shows the effect of the $PhCO_3{}^tBu$ loading on the reaction rate, revealing a significantly shorter initiation period—defined as the time course of the reaction between t=0 and the maximum rate—at higher $PhCO_3{}^tBu$ loadings. This suggests that the oxidant may be involved in catalyst activation. Furthermore, when the same data set was plotted as conversion vs. time (Scheme 81, bottom), stalling of the reactions at oxidant loadings higher than 2 eq. after ~90 min is observed – in contrast to the higher initial rates under such conditions in the initial 30 min of the reaction. This is consistent with an inhibitory effect of $PhCO_2H$ at higher conversions (and significant concentrations), and is in agreement with the negative first order dependence on $PhCO_2H$ loading determined via the method of initial rates (see Section 3.7.10 above).

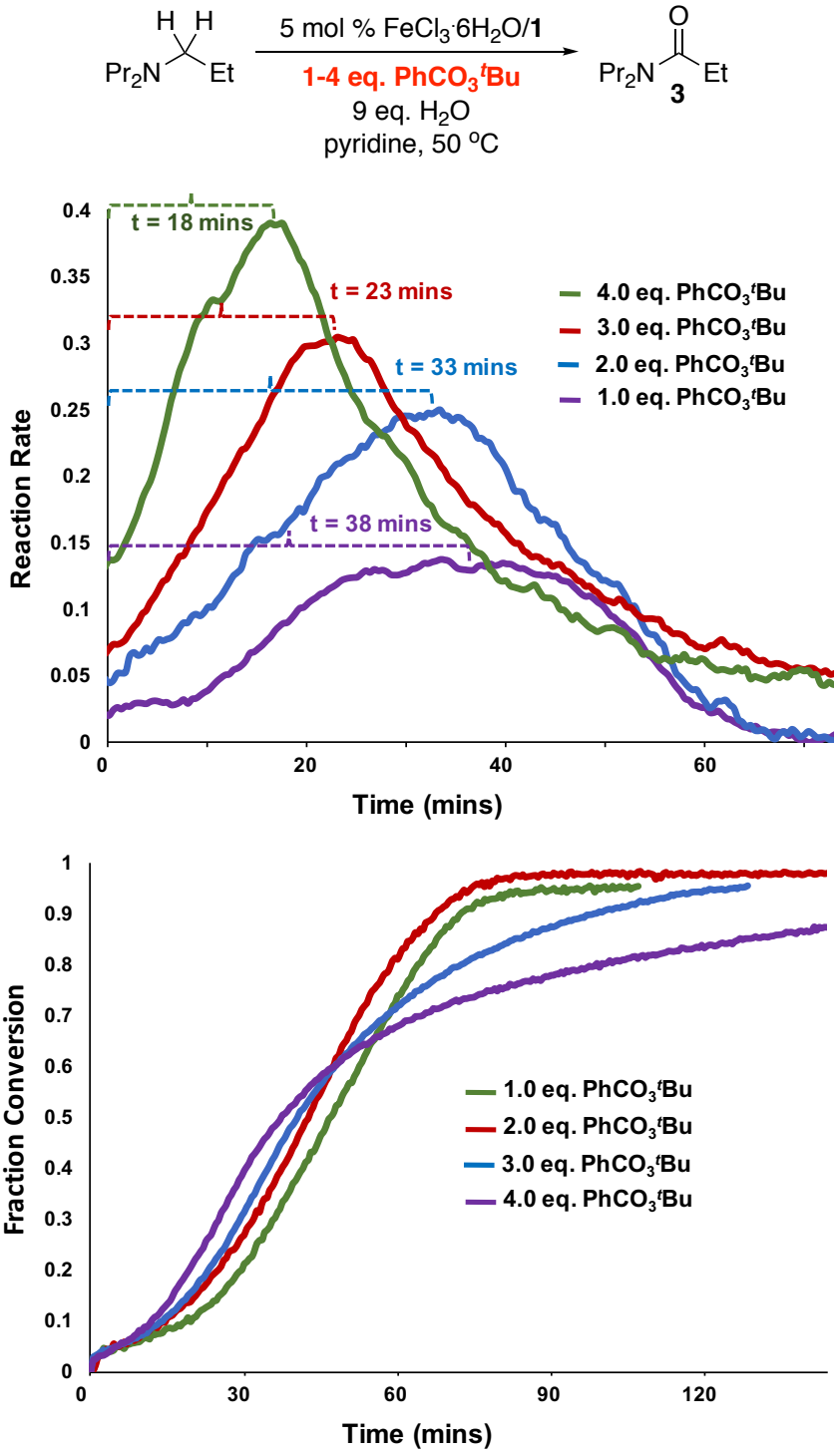

Scheme 81: Effect of $PhCO_3{}^tBu$ Loading on Initiation Period and Reaction Rate.

3.10.3 Influence of [NPr_3] on Catalyst Initiation Period

We next investigated the effect of NPr_3 substrate loading on the initiation period. Based on *in-situ* IR data obtained at varying loadings of NPr_3, a plot of conversion versus time was created (Scheme 82, top). These studies show a clear decrease in initiation period length with increased NPr_3 loading, which suggests that the amine substrate contributes to reactions proceeding during catalyst activation. Remarkably, at 10 eq. NPr_3, the initiation period becomes almost invisible in a plot of conversion vs. time (Scheme 82, bottom).

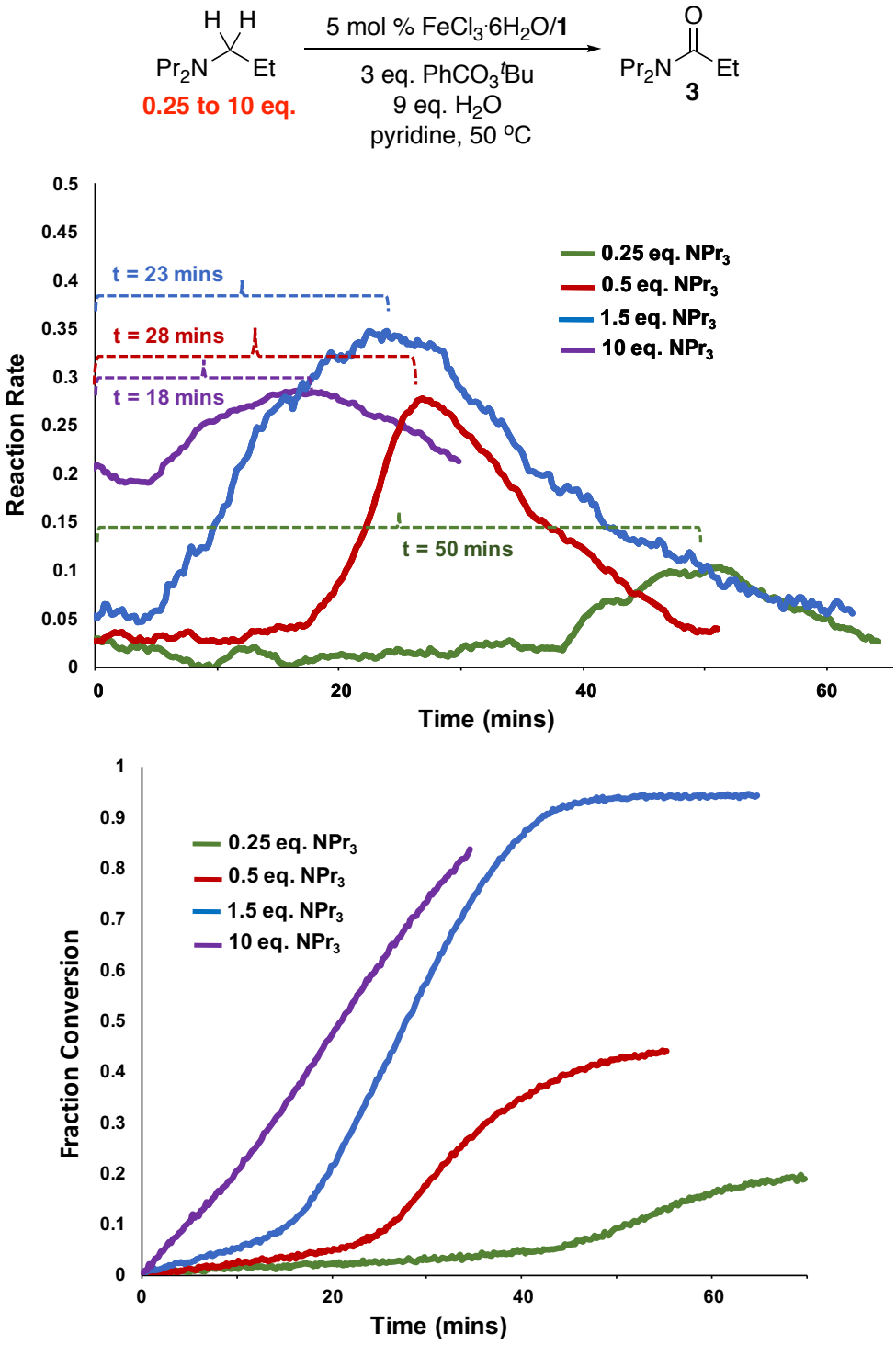

Scheme 82: Effect of NPr_3 Loading on Initiation Period.

3.10.4 Influence of [H_2O] on Initiation Period

Investigations of the reaction rate with respect to water loading revealed that low H_2O loadings increase the maximum reaction rate, as consistent with the negative 2nd order dependence of the rate on [H_2O] established previously. To

investigate the potential involvement of H_2O in catalyst activation, reaction conversion was plotted vs. time for a series of different H_2O loadings (Scheme 83, top). A significant reduction in initiation period length was observed at lower H_2O loadings. Based on these data, we hypothesize that H_2O is involved in the reaction initiation period, and may play a key role in catalyst activation.

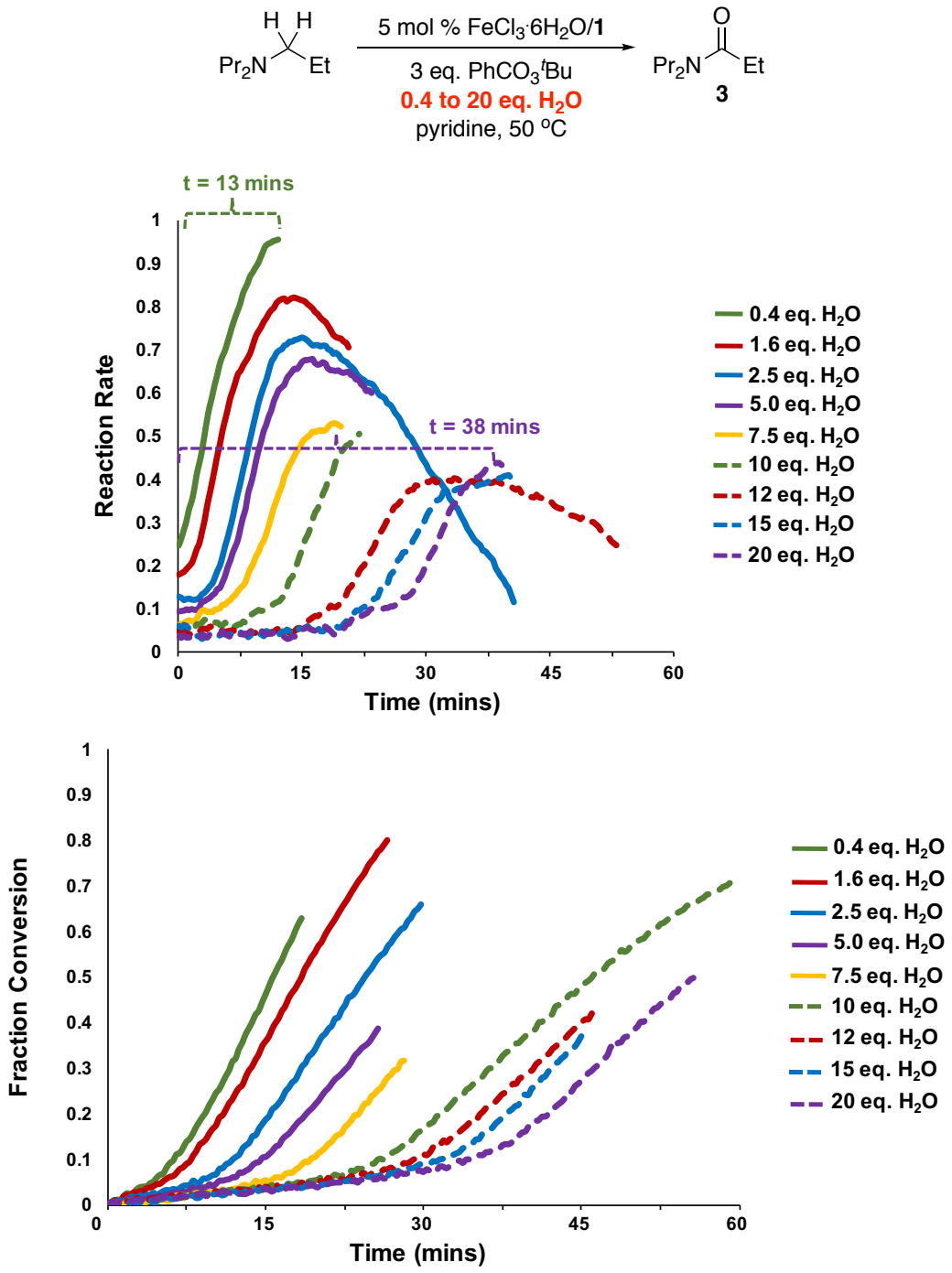

Scheme 83: Effect of H_2O Loading on Initiation Period.

3.10.5 Influence of [$PhCO_2H$] on Catalyst Initiation Period

We next investigated the influence of $PhCO_2H$ on the initiation period, as $PhCO_2H$ is a product of $PhCO_3{}^tBu$-driven amine oxidation. Addition studies (see Scheme 80, pg. 78) had shown that only 5 mol % of added $PhCO_2H$ had no significant effect on the length of the initiation period. In contrast, when comparing complete kinetic traces obtain via *in-situ* IR at loadings of 1 to 4 eq. $PhCO_2H$ (Scheme 84), a clear effect was observed: Increased $PhCO_2H$ loadings led to an increased length of the initiation period. This suggests that $PhCO_2H$ may inhibit catalyst activation, possibly counteracting the effects of basic amine substrate.

3.10.6 Influence of ^{t}BuOOH / ^{t}BuO$^\bullet$ on Catalyst Initiation Period

As described in detail in Section 3.4.2 (Scheme 48, pg. 44), initial investigations had revealed that the addition of the radical scavenger TEMPO reduced reaction yields (even though TEMPO did not entirely eliminate reactivity). This suggested that radical species may play a role in the Fe catalyzed C_α-H oxidation of amines. However, this result seems to be in contrast to the findings obtained with 2-methyl-1-phenylpropan-2-yl benzoperoxoate (**14**) as oxidant (see Section 3.9.2, Scheme 78, pg. 76), which revealed that oxidation in Fe catalyzed amide formation primarily proceeds via heterolytic cleavage of the oxidant, with homolytic cleavage only being a minor process. Indeed, the amount of product (acetone) stemming from radical pathways was obtained in similar amounts (7%) as the amount of catalyst used (5 mol %). This realization led us to hypothesize that radicals, while not playing a key role in the catalytic cycle, may be involved in activating the catalyst during the initiation period. A literature search revealed that ^{t}BuOOH, a potential hydrolysis product of the oxidant $PhCO_3{}^tBu$ under basic conditions, readily forms the stable radical ^{t}BuO$^\bullet$ in the presence of pyridine [78]. Thus, we hypothesized that if catalyst activation would require a radical process, initiation should be more rapid in the presence of ^{t}BuOOH. To test this hypothesis, 5 mol % ^{t}BuOOH was added to a reaction that was otherwise performed in analogy to standard reaction conditions; the corresponding kinetic traces for standard conditions (no added ^{t}BuOOH) are shown as the blue curve in Scheme 86. Comparing the resulting reaction profile from the reaction in the presence of ^{t}BuOOH (obtained by *in-*

situ IR) to a kinetic trace obtained under non-modified standard conditions (Scheme 85) resulted in a significant shortening of the initiation period. This indicates that the radical species ^{t}BuO•, obtained via hydrolysis of $PhCO_3{}^{t}Bu$ followed by pyridine-promoted homolytic O-O bond cleavage of ^{t}BuOOH, may indeed play a key role in catalyst activation.

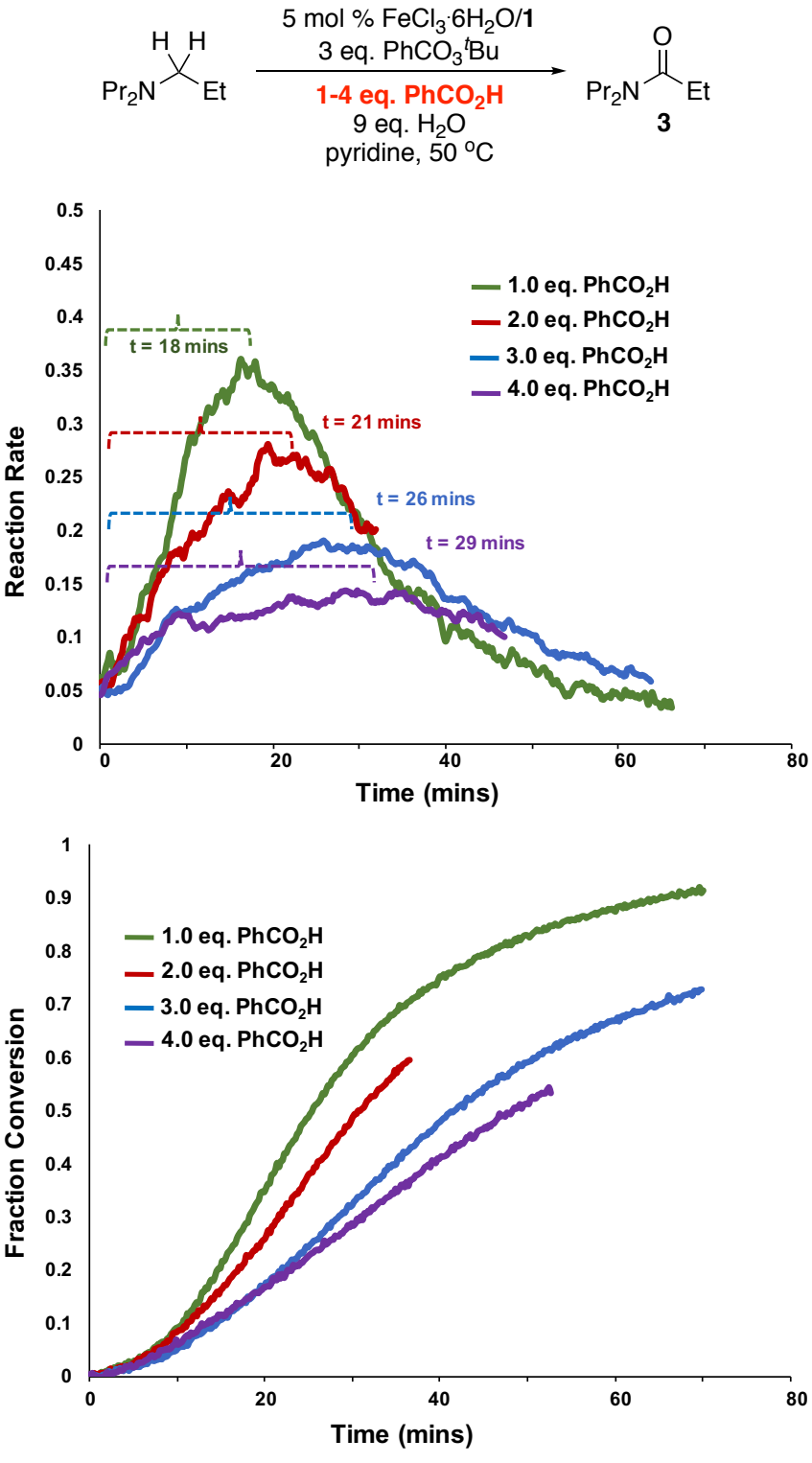

Scheme 84: Effect of $PhCO_2H$ Loading on Initiation Period.

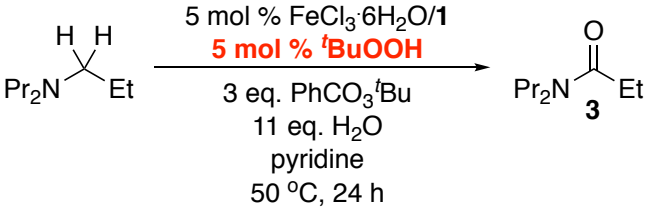

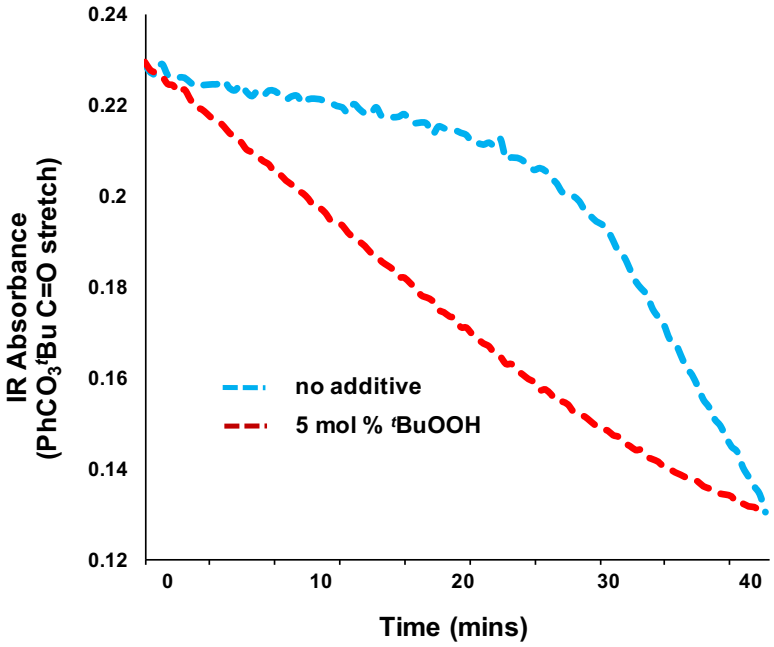

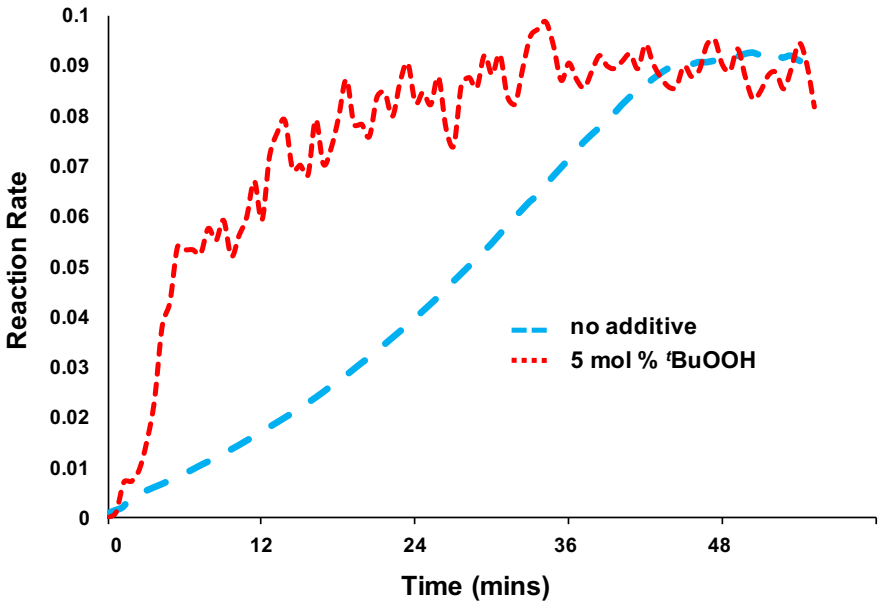

Scheme 85: Effect of ^{t}BuOOH on Initiation Period.

3.10.7 Dependence of Initiation Period on Order of Reagent Addition

We further investigated if the length of the initiation period depends on the order of reagent addition. Under typical experimental conditions for measuring initial rates, NPr_3 substrate was added as the last reaction component. This procedure produced the kinetic profile shown in Scheme 86 **Error! Reference source not found.**(blue curve). It is remarkable that the maximum reaction rate ($-k_{obs}[PhCO_3{}^tBu]$) is not being reached until ~25 minutes after the addition of substrate.

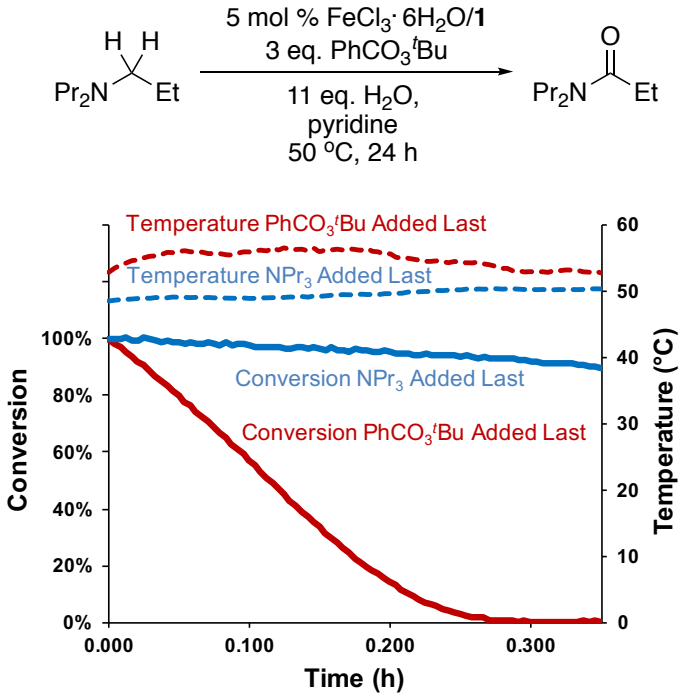

Scheme 86: Effect of Substrate/Oxidant Addition Order on Initiation Period and Reaction Temperature.

In contrast, our kinetic studies revealed that adding NPr_3 substrate to the reaction mixture *before* $PhCO_3{}^tBu$ drastically reduced the length of the initiation period (Scheme 86**Error! Reference source not found.**, red). Additionally, this procedure led to a significant increase in reaction temperature, which was likely caused by increased reactivity (Scheme 85, red and blue dotted lines). These data suggest that NPr_3 is involved in the reaction sequence that leads to the initiation period and catalyst activation *before* $PhCO_3{}^tBu$ is involved. Consequently, when NPr_3 is added first, the sequence of reactions leading to catalyst activation can partially

proceed, even in the absence of $PhCO_3{}^tBu$. Therefore, the overall activation sequence proceeds faster when $PhCO_3{}^tBu$ is added last, leading to a highly exothermic initiation cascade.

3.11 Mechanistic Proposal for Catalyst Activation Resulting in Initiation Period

Collectively, the kinetic profiling under different conditions as discussed in Sections **Error! Reference source not found.** through 3.10.6 allowed us to propose the catalyst formation reaction shown in Scheme 87.

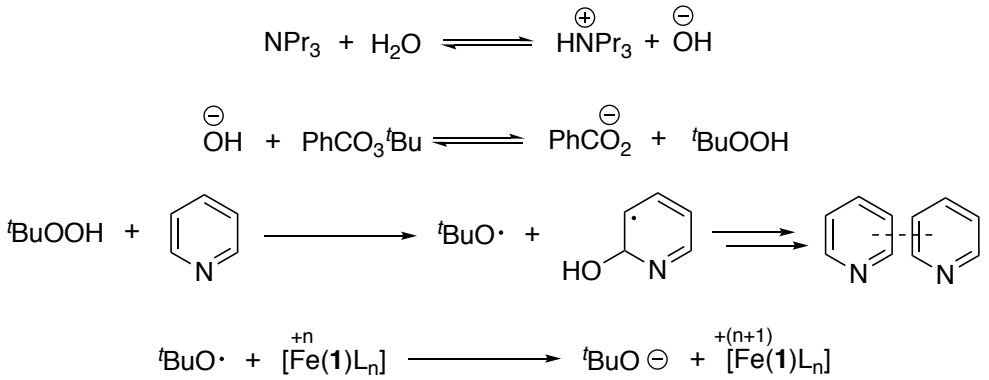

Scheme 87: Proposed Mechanism of Catalyst Activation.

We hypothesize that $PhCO_3{}^tBu$ undergoes hydrolysis to form ^tBuOOH by reaction with OH^- that is formed upon reaction of NPr_3 with H_2O in the reaction mixture. This sequence of events is consistent with the faster initiation observed when $PhCO_3{}^tBu$ is added to the reaction mixture as last reagent. ^tBuOOH then reacts with pyridine to afford the $^tBuO^{\cdot}$ radical species, in analogy to detailed studies in the literature [101]. Next, we propose that $^tBuO^{\cdot}$ accepts an electron from Fe to form the active catalyst species. We thus propose that catalyst activation occurs via one-electron oxidation of an Fe precursor, forming the resting state **A** of the previously postulated catalytic cycle. The observed shorter initiation periods observed in the kinetic profiles with higher NPr_3 and $PhCO_3{}^tBu$ loadings is in agreement with Le Chatelier's principle, as both reagents are consumed in the proposed catalyst initiation reactions shown in Scheme 87.

3.12 Summary of Mechanistic Studies

The data discussed in the last sections (3.10 through 3.11) allow us to propose a detailed mechanistic picture of the Fe/picolinic acid-catalyzed amine C_α-H oxidation (Scheme 88).

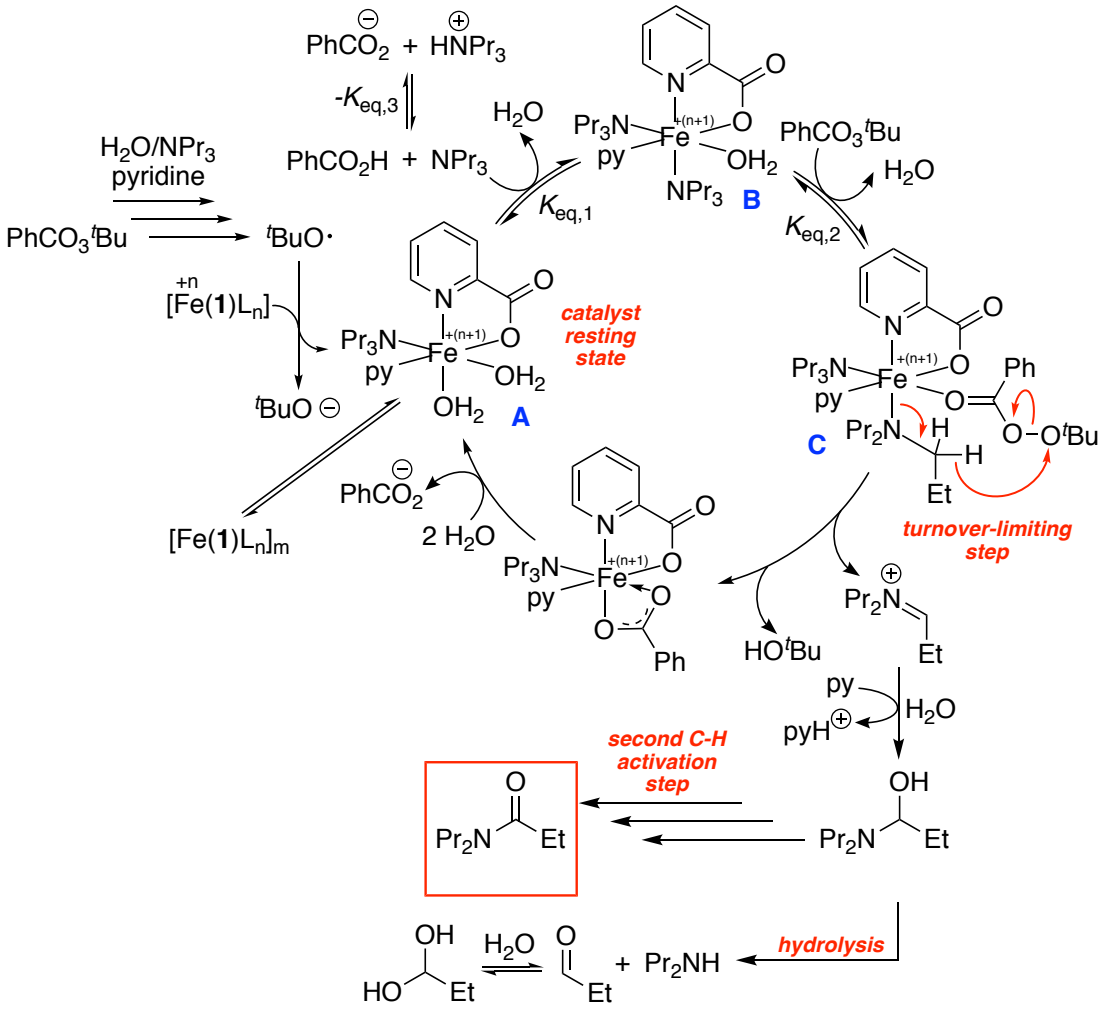

Scheme 88: Proposed Catalytic Cycle for Fe-Picolinic Acid-Catalyzed C_α-H oxidation of NPr_3.

We propose that the resting state of the catalyst is the Fe species **A**, consistent with kinetic order studies and amine, pyridine, oxidant and 2-picolinic acid (**1**) coordination studies. The active catalyst species **A** is likely formed via one-electron oxidation of a similar precursor by reaction with ^{t}BuO·. Furthermore, **A** is in equilibrium with an off-cycle, polymeric species, which causes low reaction rates at high Fe/**1** concentrations. Once the Fe catalyst undergoes transformation to its active state and the catalytic cycle is initiated, NPr_3 enters and displaces one H_2O ligand at

the Fe center to form intermediate **B**. Next, $PhCO_3{}^tBu$ enters the catalytic cycle and displaces one H_2O ligand to form intermediate **C**. KIE studies, a $\Delta S^{\ddagger}$ value of -10.8 cal/(K mol) as well as the studies using radical probe oxidant **13** lead to proposing a concerted C-H activation step as the turnover-limiting step in the catalytic cycle. This type of C-H activation has commonalities with both concerted metalation/deprotonation (CMD) and ß-hydride elimination pathways (Scheme 3, pg. 12, section 1.3.1): the product is a product that could also be obtained via ß-hydride elimination, but the hydride moves to a heteroatom that is bound to the transition metal center, which is similar to proposals for CMD pathways. Subsequent dissociation of $PhCO_2^-$, ^{t}BuOH, and the iminium intermediate **4,** as well as coordination of two molecules of H_2O reforms the resting state **A**.

Once the iminium intermediate **4** leaves the catalytic cycle, it is subjected to nucleophilic attack by H_2O to form hemiaminal **5**, which can either undergo a second C-H oxidation or hydrolyze to form the corresponding secondary amine and aldehyde. The latter reaction is driven by the formation of an aldehyde hydrate in the presence of H_2O. Based on our previous studies the relative yields of amide versus hydrolysis products can be modulated as a function of H_2O loading, which is consistent with this proposed pathway.

One goal of our detailed mechanistic studies is to find alternatives to the use of large amounts of pyridine in Fe catalyzed amines C_α-H oxidation. Our studies allow us to conclude that in the absence of pyridine, the reaction would require a different radical-promoting reagent as well as an alternative ligand to provide activity and stability for the Fe catalyst.

Many other Fe/peroxide-catalyzed systems, such as Gif oxidation systems, enable similar oxidation products as our system. However, these reactions also afford *O*-demethylation, aromatic hydroxylation, and *N*-oxidation products, none of which are observed when complex pharmaceuticals are used in in combination with the discussed catalyst system. The system's particularly high chemoselectivity may arise from the necessity of the amine substrate *and* oxidant to bind to the Fe catalyst, to place the amine C_α-H bond into a reactive environment. Additionally, the proposed two electron oxidation pathway may reduce the formation of free radicals, such as $HO^{\cdot}$, which tend to be highly reactive as well as promiscuous, resulting in non-selective oxidation products. As such, the novel type of two-electron mechanism documented herein is key to achieving high selectivity for oxidation of C_α-H bonds.

4 Summary and Future Directions

In summary, the work presented herein describes the detailed reaction development and in-depth mechanistic investigations of the Fe/picolinic acid catalyzed C_α-H oxidation of tertiary amines. The system was successfully applied to a series of small molecule and complex pharmaceutical amines. The mechanism is characterized by a concerted C-H activation step as well as a two electron oxidation pathway, which is on contrast to many Fe-peroxide-catalyzed systems.

Although our system produces synthetically useful amide yields with small molecule amines, it does so with the use of pyridine—a relatively toxic and unsafe reagent. A variety of different solvents were evaluated in this reaction, but pyridine was the only solvent to afford high amide yields. We later learned through our mechanistic studies that the likely reason for this result is that pyridine also acts as a ligand on the Fe catalyst, as well as a radical promoter to facilitate catalyst activation. With an enhanced understanding of the role of pyridine in this system, we may now be able to move away from this undesirable solvent by synthesizing modified pyridine ligands. In turn, this may allow us to use alternative solvents, as pyridine's role as ligand would be preserved in this scenario. If alternative radical promoting reagents could be used for catalyst activation in the reaction, then we would be well on our way to developing an environmentally-friendly version of this chemical system.

Because of the promiscuous nature of the proposed iminium ion intermediate, we expect other nucleophiles to be compatible with this reaction to form new C-O [102], C-N [103, 104], C-P [105] and C-C bonds [106-108], all of which have been successfully employed in other α-C-H functionalizations of N-alkyl anilines or cyclic amines. Successfully achieving a broad spectrum of amine functionalizations from a common iminium intermediate would greatly expand the synthetic utility of our reaction.

The Fe-catalyzed amine oxidation system presented herein is able to oxidize the active pharmaceutical ingredients Lidocaine and Donepezil, and afford products that are known metabolites of CYP450. Typically, drug metabolites are accessible through *in-vitro* metabolism studies, although they are usually produced only in trace

amounts [109]. This method of obtaining the metabolites is not conducive to isolation and characterization, making its use limited in a research setting [110]. Consequently, bench-scale methodologies for the synthesis of these metabolites would be beneficial to drug discovery efforts. Efforts in our group are underway to explore the efficacy of our Fe-picolinic acid catalysis system for additional biomimetic oxidations. Thus far, we have used this reaction to obtain known CYP450 metabolites of Imipramine, Venlafaxine and Amitriptyline. These results are encouraging to continue to access new biomimetic oxidation reactions with our catalytic system and to provide metabolites for structure elucidation in medicinal chemistry settings.

Overall, this project demonstrates how thorough mechanistic understanding can aid in reaction development and elucidate new pathways towards more efficient catalytic systems. As such, we demonstrate that kinetic analyses in particular are not simply a tool to understand mechanistic pathways, but also provide the opportunity to further develop catalysts based on a rational understanding of catalyst activation and structural features required for efficient catalysis. Therefore, the results from these studies enable powerful, mechanistically guided, and impactful design choices for future development—in contrast to common empirically-driven methodology developments.

5 Experimental Section

5.1 General Procedures

All reagents were purchased and used as received. Stirbars used in catalytic reactions were cleaned with aqua regia for at least 3 h under gentle stirring, rinsed with copious amounts of water, and dried in an oven at 120 °C prior to use. Standard solutions were prepared using volumetric flasks. All liquid reagents were dispensed by difference using gas-tight Hamilton syringes. Yields are reported as average yields of at least 2 experiments. The reported error is the standard deviation of at least two replicate trials. Unless noted otherwise, no efforts were made to exclude atmospheric air or moisture.

All reaction yields were determined using GC analysis using PhCl as internal standard. Yields are reported as average yields of at least 2 experiments. All standard deviations are below 3.0 %.

The following reagents were purchased and used without further purification: Alfa Aesar: $FeCl_3.6H_2O$; pyridine; 2-picolinic acid; tert-butyl peroxybenzoate; tert-butyl hydroperoxide. Strem Chemicals: CuBr.

$FeCl_3.6H_2O$ and CuBr were stored in a desiccator under dry conditions. tert-butyl peroxybenzoate and tert-butyl hydroperoxide were stored in a refrigerator at approximately 5 °C. All other reagents were stored in a ventilated cabinet.

The substrate tripropylamine was used in initial studies. Tripropylamine was chosen because of the common use of AcOH as an additive in many transition metal catalyzed reactions. Triethylamine could potentially decompose into diethylamine in the presence of the catalyst. Diethylamine could then nucleophilically attack AcOH and produce the amide product via an alternative, non-catalyzed pathway. Thus, the use of triethylamine would hinder the determination of reaction yield.

2-methyl-1-phenylpropan-2-yl benzoperoxoate was synthesized independently according to the literature [111].

5.2 Analytical methods

5.2.1 Gas Chromatography

GC analyses were performed on an Agilent 7890A Series GC equipped with FID detector, an Agilent HP-5 capillary column (length 30m, diameter 0.32 mm, film thickness 0.25 µm), and a 7693A auto injector module. Yields were calculated by calibrating prepared samples and standard to the response of the instrument. GC-MS investigations were carried out on an Agilent 5975C instrument using a 19091S-433 (HP-5MS; 30 m, 0.25 mm i.d., 0.25 µm df) column. The identities of all products were verified by comparison of the obtained data with GC and GC-MS data of original samples.

5.2.2 Gas Chromatography-Mass Spectroscopy

GC-MS analyses were carried out on an Agilent 7890B instrument using a 19091S-433 (HP-5MS; 30 m, 0.25 mm i.d., 0.25 µm df) column.

5.2.3 NMR Spectroscopy

Quantitative 1H NMR measurements were performed using an adjusted method (15 s relaxation time, NS = 32) with dibutyl ether or 1,3-dinitrobenzene as internal standard.

5.2.4 In Situ Infrared Spectroscopy

in-situ IR measurements were performed on a Mettler Toledo ReactiR 15 instrument (serial number: R15-20251) using a 6.3 mm AgX DiComp probe and iC IR software. Mettler Toledo ConcIRT™ software was used for all *in situ* IR analyses. The ConcIRT™ algorithm automatically estimates the number of reaction components in a chemical reaction and generates accurate component profiles and calculated pure component spectra for each of the components. IR absorbance trends were manually determined to ensure complete agreement with the ConcIRT™ software.

5.2.5 Infrared Spectroscopy

IR analyses were performed on an ATR instrument (Bruker Vertex 70) using a NaCl disc purchased from International Crystal Labs.

5.2.6 Electron Spray Ionization-Mass Spectroscopy

ESI-MS investigations were carried out on a Thermo Quest Finnigan LCQ DECA mass spectrometer using Tune Plus (v. 2.0) software

5.2.7 Literature Search

Literature search was based on computer-assisted programs: *SciFinder* and Reaxys; *Cambridge Structural Database* (*CSD*) for crystallographic data.

5.3 Catalytic Studies

5.3.1 General Procedure for Optimization of Catalytic Reactions

To a 4 mL scintillation vial, equipped with a Teflon-coated stirbar, all solid reagents were added. Subsequently, solvent was added, and then all other liquid reagents were added, with substrate added last. The vial was sealed with a Teflon-lined vial cap and heated on a pre-heated vial plate under vigorous stirring (1500 rpm). After the reaction time was completed the vial was taken off the heating block and the mixture was allowed to cool to room temperature. 10 µL of PhCl of were added as internal GC standard. 10 mL of EtOAc and 5 mL of a saturated aqueous citric acid solution were added to this vial. After stirring the biphasic mixture vigorously, the phases were separated and the organic phase was filtered through a plug of Celite. The filtrate was diluted to a total volume of 20 mL with ethyl acetate and the amide yield was determined by calibrated GC analysis.

5.3.2 General Procedure for Fe]Catalyzed Amide Synthesis from NPr_3

To a 4 mL scintillation vial, equipped with a Teflon-coated stirbar, 2-picolinic acid (3.1 mg, 0.025 mmol, 5.0 mol %) was added. 1.80 mL (equivalent to 0.025 mmol, 5.0 mol % of $FeCl_3$) of a standard solution of $FeCl_3.6H_2O$ (94 mg, 0.35 mmol) in 25 mL pyridine was added. Subsequently, $PhCO_3{}^tBu$ (280 µL, 291 mg, 1.50 mmol, 3.00 equiv), deionizied H_2O (9.0 µL, 9.0 mg, 0.10 mmol, 1.0 equiv.), and tripropylamine (95 µL, 71 mg, 0.50 mmol, 1.0 equiv.) were added to the vial in this sequence. The vial was sealed with a Teflon-lined vial cap and heated to 100 °C on a pre-heated vial plate under vigorous stirring (1500 rpm). After the reaction time was completed (24 h) the vial was taken off the heating block and the mixture was allowed to cool to room temperature. 10 µL of PhCl of were added as internal GC standard. 10 mL of EtOAc and 5 mL of a saturated aqueous citric acid solution were added to this vial. After stirring the biphasic mixture vigorously, the phases were separated and the organic phase was filtered through a plug of Celite. The filtrate was diluted to a total volume of 20 mL with ethyl acetate and the amide yield was determined by calibrated GC analysis.

5.3.3 Procedure for Optimization of Amide Yield for Oxidation of NPr_3

In analogy to the general procedure for the optimization of catalytic reactions, $FeCl_3$•$6H_2O$ (6.8 mg, 0.025 mmol, 5.0 mol %) and Tri(n-propyl)amine (95 µL, 71 mg, 0.50 mmol, 1.00 equiv.) were reacted in pyridine (1.80 mL) at 100 °C for 24 h. In addition to this procedure, the conditions in Table 2 were used.

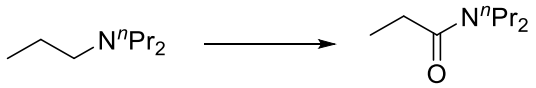

Table 2: Optimization of Amide Yield for Oxidation of NPr_3.

Entry	Reagents and Additives	GC Yield Amide
1	-	0%
2	^{t}BuOOH (5-6 M in decane; 182 µL, 128 mg, 1.00 mmol, 2.00 equiv.)	0%
3	^{t}BuOOH (70% solution in H_2O; 138 µL, 147 mg, 1.00 mmol, 2.00 equiv.)	0%
4	H_2O_2 (30% solution in H_2O; 102 µL, 113 mg, 1.00 mmol, 2.00 equiv.)	0%
5	^{t}BuOO^{t}Bu (99%; 186 µL, 149 mg, 1.00 mmol, 2.00 equiv.)	0%
6	$PhCO_2$-O_2CPh (247 mg, 1.00 mmol, 2.00 equiv.)	0%
7	$PhI(OAc)_2$ (322 mg, 1.00 mmol, 2.00 equiv.)	0%
8	PhI(=O) (220 mg, 1.00 mmol, 2.00 equiv.)	0%
9	mCPBA (203 mg, 1.00 mmol, 2.00 equiv.)	0%
10	$H_3CCO_3{}^t$Bu (319 µL, 264 mg, 1.00 mmol, 2.00 equiv.)	3 ± 0%
11	$H_3CCO_3{}^t$Bu (50% in spirits, 484 µL, 397 mg, 1.6 mmol, 3.2 equiv.)	5 ± 1%
12	$H_3CCO_3{}^t$Bu (50% in spirits, 644 µL, 528 mg, 2.1 mmol, 4.2 equiv.)	6 ± 1%
13	$PhCO_3{}^t$Bu (186 µL, 194 mg, 1.00 mmol, 2.00 equiv.)	3 ± 1%
14	$PhCO_3{}^t$Bu (233 µL, 242 mg, 1.25 mmol, 2.50 equiv.)	6 ± 1%
15	$PhCO_3{}^t$Bu (280 µL, 291 mg, 1.50 mmol, 3.00 equiv.)	9.0 ± 0.4%
16	$PhCO_3{}^t$Bu (373 µL, 288 mg, 2.00 mmol, 4.00 equiv.)	10 ± 1%
17	$PhCO_3{}^t$Bu (140 µL, 146 mg, 0.750 mmol, 1.50 equiv.)	0%
18	$PhCO_3{}^t$Bu (93.3 µL, 97.1 mg, 0.500 mmol, 1.00 equiv.)	0%
19	**$PhCO_3{}^t$Bu (280 µL, 291 mg, 1.50 mmol, 3.00 equiv.), 2 (3.1 mg, 0.025 mmol, 5.0 mol %)**	**16 ± 1%**
20	**$PhCO_3{}^t$Bu (280 µL, 291 mg, 1.5 mmol, 3.0 equiv.), 2 (12.4 mg, 0.10 mmol, 20 mol %), $FeCl_3$·$6H_2O$ (27.2 mg, 0.100 mmol, 20.0 mol %)**	**36 ± 2%**
21	$PhCO_3{}^t$Bu (373 µL, 288 mg, 2.0 mmol, 4.0 equiv.), **2** (3.1 mg, 0.025 mmol, 5.0 mol %)	16 ± 1%
22	$H_3CCO_3{}^t$Bu (50% in spirits, 484 µL, 397 mg, 1.6 mmol, 3.2 equiv.), **2** (3.1 mg, 0.025 mmol, 5.0 mol %)	3 ± 1%
23	$H_3CCO_3{}^t$Bu (50% in spirits, 644 µL, 528 mg, 2.1 mmol, 4.2 equiv.), **2** (3.1 mg, 0.025 mmol, 5.0 mol %)	4 ± 1%
24	$PhCO_3{}^t$Bu (280 µL, 291 mg, 1.5 mmol, 3.0 equiv.), **2** (6.2 mg, 0.05 mmol, 10 mol %)	8 ± 1%
25	$PhCO_3{}^t$Bu (280 µL, 291 mg, 1.5 mmol, 3.0 equiv.), **2** (12.4 mg, 0.10 mmol, 20 mol %)	7.2 ± 0.5%
26	$PhCO_3{}^t$Bu (280 µL, 291 mg, 1.5 mmol, 3.0 equiv.), **2** (1.6 mg, 0.0125 mmol, 2.5 mol %)	8 ± 1%
27	$PhCO_3{}^t$Bu (280 µL, 291 mg, 1.5 mmol, 3.0 equiv.), **10** (3.0 mg, 0.025 mmol, 5.0 mol %)	8.9 ± 0.4%
28	$PhCO_3{}^t$Bu (280 µL, 291 mg, 1.5 mmol, 3.0 equiv.), **11** (3.1 mg, 0.025 mmol, 5.0 mol %)	8 ± 1%
29	$PhCO_3{}^t$Bu (280 µL, 291 mg, 1.5 mmol, 3.0 equiv.), **12** (3.6 mg, 0.025 mmol, 5.0 mol %)	7 ± 1%
30	$PhCO_3{}^t$Bu (280 µL, 291 mg, 1.5 mmol, 3.0 equiv.), **13** (3.6 mg, 0.025 mmol, 5.0 mol %)	5 ± 1%

31	$PhCO_3{}^tBu$ (280 µL, 291 mg, 1.5 mmol, 3.0 equiv.), **14** (3.9 mg, 0.025 mmol, 5.0 mol %)	7 ± 2%
32	$PhCO_3{}^tBu$ (280 µL, 291 mg, 1.5 mmol, 3.0 equiv.), **15** (5.9 mg, 0.025 mmol, 5.0 mol %)	8.7 ± 0.4%
33	$PhCO_3{}^tBu$ (280 µL, 291 mg, 1.50 mmol, 3.00 equiv.), no $FeCl_3$, Fe(**16**)$(MeCN)_2(SbF_6)_2$ (23.3 mg, 0.025 mmol, 5.0 mol %)	3 ± 1%
34	$PhCO_3{}^tBu$ (280 µL, 291 mg, 1.5 mmol, 3.0 equiv.), AcOH (1.43 µL, 1.5 mg, 0.025 mmol, 5.0 mol %)	8 ± 1%
35	$PhCO_3{}^tBu$ (280 µL, 291 mg, 1.5 mmol, 3.0 equiv.), CF_3CO_2H (1.86 µL, 2.8 mg, 0.025 mmol, 5.0 mol %)	10 ± 1%
36	$PhCO_3{}^tBu$ (280 µL, 291 mg, 1.5 mmol, 3.0 equiv.), Na_2CO_3 (2.7 mg, 0.025 mmol, 5.0 mol %)	8.8 ± 0.4%
37	$PhCO_3{}^tBu$ (280 µL, 291 mg, 1.5 mmol, 3.0 equiv.), NaOAc (2.1 mg, 0.025 mmol, 5.0 mol %)	9 ± 1%
38	**no oxidant**, **2** (3.1 mg, 0.025 mmol, 5.0 mol %)	0%
39	$PhCO_3{}^tBu$ (280 µL, 291 mg, 1.50 mmol, 3.00 equiv.), **2** (3.1 mg, 0.025 mmol, 5.0 mol %), 1.0 mL pyridine	15 ± 2%
40	**$PhCO_3{}^tBu$ (280 µL, 291 mg, 1.50 mmol, 3.00 equiv.), 2 (3.1 mg, 0.025 mmol, 5.0 mol %), 5.0 mL pyridine**	**35 ± 3%**

5.3.4 Procedure for Optimization of Reaction Temperature

In analogy to the general procedure for the optimization of catalytic reactions, Tri(*n*-propyl)amine (95 µL, 71 mg, 0.50 mmol, 1.0 equiv.), $PhCO_3{}^tBu$ (280 µL, 291 mg, 1.50 mmol, 3.00 equiv.), 2-picolinic acid (3.1 mg, 0.025 mmol, 5.0 mol %), $FeCl_3 \cdot 6H_2O$ (6.8 mg, 0.025 mmol, 5.0 mol %), were reacted in pyridine (1.80 mL) for 24 h. In addition to this procedure, the conditions in Table 3 were used.

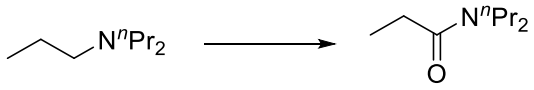

Table 3: Optimization of Reaction Temperature.

Entry	Reaction Temperature	Product (GC Yield)
1	100 °C	16 ± 1%
2	90 °C	13 ± 2%
3	80 °C	13 ± 1%
4	70 °C	12 ± 1%
5	60 °C	12 ± 1%
6	50 °C	13 ± 2%
7	40 °C	9 ± 2%
8	30 °C	8 ± 1%

5.3.5 Optimization of Water Loading at 50 ºC

In analogy to the general procedure for the optimization of catalytic reactions, Tri(*n*-propyl)amine (95 µL, 71 mg, 0.50 mmol, 1.0 equiv.), $PhCO_3{}^tBu$ (280 µL, 291 mg, 1.50 mmol, 3.00 equiv.), 2-picolinic acid (3.1 mg, 0.025 mmol, 5.0 mol %),

$FeCl_3 \cdot 6H_2O$ (6.8 mg, 0.025 mmol, 5.0 mol %), were reacted in pyridine (1.80 mL) at 50 °C for 24 h. In addition to this procedure, the conditions in Table 4 were used.

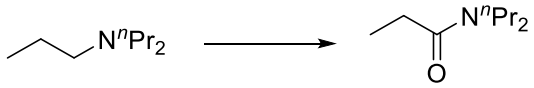

Table 4: Optimization of Water Loading at 50 ºC

Entry	Added H_2O	Product (GC Yield)
1	-	11 ± 1%
2	9.0 µL, 9.0 mg, 0.50 mmol, 1.0 equiv.	28 ± 1%
3	45 µL, 45 mg, 2.5 mmol, 5.0 equiv.	43 ± 2%
4	54 µL, 54 mg, 3.0 mmol, 6.0 equiv.	44.3 ± 0.5%
5	63 µL, 63 mg, 3.5 mmol, 7.0 equiv.	45 ± 2%
6	72 µL, 72 mg, 4.0 mmol, 8.0 equiv.	47 ± 1%
7	81 µL, 81 mg, 4.5 mmol, 9.0 equiv.	48 ± 1%
8	90 µL, 90 mg, 5.0 mmol, 10 equiv.	49 ± 1%
9	**99 µL, 99 mg, 5.5 mmol, 11 equiv.**	**56 ± 1%**
10	**108 µL, 108 mg, 6.0 mmol, 12 equiv.**	**50.5 ± 0.5%**
11	**117 µL, 117 mg, 6.5 mmol, 13 equiv.**	**51 ± 2%**
12	**126 µL, 126 mg, 7.0 mmol, 14 equiv.**	**53 ± 1%**
13	135 µL, 135 mg, 7.5 mmol, 15 equiv.	48 ± 1%
14	180 µL, 180 mg, 10 mmol, 20 equiv.	32 ± 1%
15	450 µL, 450 mg, 25 mmol, 50 equiv.	24 ± 1%
16	900 µL, 900 mg, 50 mmol, 100 equiv.	5 ± 2%

5.3.6 Procedure for Background Reactions Under N_2

All reaction solutions were prepared in analogy to the procedure described above in the representative procedure for amide synthesis. Before the vial was sealed with a Teflon-lined screw cap, N_2 was bubbled through the solution for at least 5 min in order to remove the majority of air. After sealing the vial, the reactions were heated to 50 ºC for 24 h; workup and analysis were performed as described above.

In analogy to the general procedure for the optimization of catalytic reactions, Tri(*n*-propyl)amine (95 µL, 71 mg, 0.50 mmol, 1.0 equiv.), oxidant (2.5 to 4.0 equiv.), 2-picolinic acid (3.1 mg, 0.025 mmol, 5.0 mol %), $FeCl_3 \cdot 6H_2O$ (6.8 mg, 0.025 mmol, 5.0 mol %) and H_2O (99 µL, 99 mg, 5.5 mmol, 11 equiv.) were reacted in pyridine (1.80 mL dried over activated MS 4Å prior to use) at 50 °C for 24 h. In addition to this procedure, the conditions in Table 5 were used.

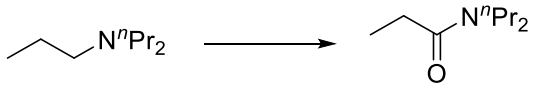

Table 5: Background Reactions Under N_2.

Entry	Reagents and Additives	GC Yield Amide
Oxidant Studies		
1	$PhCO_3{}^tBu$ (326 µL, 340 mg, 1.75 mmol, 3.5 equiv.)	53 ± 1%
2	$PhCO_3{}^tBu$ (233 µL, 243 mg, 1.25 mmol, 2.5 equiv.)	54 ± 1%
3	$H_3CCO_3{}^tBu$ (50% in spirits; 402 µL, 330 mg, 1.3 mmol, 2.6 equiv.)	0%
4	$H_3CCO_3{}^tBu$ (50% in spirits; 484 µL, 397 mg, 1.6 mmol, 3.2 equiv.)	0.2 ± 0.0%
5	$H_3CCO_3{}^tBu$ (50% in spirits; 566 µL, 464 mg, 1.85 mmol, 3.7equiv.)	1.2 ± 0.2%
6	$H_3CCO_3{}^tBu$ (50% in spirits; 644 µL, 528 mg, 2.1 mmol, 4.2 equiv.)	2.5 ± 0.1%
Background Studies		
7	No oxidant	0%
8	No $FeCl_3$, 3.0 equiv. $PhCO_3{}^tBu$	15 ± 1%
9	No $FeCl_3$, 3.0 equiv. $PhCO_3{}^tBu$, no **2**	12 ± 1%
10	No $FeCl_3$, 3.0 equiv. $PhCO_3{}^tBu$, under N_2	0%
11	No $FeCl_3$, 3.0 equiv. $PhCO_3{}^tBu$, no **2**, under N_2	0%
12	Under N_2, 3.0 equiv. $PhCO_3{}^tBu$	58 ± 2%

5.3.7 Procedure for Optimization of Reaction Time

In analogy to the general procedure for the optimization of catalytic reactions, Tri(*n*-propyl)amine (95 µL, 71 mg, 0.50 mmol, 1.0 equiv.), $PhCO_3{}^tBu$ (280 µL, 291 mg, 1.50 mmol, 3.00 equiv.), 2-picolinic acid (3.1 mg, 0.025 mmol, 5.0 mol %), $FeCl_3{\cdot}6H_2O$ (6.8 mg, 0.025 mmol, 5.0 mol %) and H_2O (99 µL, 99 mg, 5.5 mmol, 11 equiv.) were reacted in pyridine (1.80 mL dried over activated MS 4Å prior to use) at 50 °C for 24 h. GC yields were determined at each time point in Table 6.

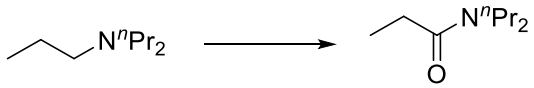

Table 6: Optimization of Reaction Time.

Entry	Reaction Time	Products (GC Yield)
1	0.5 h	38 ± 4%
2	1 h	46 ± 3%
3	2 h	55 ± 2%
4	4 h	55 ± 2%
5	6 h	63 ± 1%
6	8 h	61 ± 5%
7	10 h	62 ± 2%
8	12 h	59 ± 3%
9	14 h	58 ± 1%
10	20 h	59 ± 2%
11	24 h	56 ± 1%
12	48 h	56 ± 1%

5.3.8 Procedure for Testing Literature Conditions For Amide Formation

Literature procedures were followed as documented in the respective reference provided in Table 7, using NPr_3 as substrate. After the tabulated reaction times were complete, the reaction mixture was allowed to cool to room temperature. 10 µL of PhCl of were added as internal GC standard. 10 mL of EtOAc and 5 mL of a saturated aqueous citric acid solution were added to the vial. After stirring the biphasic mixture vigorously, the phases were separated and the organic phase was filtered through a plug of Celite. The filtrate was diluted to a total volume of 20 mL with ethyl acetate and the yield of amide was determined by calibrated GC analysis.

Table 7: Results of literature conditions for oxidative amine to amide conversions with tripropylamine as substrate.

Entry	Conditions	Reference
Cu Catalyzed Protocols		
1	$N(^nPr)_3$ (95.1 µL, 71.6 mg, 0.5 mmol, 1.00 equiv.), CuBr (10 mol %), K_2CO_3 (2.0 equiv), DMSO (2 mL), H_2O (40 µL, 4.4 equiv), 1 atm O_2, 150 ºC, 24 h	*2*
2	$N(^nPr)_3$ (95.1 µL, 71.6 mg, 0.5 mmol, 1.00 equiv.), CuBr (10 mol %), bpy (10 mol %), pyridine (2.0 equiv), toluene (5 mL), air (1 atm), 90 ºC, 24 h	*3*
3	$N(^nPr)_3$ (95.1 µL, 71.6 mg, 0.5 mmol, 1.00 equiv.), CuBr (10 mol %), bpy (10 mol %), pyridine (2.0 equiv), toluene (5 mL), air (1 atm), 90 ºC, 24 h, **H_2O (11 equiv.)**	*3*
4	$N(^nPr)_3$ (95.1 µL, 71.6 mg, 0.5 mmol, 1.00 equiv.), $CuCl_2 \cdot 2H_2O$ (20 mol %), H_2O (1.5 mmol, 3 equiv), MeOH (2 mL), O_2 balloon, room temperature, 24 h	*4*
5	$N(^nPr)_3$ (95.1 µL, 71.6 mg, 0.5 mmol, 1.00 equiv.), CuBr (5 mol %), H_2O (3 equiv), ^{t}BuOOH (91 µL, 0.5 mmol, 1 equiv, solution in decane), under N_2, 100 ºC, 24 h	*5*
6	$N(^nPr)_3$ (95.1 µL, 71.6 mg, 0.5 mmol, 1.00 equiv.), $CuBr_2$ (10 mol %), AcOH (20 mol %), dioxane (0.5 mL), 80 ºC, O_2 (1 atm), 24 h	*6*
7	$N(^nPr)_3$ (95.1 µL, 71.6 mg, 0.5 mmol, 1.00 equiv.), $CuBr_2$ (10 mol %), AcOH (20 mol %), dioxane (0.5 mL), 80 ºC, O_2 (1 atm), 24 h, **H_2O (11 equiv.)**	*6*
8	$N(^nPr)_3$ (95.1 µL, 71.6 mg, 0.5 mmol, 1.00 equiv.), CuI (10 mol %), TEMPO (10 mol %), bpy (10 mol %), O_2 balloon, 60 ºC, MeCN (2 mL), 24 h	*7*
9	$N(^nPr)_3$ (95.1 µL, 71.6 mg, 0.5 mmol, 1.00 equiv.), CuI (10 mol %), TEMPO (10 mol %), bpy (10 mol %), O_2 balloon, 60 ºC, MeCN (2 mL), 24 h, **H_2O (11 equiv.)**	*7*
10	$N(^nPr)_3$ (95.1 µL, 71.6 mg, 0.5 mmol, 1.0 equiv.), CuI (20 mol %), O_2 balloon, 120 ºC, 24 h	*8*
11	$N(^nPr)_3$ (95.1 µL, 71.6 mg, 0.5 mmol, 1.0 equiv.), CuI (20 mol %), O_2 balloon, 120 ºC, 24 h, **H_2O (11 equiv.)**	*8*
12	$N(^nPr)_3$ (95.1 µL, 71.6 mg, 0.5 mmol, 1.0 equiv.), HCl (41 µL, 12 M, 0.5 mmol 1.0 equiv), CuI (1.0 mol %), $AgIO_3$ (1.0 mol %), T-HYDRO (70 wt% in H_2O, 1.1 eq.), MeCN (0.2 mL), 40 ºC, N_2, 24 h	*9*
13	$N(^nPr)_3$ (95.1 µL, 71.6 mg, 0.5 mmol, 1.0 equiv.), HCl (41 µL, 12 M, 0.5 mmol,1.0 equiv), CuI (1.0 mol %), $AgIO_3$ (1.0 mol %), T-HYDRO (70 wt% in H_2O, 1.1 eq.), MeCN (0.2 mL), 40 ºC, N_2, 24 h, **H_2O (11 equiv.)**	*9*

14	$N(^nPr)_3$ (95.1 µL, 71.6 mg, 0.5 mmol, 1.0 equiv.), CuI (1.0 mol %), $AgIO_3$ (1.0 mol %), T-HYDRO (70 wt% in H_2O, 1.1 eq.), MeCN (0.2 mL), 40 ºC, N_2, 24 h	*9*
15	$N(^nPr)_3$ (95.1 µL, 71.6 mg, 0.5 mmol, 1.0 equiv.), CuI (1.0 mol %), $AgIO_3$ (1.0 mol %), T-HYDRO (70 wt% in H_2O, 1.1 eq.), MeCN (0.2 mL), 40 ºC, N_2, 24 h, **H_2O (11 equiv.)**	*9*
16	$N(^nPr)_3$ (95.1 µL, 71.6 mg, 0.5 mmol, 1.0 equiv.), $Cu(OTf)_2$ (10 mol %), bpy (10 mol %), TEMPO (10 mol %), NaOH (0.05 M in H_2O; 10 mol%), MeCN (2 mL), open to air, room temperature, 24 h	*10*
17	$N(^nPr)_3$ (95.1 µL, 71.6 mg, 0.5 mmol, 1.0 equiv.), $Cu(OTf)_2$ (10 mol %), bpy (10 mol %), TEMPO (10 mol %), NaOH (0.05 M in H_2O; 10 mol%), MeCN (2 mL), open to air, room temperature, 24 h, **H_2O (11 equiv.)**	*10*
Fe Catalyzed Protocols		
18	$N(^nPr)_3$ (95.1 µL, 71.6 mg, 0.5 mmol, 1.00 equiv.), $FeCl_3 \cdot 6\ H_2O$ (10 mol %), MeCN (1.5 mL), ^{t}BuOOH (70% in H_2O, 1.0 equiv), room temperature, 24 h	*11*
19	$N(^nPr)_3$ (95.1 µL, 71.6 mg, 0.5 mmol, 1.00 equiv.), $FeCl_3 \cdot 6\ H_2O$ (10 mol %), MeCN (1.5 mL), ^{t}BuOOH (70% in H_2O, 1.0 equiv), room temperature, 24 h, **H_2O (11 equiv.)**	*11*
20	$N(^nPr)_3$ (95.1 µL, 71.6 mg, 0.5 mmol, 1.00 equiv.), $FeCl_2$ (2.5 mol %), MeCN (3 mL), ^{t}BuOOH (55% in decane; 2 equiv), N_2, RT during addition, 85 ºC, 24 h	*12*
21	$N(^nPr)_3$ (95.1 µL, 71.6 mg, 0.5 mmol, 1.00 equiv.), $FeCl_2$ (2.5 mol %), MeCN (3 mL), ^{t}BuOOH (55% in decane; 2 equiv), N_2, RT during addition, 85 ºC, 24 h, **H_2O (11 equiv.)**	*12*
22	$N(^nPr)_3$ (95.1 µL, 71.6 mg, 0.5 mmol, 1.00 equiv.), $Fe(NO_3)_3 \cdot 9H_2O$ (5 mol %), ^{t}BuOOH (in decane, 1.4 equiv), 24 h, 50 ºC	*13*
23	$N(^nPr)_3$ (95.1 µL, 71.6 mg, 0.5 mmol, 1.00 equiv.), $Fe(NO_3)_3 \cdot 9H_2O$ (5 mol %), ^{t}BuOOH (in decane, 1.4 equiv), 24 h, 50 ºC, **H_2O (11 equiv.)**	*13*
24	$N(^nPr)_3$ (95.1 µL, 71.6 mg, 0.5 mmol, 1.00 equiv.), $Fe(NO_3)_3 \cdot 9H_2O$ (5 mol %), TEMPO (5 mol %), toluene (0.5 mL), 80 ºC, 24 h, air	*14*
25	$N(^nPr)_3$ (95.1 µL, 71.6 mg, 0.5 mmol, 1.00 equiv.), $Fe(NO_3)_3 \cdot 9H_2O$ (5 mol %), TEMPO (5 mol %), toluene (0.5 mL), 80 ºC, 24 h, **H_2O (11 equiv.)**	*14*
26	$N(^nPr)_3$ (41.3 µL, 30.7 mg, 0.214 mmol, 1.00 equiv.), Fe(**16**)$(MeCN)_2(SbF_6)_2$ (15 mol % total), AcOH (1.5 equiv total), MeCN (5.3 mL total), H_2O_2 (30 % in H_2O, 3.6 equiv total), room temperature, 24 h	*15*
Ru Catalyzed Protocols		
27	$N(^nPr)_3$ (95.1 µL, 71.6 mg, 0.5 mmol, 1.00 equiv.), $PhCF_3$ (0.75 mL), $Ru(OH)_x/Al_2O_3$ (2.5 mol% Ru), 83 ºC, O_2 balloon, 24 h	*16*
28	$N(^nPr)_3$ (95.1 µL, 71.6 mg, 0.5 mmol, 1.00 equiv.), $PhCF_3$ (0.75 mL), $Ru(OH)_x/Al_2O_3$ (2.5 mol% Ru), 83 ºC, O_2 balloon, 24 h, **H_2O (11 equiv.)**	*16*
29	$N(^nPr)_3$ (95.1 µL, 71.6 mg, 0.5 mmol, 1.0 equiv.), benzene (2 mL), tBuOOH (1.1 mmol in decane), $RuCl_3$ (3 mol %), PPh_3 (9 mol %), N_2, 3 h, RT	*17*
30	$N(^nPr)_3$ (95.1 µL, 71.6 mg, 0.5 mmol, 1.0 equiv.), benzene (2 mL), tBuOOH (1.1 mmol in decane), $RuCl_3$ (3 mol %), PPh_3 (9 mol %), N_2, 3 h, RT, **H_2O (11 equiv.)**	*17*
31	$N(^nPr)_3$ (95.1 µL, 71.6 mg, 0.5 mmol, 1.0 equiv.), $RuCl_3$ (5 mol %), MeOH (4 mL), H_2O_2 (30 % in H_2O, 4.0 equiv), room temperature, 2 h	*18*
32	$N(^nPr)_3$ (95.1 µL, 71.6 mg, 0.5 mmol, 1.0 equiv.), $RuCl_3$ (5 mol %), MeOH (4 mL), H_2O_2 (30 % in H_2O, 4.0 equiv), room temperature, 2 h, **H_2O (11 equiv.)**	*18*
33	$N(^nPr)_3$ (95.1 µL, 71.6 mg, 0.5 mmol, 1.0 equiv.), $RuCl_3$ (20 mol %), AcOH (5 mL), CH_3CO_3H (4.0 equiv.), 4 h, room temperature	*19*
34	$N(^nPr)_3$ (95.1 µL, 71.6 mg, 0.5 mmol, 1.0 equiv.), $RuCl_3$ (20 mol %), AcOH (5 mL), CH_3CO_3H (4.0 equiv.), 4 h, room temperature, **H_2O**	*19*

	(11 equiv.)	
35	$N(^nPr)_3$ (95.1 µL, 71.6 mg, 0.5 mmol, 1.0 equiv.), $RuCl_3$ (5.0 mol %), MeOH (0.6 mL), AcOH (0.2 mL), O_2 balloon, 60 ºC, 24 h	*20*
36	$N(^nPr)_3$ (95.1 µL, 71.6 mg, 0.5 mmol, 1.0 equiv.), $RuCl_3$ (5.0 mol %), MeOH (0.6 mL), AcOH (0.2 mL), O_2 balloon, 60 ºC, 24 h, **H_2O (11 equiv.)**	*20*
Pd Catalyzed Protocol		
37	$N(^nPr)_3$ (95.1 µL, 71.6 mg, 0.5 mmol, 1.0 equiv.), $PdCl_2$ (5 mol %), PPh_3 (10 mol %), DMF (5 mL), MS 3Å (0.25 g, powdered, activated), O_2 balloon, NaOAc (0.5 mmol), 40 ºC, 24 h	*21*
38	$N(^nPr)_3$ (95.1 µL, 71.6 mg, 0.5 mmol, 1.0 equiv.), $PdCl_2$ (5 mol %), PPh_3 (10 mol %), DMF (5 mL), MS 3Å (0.25 g, powdered, activated), O_2 balloon, NaOAc (0.5 mmol), 40 ºC, 24 h, **H_2O (11 equiv.)**	*21*
Fe Mediated Protocol		
39	$N(^nPr)_3$ (95.1 µL, 71.6 mg, 0.5 mmol, 1.0 equiv.), HCl (0.4 M in H_2O, 3.2 equiv.), NaOH (10 weight-% in H_2O; 48 equiv.), $K_3[Fe(CN)_6]$ (1.3 g, 3.96 mmol, 7.9 equiv.), H_2O (10 mL), RT, 40 min	*22*

5.4 Independent Synthesis of Amide Products

5.4.1 N,N-Dipentylbenzamide

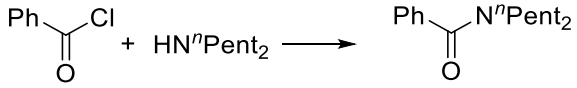

To a 50 mL round bottom flask containing 20 mL of dichloromethane and equipped with a Teflon-coated stirbar, dipentylamine (3.02 mL, 2.36 g, 15 mmol) and triethylamine (2.34 mL, 1.72 g, 17 mmol) were added. The reaction mixture was cooled to 0 °C in an ice bath. Benzoyl chloride (1.63 mL, 1.97 g, 14 mmol) was then added dropwise over 20 minutes. The reaction was allowed to stir at room temperature for 3 h. The reaction mixture was then washed with 1M HCl (3 x 30 mL), water (3 x 30 mL) and a saturated brine solution (3 x 30 mL). The organic phase was dried over $MgSO_4$ and the solvent was removed under vacuum affording the title compound as a light yellow, almost colorless oil (2.61 g, 71%).

5.5 Synthesis of Amine Substrates

5.5.1 N-Benzyl-N-pentylpentan-1-amine

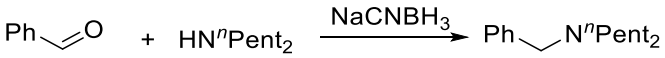

To a 50mL round bottom flask containing 9 mL of methanol and equipped with a Teflon-coated stirbar was added dipentylamine (4.84 mL, 3.77 g, 16 mmol) and benzaldehyde (4.88 mL, 5.09 g, 32 mmol). The reaction mixture was heated to 60 °C. A solution of sodium cyanoborohydride (1.73 g, 27.6 mmol in 18.7 mL methanol) was prepared in a separated flask. An aliquot of 4.6 mL of this sodium cyanoborohydride solution was added dropwise over 30 minutes, followed by three subsequent 4.6 mL additions; each addition was separated by 1 hour of stirring the reaction mixture at 60 °C without adding further reductant. After the fourth addition of the sodium cyanoborohydride solution, the reaction was allowed to stir at 60 °C for one hour. Then, methanol was completely removed under vacuum and diethylether (30 mL) was added. The organic phase was washed with water (3 x 50 mL) and dried over $MgSO_4$. After filtration, diethyl ether was removed from the filtrate under vacuum. The resulting yellow oil was purified by column chromatography (silica gel; R_f = 0.53 in hexanes/ethyl acetate 7:1) to afford *N*-benzyl-*N*-pentylpentan-1-amine as a light yellow oil (2.53 g, 64%).

5.6 Isolation of Amide Products from Reaction Mixture

5.6.1 N,N-Dipentylpentanamide

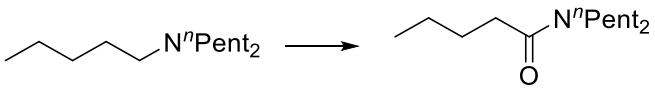

In analogy to the general procedure for catalytic amide synthesis, 2-picolinic acid (15.5 mg, 0.125 mmol, 5.0 mol %) was added to 20 mL scintillation vial equipped with a microstirbar. 9.0 mL of a 0.014 M standard solution of $FeCl_3$•$6H_2O$ (corresponding to 33.8 mg, 0.125 mmol, 5.0 mol % of $FeCl_3$) in pyridine was added. Subsequently, $PhCO_3{}^tBu$ (1.40 mL, 1.46 mg, 7.50 mmol, 3.00 equiv), deionizied H_2O (675 µL, 675 mg, 37.5 mmol, 15.0 equiv.), and tripentylamine (725 µL, 568 mg, 2.50

mmol, 1.00 equiv.) were added, the vial was sealed with a Teflon-lined vial cap, and the mixture was reacted at 50 °C for 48 h. After the reaction time was complete, the reaction mixture was allowed to cool to room temperature and diethyl ether (150 mL) was added. The organic phase was washed with 1 M HCl (3 x 100 mL), 4 M NaOH (3 x 100 mL), and brine (3 x 100 mL) and then dried over $MgSO_4$. After filtration, the volatiles were removed under vacuum. The obtained brown syrup was purified by flash chromatography (silica; R_f = 0.32 in hexanes/ethyl acetate 5:1) to afford the title compound as a colorless oil (380 mg, 63%).

5.6.2 N,N-Dibenzylbenzamide

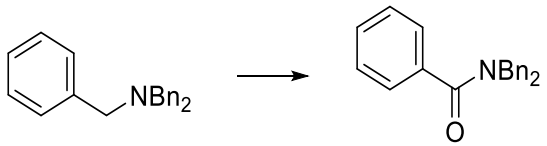

In analogy to the general procedure for catalytic amide synthesis, 2-picolinic acid (15.5 mg, 0.125 mmol, 5.0 mol %) was added to 20 mL scintillation vial equipped with a microstirbar. 1.0 mL of a 0.125 M standard solution of $FeCl_3$•$6H_2O$ (corresponding to 33.8 mg, 0.125 mmol, 5.0 mol % of $FeCl_3$) in pyridine was added. Subsequently, $PhCO_3{}^tBu$ (1213 µL, 1261mg, 6.50 mmol, 2.60 equiv), deionizied H_2O (34 µL, 34.0 mg, 1.88 mmol, 0.75 equiv.), and tribenzylamine (720 mg, 2.50 mmol, 1.0 equiv.) were added, the vial was sealed with a Teflon-lined screw cap, and the mixture was reacted at 80 °C for 24 h. After the reaction time was complete, diethyl ether was added to the reaction mixture. Then, the organic phase was washed with an aqueous, saturated solution of citric acid (3 x 50 mL) and dried over $MgSO_4$. After removing volatiles under vacuum, the brown residue was purified by flash chromatography (silica; R_f = 0.33 in ethyl acetate/hexanes 5:1). The obtained raw product was further purified by recrystallization in the heat out of ethyl acetate/hexane (1:3; 5 mL), affording the title compound as a white solid (440 mg, 58%).

5.6.3 N,N-Dibutylbutyramide

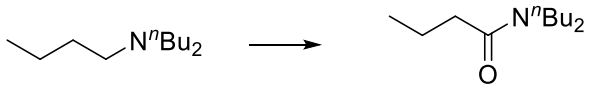

In analogy to the general procedure for catalytic amide synthesis, 2-picolinic acid (15.5 mg, 0.125 mmol, 5.0 mol %) was added to a 20 mL scintillation vial equipped with a microstirbar. 9.0 mL of a 0.014 M standard solution of $FeCl_3$•$6H_2O$ (corresponding to 33.8 mg, 0.125 mmol, 5.0 mol % of $FeCl_3$) in pyridine was added. Subsequently, $PhCO_3{}^tBu$ (1.40 mL, 1.46 g, 7.50 mmol, 3.00 equiv), deionizied H_2O (495 µL, 495 mg, 27.5 mmol, 11.0 equiv.), and tributylamine (594 µL, 463 mg, 2.50 mmol, 1.00 equiv.) were added, the vial was sealed with a Teflon-lined vial cap, and the mixture was reacted at 50 °C for 24 h. After the reaction time was complete, the mixture was allowed to cool to room temperature and diethyl ether (150 mL) was added. The organic phase was washed with 1 M HCl (3 x 100 mL), 4 M NaOH (3 x 100 mL), and brine (3 x 100 mL) and then dried over $MgSO_4$. After filtration, the volatiles were removed under vacuum. The obtained brown syrup was purified by flash chromatography (silica; R_f = 0.35 in hexanes/ethyl acetate 5:1) to afford the title compound as a colorless oil (288 mg, 58%).

5.7 Procedure for $H_2{}^{18}O$ Studies

5.7.1 Procedure for Reaction of Tri(*n*-butyl)amine with $H_2{}^{18}O$

In analogy to the representative procedure for catalytic amide synthesis, 2-picolinic acid (3.1 mg, 0.025 mmol, 5.0 mol %). $FeCl_3{\cdot}6H_2O$ (6.8 mg, 0.025 mmol, 5.0 mol %), $PhCO_3{}^tBu$ (280 µL, 291 mg, 1.50 mmol, 3.00 equiv) and ^{18}O-labeled H_2O (97% ^{18}O, Cambridge Isotope Laboratories; 100 µL, 111 mg, 5.5 mmol, 11 equiv.), and tributylamine (119 µL, 92.6 mg, 0.50 mmol, 1.0 equiv.) were reacted at 50 °C for 24 h. After addition of 10 µL of PhCl as internal GC standard, the solution was divided into two approximately equal parts. One part was diluted with EtOAc (10 mL) and extracted with 5 mL of a saturated aqueous citric acid solution. After stirring the biphasic mixture vigorously, the phases were separated and the organic phase was filtered through a plug of Celite. The filtrate was diluted to a total volume of 10 mL with EtOAc and the yield of **6** was determined by calibrated GC analysis. The other

part of the solution was diluted with EtOAc (10 mL) and extracted with 5 mL of a saturated aqueous citric acid solution. After stirring the biphasic mixture vigorously, the phases were separated and the organic phase was filtered through a plug of Celite. The filtrate was diluted to a total volume of 10 mL with EtOAc. The ^{18}O content of the amide product was determined by GCMS analysis of the mass peaks at m/z 199 (^{16}O amide; abundance 3647) and 201 (^{18}O amide; abundance 30240) to be 30240/(3647 + 30240) = 89% ^{18}O incorporation.

5.7.2 Procedure for Potential Background Reaction of N,N-Dibutylbutyramide with $H_2{}^{18}O$

In analogy to the representative procedure for amide synthesis, 2-picolinic acid (3.1 mg, 0.025 mmol, 5.0 mol %). $FeCl_3 \cdot 6H_2O$ (6.8 mg, 0.025 mmol, 5.0 mol %), $PhCO_3{}^tBu$ (280 µL, 291 mg, 1.50 mmol, 3.00 equiv) and ^{18}O-labeled H_2O (97% ^{18}O, Cambridge Isotope Laboratories; 100 µL, 111 mg, 5.5 mmol, 11 equiv.), and tributylamine (119 µL, 92.6 mg, 0.50 mmol, 1.0 equiv.) were reacted at 50 °C for 24 h. After addition of 10 µL of PhCl as internal GC standard, the solution was divided into two approximately equal parts. One part was diluted with EtOAc (10 mL) and extracted with 5 mL of a saturated aqueous citric acid solution. After stirring the biphasic mixture vigorously, the phases were separated and the organic phase was filtered through a plug of Celite. The filtrate was diluted to a total volume of 10 mL with EtOAc and the yield of **6** was determined by calibrated GC analysis. The other part of the solution was diluted with EtOAc (10 mL) and extracted with 5 mL of a saturated aqueous citric acid solution. After stirring the biphasic mixture vigorously, the phases were separated and the organic phase was filtered through a plug of Celite. The filtrate was diluted to a total volume of 10 mL with EtOAc. The ^{18}O content of the amide product was determined by GCMS analysis of the mass peaks at m/z 199 (^{16}O amide; abundance 3647) and 201 (^{18}O amide; abundance 30240) to be 30240/(3647 + 30240) = 89% ^{18}O incorporation.

5.7.3 Procedure for Potential Background Reaction of N,N-dibutylbutyramide with $H_2{}^{18}O$ in the presence of $PhCO_2H$ and ^tBuOH

N,N-dibutylbutyramide (114 µL, 100 mg, 0.50 mmol, 1.0 equiv.), 2-picolinic acid (3.1 mg, 0.025 mmol, 5.0 mol %), $FeCl_3 \cdot 6H_2O$ (6.8 mg, 0.025 mmol, 5.0 mol %), $PhCO_2H$ (184 mg, 1.5 mmol, 3 equiv.), ^{t}BuOH (144 µL, 111 mg, 1.5 mmol, 3 equiv.) and ^{18}O-H_2O (97% ^{18}O, Cambridge Isotope Laboratories; 100 µL, 111 mg, 5.5 mmol, 11 equiv.) were reacted in 1.8 mL pyridine (dried over 4 Å molecular sieves) at 50 °C for 24 h. The solution was diluted with EtOAc (10 mL) and extracted with 5 mL of a saturated aqueous citric acid solution. After phase separation, the organic phase was filtered through a plug of Celite. The filtrate was diluted to a total volume of 10 mL with EtOAc. The ^{18}O content of the amide product was determined by GCMS analysis of the mass peaks at m/z 199 (^{16}O amide; abundance 1433088) and 201 (^{18}O amide; abundance 45736) to be 45736/(1433088 + 45736) = 2.7% ^{18}O incorporation.

5.8 Procedure for Dealkylation Studies

5.8.1 Representative Procedure for Determining Yields of Dealkylation Product

In analogy to the representative procedure for amide synthesis, tri(*n*-butyl)amine (119 µL, 92.6 mg, 0.500 mmol, 1.00 equiv.), $PhCO_3{}^tBu$ (1.0 to 3.0 equiv.), 2-picolinic acid (**2**) (3.1 mg, 0.025 mmol, 5.0 mol %), $FeCl_3 \cdot 6H_2O$ (6.8 mg, 0.025 mmol, 5.0 mol %), (1.80-0.30) mL pyridine (dried over activated MS 4Å prior to use), 99 to 1500 µL H_2O (5.5 to 83.5 mmol, 11 to 167 equiv) were reacted at 50 ºC for 24 h. After the reaction time was completed, the vial was removed from the heating block and the mixture was allowed to cool to room temperature. 10.0 µL of PhCl of were added as internal GC standard and 51 µL (0.30 mmol; 0.60 equiv.) of dibutylether were added as internal NMR standard. 10 mL EtOAc were added and the reaction mixture was separated into 3 portions of an approximately equal volume. Portion 1 was treated as described in the representative procedure for amide synthesis and the yield of **6** was determined by calibrated GC analysis. 2 M NaOH

solution (1 mL) was added to portion 2, which was then extracted with pentane (2 mL). The combined organic phases were reduced to less than 0.2 mL in vacuum (rotary evaporator) and were diluted with $CDCl_3$ (2 mL). The resulting yield of dibutylamine (**5**) was then determined by quantitative ^1H NMR measurement. To the third portion of the original reaction mixture, 1 mL of 12 M HCl were added. The resulting biphasic mixture was then extracted with pentane (2 mL). The combined organic phases were reduced to 0.2 mL under reduced pressure (rotary evaporator) and $CDCl_3$ (2 mL) were added. The amount of aldehyde was then determined by quantitative 1H NMR spectroscopy (Table 8).

Table 8. Oxidation of Tri(*n*-butyl)amine with different H_2O loadings. Conditions: Tri(*n*-butyl)amine (119 µL, 92.6 mg, 0.500 mmol, 1.00 equiv.), $PhCO_3{}^tBu$ (1.0 to 3.0 equiv.), 2-picolinic acid (2) (3.1 mg, 0.025 mmol, 5.0 mol %), $FeCl_3 \cdot 6H_2O$ (6.8 mg, 0.025 mmol, 5.0 mol %), (1.80-0.3) mL pyridine (dried over activated MS 4Å prior to use), 99 to 1500 µL H_2O (5.5 to 83.5 mmol, 11 to 167 equiv), 50 ºC, 24 h.

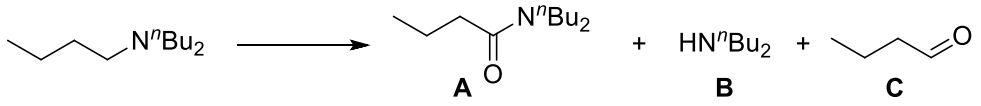

Table 8: Oxidation of Tri(n-butyl)amine with different H2O loadings.

Entry	H_2O / pyridine	GC Yield A	NMR Yield B	NMR Yield C
1[a]	99 µL /1701 µL	64 ± 1%	6 ± 1%	0.3 ± 0.1%
2[a]	200 µL / 1600 µL	45 ± 3%	21 ± 3%	0.3 ± 0.0%
3[a]	500 µL / 1300 µL	24 ± 2%	55 ± 2%	0.3 ± 0.0%
4[a]	1000 µL / 800 µL	8 ± 1%	41 ± 1%	1.3 ± 0.1%
5[a]	1500 µL / 300 µL	0%	42 ± 2%	3.1 ± 0.4%
6[b]	99 µL / 1701 µL	47 ± 1%	29 ± 1%	2.0 ± 0.0%
7[b]	200 µL / 1600 µL	48 ± 2%	34 ± 1%	2.0 ± 0.0%
8[b]	500 µL / 1300 µL	18 ± 1%	52 ± 2%	2.0 ± 0.4%
9[b]	1000 µL / 800 µL	7 ± 1%	39 ± 1%	4.0 ± 0.0%
10[b]	1500 µL / 300 µL	0%	37 ± 2%	4.0 ± 0.0%
11[c]	99 µL / 1701 µL	8 ± 1%	61 ± 1%	6 ± 1%
12[c]	200 µL / 1600 µL	10 ± 1%	64 ± 1%	5.0 ± 0.0%
13[c]	500 µL / 1300 µL	7 ± 1%	57 ± 1%	5.0 ± 0.0%
14[c]	1000 µL / 800 µL	0.05 ± 0.00%	29 ± 2%	5.0 ± 0.0%
15[c]	1500 µL / 300 µL	0.05 ± 0.00%	12 ± 2%	3 ± 1%

[a]3.0 equiv. (280 µL, 291 mg, 1.50 mmol) of $PhCO_3{}^tBu$ was used. [b]2.0 equiv. (186 µL, 194 mg, 1.00 mmol) of $PhCO_3{}^tBu$ was used. [c]1.0 equiv. (93 µL, 97 mg, 0.50 mmol) of $PhCO_3{}^tBu$ was used.

5.9 Procedure for Hemiaminal Studies

5.9.1 Amide Formation from Propionaldehyde and HN^{n}Pr$_2$

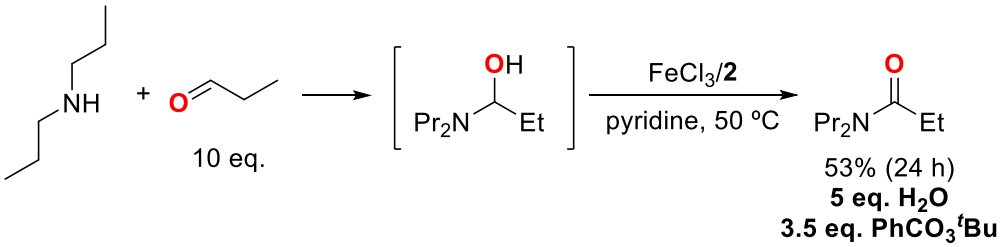

To a 4 mL scintillation vial equipped with a Teflon-coated stirbar, 2-picolinic acid (6.2 mg, 0.050 mmol, 10 mol %), 1.80 mL (equivalent to 0.050 mmol, 10 mol % $FeCl_3$) of a standard solution of $FeCl_3 \cdot 6H_2O$ (189 mg, 0.70 mmol) in 25 mL pyridine, deionizied H_2O (45 µL, 45 mg, 2.5 mmol, 5.0 equiv.), dipropylamine (69 µL, 41 mg, 0.5 mmol, 1.0 equiv.) and propionaldehyde (360 µL, 290 mg, 5.0 mmol, 10.0 equiv.) were added in that sequence. Lastly, $PhCO_3{}^tBu$ (327 µL, 340 mg, 1.75 mmol, 3.50 equiv) was added and the vial was sealed with a Teflon-lined vial cap and heated to 50 °C on a pre-heated vial plate under vigorous stirring (1500 rpm). After 24 h, the vial was taken off the heating block and the mixture was allowed to cool to room temperature. 10 µL of PhCl of were added as internal GC standard. 10 mL of EtOAc and 5 mL of a saturated aqueous citric acid solution were added to the vial. After stirring the biphasic mixture vigorously, the phases were separated and the organic phase was filtered through a plug of Celite. The filtrate was diluted to a total volume of 20 mL with ethyl acetate and the yield of *N*,*N*-dipropylpropionamide was determined by calibrated GC analysis.

5.10 Procedure Cyanation Studies

5.10.1 Procedure for Amine α-C-H Cyanation under Amide Formation Conditions

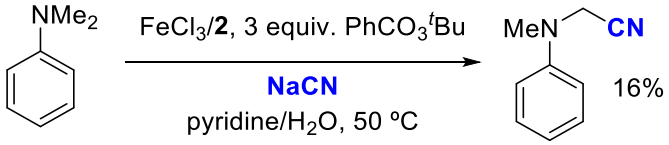

In analogy to the representative procedure for amide synthesis, *N*,*N*-dimethyl aniline (61 mg, 0.50 mmol, 1.00 equiv.), $PhCO_3{}^tBu$ (291 mg, 1.50 mmol, 3.00 equiv.), 2-picolinic acid (**2**) (3.1 mg, 0.025 mmol, 5.0 mol %), $FeCl_3 \cdot 6H_2O$ (6.8 mg, 0.025 mmol, 5.0 mol %), NaCN (29 mg, 0.60 mmol, 1.2 equiv.), 1.7 mL pyridine (dried over activated MS 4Å prior to use), and 99 µL H_2O (99 mg, 5.5 mmol, 11 equiv) were reacted at 50 °C for 24 h. After the reaction time was completed, the vial was removed from the heating block and the mixture was allowed to cool to room temperature. 10 µL of PhCl of were added as internal GC standard. 5 drops of the resulting mixture were diluted to a total volume of 2 mL with EtOAc and the yield (16 ± 2%) of cyanated product **9** was determined by calibrated GC analysis.

5.10.2 Optimized Procedure for Amine α-C-H Cyanation

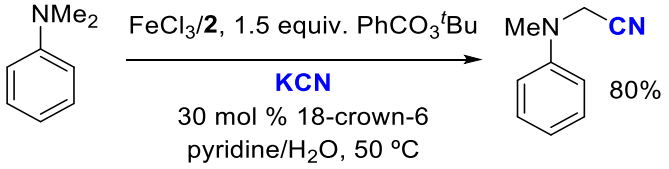

In analogy to the representative procedure for amide synthesis, *N*,*N*-dimethyl aniline (61 mg, 0.50 mmol, 1.00 equiv.), $PhCO_3{}^tBu$ (146 mg, 0.75 mmol, 1.50 equiv.), 2-picolinic acid (**2**) (3.1 mg, 0.025 mmol, 5.0 mol %), $FeCl_3 \cdot 6H_2O$ (6.8 mg, 0.025 mmol, 5.0 mol %), 1.7 mL pyridine (dried over activated MS 4Å prior to use), H_2O (108 mg, 6.0 mmol, 12 equiv.), KCN (39.1 mg, 0.6 mmol, 1.2 equiv.).) and 18-crown-6 (48 mg 0.15 mmol, 30 mol %) were reacted at 50 °C for 24 h. The solvent was

evaporated in vacuum (oil pump). Then, 0.5 ml of an NMR standard solution (100 mg 1,3-dinitrobenzene in 10 mL $CDCl_3$), corresponding to 5 mg 1,3-dinitrobenzene as internal NMR standard, was added to dissolve the reaction mixture. After filtration, the product yield was determined by quantitative ^1H NMR analysis: The amount of product was determined by integration of the NMR signals at 8.56 ppm (2 H, 1,3-dinitrobenzene) and 4.20 ppm (2 H, $PhN(CH_3)CH_2CN$).

5.11 Procedure Oxidation of Complex Molecules

5.11.1 Oxidation of Lidocaine

In analogy to the representative procedure for amide synthesis, 2-picolinic acid (3.1 mg, 0.025 mmol, 5.0 mol %), 1.80 mL (equivalent to 0.025 mmol, 5.0 mol % of $FeCl_3$) of a standard solution of $FeCl{\cdot}6H_2O$ (94 mg, 0.35 mmol) in 25 mL pyridine, $PhCO_3{}^tBu$ (280 µL, 291 mg, 1.50 mmol, 3.00 equiv), deionizied H_2O (81 µL, 81 mg, 4.5 mmol, 9.0 equiv.), and Lidocaine (118 mg, 0.50 mmol, 1.0 equiv.) were reacted at 50 ºC for 24 h. After the reaction time was complete, the vial was taken off the heating block and the mixture was allowed to cool to room temperature. The reaction mixture was diluted in 20 mL MeOH (ultra pure, HPLC grade, 99.8+ %) and analyzed by LCMS without further workup.

5.12 Procedure for Method of Initial Rates

5.12.1 Representative Procedure for Method of Initial Rates

To a 20 mL scintillation vial equipped with a Teflon-coated stirbar, $FeCl_3{\cdot}6H_2O$ (34 mg, 125 µmol, 5.0 mol %), picolinic acid (15 mg, 125 µmol, 5.0 mol %), pyridine (15 mL; 1.2 mM H_2O) and then deionizied water (406 µL, 406 mg, 22.5 mmol, 9 eq.) was added. Three drops of mineral oil were placed in the bottom of a vial heating block well to improve heat transfer. The solution vial was pressed into the vial well and twisted to maximize oil contact. The reaction was vigorously stirred (1500 rpm) to maximize heat transfer. The ReactIR 15 probe (see Materials and Methods) was then inserted into the open-top reaction vial and IR analysis was initiated. IR scans were

taken at 15 s intervals. NPr_3 and $PhCO_3{}^tBu$, along with the solution, were preheated to 50 °C on the heating block. Reaction temperature was monitored using the IR probe. Once thermal equilbrium was reached at 50 °C, $PhCO_3{}^tBu$ (1.4 mL, 1.5 g, 7.5 mmol) was transferred to the reaction vial using a volumetric syringe. The concentration of $PhCO_3{}^tBu$ was monitored by selecting the IR band at ν =1757 cm^{-1} (C=O stretch). This IR band was unobscured by other bands in the spectrum; solvent subtraction was not performed. Once a steady signal was reached, NPr_3 (476 μL, 358 mg, 2.5 mmol) was quickly added to the reaction. IR analysis was conducted to generate the spectra below.

From the experiments described in the previous paragraph, absorbance (ν =1757 cm^{-1}; C=O stretch) was plotted against reaction time and the maximum slope (–[$PhCO_3{}^tBu$]) was determined. These reaction rates (slopes) were then plotted against equivilents analyte reagent.

$$\text{rate} = -\frac{d[R]}{dt} = \frac{d[P]}{dt} \qquad (Eq.1)$$

Equation 1: Relationship Between Reaction Rate and Concentration of Reactants/Products.

5.12.2 Kinetic Order in NPr_3

In analogy to the general procedure for method of initial rates, $FeCl_3 \cdot 6H_2O$ (34 mg, 125 μmol, 5.0 mol %), picolinic acid (15 mg, 125 μmol, 5.0 mol %), pyridine (15 mL) and then deionized H_2O (406 μL, 406 mg, 22.5 mmol, 9 eq.) was added to a 20 mL scintillation vial equipped with a microstirbar. The reaction mixture was heated to 50 °C on a pre-heated vial plate and vigorously stirred (1500 rpm). The ReactIR15 probe (see Materials and Methods) was inserted into the reaction vial and IR analysis was initiated. Subsequently, preheated $PhCO_3{}^tBu$ (1.4 mL, 1.5 g, 7.5 mmol) and then NPr_3 (Table 9) were added to the reaction. IR analysis was conducted for 4 h to generate the spectra below (Figure 2 below). The spectra were generated by monitoring $PhCO_3{}^tBu$ (ν =1757 cm^{-1}; C=O stretch) using the Mettler Toledo iC IR software.

Table 9: Dependence of Maximum Reaction Rate on NPr_3 Loading.

Entry	Eq. NPr_3	$-k_{obs}$ [$PhCO_3{}^tBu$]
1	0.25	2.86 ± 0.4
2	0.5	4.44 ± 0.3
3	0.75	5.84 ± 0.1
4	1	7.63 ± 0.1

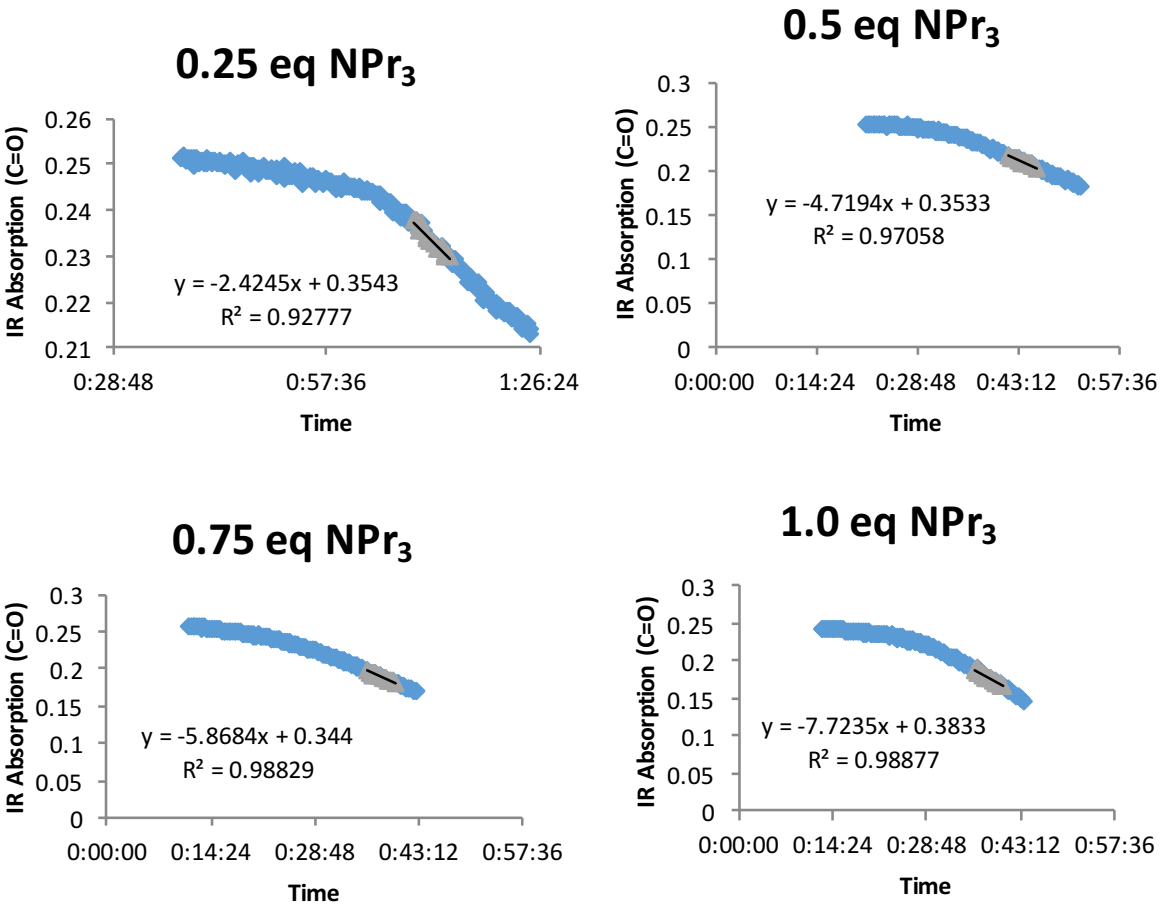

Figure 2: Decrease of [PhCO3tBu] versus Time for Different [NPr3].

5.12.3 Kinetic Order in $PhCO_3{}^tBu$

In analogy to the general procedure for method of initial rates, $FeCl_3 \cdot 6H_2O$ (34 mg, 125 μmol, 5.0 mol %), picolinic acid (15 mg, 125 μmol, 5.0 mol %), pyridine (15 mL) and then deionized H_2O (406 μL, 406 mg, 22.5 mmol, 9 eq.) was added to a 20 mL scintillation vial equipped with a microstirbar. The reaction mixture was heated to 50 °C on a pre-heated vial plate and vigorously stirred (1500 rpm). The ReactIR15 probe (see Materials and Methods) was inserted into the reaction vial and IR analysis

was initiated. Subsequently, preheated $PhCO_3{}^tBu$ (Table 10) and then NPr_3 (476 μL, 358 mg, 2.5 mmol) were added to the reaction. IR analysis was conducted for 4 h to generate the spectra below (Figure 3 below). The spectra were generated by monitoring $PhCO_3{}^tBu$ (ν =1757 cm^{-1}; C=O stretch) using the Mettler Toledo iC IR software.

Table 10: Dependence of Maximum Reaction Rate on $PhCO_3{}^tBu$ Loading.

Entry	Eq. $PhCO_3{}^tBu$	$-k_{obs}$ [$PhCO_3{}^tBu$]
1	1.0	3.5 ± 0.1
2	2.0	5.6 ± 0.4
3	3.0	7.55 ± 0.3
4	4.0	10.0 ± .2

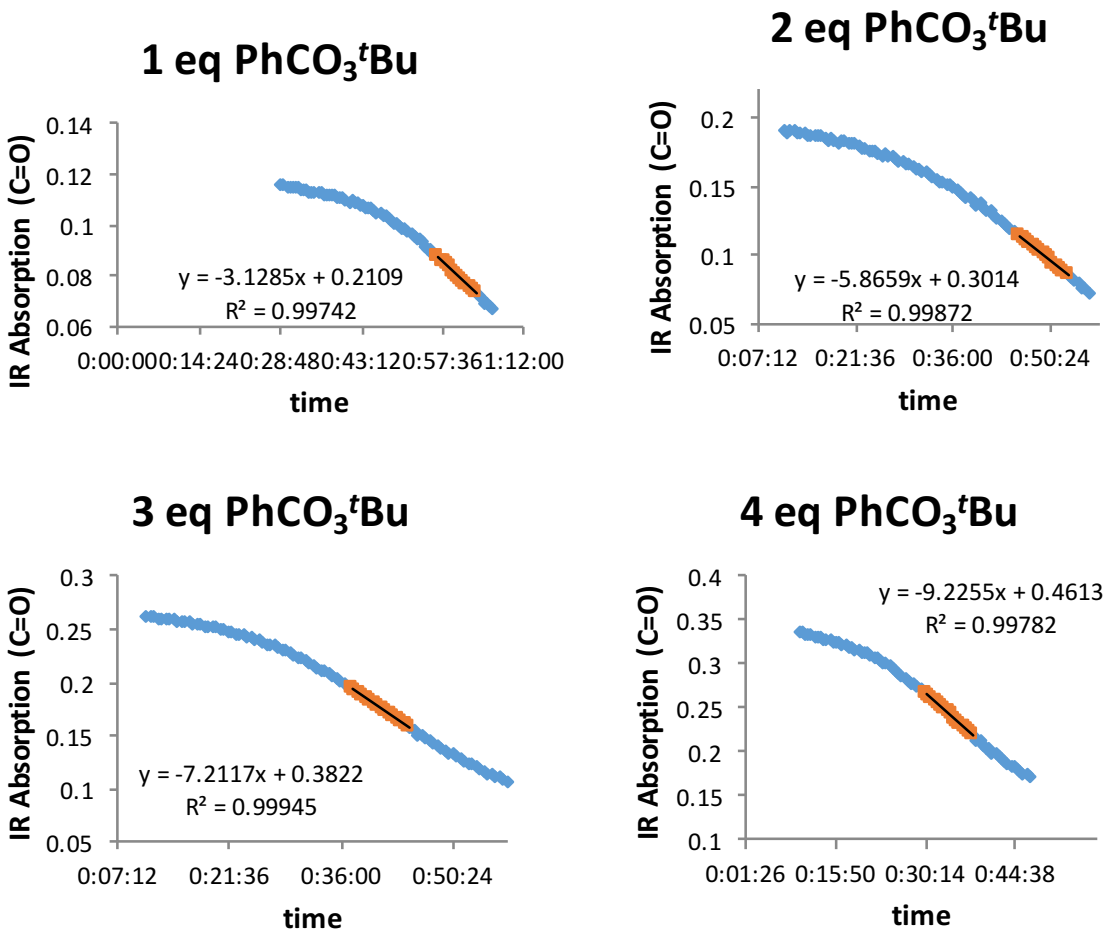

Figure 3: Decrease of [PhCO3tBu] versus Time for Different [PhCO3tBu].

5.12.4 Kinetic Order in H_2O

In analogy to the general procedure for method of initial rates, $FeCl_3 \cdot 6H_2O$ (34 mg, 125 μmol, 5.0 mol %), picolinic acid (15 mg, 125 μmol, 5.0 mol %), pyridine (15 mL) and then deionized H_2O (Table 11) was added to a 20 mL scintillation vial equipped with a microstirbar. The reaction mixture was heated to 50 °C on a pre-heated vial plate and vigorously stirred (1500 rpm). The ReactIR15 probe (see Materials and Methods) was inserted into the reaction vial and IR analysis was initiated. Subsequently, preheated $PhCO_3{}^tBu$ (1.4 mL, 1.5 g, 7.5 mmol) and then NPr_3 (476 μL, 358 mg, 2.5 mmol) were added to the reaction. IR analysis was conducted for 4 h to generate the spectra below (Figure 4 below). The spectra were generated by monitoring $PhCO_3{}^tBu$ (ν =1757 cm^{-1}; C=O stretch) using the Mettler Toledo iC IR software.

Table 11: Dependence of Maximum Reaction Rate on H_2O Loading.

Entry	Eq. H_2O	$-k_{obs}$ [$PhCO_3{}^tBu$]
1	0.4	23.3 ± 0.5
2	0.8	19.4 ± 0.3
3	1.25	16.8 ± 0.2
4	1.6	16.6 ± 0.1
5	2.0	16.2 ± 0.4
6	2.5	13.7 ± 1.3
7	5.0	12.5 ± 0.4
8	7.5	10.9 ± 1.2
9	10.0	9.8 ± 0.1
10	12.5	9.4 ± 0.1
11	15.0	9.1 ± 0.6
12	20.0	7.2 ± 0.2

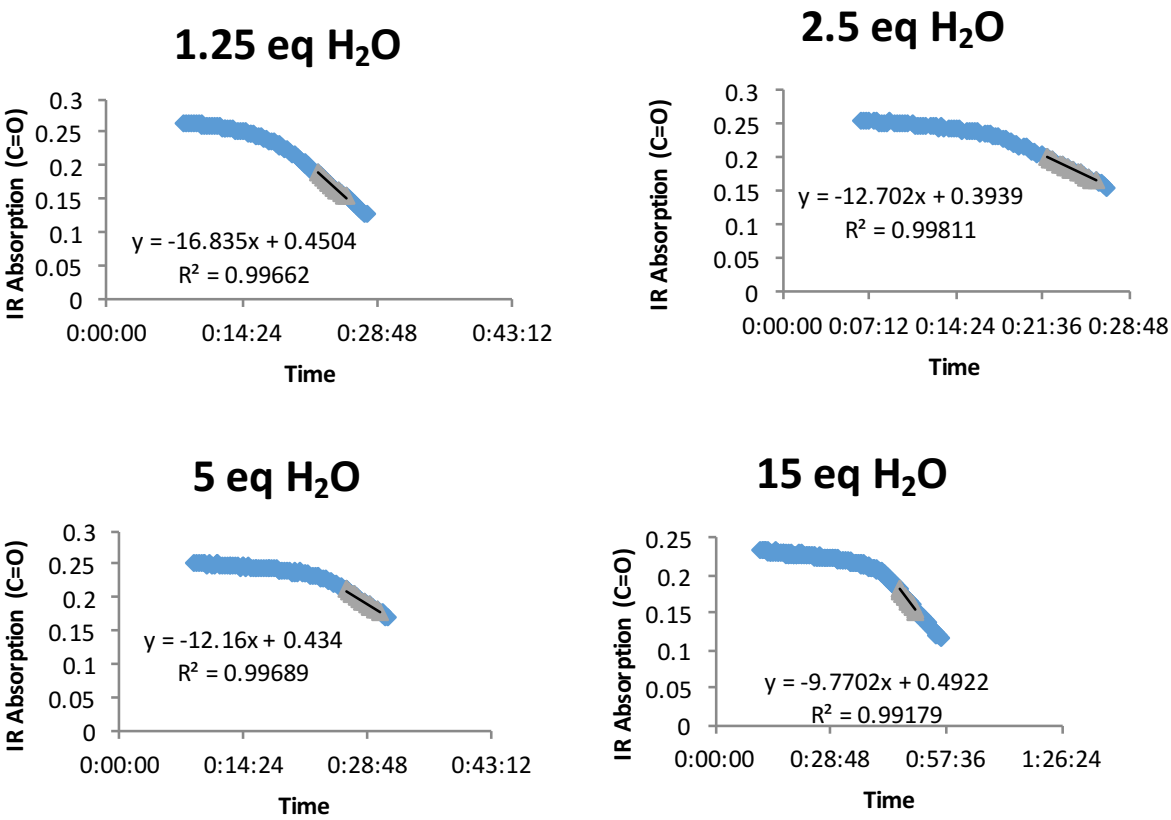

Figure 4: Examples of Decrease of [PhCO3tBu] versus Time for Selected [H2O].

5.12.5 Kinetic Order in $FeCl_3 \cdot 6H_2O$/Picolinic Acid (1:1)

In analogy to the general procedure for method of initial rates, $FeCl_3 \cdot 6H_2O$ (Table 12), picolinic acid (Table 12), pyridine (15 mL) and then deionized H_2O (406 µL, 406 mg, 22.5 mmol, 9 eq.) was added to a 20 mL scintillation vial equipped with a microstirbar. The reaction mixture was heated to 50 °C on a pre-heated vial plate and vigorously stirred (1500 rpm). The ReactIR15 probe (see Materials and Methods) was inserted into the reaction vial and IR analysis was initiated. Subsequently, preheated $PhCO_3{}^tBu$ (1.4 mL, 1.5 g, 7.5 mmol) and then NPr_3 (476 µL, 358 mg, 2.5 mmol) were added to the reaction. IR analysis was conducted for 4 h to generate the spectra below (Figure 5). The spectra were generated by monitoring $PhCO_3{}^tBu$ (ν =1757 cm^{-1}; C=O stretch) using the Mettler Toledo iC IR software.

Table 12: Dependence of Maximum Reaction Rate on $FeCl_3$/picolinic acid (1:1) Loading.

Entry	mol % Fe/picH (1:1)	$-k_{obs}$ [$PhCO_3{}^tBu$]
1	0.5	7.2 ± 0.2
2	1.5	9.2 ± 0.3
3	2	9.8 ± 0.1
4	3	10.5 ± 0.1
5	5	10.8 ± 0.3
6	7	11.3 ± 0.1
7	10	11.6 ±0.2
8	17	12.4 ± 0.4
9	25	8.2 ± 0.4
10	32	7.0 ± 0.2
11	40	4.2 ± 0.1

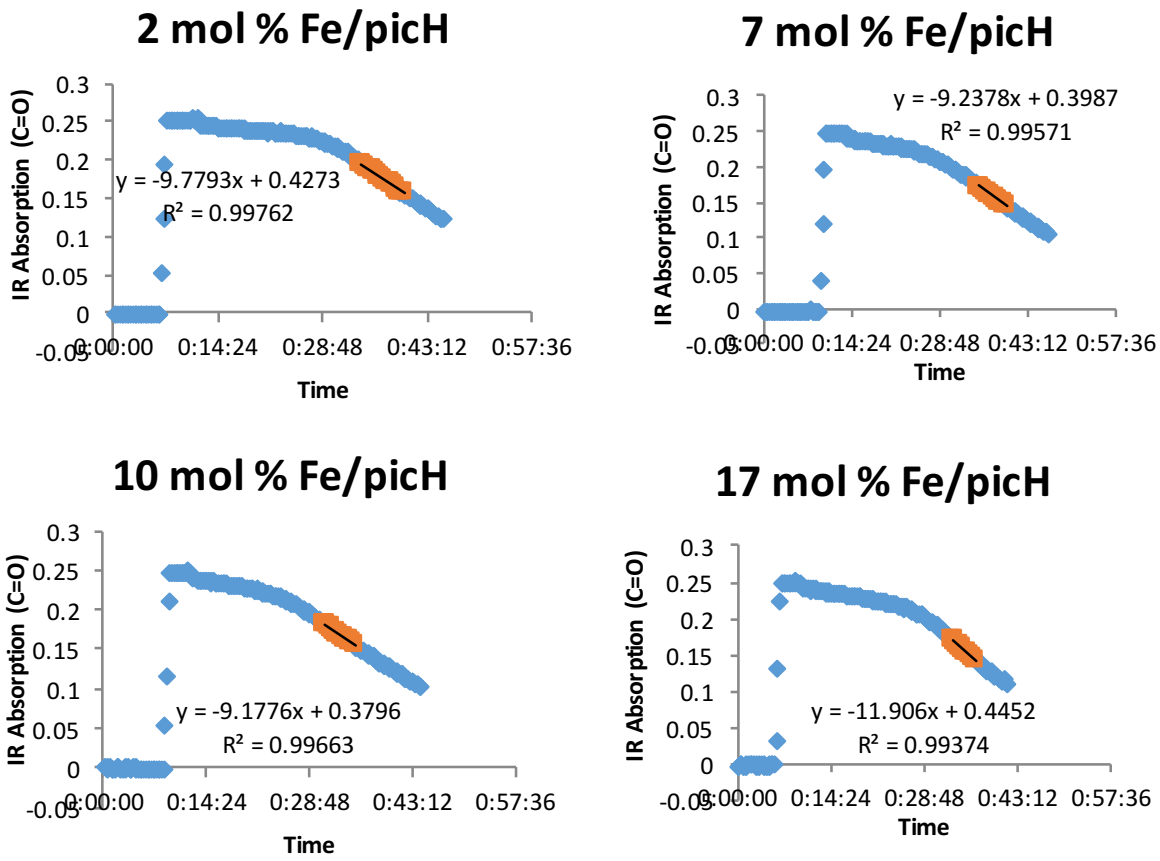

Figure 5: Examples of Decrease of [PhCO3tBu] versus Time for Selected [$FeCl_3$/2-picolinic acid] (1:1).

5.12.6 Optimization of 2-Picolinic Acid Loading

In analogy to the general procedure for method of initial rates, $FeCl_3 \cdot 6H_2O$ (34 mg, 125 μmol, 5.0 mol %), picolinic acid (Table 13), pyridine (15 mL) and then deionized H_2O (406 μL, 406 mg, 22.5 mmol, 9 eq.) was added to a 20 mL scintillation vial equipped with a microstirbar. The reaction mixture was heated to 50 °C on a pre-heated vial plate and vigorously stirred (1500 rpm). The ReactIR15 probe (see Materials and Methods) was inserted into the reaction vial and IR analysis was initiated. Subsequently, preheated $PhCO_3{}^tBu$ (1.4 mL, 1.5 g, 7.5 mmol) and then NPr_3 (476 μL, 358 mg, 2.5 mmol) were added to the reaction. IR analysis was conducted for 4 h to generate the spectra below (Figure 6). The spectra were generated by monitoring $PhCO_3{}^tBu$ (ν =1757 cm^{-1}; C=O stretch) using the Mettler Toledo iC IR software.

Table 13: Dependence of Maximum Reaction Rate on Loading of 2-Picolinic Acid at 5 mol % $FeCl_3$ Loading.

Entry	Mol %. PicH	$-k_{obs}$ [$PhCO_3{}^tBu$]
1	0.5	9.5 ± 0.4
2	1.0	10.8 ± 0.3
3	1.5	10.4 ± 0.3
4	2.0	9.8 ± 0.2

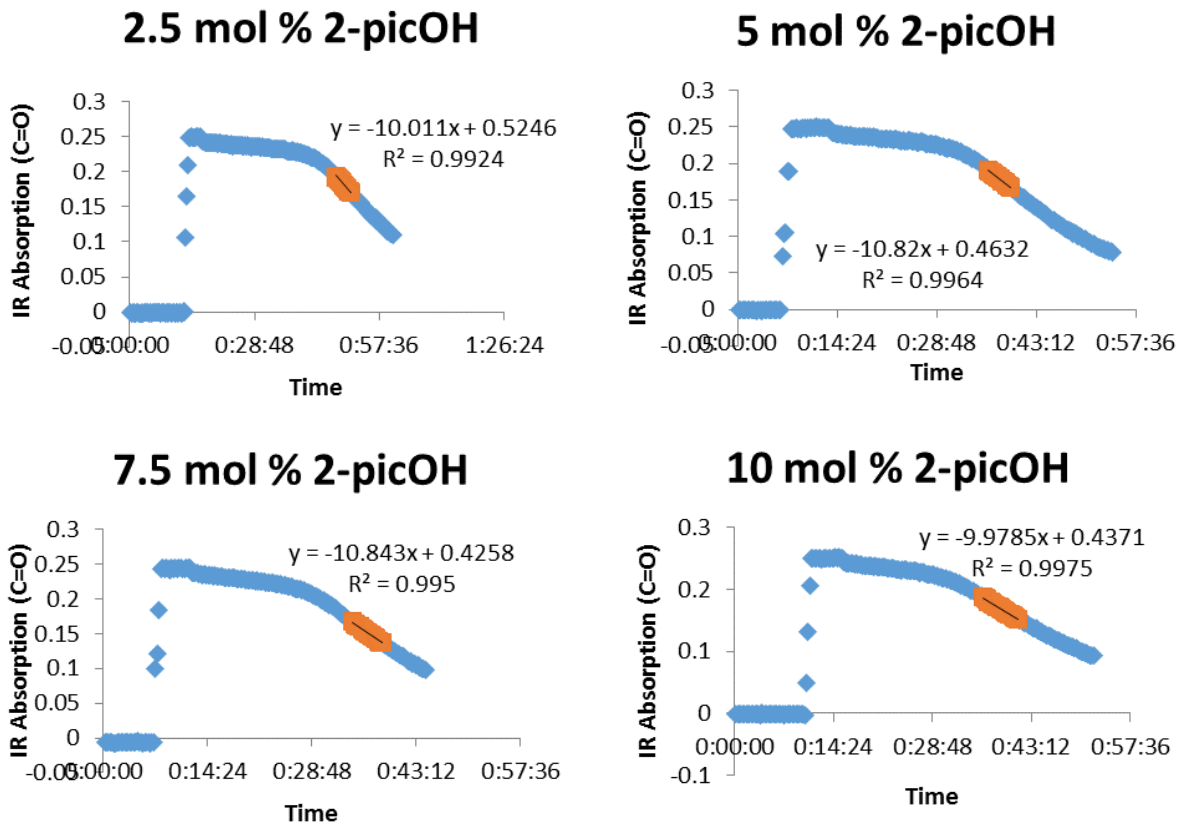

Figure 6: Decrease of [PhCO3tBu] versus Time for Different 2-Picolinic Acid Loadings (Fe Loading 5.0 mol %).

5.12.7 Kinetic Order in $PhCO_2H$

In analogy to the general procedure for method of initial rates, $FeCl_3 \cdot 6H_2O$ (34 mg, 125 µmol, 5.0 mol %), picolinic acid (15 mg, 125 µmol, 5.0 mol %), $PhCO_2H$ (Table 14), pyridine (15 mL) and then deionized H_2O (406 µL, 406 mg, 22.5 mmol, 9 eq.) was added to a 20 mL scintillation vial equipped with a microstirbar. The reaction mixture was heated to 50 °C on a pre-heated vial plate and vigorously stirred (1500 rpm). The ReactIR15 probe (see Materials and Methods) was inserted into the reaction vial and IR analysis was initiated. Subsequently, preheated $PhCO_3{}^tBu$ (1.4 mL, 1.5 g, 7.5 mmol) and then NPr_3 (476 µL, 358 mg, 2.5 mmol) were added to the reaction. IR analysis was conducted for 4 h to generate the spectra below (Figure 7

below). The spectra were generated by monitoring $PhCO_3{}^tBu$ (ν =1757 cm^{-1}; C=O stretch) using the Mettler Toledo iC IR software.

Table 14: Dependence of Maximum Reaction Rate on $PhCO_2H$ Addition.

Entry	Eq. $PhCO_2H$	$-k_{obs}$ [$PhCO_3{}^tBu$]
1	1.0	7.2 ± 1.6
2	2.0	5.0 ± 0.6
3	3.0	4.1 ± 0.7
4	4.0	2.6 ± 0.4

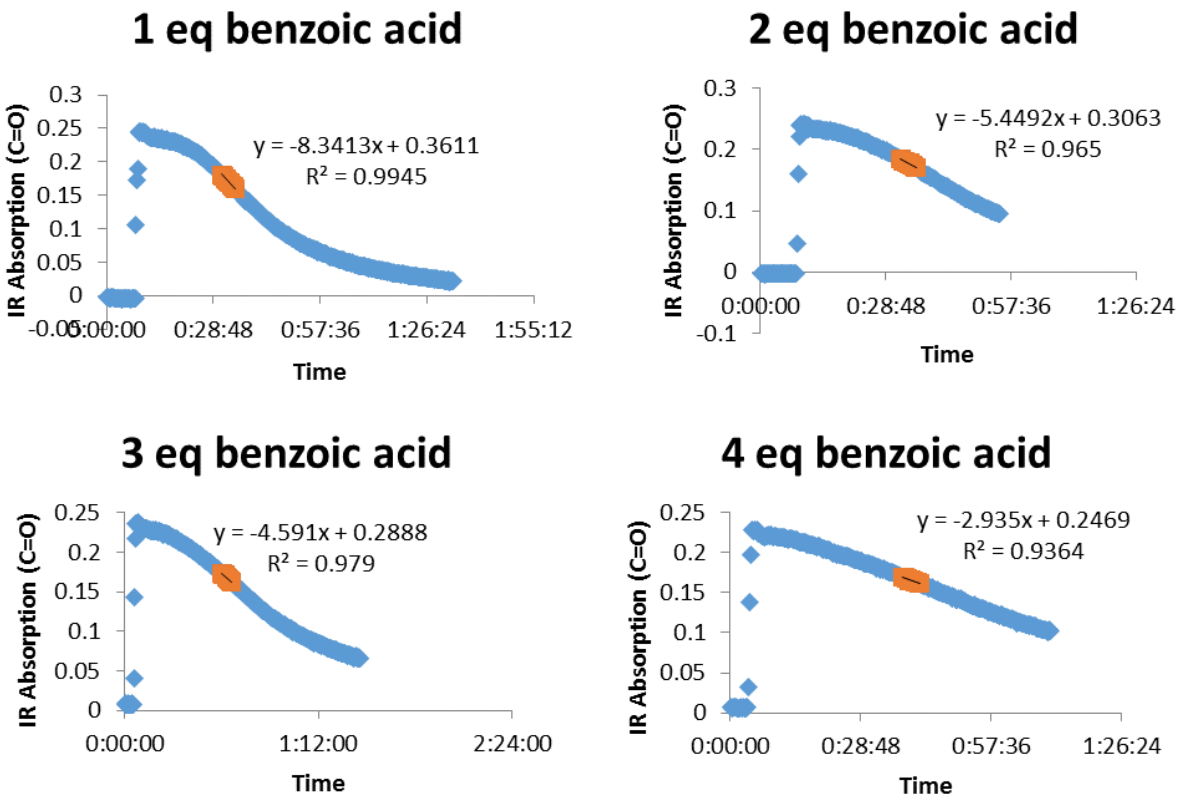

Figure 7: Decrease of [PhCO3tBu] versus Time for Selected PhCO2H Loadings.

5.12.8 Kinetic Order in ^{t}BuOH

In analogy to the general procedure for method of initial rates, $FeCl_3 \cdot 6H_2O$ (34 mg, 125 μmol, 5.0 mol %), picolinic acid (15 mg, 125 μmol, 5.0 mol %), pyridine (15 mL), deionized H_2O (406 μL, 406 mg, 22.5 mmol, 9 eq.) and then ^{t}BuOH (Table 15) was added to a 20 mL scintillation vial equipped with a microstirbar. The reaction

mixture was heated to 50 °C on a pre-heated vial plate and vigorously stirred (1500 rpm). The ReactIR15 probe (see Materials and Methods) was inserted into the reaction vial and IR analysis was initiated. Subsequently, preheated $PhCO_3{}^tBu$ (1.4 mL, 1.5 g, 7.5 mmol) and then NPr_3 (476 µL, 358 mg, 2.5 mmol) were added to the reaction. IR analysis was conducted for 4 h to generate the spectra below (Figure 8 below). The spectra were generated by monitoring $PhCO_3{}^tBu$ (ν =1757 cm^{-1}; C=O stretch) using the Mettler Toledo iC IR software.

Table 15: Dependence of Maximum Reaction Rate on tBuOH Addition.

Entry	Eq. ^{t}BuOH	$-k_{obs}$ [$PhCO_3{}^tBu$]
1	1.0	7.3 ± 1.2
2	2.0	7.2 ± 1.4
3	3.0	7.1 ± 1.5
4	4.0	6.9 ± 0.3

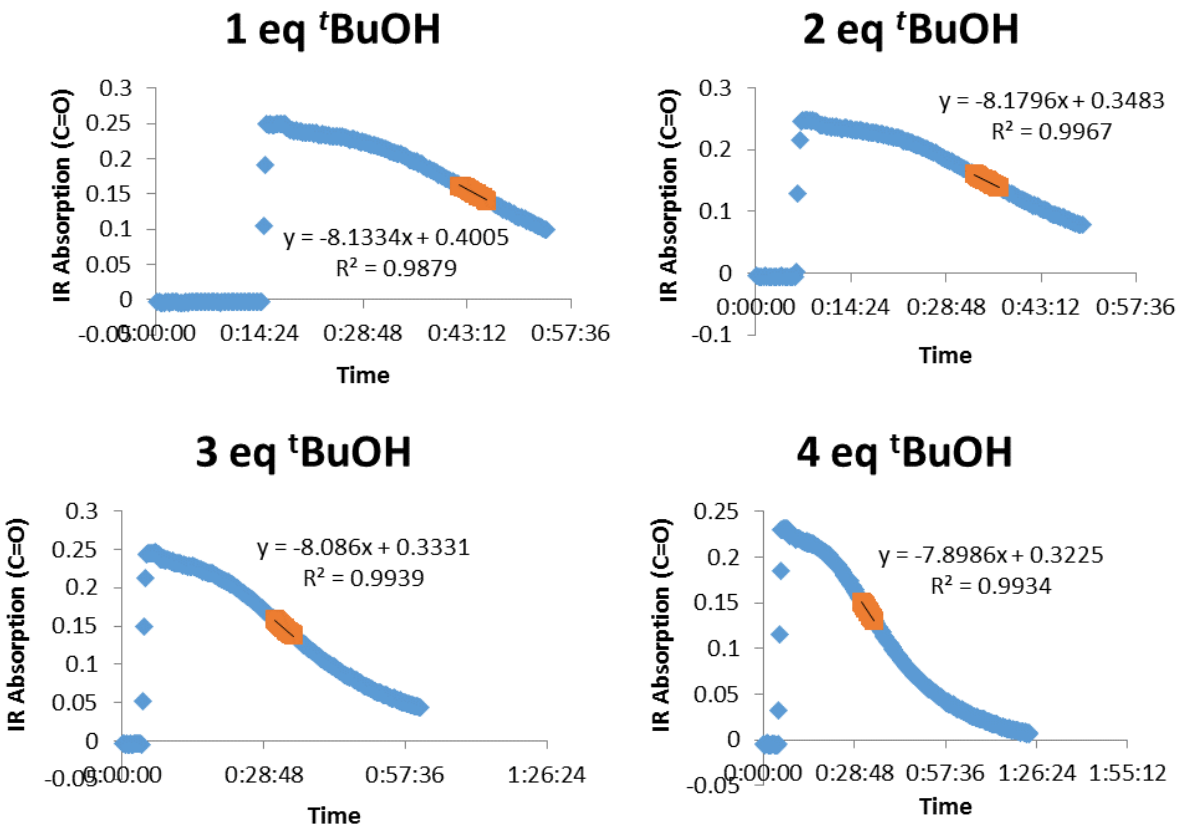

Figure 8: Decrease of [$PhCO_3{}^tBu$] versus Time for Selected ^{t}BuOH Loadings.

5.12.9 Kinetic Order in Fe Salts

In analogy to the general procedure for method of initial rates, Fe salt (Table 16), picolinic acid (15 mg, 125 μmol, 5.0 mol %), pyridine (15 mL) and then deionized H_2O (406 μL, 406 mg, 22.5 mmol, 9 eq.) was added to a 20 mL scintillation vial equipped with a microstirbar. The reaction mixture was heated to 50 °C on a pre-heated vial plate and vigorously stirred (1500 rpm). The ReactIR15 probe (see Materials and Methods) was inserted into the reaction vial and IR analysis was initiated. Subsequently, preheated $PhCO_3{}^tBu$ (1.4 mL, 1.5 g, 7.5 mmol) and then NPr_3 (476 μL, 358 mg, 2.5 mmol) were added to the reaction. IR analysis was conducted for 4 h to generate the spectra below (Figure 9 and 10). The spectra were generated by monitoring $PhCO_3{}^tBu$ (ν =1757 cm^{-1}; C=O stretch) using the Mettler Toledo iC IR software.

Table 16: Dependence of Maximum Reaction Rate on Identity of Fe(III) Salt.

Entry	Fe Salt	Loading (mol %)	Pk_a of Corresponding Acid	$-k_{obs}$ [$PhCO_3{}^tBu$]
1	Fe(OTf)	5.0	-14.7	7.1 ± 0.1
2	$FeCl_3{\cdot}6H_2O$	5.0	-8	6.9 ± 0.1
3	$Fe(NO_3)_3$	5.0	-1.3	8.1 ± 0.3
4	$Fe_2(SO_4)_3$	2.5	2.0	7.6 ± 0.3
5	Fe(acac)	5.0	9.8	8.0 ± 0.2

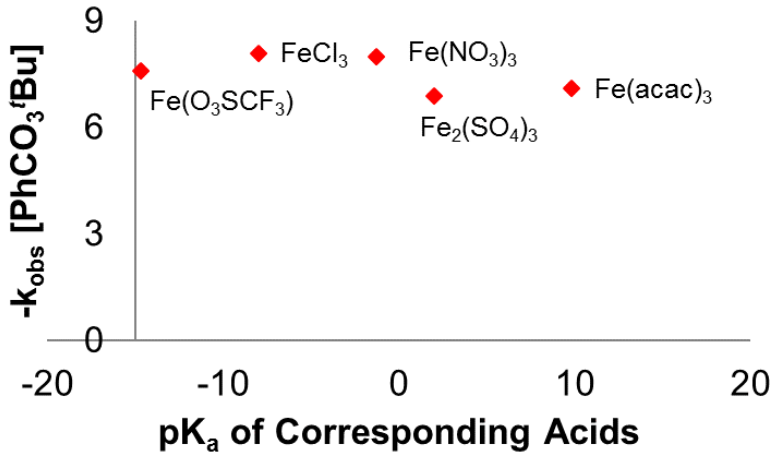

Figure 9: Maximum Reaction Rate versus pKa of Corresponding Acid for different X-type Ligands.

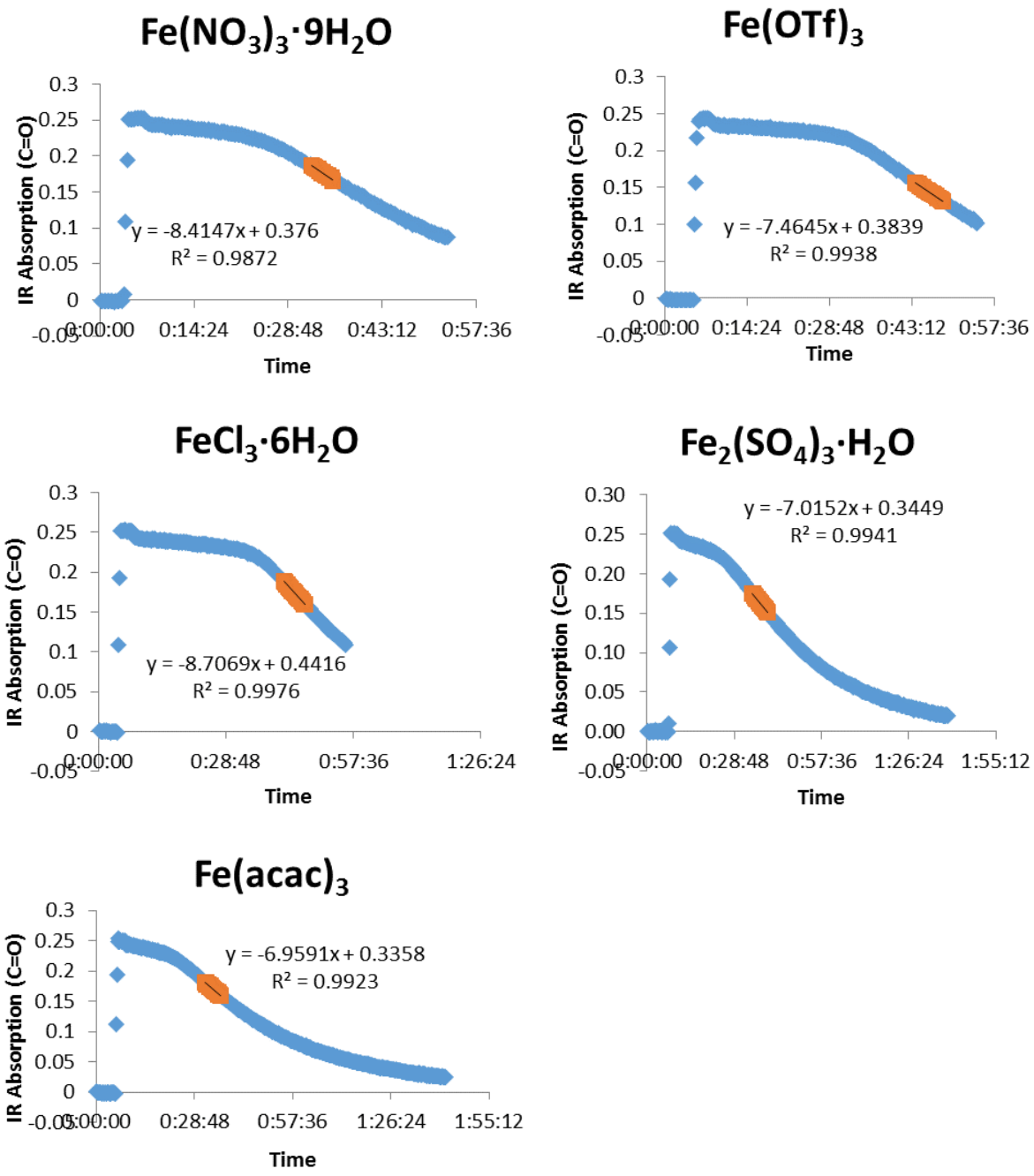

Figure 10: Decrease of [$PhCO_3{}^tBu$] versus Time for Different Fe(III) Catalyst Precursors.

5.12.10 Kinetic Isotope Effect

In analogy to the general procedure for method of initial rates, $FeCl_3 \cdot 6H_2O$ (17 mg, 62.5 μmol, 5.0 mol %), picolinic acid (8 mg, 62.5 μmol, 5.0 mol %), pyridine (8 mL), and then deionized H_2O (203 μL, 203 mg, 11.3 mmol, 9 eq.) was added to a 20 mL scintillation vial equipped with a microstirbar. The reaction mixture was heated to

50 °C on a pre-heated vial plate and vigorously stirred (1500 rpm). The ReactIR15 probe (see Materials and Methods) was inserted into the reaction vial and IR analysis was initiated. Subsequently, preheated $PhCO_3{}^tBu$ (700 µL, 728 mg, 3.8 mmol) and then substrate (Table 17) were added to the reaction. IR analysis was conducted for 4 h to generate the spectra below (Figure 11). The spectra were generated by monitoring $PhCO_3{}^tBu$ (ν =1757 cm^{-1}; C=O stretch) using the Mettler Toledo iC IR software.

Table 17: Maximum Reaction Rates for NEt_3 and D_{15}-NEt_3.

Entry	Substrate	Loading	$-k_{obs}$ [$PhCO_3{}^tBu$]
1	NEt_3	174 µL, 126 mg, 1.25 mmol, 5 mol %	14.2 ± 0.1
2	NEt_3-D_{15}	175 µL, 145 mg, 1.25 mmol, 5 mol %	8.2 ± 0.1

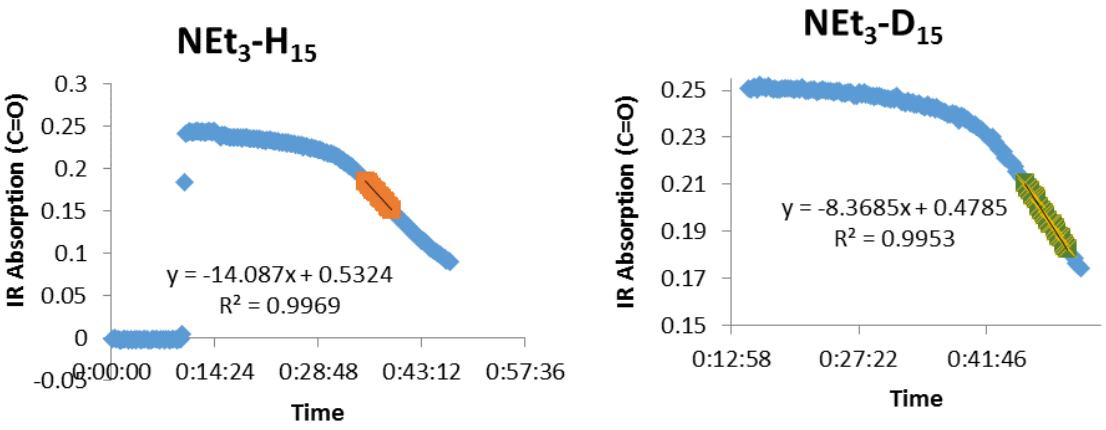

Figure 11: Decrease of [$PhCO_3{}^tBu$] versus Time for NEt_3 and NEt_3-D_{15}.

5.12.11 Dependence of Initiation Period Length on Order of Reagent Addition

In analogy to the general procedure for method of initial rates, $FeCl_3$·6H2O (34 mg, 125 mol, 5.0 mol %), picolinic acid (15 mg, 125 mol, 5.0 mol %), pyridine (15 mL), and then deionized H2O (406 µL, 406 mg, 22.5 mmol, 9 eq.) was added to a 20 mL scintillation vial equipped with a microstirbar. The reaction mixture was heated to 50 °C on a pre-heated vial plate and vigorously stirred (1500 rpm). The ReactIR 15 probe (see Materials and Methods) was inserted into the reaction vial and IR analysis was initiated. Subsequently, preheated NPr_3 (476 µL, 358 mg, 2.5 mmol) and then

$PhCO_3{}^tBu$ (1.4 mL, 1.5 g, 7.5 mmol) were added to the reaction (Table 18, Entry 2). Alternatively, the originally used order of reagent addition was used: first preheated $PhCO_3{}^tBu$ (1.4 mL, 1.5 g, 7.5 mmol) and then preheated NPr_3 (476 µL, 358 mg, 2.5 mmol; see entry 1, Table 18).

IR analysis was conducted to generate the reaction process traces shown below (Figure 12); temperature was recorded in addition to IR absorption (Figure 13). $-k_{obs}$ $[PhCO_3{}^tBu]$ was determined by determining the maximum slope of the reaction trace after the initiation period. The studies were repeated at least twice and the average values of $-k_{obs}$ $[PhCO_3{}^tBu]$ as well as the obtained standard deviations are tabulated in Table 18.

Table 18: Maximum Reaction Rates for Different Sequences of Oxidant/Substrate Addition.

Entry	**Addition Order**	**$-k_{obs}$ $[PhCO_3{}^tBu]$**
1	1.) $PhCO_3{}^tBu$; 2.) NPr_3	7.6 ± 0.1
2	1.) NPr_3; 2.) $PhCO_3{}^tBu$	99.0 ± 0.1

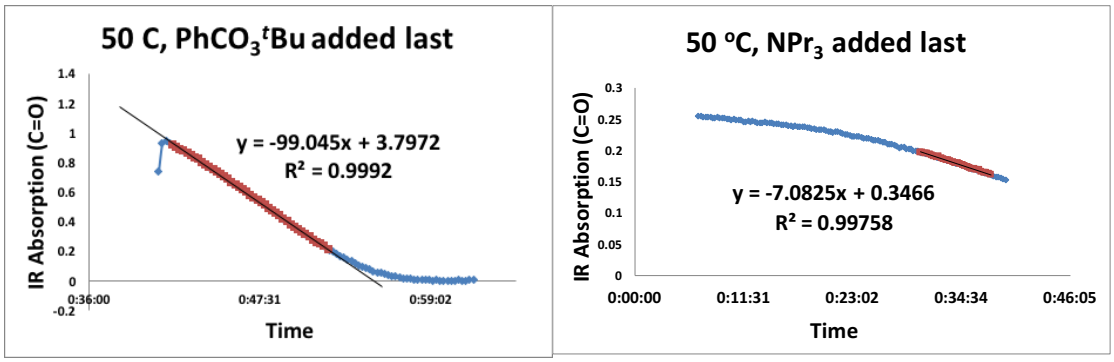

Figure 12: Decrease of $[PhCO_3{}^tBu]$ versus Time for Different Sequences of Oxidant/Substrate Addition.

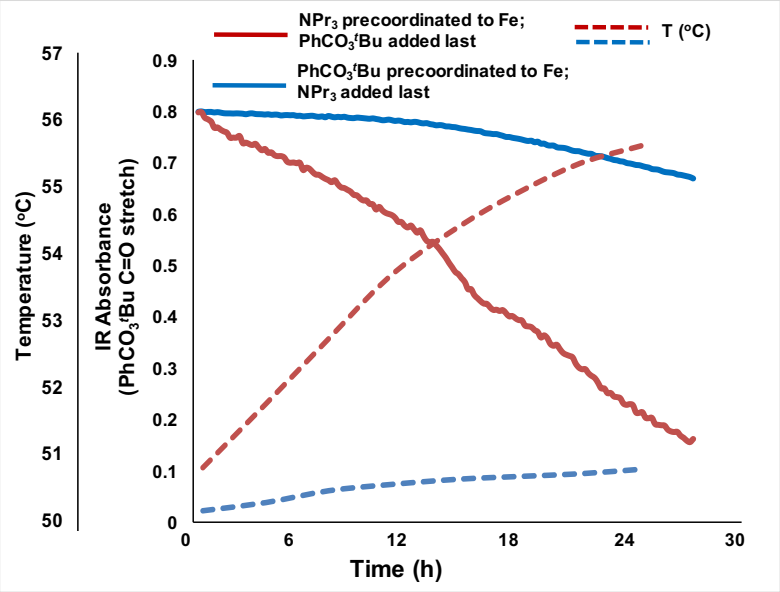

Figure 13: Decrease of [$PhCO_3{}^tBu$] versus Time and Development of Reaction Temperature versus Time for Different Sequences of Oxidation/Substrate Addition.

5.12.12 Procedure for Eyring Study

In analogy to the general procedure for method of initial rates, $FeCl_3 \cdot 6H_2O$ (34 mg, 125 μmol, 5.0 mol %), picolinic acid (15 mg, 125 μmol, 5.0 mol %), pyridine (15 mL), and then deionized H_2O (406 μL, 406 mg, 22.5 mmol, 9 eq.) was added to a 20 mL scintillation vial equipped with a microstirbar. The reaction mixture was heated (Table 19) on a pre-heated vial plate and vigorously stirred (1500 rpm). The ReactIR15 probe (see Materials and Methods) was inserted into the reaction vial and IR analysis was initiated. Subsequently, preheated $PhCO_3{}^tBu$ (1.4 mL, 1.5 g, 7.5 mmol) and then NPr_3 (476 μL, 358 mg, 2.5 mmol) were added to the reaction. IR analysis was conducted for 4 h to generate the spectra below (Figure 14 and 15). The spectra were generated by monitoring $PhCO_3{}^tBu$ (ν =1757 cm^{-1}; C=O stretch) using the Mettler Toledo iC IR software.

Table 19: Dependence of Maximum Reaction Rate on Temperature.

Entry	Temp (°C)	$-k_{obs}$ [$PhCO_3{}^tBu$]
1	40	4.6 ± 0.1
2	50	7.6 ± 0.1
3	60	17.5 ± 0.1
4	70	35.3 ± 0.1

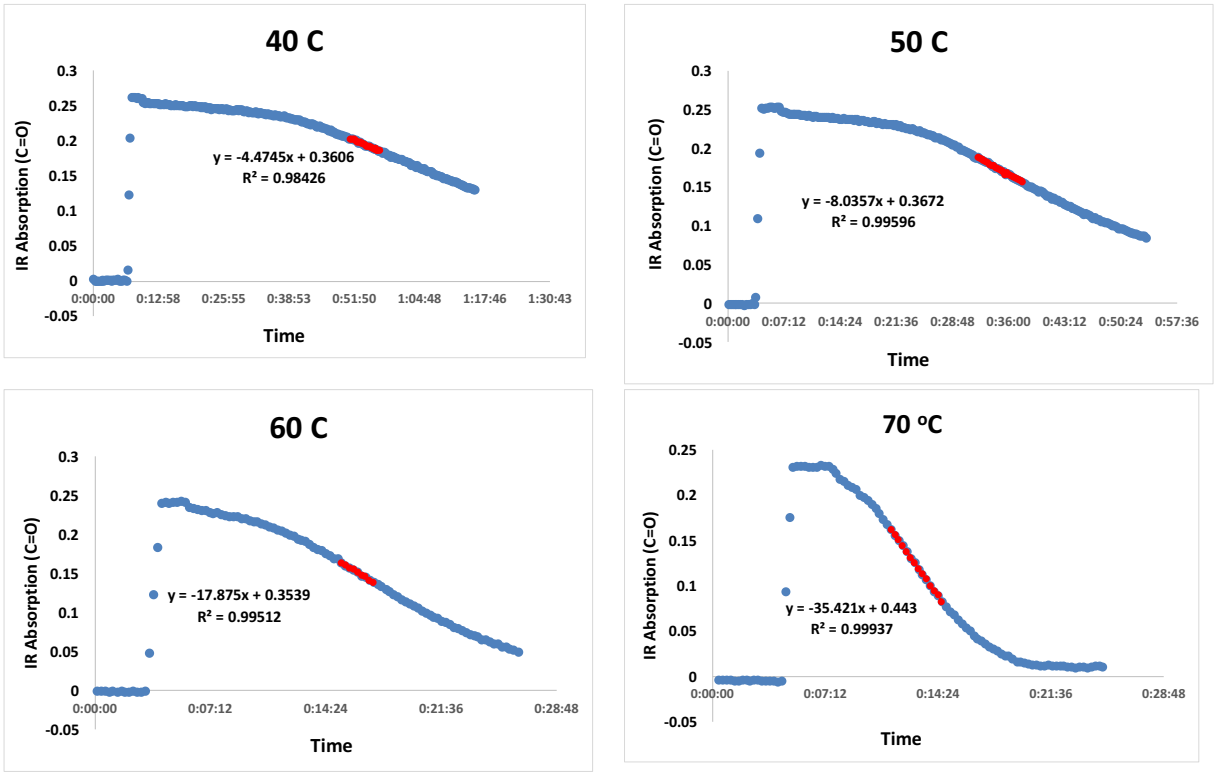

Figure 14: Decrease of [$PhCO_3{}^tBu$] versus Time for Different Temperatures.

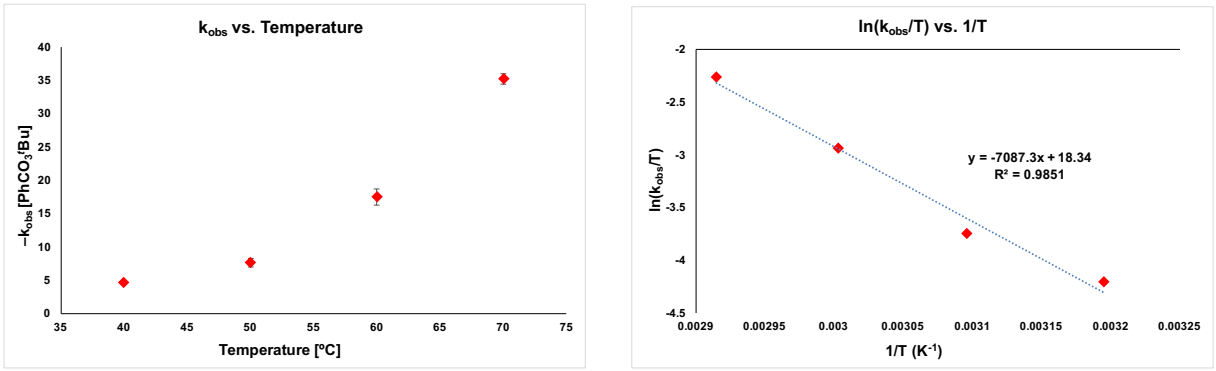

Figure 15: Plot of Rate versus Temperature (left); Plot of $\ln(k_{obs}/T)$ versus 1/T.

5.12.13 Procedure for Hammett Study

In analogy to the general procedure for method of initial rates, $FeCl_3 \cdot 6H_2O$ (34 mg, 125 μmol, 5.0 mol %), picolinic acid (15 mg, 125 μmol, 5.0 mol %), pyridine-type solvent (15 mL, see Table 20), and then deionized H_2O (406 μL, 406 mg, 22.5 mmol, 9 eq.) was added to a 20 mL scintillation vial equipped with a microstirbar. The reaction mixture was heated on a pre-heated vial plate and vigorously stirred (1500 rpm). The ReactIR15 probe (see Materials and Methods) was inserted into the reaction vial and IR analysis was initiated. Subsequently, preheated $PhCO_3{}^tBu$ (1.4 mL, 1.5 g, 7.5 mmol) and then NPr_3 (476 μL, 358 mg, 2.5 mmol) were added to the reaction. IR analysis was conducted for 4 h to generate the spectra below (Figure 16 and 17). The spectra were generated by monitoring $PhCO_3{}^tBu$ (ν =1757 cm^{-1}; C=O stretch) using the Mettler Toledo iC IR software.

Table 20: Dependence of Maximum Reaction Rate on Pyridine solvent.

Entry	Solvent	Hammett Constant σ_p (σ_m)	$-k_{obs}$ [$PhCO_3{}^tBu$]
1	4-MeO-py	-0.27	2.2 ± 0.1
2	4-CH_3-py	-0.17	3.7 ± 0.1
3	Py	0.0	7.6 ± 0.6
4	4-Cl-Py	+0.23	6.0 ± 0.1
5	3-F-Py	+0.34	5.6 ± 0.4
6	4-CF_3-py	+0.54	2.2 ± 0.7

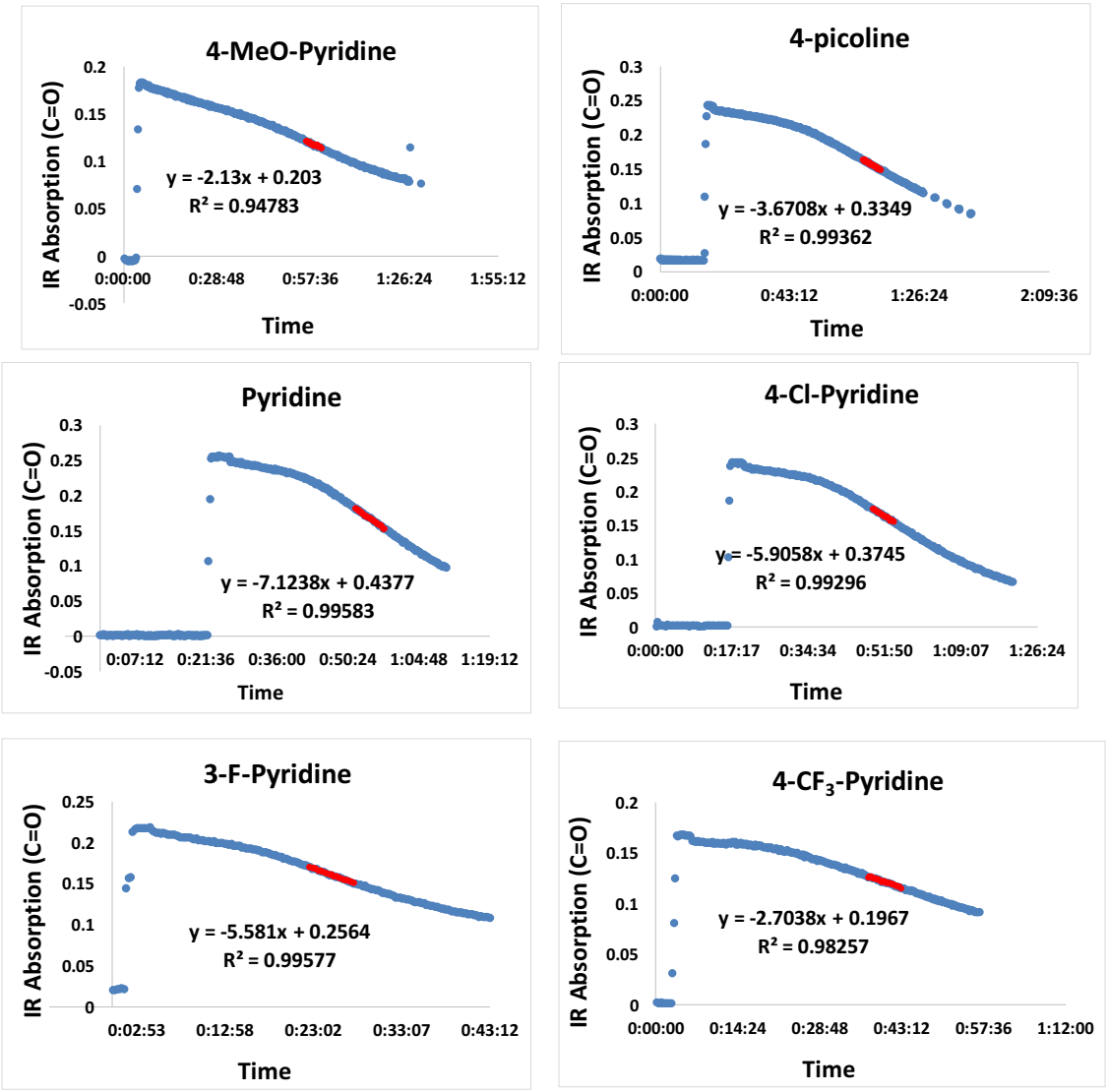

Figure 16: Decrease of [$PhCO_3{}^tBu$] versus Time for Different Pyridine Solvents.

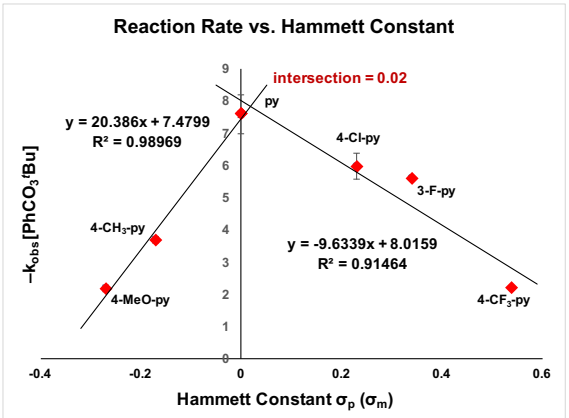

Figure 17: Plot of Rate versus Hammett Constant

5.13 Procedure for Catalyst Resting State Studies

5.13.1 Procedure for Reaction of 2-Picolinic Acid With $FeCl_3 \cdot 6H_2O$ in Pyridine

To a 20 mL scintillation vial equipped with a Teflon-coated stirbar, $FeCl_3 \cdot 6H_2O$ (270 mg, 1.0 mmol) and 12 mL pyridine were added. The solution was vigorously stirred (1500 rpm) at 25 °C. The ReactIR15 probe (see Materials and Methods) was inserted into the reaction vial and IR analysis was initiated. Subsequently, 250 µL aliquots (equivalent to 0.5 mmol, 0.5 equiv. 2-picolinic acid) of a standard solution of 2-picolinic acid (2.46 g, 20.0 mmol) in 10 mL pyridine were sequentially added in approximately 3 min. intervals (up to 4.5 equivs.). The spectra shown in Figure 18 were generated using the ConcIRT function of the iC IR software.

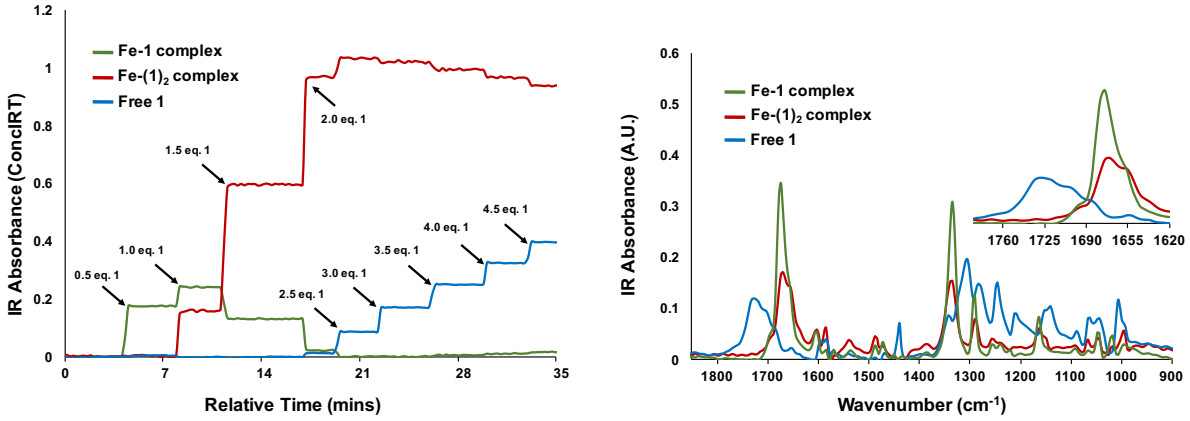

Figure 18: IR Absorbance for the Titration of Picolinic Acid into $FeCl_3$ in Pyridine.

5.13.2 Procedure for Background Reaction of Hydrochloric Acid With $FeCl_3 \cdot 6H_2O$ in Pyridine

To a 20 mL scintillation vial equipped with a Teflon-coated stirbar, $FeCl_3 \cdot 6H_2O$ (270 mg, 1.0 mmol) and 12 mL pyridine was added and vigorously stirred (1500 rpm) at 25 °C. The ReactIR15 probe (see Materials and Methods) was inserted into the reaction vial and IR analysis was initiated. Subsequently, 15 µL aliquots of hydrochloric acid (37% w/w, 18 mg, 0.5 mmol) were sequentially added (up to 2 equiv.) in approximately 3 min. intervals. Finally, 2 equiv. aliquots of picolinic acid

(246 mg, 2.00 mmol) were added (up to 4 equiv). The spectra shown in Figure 19 were generated using the ConcIRT function of the iC IR software.

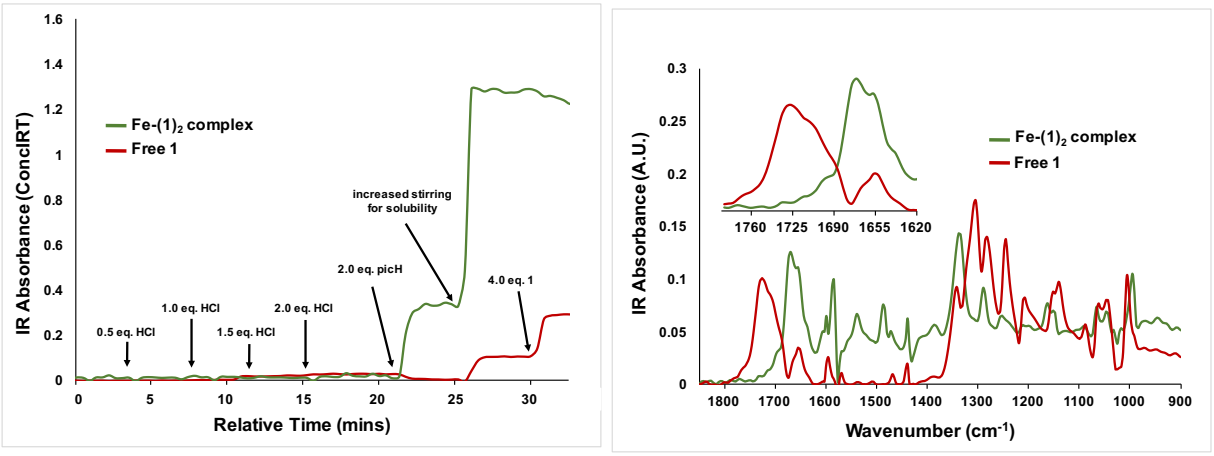

Figure 19: IR Absorbance for the Titration of HCl, Followed by Picolinic Acid into $FeCl_3$ in Pyridine.

5.13.3 Procedure for Reaction of $FeCl_3 \cdot 6H_2O$ with Pyridine in H_2O

To a 20 mL scintillation vial equipped with a Teflon-coated stirbar, pyridine (81 µL, 79 mg, 1.0 mmol, 3 equiv.) and 12 mL deionized H_2O were added. The solution was vigorously stirred (1500 rpm) at 25 °C. The ReactIR15 probe (see Materials and Methods) was inserted into the reaction vial and IR analysis was initiated. Subsequently, 250 µL aliquots (equivalent to 0.3 mmol, 0.3 equiv. $FeCl_3 \cdot 6H_2O$) of a standard solution of $FeCl_3 \cdot 6H_2O$ (1.08 g, 4.0 mmol) in 10 mL deionized H_2O were sequentially added in approximately 2 min. intervals (up to 1.7 equivs.). The spectra shown in Figure 20 were generated using the ConcIRT function of the iC IR software.

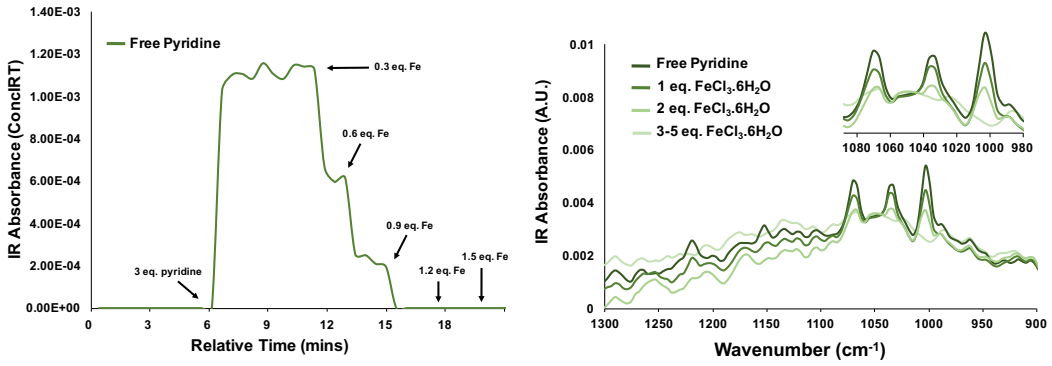

Figure 20: IR Absorbance for the Titration of $FeCl_3$ into Pyridine in Water.

5.13.4 Procedure for Background Reaction of HCl with Pyridine in H_2O

To a 20 mL scintillation vial equipped with a Teflon-coated stirbar, pyridine (81 µL, 79 mg, 1.0 mmol, 3 equiv.) and 12 mL deionized H_2O were added. The solution was vigorously stirred (1500 rpm) at 25 °C. The ReactIR15 probe (see Materials and Methods) was inserted into the reaction vial and IR analysis was initiated. Subsequently, 8.0 µL aliquots of hydrochloric acid (37% w/w, 7.8 mg, 0.3 mmol) were sequentially added (up to 1.7 equiv.) in approximately 2 min. intervals.. The spectra shown in Figure 21 were generated using the ConcIRT function of the iC IR software.

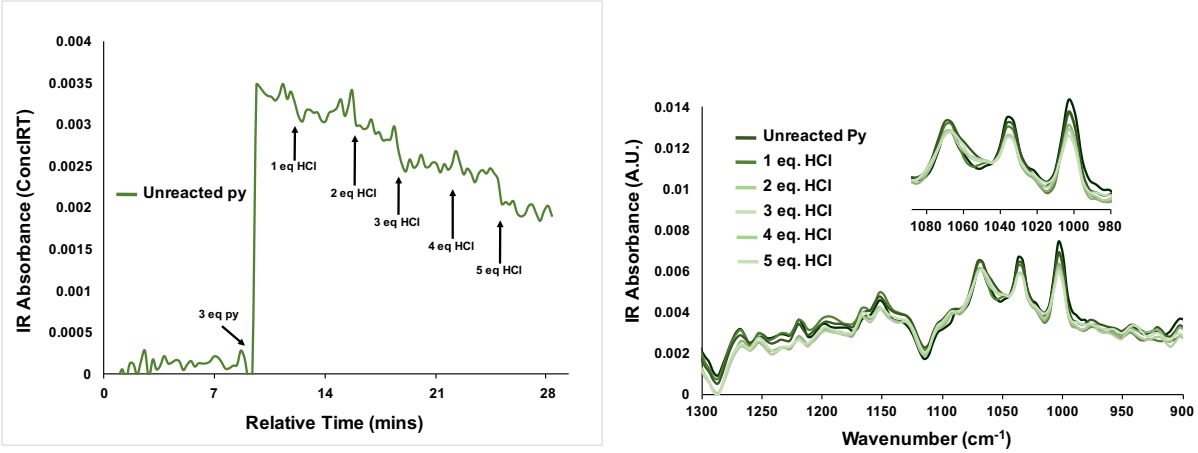

Figure 21: IR Absorbance for the Titration of HCl into Pyridine in Water.

5.13.5 Procedure for Reaction of NPr_3 with $FeCl_3 \cdot 6H_2O$/picH (1:1) in Pyridine

To a 20 mL scintillation vial equipped with a Teflon-coated stirbar, $FeCl_3 \cdot 6H_2O$ (270 mg, 1.0 mmol), picolinic acid (123 mg, 1.0 mmol) and 20 mL pyridine were added. The solution was vigorously stirred (1500 rpm) at 25 °C. The ReactIR15 probe (see Materials and Methods) was inserted into the reaction vial and IR analysis was initiated. Subsequently, 95 µL aliquots (72 mg, 0.5 mmol, 0.5 equiv.) NPr_3 were sequentially added in approximately 3 min. intervals (up to 5.0 equivs.). The spectra shown in Figure 22 were generated using the ConcIRT function of the iC IR software.

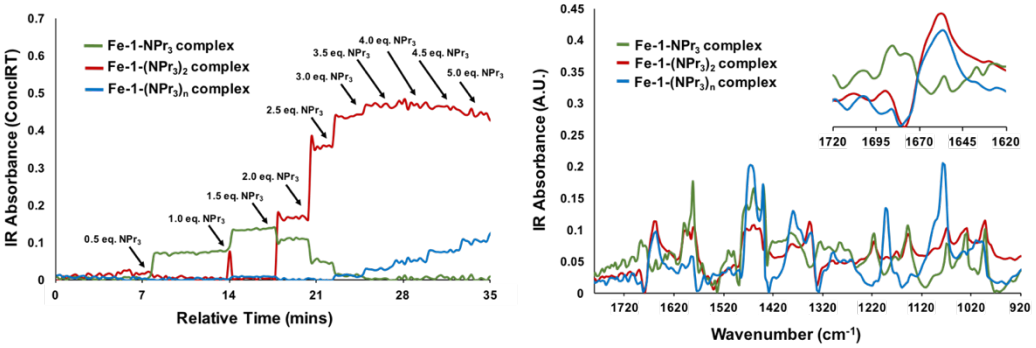

Figure 22: IR Absorbance for the Titration of NPr_3 into $FeCl_3$/Picolinic Acid (1:1) Pyridine

5.13.6 Procedure for Reaction of 2-Picolinic Acid With $FeCl_3 \cdot 6H_2O$ /NPr_3/ $PhCO_3{}^tBu$/H_2O in Pyridine

In analogy to the general procedure for method of initial rates, $PhCO_3{}^tBu$ (1.4 mL, 1.5 g, 7.5 mmol) and pyridine (15 mL), were added to a 20 mL scintillation vial equipped with a microstirbar. The reaction mixture was heated to 50 °C on a pre-heated vial plate and vigorously stirred (1500 rpm). The ReactIR15 probe (see Materials and Methods) was inserted into the reaction vial and IR analysis was initiated. Subsequently, the following reagents were preheated to 50 °C and added, in order, in approximately 15 min. intervals: (1) NPr_3 (476 µL, 358 mg, 2.5 mmol); (2) deionized H_2O (406 µL, 406 mg, 22.5 mmol, 9 eq.); (3) $FeCl_3 \cdot 6H_2O$ (34 mg, 125 µmol, 5.0 mol %); and finally (4) picolinic acid (15 mg, 125 µmol, 5.0 mol %). IR analysis was conducted for 4 h to generate the spectra below (Figure 23). The spectra were generated by monitoring $PhCO_3{}^tBu$ (ν =1757 cm^{-1}; C=O stretch) using the Mettler Toledo iC IR software.

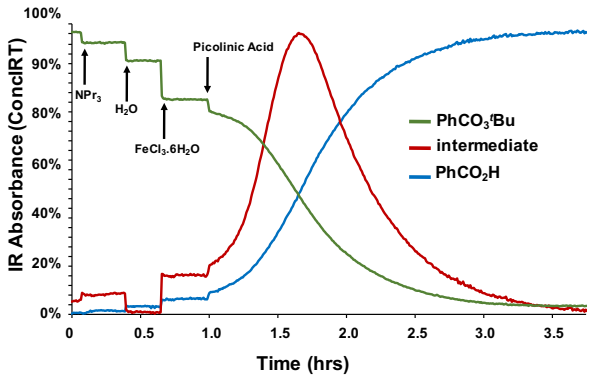

Figure 23: IR Absorbance for the Sequential Addition of Reagents in Fe-Catalyzed NPr_3 Oxidation

6 Attachments

6.1 Spectra

6.1.1 Determination of Sideproducts from Crude Tri(*n*-propyl)amine Catalytic Oxidation Mixture

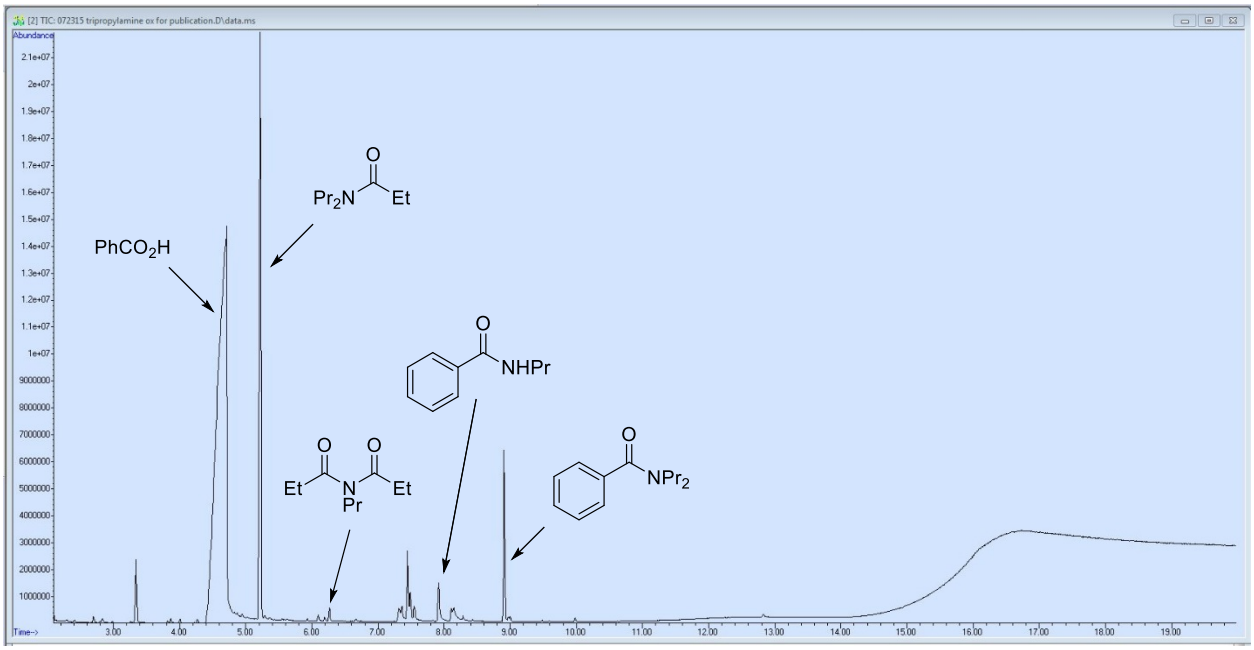

Figure 24: GCMS Chromatogram and Peak Assignments for Crude Tri(n-propyl)amine Oxidation Mixture.

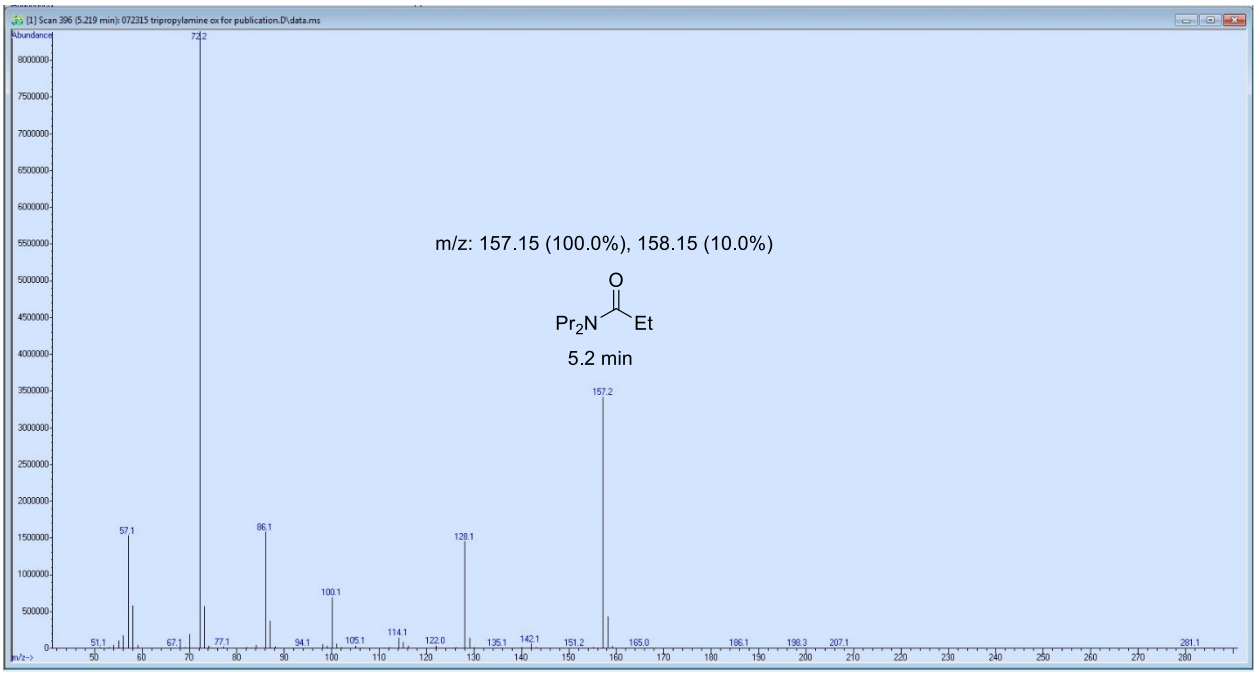

Figure 25: MS Spectrum derived from peak at 5.2 min.

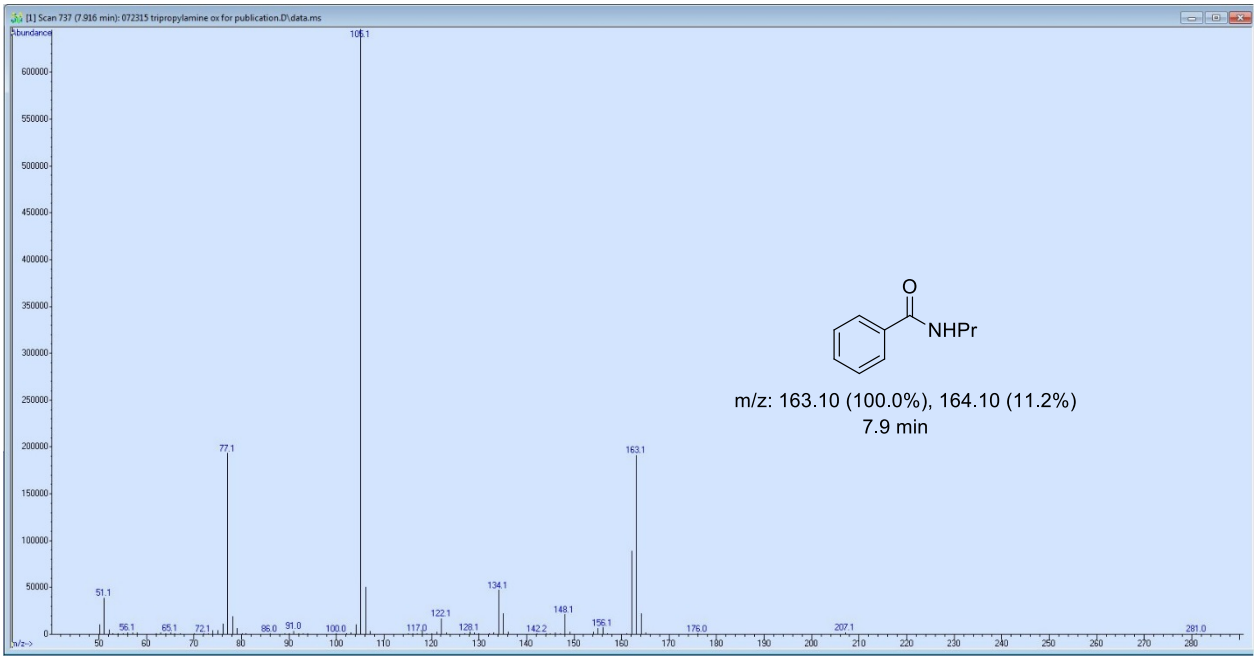

Figure 26: MS Spectrum derived from peak at 7.9 min.

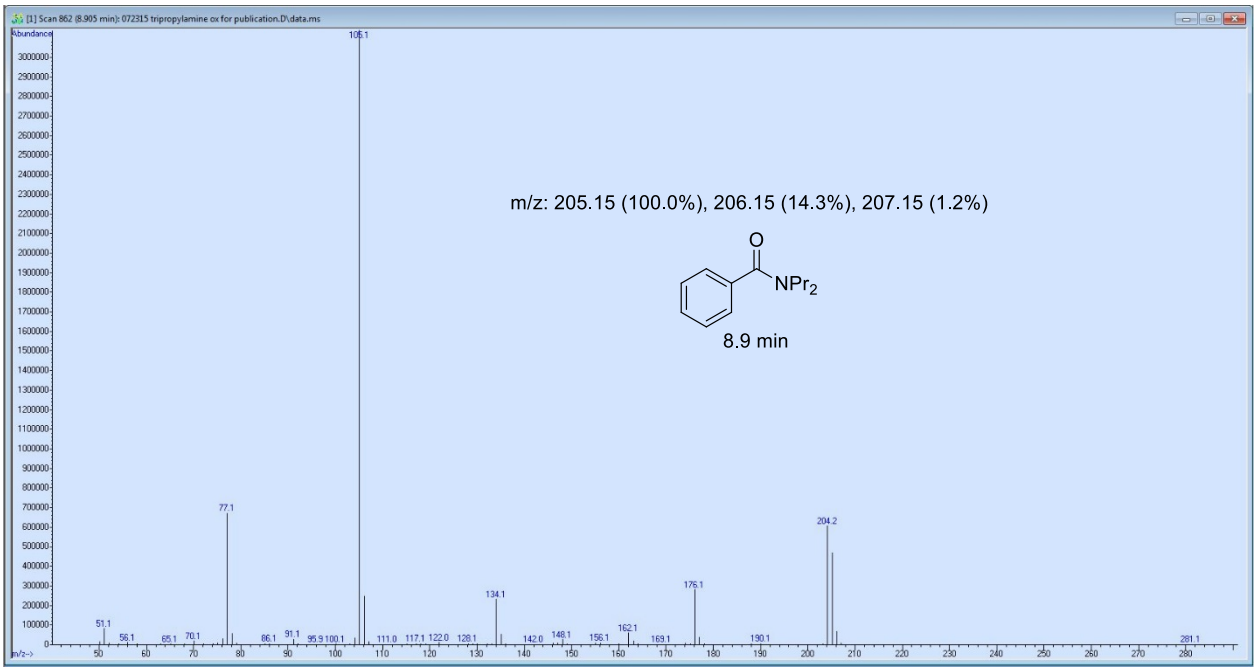

Figure 27: MS Spectrum derived from peak at 8.9 min.

6.1.2 NMR spectra of N,N-dipentylbenzamide in $CDCl_3$.

^{1}H NMR (500 MHz, $CDCl_3$, 25 ºC): δ = 7.32-7.39 (m, 5H), 3.48 (br, 2H), 3.17 (br, 2H), 0.81-1.66 (m, br, 18H) ppm.

^{13}C NMR (125 MHz, CDCl3, 25 ºC): δ = 171.8, 137.6, 129.1, 128.5, 126.6, 49.1, 44.8, 29.4, 28.8, 28.5, 27.4, 22.7, 22.3, 14.2, 14.0 ppm.

IR (thin film, NaCl disc): v = 2955, 2930, 2870, 2860, 1634, 1578, 1495, 1466, 1423, 1377, 1314, 1279, 1104, 786, 725, 700, 651 cm^{-1}

HRMS (M+H) calc. 262.216541; found 262.215789

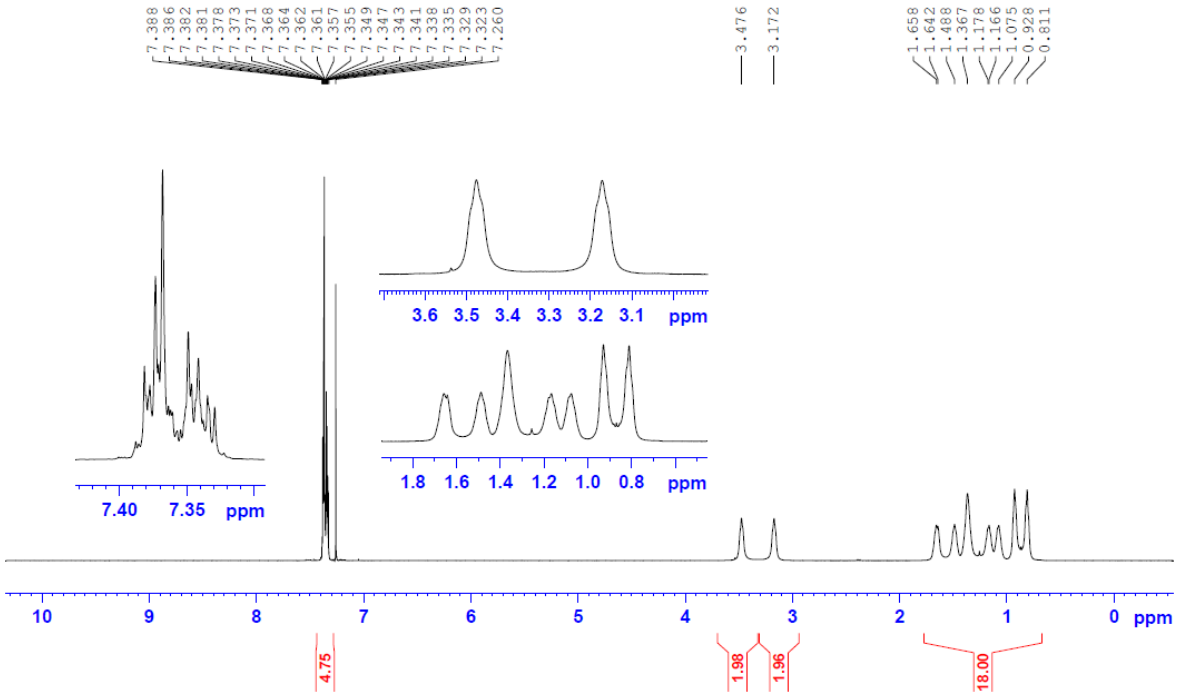

Figure 28: ^{1}H NMR spectrum of N,N-dipentylbenzamide in $CDCl_3$.

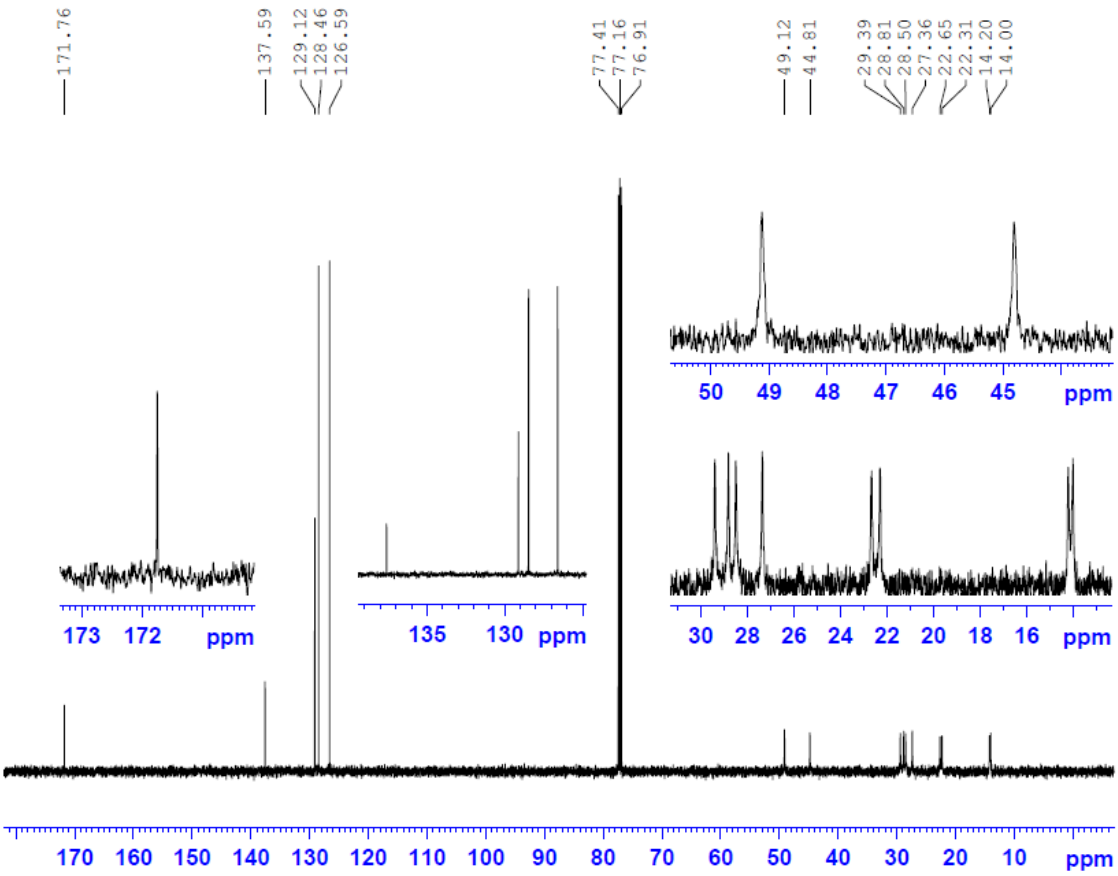

Figure 29: ^{13}C NMR spectrum of N,N-dipentylbenzamide in $CDCl_3$.

6.1.3 NMR spectra of *N*-Benzyl-*N*-pentylpentan-1-amine

^{1}H NMR (500 MHz, $CDCl_3$, 25 ºC): δ = 7.28-7.34 (m, 4H), 7.21-7.24 (m, 1H), 3.55 (s, 2H), 2.38-2.41 (t, *J* = 7.2 Hz, 4H), 1.44-1.50 (quint, *J* = 7.5 Hz, 4H), 1.22-1.33 (m, 8H), 0.87-0.90 (t, *J* = 7.0 Hz, 6H) ppm.

^{13}C NMR (125 MHz, CDCl3, 25 ºC): δ = 140.5, 129.0, 128.1, 126.7, 58.8, 54.0, 29.8, 26.9, 22.8, 14.3 ppm.

IR (thin film, NaCl disc): v IR (thin film, NaCl disc): v = 2954, 2930, 2871, 2859, 2795, 1494, 1465, 1453, 1377, 1367, 1098, 1083, 1069, 1028, 734, 697 cm^{-1}

HRMS (M+H) calc. 248.237276; found 248.237399

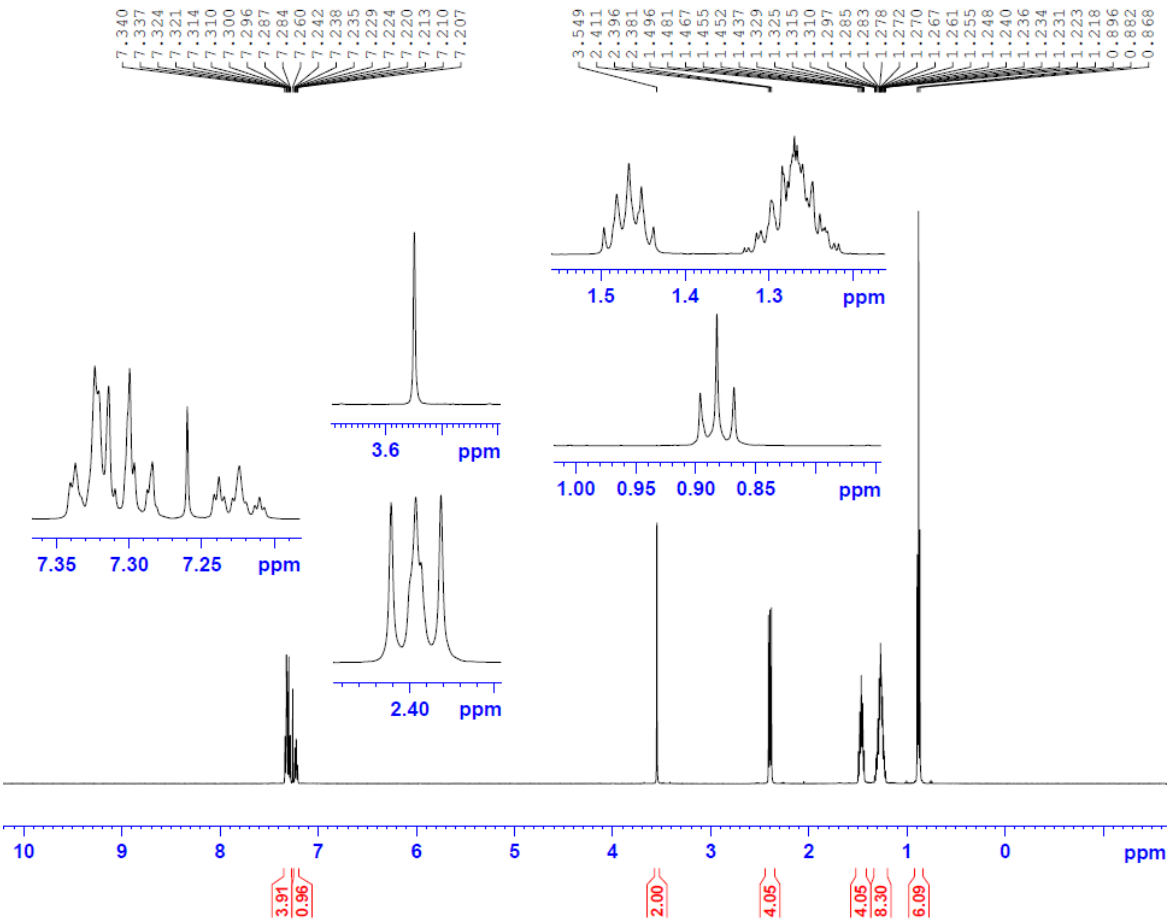

Figure 30: ^{1}H NMR spectrum of N-benzyl-N-pentylpentan-1-amine in $CDCl_3$.

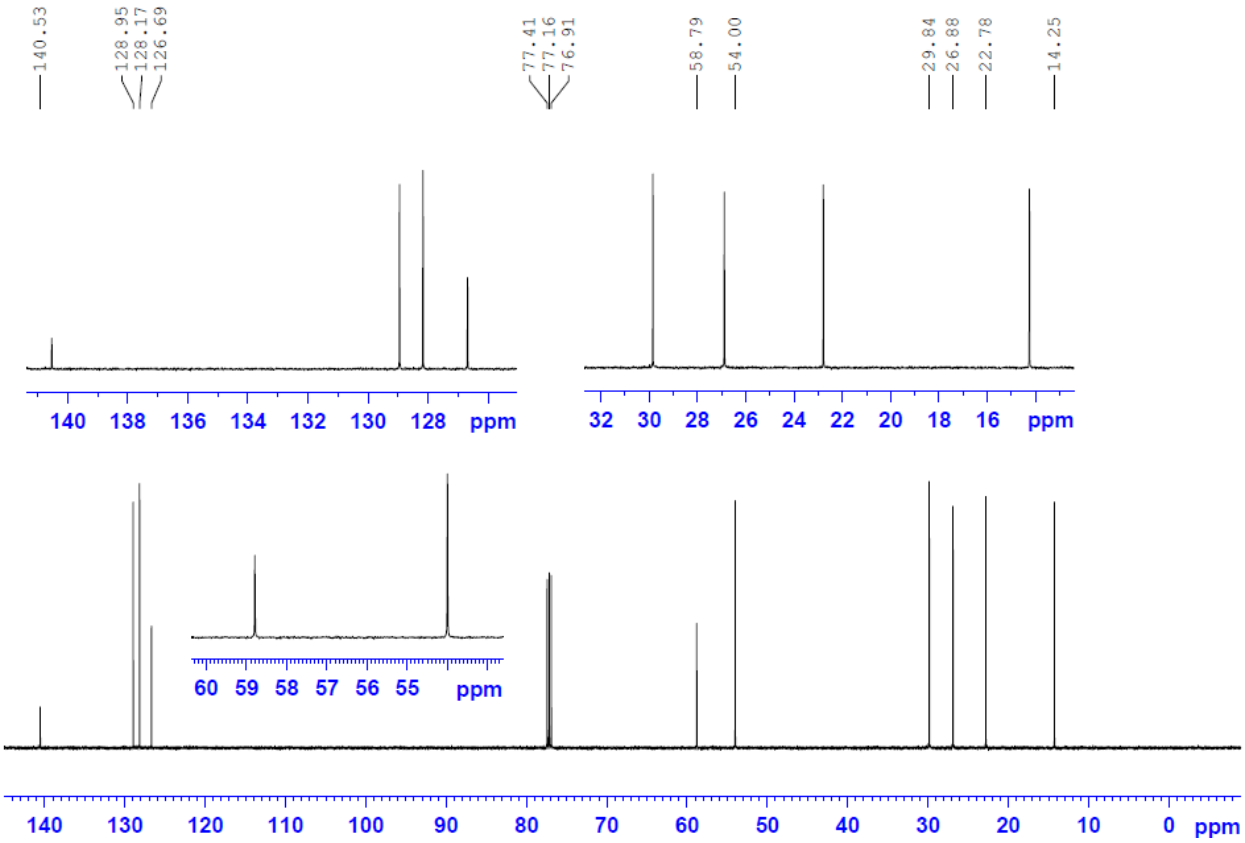

Figure 31: ^{13}C NMR spectrum of N-benzyl-N-pentylpentan-1-amine in $CDCl_3$.

6.1.5 NMR spectra of *N*,*N*-Dipentylpentanamide

^{1}H NMR (400 MHz, $CDCl_3$, 25 ºC): δ = 3.29 (t, *J* = 8.0 Hz, 2H), 3.20 (t, *J* = 8.0 Hz, 2H), 2.28 (t, *J* = 7.8 Hz, 2H), 1.59-1.65 (m, 2H), 1.48-1.58 (m, 4H), 1.21-1.39 (m, 10H), 0.86-0.94 (m, 9H) ppm.

^{13}C NMR (100 MHz, $CDCl_3$, 25 ºC): δ = 172.67, 48.01, 45.87, 32.92, 29.28, 29.11, 28.92, 27.72, 27.54, 22.67, 22.54, 22.49, 14.08, 14.02, 13.97 ppm.

IR (thin film, NaCl disc): v = 2958, 2930, 2872, 2860, 1646, 1466, 1422, 1378, 1270, 1240, 1195, 1146, 1103, 937, 884, 728 cm^{-1}

HRMS (M+H) calc. 241.2478; found 232.2459 (M+H).

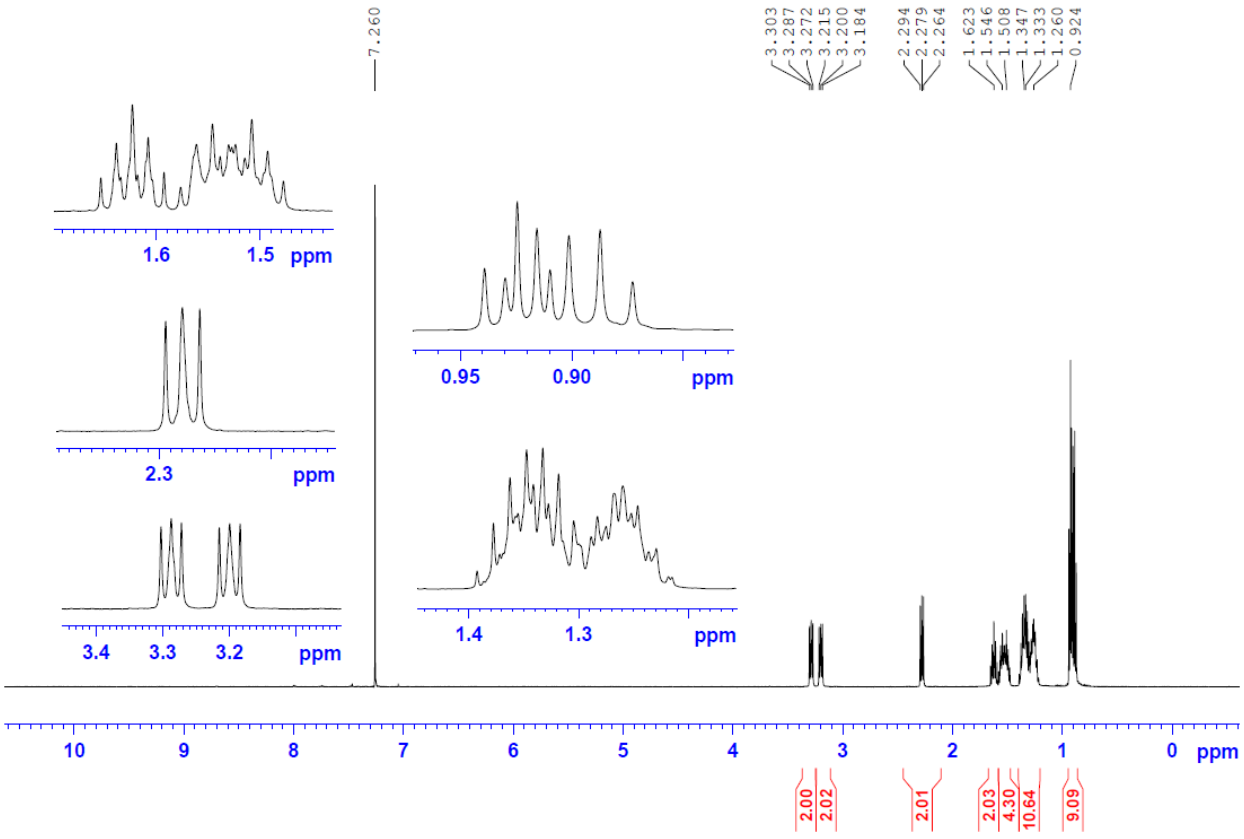

Figure 32: ^{1}H NMR spectrum of N,N-Dipentylpentanamide in $CDCl_3$.

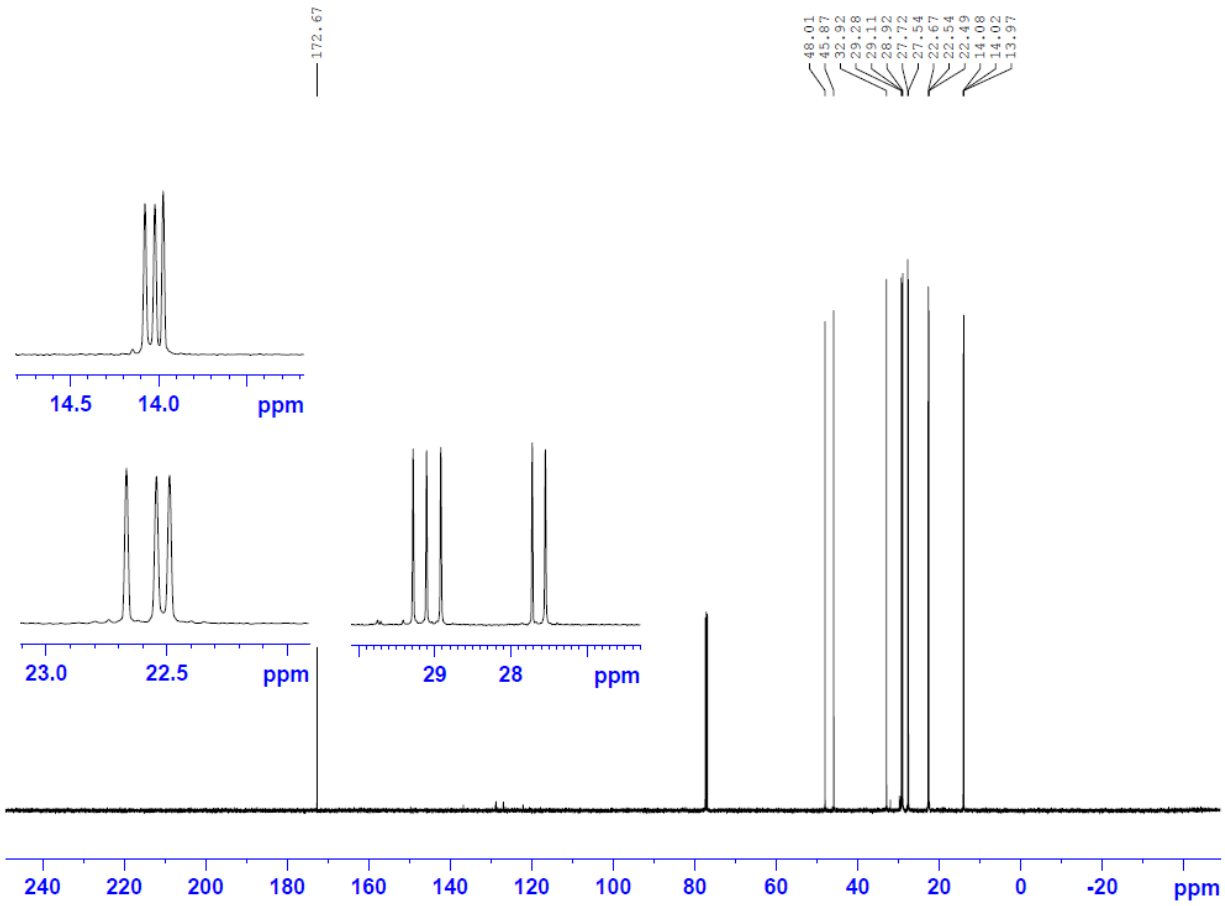

Figure 33: ^{13}C NMR spectrum of N,N-Dipentylpentanamide in $CDCl_3$.

6.1.6 LCMS Spectra of Lidocaine Catalytic Oxidation Reaction

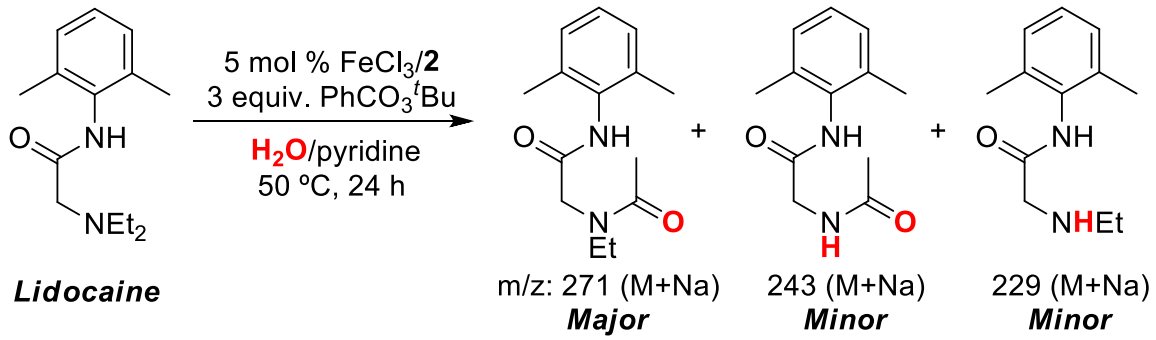

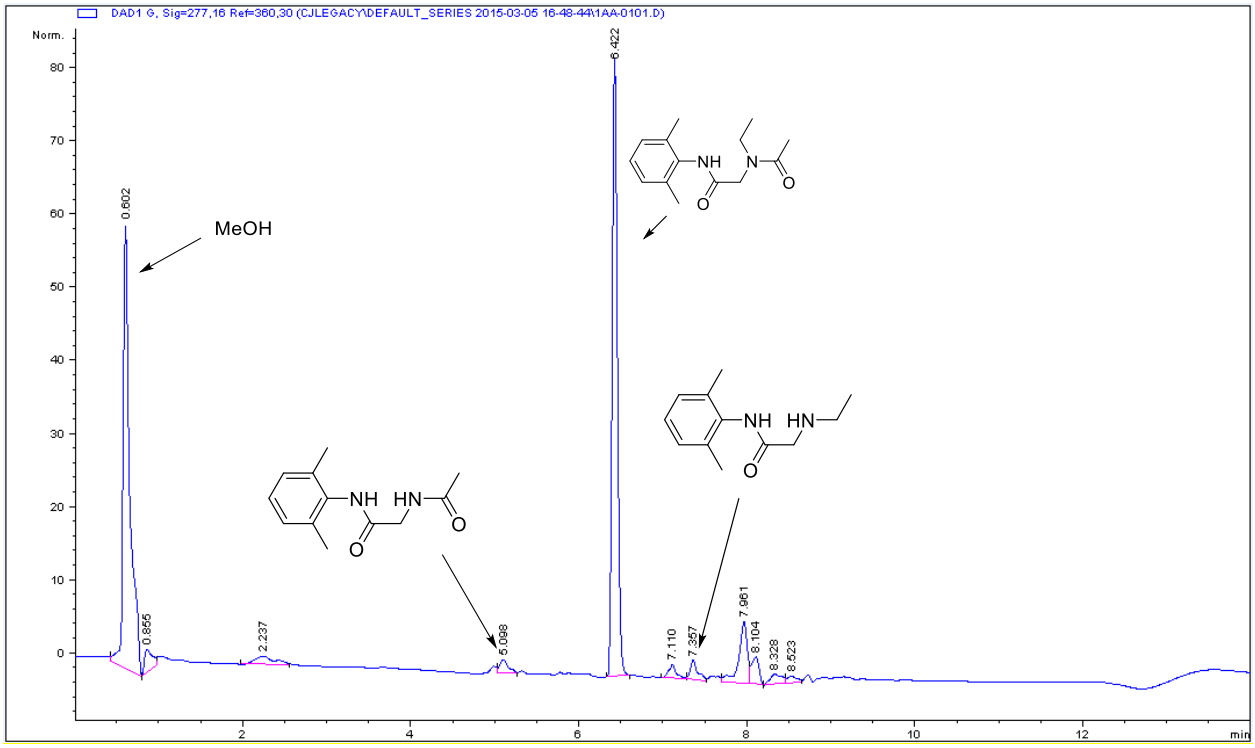

Figure 34: LCMS UV trace of Lidocaine Oxidation.

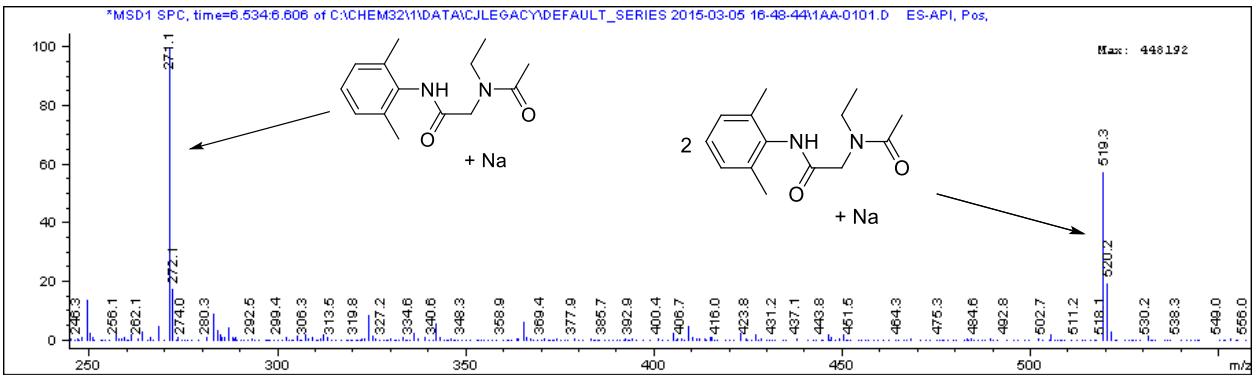

Figure 35: ESI-MS spectrum of main product at 6.5 min.

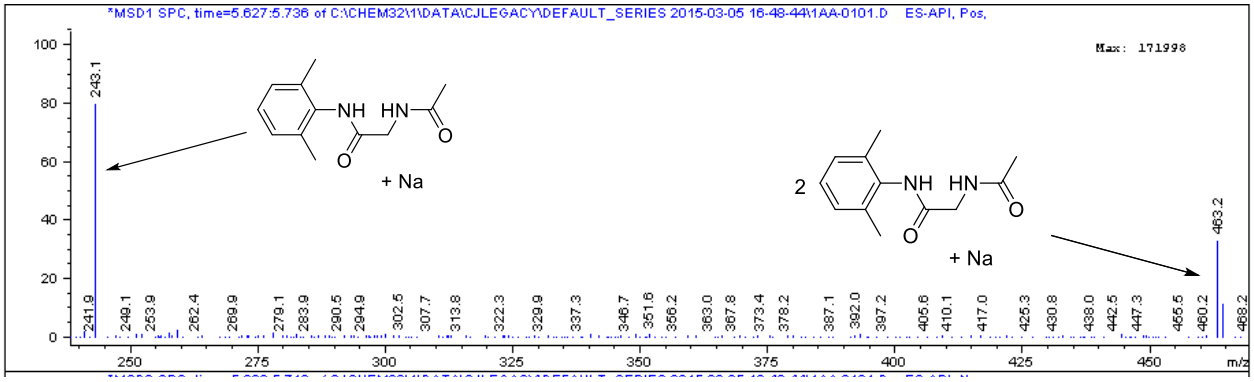

Figure 36: ESI-MS spectrum of dealkylation/oxidation product at 5.6 min.

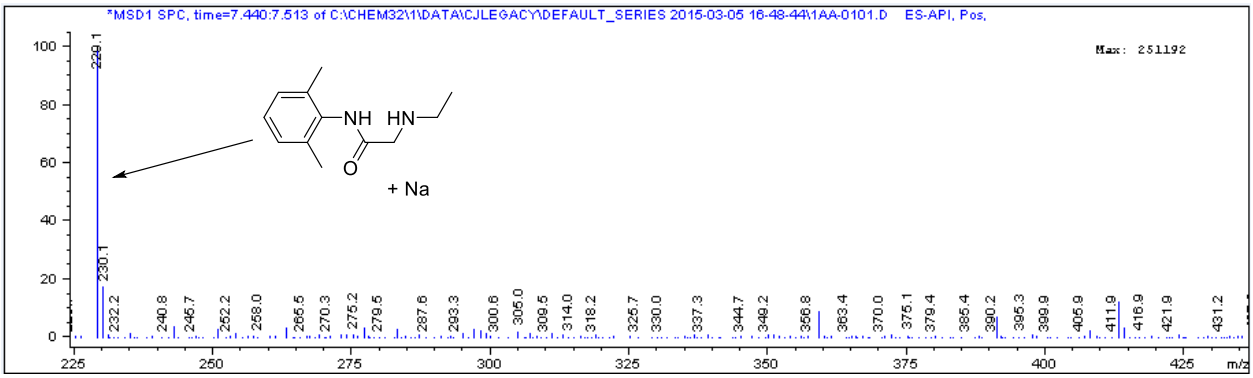

Figure 37: ESI-MS spectrum of dealkylation product at 7.4 min.

6.1.7 NMR Spectrum of Reaction with 2-methyl-1-phenylpropan-2-yl benzoperoxoate

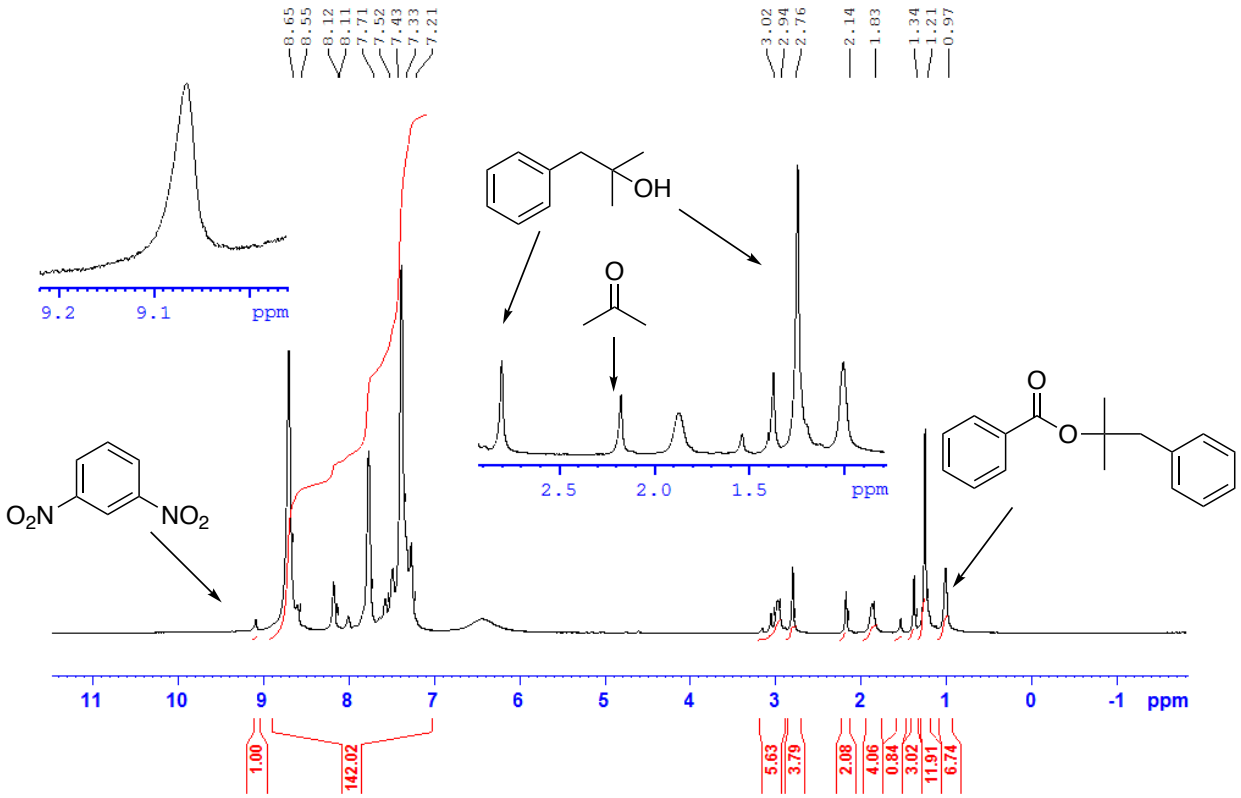

Figure 38: ^{1}H NMR spectrum of Reaction with 2-methyl-1-phenylpropan-2-yl benzoperoxoate.

7 References

[1] Aoki, White, and Fellers, A rheological and optical properties investigation of aliphatic (nylon 66, PγBLG) and aromatic (kelvar, nomex) polyamide solutions. *J. Appl. Polym. Sci.* **1979**, (23): 2293–2314.

[2] Chen, Holtz and Asher, UV Resonance Raman-Selective Amide Vibrational Enhancement: Quantitative Methodology for Determining Protein Secondary Structure. *Biochemistry* **1998**, *37* (9), 2854-2864.

[3] Constable, Dunn, Hayler, Humphrey, Leazer, Linderman, Lorenz, Manley, Pearlman, Wells, Zaks and Zhang, Key green chemistry research areas-a perspective from pharmaceutical manufacturers. *Green Chemistry* **2007**, *9* (5), 411-420.

[4] Anastas, *Green Chemistry: Theory and Practice*. Oxford **2000**.

[5] Rosen, Quasdorf, Wilson, Zhang, Resmerita, Garg and Percec, Nickel-Catalyzed Cross-Couplings Involving Carbon−Oxygen Bonds. *Chemical Reviews* **2010**, *111* (3), 1346-1416.

[6] Nomura and Zhang, Design of Vanadium Complex Catalysts for Precise Olefin Polymerization. *Chemical Reviews* **2010**, 111 (3), 2342-2362.

[7] Neumann and Gara, The Manganese-Containing Polyoxometalate, [WZnMnII2(ZnW9O34)2]12-, as a Remarkably Effective Catalyst for Hydrogen Peroxide Mediated Oxidations. *Journal of the American Chemical Society* **1995**, *117* (18), 5066-5074.

[8] Cahiez, Cobalt-Catalyzed Cross-Coupling Reactions. *Chemical Reviews* **2010**, 110 (3), 1435-1462.

[9] Colby, Tsai, Bergman and Ellman, Rhodium Catalyzed Chelation-Assisted C–H Bond Functionalization Reactions. *Accounts of Chemical Research* **2011**, *45* (6), 814-825.

[10] Rubottom and Gruber, m-Chloroperbenzoic acid oxidation of 2-trimethylsilyloxy-1,3-dienes. Synthesis of .alpha.-hydroxy and .alpha.-acetoxy enones. *The Journal of Organic Chemistry* **1978**, *43* (8), 1599-1602.

[11] Brown, Rao and Kulkarni, Stoichiometry of the oxidation of primary alcohols with pyridinium chlorochromate. Evidence for a two-electron change. *The Journal of Organic Chemistry* **1979**, *44* (15), 2809-2810.

[12 Anastasa, Kirchhoff and Williamson, Catalysis as a foundational pillar of green chemistry. *Applied Catalysis A* **2001**, 221 (2), 3-13.

[13] Dong, Saisaha, Meinds, Alsters, Ijpeij, Van Summeren, Mao, Fañanás-Mastral, de Boer, Hage, Feringa and Browne, Oxidation of Alkenes with H_2O_2 by an in-Situ Prepared Mn(II)/Pyridine-2-carboxylic Acid Catalyst and the Role of Ketones in Activating H2O2. *ACS Catalysis* **2012**, *2* (6), 1087-1096.

[14] Dhakshinamoorthy, Alvaro and Garcia, Aerobic Oxidation of Styrenes Catalyzed by an Iron Metal Organic Framework. *ACS Catalysis* **2011**, *1* (8), 836-840.

[15] Andraos, Unification of Reaction Metrics for Green Chemistry II: Evaluation of Named Organic Reactions and Application to Reaction Discovery. *Organic Process Research & Development* **2005**, *9* (4), 404-431.

[16] Jin-Quan, C-H Activation. Springer **2010**, 292.

[17] Gorzynski Smith, *Organic Chemistry*. McGraw Hill **2008**.

[18] Constable, Curzons and Cunningham, Metrics to 'green' chemistry—which are the best *Green Chem.,* **2002**, 4, 521-527.

[19] Clark, Green chemistry: challenges and opportunities. *Green Chem* **1999**, 1, 1-8.
[20] Crabtree, The Organometallic Chemistry of the Transition Metals. Wiley **2009**.
[21] Wang, Tetrahedron Letters Palladium-catalyzed aerobic oxidation of amines. *Tetrahedron Letters* **2006**, 47 (47), 8293-8297.
[22] Holtcamp, Intramolecular and intermolecular C-H activation at a cationic PtII center. *Inorganica Chimica Acta* **1998**, 270 (2),467–478.
[23] Hull, Anani, and Sanford, Palladium-Catalyzed Fluorination of Carbon−Hydrogen Bonds. *Journal of the American Chemical Society* **2006,** *128* (22), 7134-7135.
[24] Cho, Tse, Holmes, Maleczka Jr., and Smith III, Remarkably Selective Iridium Catalysts for the Elaboration of Aromatic C-H Bonds. *Science* **2002**, 295 (5553) 305-308.
[25] Colby, Bergman, and Ellman, Rhodium-Catalyzed C−C Bond Formation via Heteroatom-Directed C−H Bond Activation. *Chemical Reviews* **2010**, 110 (2), 624-655.
[26] Arockiam, Bruneau, and Dixneuf, Ruthenium(II)-Catalyzed C–H Bond Activation and Functionalization. *Chemical Reviews* **2012**, 112 (11), 5879-5918.
[27] Patil and Adimurthy, Copper-Catalyzed Aerobic Oxidation of Amines to Imines under Neat Conditions with Low Catalyst Loading. *Adv. Synth. Catal*. **2001**, 353, 1695–1700.
[28] Shen, Li ,Wang , Zhan , Tan and Guo, An efficient copper-catalyzed oxidative Mannich reaction between tertiary amines and methyl ketones. *Chem. Commun.* **2009**, 953-955.
[29] Sun, Li and Shi, Direct C−H Transformation via Iron Catalysis. *Chemical Reviews* **2010**, *111* (3), 1293-1314.
[30] Murahashi, Komiya, Terai and Nakae, Aerobic Ruthenium-Catalyzed Oxidative Cyanation of Tertiary Amines with Sodium Cyanide. *Journal of the American Chemical Society* **2003**, 125 (50), 15312-15313.
[31] Zhang, Tian, Xu, Yu, Xu, Iron-Catalyzed Direct Synthesis of Imines from Amines or Alcohols and Amines via Aerobic Oxidative Reactions under Air. Organic Letters **2013**, 15 (11), 2704-2707.
[32] Pan, Liu, Li, Wang, Guo and Li, Iron-Catalyzed N-Alkylation of Azoles via Oxidation of C−H Bond Adjacent to an Oxygen Atom. *Organic Letters* **2010**, *12* (9), 1932-1935.
[33] Han and Ofial, Iron catalyzed oxidative cyanation of tertiary amines. *Chem. Commun.* **2009**, 5024 – 5026.
[34] Xu, Jiang, and Fu, Copper-Catalyzed Aerobic Oxidative Synthesis of Primary Amides from (Aryl)methanamines. *Synlett* **2012**, 23, 801.
[35] Ratnikov and Doyle, Mechanistic Investigation of Oxidative Mannich Reaction with tert-Butyl Hydroperoxide. The Role of Transition Metal Salt. *Journal of the American Chemical Society* **2013**, 135 (4), 1549-1557.
[36] Barton, Gif chemistry: The present situation. Tetrahedron **1998**, 54 (22) 28, 5805-5817
[37] Barton and Doller, The Selective Functionalization of Saturated Hydrocarbons: Gif Chemistry. *Acc. Chem. Res*. **1992**, 25, 504-512
[38] Barton and Li, The selective functionalization of saturated hydrocarbons. Part 43. Modified Gif oxidation in acetonitrile. Tetrahedron **1998**, 54 (9) 26 1735-1744. Tetrahedron
[39] White, Adding Aliphatic C–H Bond Oxidations to Synthesis. *Science* **2012**, 17 807-809.
[40] Oloo and Que, Jr., Bioinspired Nonheme Iron Catalysts for C–H and C═C Bond

Oxidation: Insights into the Nature of the Metal-Based Oxidants. *Accounts of Chemical Research* **2015**, 48 (9), 2612-2621.
[41] Furge and Guengerich, Cytochrome P450 enzymes in drug metabolism and chemical toxicology: An introduction. *Biochem. Mol. Biol. Educ.* **2006**, 34, 66–74.
[42] Mansuy, Coordination Chemistry Reviews Activation of alkanes : the biomimetic approach Coordination. *Chemistry Reviews* **1993**, 125(2), 129-141.
[43] White, Doyle, and Jacobsen, A Synthetically Useful, Self-Assembling MMO Mimic System for Catalytic Alkene Epoxidation with Aqueous H_2O_2. *J. Am. Chem. Soc*., **2001**, 123 (29), 7194–7195.
[44] Nordstrøm, Vogt, and Madsen, Amide Synthesis from Alcohols and Amines by the Extrusion of Dihydrogen. *Journal of the American Chemical Society* **2008**, 130 (52), 17672-17673.
[45] Soulé, Miyamura, and Kobayashi, Powerful Amide Synthesis from Alcohols and Amines under Aerobic Conditions Catalyzed by Gold or Gold/Iron, -Nickel or -Cobalt Nanoparticles. *Journal of the American Chemical Society* **2011**, 133 (46), 18550-18553.
[46] Cho, Yoo, Bae, and Chang, Copper-Catalyzed Hydrative Amide Synthesis with Terminal Alkyne, Sulfonyl Azide, and Water. *Journal of the American Chemical Society* **2005**, 127 (46), 16046-16047.
[47] Muthaiah, Ghosh, Jee, Chen, Zhang, and Hong, Direct Amide Synthesis from Either Alcohols or Aldehydes with Amines: Activity of Ru(II) Hydride and Ru(0) Complexes. *The Journal of Organic Chemistry* **2010**, 75 (9), 3002-3006.
[48] Kang, Fu, and Hong, Ruthenium-Catalyzed Redox-Neutral and Single-Step Amide Synthesis from Alcohol and Nitrile with Complete Atom Economy. *Journal of the American Chemical Society* **2013**, 135 (32), 11704-11707.
[49] Chen, Zhang, and Hong, N-Heterocyclic Carbene Based Ruthenium-Catalyzed Direct Amide Synthesis from Alcohols and Secondary Amines: Involvement of Esters. *J. Org. Chem*. **2011**, 76 (24), 10005-10010.
[50] Constable, Dunn, Hayler, Humphrey, Leazer, Linderman, Lorenz, Manley, Pearlman, Wells, Zaks and Zhang, Key green chemistry research areas-a perspective from pharmaceutical manufacturers. *Green Chemistry* **2007**, *9* (5), 411-420.
[51] Schümperli, Hammond and Hermans, Developments in the Aerobic Oxidation of Amines. *ACS Catalysis* **2012**, *2* (6), 1108-1117.
[52] Xu, Jiang, and Fu, Copper-Catalyzed Aerobic Oxidative Synthesis of Primary Amides from (Aryl)methanamines. *Synlett* **2012**, 23, 801.
[53] Preedasuriyachai, Chavasiri, Sakurai, Aerobic oxidation of cyclic amines to lactams catalyzed by PVP-stabilized nanogold. *Synlett* **2011**, 1121.
[54] Klobukowski, Mueller, Angelici, Woo, Conversions of Cyclic Amines to Nylon Precursor Lactams Using Bulk Gold and Fumed Silica Catalysts. *ACS Catal.* **2011**, 1, 703.
[55] Murahashi, Mitani and Kitao, Ruthenium-catalyzed glycine-selective oxidative backbone modification of peptides. *Tetrahedron Letters* **2000**, *41* (52), 10245-10249.
[56] Khusnutdinova, Ben-David, and Milstein, Oxidant-Free Conversion of Cyclic Amines to Lactams and H2 Using Water As the Oxygen Atom Source. *Journal of the American Chemical Society* **2014**, 136 (8), 2998-3001.
[57] Yoshikai, Mieczkowski, Matsumoto, Ilies and Nakamura, Iron-Catalyzed C−C Bond Formation at α-Position of Aliphatic Amines via C−H Bond Activation through 1,5-Hydrogen Transfer. *Journal of the American Chemical Society* **2010**, *132* (16), 5568-5569.

[58] Genovino, Lütz, Sames, and Touré, Complementation of Biotransformations with Chemical C–H Oxidation: Copper-Catalyzed Oxidation of Tertiary Amines in Complex Pharmaceuticals. *Journal of the American Chemical Society* **2013,** *135* (33), 12346-12352.

[59] Genovinoa, Dalibo, and Touréa, Access to drug metabolites via C–H functionalization: copper-catalyzed aerobic oxidation of N,N-dimethylalkylamines in complex pharmaceuticals. *Tetrahedron Letters* **2015**, 56 (23), 3066-3069.

[60] Jacolot, Simon, Dreano, Beaune, Riche, Berthou, Identification of the cytochrome P450 IIIA family as enzymes involved in N-demethylation of tamoxifen in human liver microsomes. *Biochemical Pharmacology* **1991**, *41* (12), 1911-1919.

[61] Matsui, Mishima, Nagai, Yuzuriha, and Yoshimura, Absorption, Distribution, Metabolism, and Excretion of Donepezil (Aricept) after a Single Oral Administration to Rat. *Drug Metabolism and Disposition* **1999**, *27* (12), 1406-1414.

[62] Constable, Dunn, Hayler, Humphrey, Leazer, Linderman, Lorenz, Manley, Pearlman, Wells, Zaks and Zhang, Key green chemistry research areas-a perspective from pharmaceutical manufacturers. *Green Chemistry* **2007**, *9* (5), 411-420.

[63] Barton, On the mechanism of Gif reactions. *Chem. Soc. Rev.* **1996**, 25, 237-239.

[64] Murahashi, Mitani and Kitao, Ruthenium-catalyzed glycine-selective oxidative backbone modification of peptides. *Tetrahedron Letters* **2000**, *41* (52), 10245-10249.

[65] Li, Yang, Shi, Recent Advances in Direct Arylation via Palladium-Catalyzed Aromatic C-H Activation. *Synlett* **2008**,(7), 949-957.

[66] Lyons and Sanford, Palladium-Catalyzed Ligand-Directed C−H Functionalization Reactions. *Chemical Reviews* **2010** *110* (2), 1147-1169.

[67] Li, Yang, and Shi, Recent Advances in Direct Arylation via Palladium-Catalyzed Aromatic C-H Activation. *Synlett* **2008**, (7), 949-957.

[68] Jiang , Jin , Tian , Yuan , Yu and Xu, Direct and mild palladium-catalyzed aerobic oxidative synthesis of imines from alcohols and amines under ambient conditions. *Chem. Commun.* **2011**, 47, 10833-10835.

[69] Chu, Zhang and Qing, CuBr-Catalyzed Oxidative Difluoromethylation of Tertiary Amines with Difluoroenol Silyl Ethers. *Org. Lett.* **2009**, 11 (10), 2197–2200.

[70] Li and Li, CuBr-Catalyzed Efficient Alkynylation of sp3 C−H Bonds Adjacent to a Nitrogen Atom. *J Am. Chem. Soc.*, **2004**, 126 (38), 11810–11811.

[71] Stavropoulos, Çelenligil-Çetin, and Tapper, The Gif Paradox. *Accounts of Chemical Research* **2001,** *34* (9), 745-752.

[72] Peter Taylor, Mechanism and synthesis, Book 10 of Molecular world. Open University, Royal Society of Chemistry **2012**, 31.

[73] Lundstedta, Seiferta, Thelinc, Nyström, Pettersena, Bergmana, Chemometrics and Intelligent Laboratory Systems Experimental design and optimization. *Chemometrics and Intelligent Laboratory Systems* **1998**, 42 (2), 3-40.

[74] Rose, and Castagnoli, The metabolism of tertiary amines. *Medicinal Research Reviews* **1983**, 3 (1), 73-88.

[75] Matsui, Mishima, Nagai, Yuzuriha, and Yoshimura, Absorption, Distribution, Metabolism, and Excretion of Donepezil (Aricept) after a Single Oral Administration to Rat. *Drug Metabolism and Disposition* **1999**, *27* (12), 1406-1414.

[76] Meunier, de Visser, Shaik, Mechanism of Oxidation Reactions Catalyzed by Cytochrome P450 Enzymes. *Chemical reviews* **2004**, *104* (9), 3947-3980.

[77] Barton, Boivin, Gaudin, Jankowski, On the gif oxidation of alicyclic tertiary amines. *Tetrahedron Letters* **1989**, 30 (11), 1381-1382.

[78] Barton, Le Gloahec, Patin, and Launay, Radical chemistry of tert-butyl hydroperoxide (TBHP). Part 1. Studies of the Fe^{III}–TBHP mechanism. *New J Chem.* **1998**, 22, 559-563.
[79] Zolotova and Denisov, Formation of radicals by the reaction of peroxides with pyridine. *Russ. Chem. Bull.* **1966**, 15 (4), 736-738.
[80] Beckwith, Bowry and Moad, Kinetics of the coupling reactions of the nitroxyl radical 1,1,3,3-tetramethylisoindoline-2-oxyl with carbon-centered radicals. *The Journal of Organic Chemistry* **1988**, *53* (8), 1632-1641.
[81] Chatani, Asaumi, Yorimitsu, Ikeda, Kakiuchi, and Murai, $Ru_3(CO)12$-Catalyzed Coupling Reaction of sp^3 C−H Bonds Adjacent to a Nitrogen Atom in Alkylamines with Alkenes. *J. Am. Chem. Soc.* **2001**, *123*, 10935.
[82] Yoshikai, Mieczkowski, Matsumoto, Ilies, and Nakamura, Iron-Catalyzed C−C Bond Formation at α-Position of Aliphatic Amines via C−H Bond Activation through 1,5-Hydrogen Transfer *J. Am. Chem. Soc.* **2010**, *132*, 5568.
[83] Li and Li, CuBr-Catalyzed Efficient Alkynylation of sp3 C−H Bonds Adjacent to a Nitrogen Atom
J. Am. Chem. Soc. **2004**, 126, 11810.
[84] Pastine, Gribkov, and Sames, sp_3 C−H Bond Arylation Directed by Amidine Protecting Group: α-Arylation of Pyrrolidines and Piperidines. *J. Am. Chem. Soc.* **2006**, 128, 14220.
[85] DiRocco, and Rovis, Catalytic Asymmetric α-Acylation of Tertiary Amines Mediated by a Dual Catalysis Mode: N-Heterocyclic Carbene and Photoredox Catalysis *J. Am. Chem. Soc.* **2012**, *134*, 8094.
[86] Murahashi, Komiya, Terai, Nakae, T. Aerobic Ruthenium-Catalyzed Oxidative Cyanation of Tertiary Amines with Sodium Cyanide
. *J. Am. Chem. Soc.* **2003**, *125*, 15312.
[87] Enders and Shilvock, Some recent applications of α-amino nitrile chemistry, *Chem. Soc. Rev.* **2000**, *29*(5), 359-373.
[88] Kennedy and Ashley, Fourier Transform Infrared Spectrometry/Attenuated Total ReflectanceStudy of the Reaction of Pentanal and Propanal with 2-(Hydroxymethyl) piperidine. *Appl. Spectrosc.***1992**, 46 (2), 266-272.
[89] Murahashi, and Imada, Amine Oxidation, in Transition Metals for Organic Synthesis: Building Blocks and Fine Chemicals. Wiley, **2004**.
[90] Blackmond, Reaction Progress Kinetic Analysis: A Powerful Methodology for Mechanistic Studies of Complex Catalytic Reactions. *Angewandte Chemie International Edition* **2005**, 44 (28) 4302–4320.
[91] Espenson, Chemical Kinetics and Reaction Mechanisms. McGraw-Hill 2002, 5-8.
[92] Raheem, Izza, and Jacobsen, Highly Enantioselective Aza-Baylis–Hillman Reactions Catalyzed by Chiral Thiourea Derivatives. *Adv. Synth. Catal.* **2005**, 347, 1701–1708.
[93] Denmark and Chung, Lewis Base Catalyzed Addition of Trimethylsilyl Cyanide to Aldehydes. *The Journal of Organic Chemistry* **2006**, 71 (10), 4002-4005
[94] Jaimes, Böhling, Serrano-Becerra, and Hashmi, Highly Active Mononuclear NAC–Gold(I) Catalysts. *Angew. Chem. Int. Ed*. **2013**, 52, 7963–7966.
[95] Anslyn and Dougherty. Modern Physical Organic Chemistry. University Science Books **2006**.
[96] Chen,Lynch, Gomez-Romero, Ben-Hussein, Jameson, O'Connor, and Que, Jr, Iron-Oxo Aggregates. Binuclear and Tetranuclear Complexes of N,N,",N'-Tetrakis(2- benzimidazolylmethyl) -2-hydroxy- 1,3-diaminopropane. *Inorg. Chem.* **1988**, 27, 2673-2681.

[97] Jain and Bhattacharyya, The oxygenation of cyclohexane under GifIV conditions – The catalytic behaviour of iron complexes. *Inorganica Chimica Acta* **2006**, 359 (13), 4398-4402.
[98] Westheimer, The magnitude of the primary kinetic isotope effect for compounds of hydrogen and deuterium. *Chemical Reviews*, **1961**, 265-273.
[99] Simmons and Hartwig, On the Interpretation of Deuterium Kinetic Isotope Effects in C[BOND]H Bond Functionalizations by Transition-Metal Complexes. *Angew. Chem. Int.* **2012**, 51, 3066–3072.
[100] Blackmond, Kinetic Profiling of Catalytic Organic Reactions as a Mechanistic Tool. *Journal of the American Chemical Society* **2015**, *137* (34), 10852-10866.
[101] Zolotova and Denisov, Formation of radicals by the reaction of peroxides with pyridine. *Russ. Chem. Bull.* **1966**, 15 (4), 736-738.
[102] Murahashi, Naota, Miyaguchi, Nakato, Ruthenium-catalyzed oxidation of tertiary amines with hydrogen peroxide in the presence of methanol. *Tetrahedron Lett*. **1992**, 33 (46), 6991- 6994.
[103] Li and Li, CuBr-Catalyzed Efficient Alkynylation of sp^3 C−H Bonds Adjacent to a Nitrogen Atom. *J. Am. Chem. Soc.* **2004**, 126 (38), 11810-11811.
[104] Xia and Chen, Iron-Catalyzed N-Alkylation of Azoles via Cleavage of an sp^3 C–H Bond Adjacent to a Nitrogen Atom. *J. Org. Chem.* 2012, 77 (20), 9366-9373.
[105] Han, Mayer, and Ofial, Iron-Catalyzed Oxidative Mono- and Bis-Phosphonation of N,N- Dialkylanilines. *Adv. Synth. Catal.* **2010**, 352 (10), 1667-1676.
[106] Ghobrial, Harhammer, Mihovilovic, Schnurch, and Facile, Solvent and ligand free iron catalyzed direct functionalization of N-protected tetrahydroisoquinolines and isochroman. *Chem. Commun* **2010**, 46, 8836-8838.
[107] Murahashi, Komiya, Terai, Nakae, Aerobic Ruthenium-Catalyzed Oxidative Cyanation of Tertiary Amines with Sodium Cyanide. *J. Am. Chem. Soc.* **2003**, 125 (50), 15312-15313.
[108] Kuninobu, Nishi, and Takai, Iron-catalyzed synthesis of glycine derivatives via carbon-nitrogen bond cleavage using diazoacetate. Chem. Commun. **2010**, 46 (46), 8860-8862.
[109] Jia and Liu, The Conduct of Drug Metabolism Studies Considered Good Practice (II): In Vitro Experiments. *Curr. Drug Metab.* **2007**, 8 (8), 822-829.
[110] Genovino, Lutz, Sames, and Toure, Complementation of biotransformations with chemical C-H oxidation: copper-catalyzed oxidation of tertiary amines in complex pharmaceuticals. *J. Am. Chem. Soc*. **2013**, 135 (33), 12346-12352.
[111] Hedaya and Winstein, The Ionic Decomposition of 2-Substituted 2-Propyl p-Nitroperbenzoates. Migration to Electron-Deficient Oxygen and Anchimeric Acceleration of Peroxide-Bond Heterolysis. Journal of the American Chemical Society **1967**, 1 (7), 89.